DISS. ETH Nr. 10845

PHYSICAL PROPERTIES AND SEISMIC RESPONSE OF CARBONATE SEDIMENTS AND ROCKS

A B H A N D L U N G
Zur Erlangung des Titels

DOKTOR DER NATURWISSENSCHAFTEN

der

EIDGENÖSSISCHEN TECHNISCHEN HOCHSCHULE ZÜRICH

vorgelegt von:

Flavio Stefano Anselmetti

Dipl. Geol. Universität Basel

geboren am 3 Sept. 1965
von Berzona, Ti

Angenommen auf Antrag von:

Prof. Dr. Daniel Bernoulli, ETH Zürich,	Referent
Prof. Dr. Gregor P. Eberli, University of Miami,	1. Korreferent
Prof. Dr. Alan Green, ETH Zürich	2. Korreferent

1994

TABLE OF CONTENTS

ABSTRACT

The relationship between seismic reflection patterns and variations in lithology of carbonate sediments and rocks is twofold: (1) Physical rock properties, in particular sonic velocity and density, form the link between the seismic record and the lithology of the carbonates. Through a detailed laboratory study lithological factors that control velocity are investigated and characteristic velocity patterns are assigned to the diagenetic stages of the rocks. (2) The seismic image of carbonate rocks is dependent on the technical parameters of the reflection seismic survey. The influence of these seismic parameters is studied using computer modeled synthetic seismic sections.

Compressional wave and shear wave velocities (Vp and Vs) of 295 carbonate minicores from different areas and of different age were measured under variable confining and pore fluid pressures. The samples range from unconsolidated carbonate mud to completely lithified limestones. The results of the measurements show that for pure carbonate rocks, unlike siliciclastic or shaly sediments, there is little direct correlation between the acoustic properties (Vp and Vs) and the burial of depth or age. Velocity inversions with increasing depth are thus common. Sonic velocity in carbonates is more controlled by the combined effect of depositional lithology and a suite of post-depositional processes, such as cementation and dissolution.

At 8 MPa effective pressure, Vp ranges from 1700 to 6500 m/s and Vs ranges from 700 to 3400 m/s. This range is caused mainly by variations in the amount of porosity and the porosity type, and not by variations in mineralogy. In general, the measured velocities show a positive correlation with density and an inverse correlation with porosity, but departures from the general trends can be as high as 2500 m/s. These deviations can be explained by the occurrence of different pore types that form during specific diagenetic phases. The data set further suggests that commonly used correlations like the general Gardner's Law (Vp - density) or the time-average-equation (Vp - porosity) should be modified, since they generally result in too low velocities for carbonates.

Velocity measurements of unconsolidated carbonate mud at different stages of experimental compaction show that velocity increases due to compaction are lower than the observed velocity increases at decreasing porosities in natural rocks. This difference

shows that diagenetic changes, such as cementation-dissolution processes, which may predate or accompany compaction, influence velocity more than simple compaction at increasing burial depth.

The knowledge of the relationship between velocity and porosity from discrete samples are applied in the interpretation of a continuous downhole record of wireline logs. A synthetic "velocity deviation" log can be calculated by taking the difference between the velocities from the sonic log and the velocities expected from the porosity value on the neutron-porosity log. These differences, either positive or negative deviations, mark zones in the cores, in which velocity is higher or lower than expected from the porosity value. As seen in the measured samples, these zones can be related to constructive or destructive diagenetic processes that can be traced continuously downhole using the velocity deviation log.

The results of the laboratory analyses were also applied in a seismic modeling study of a well-exposed carbonate platform margin and its adjacent basin (Montagna della Maiella, Italy). The resulting synthetic seismic sections explain the seismic facies of a carbonate platform margin system, but, in addition, show the limitations of relating in a simple manner seismic sequences to depositional sequences.

To define a layered impedance model, velocities and densities of all major outcropping lithologies were determined. The impedance model was converted into synthetic seismic data by applying a computer-simulated modeling procedure that uses the normal incidence raytracing method at variable frequencies, amplitude gains, and noise levels. The resulting synthetic seismic sections display a mostly transparent platform, which is onlapped on the escarpment by a succession of high-amplitude slope reflections. The different reflectivities of platform and slope are concordant with the small range of impedance contrasts in platform carbonates compared to the large range of impedance contrasts in the carbonates from the slope and basin. The seismic image with an incoherent to transparent platform, high-amplitude slope reflections and recognizable prograding units is very similar to observed seismic data from other steep carbonate platform margins, e.g. from the subsurface of Great Bahama Bank.

In outcrop, seven unconformity-bounded supersequences were mapped. A comparison with the synthetic seismic section shows that, using a dominant frequency of 20 Hz, only five of these seven depositional supersequences can be recognized by seismic unconformities. With an increase of frequency, an increasing number of unconformities becomes visible and, using a frequency of 60 Hz, all seven supersequences are imaged. However, some of the seismic unconformities are pseudo-unconformities and image erroneous or non-existent geometrical patterns. The different numbers of seismic sequences at different frequencies, plus the appearance of pseudo-

unconformities, document the problem of seismically imaging depositional sequences. Dependent on the dominant frequency, an erroneous number of sequences might be interpreted. This limitation has to be taken into account, when making sequence stratigraphic interpretations based solely on seismic information.

ZUSAMMENFASSUNG

Der Zusammenhang zwischen der Lithologie und dem seismischen Reflektionsmuster von Karbonatsedimenten und Kalksteinen kann in zwei Bereiche gegliedert werden: (1) Die physikalischen Gesteinseigenschaften, im speziellen sind dies Schallgeschwindigkeit und Gesteinsdichte, bilden das Bindeglied zwischen den seismischen Daten und der Karbonatlithologie. Detaillierte Laboranalysen wurden durchgeführt, um die Gesteinsparameter zu untersuchen, welche die Schallgeschwindigkeit beeinflussen. Charakteristische Geschwindigkeitswerte können so den verschiedenen Karbonattypen zugeordnet werden. (2) Das seismische Abbild der Karbonate ist auch abhängig von der Wahl der technischen Parameter der seismischen Untersuchung. Der Einfluss dieser Parameter kann mittels computergestützten Modellierungen von synthetischen seismischen Profilen untersucht werden.

Die Geschwindigkeiten von longitudinalen und transversalen Schallwellen (Vp und Vs) in 275 Gesteinskernen von Kalken unterschiedlichen Ursprungs und Alter wurden im Labor unter variablen Umgebungs- und Porenwasser-Drucken gemessen. Die Lithologien der gemessenen Proben reichen von unverfestigten Kalkschlammen zu vollständig zementierten Kalksteinen. Die Ergebnisse der Messungen zeigen, dass, im Gegensatz zu siliziklastischen oder tonigen Gesteinen, die akustischen Eigenschaften von reinen Karbonaten kaum mit dem Gesteinsalter oder der Versenkungstiefe zusammenhängen. Geschwindigkeitsabnahmen bei zunehmender Tiefe sind deshalb häufig anzutreffen. Vielmehr ist die Schallwellengeschwindigkeit ein kombiniertes Produkt der Lithologie des Ausgangssedimentes und der verschiedenen Prozesse der Diagenese, wie z. Bsp. Zementierungs- oder Lösungsvorgänge.

Vp variiert bei einem effektiven Druck von 8 MPa zwischen 1700 und 6500 m/s, während dem Vs Werte zwischen 700 und 3400 m/s erreicht. Diese Variationen in der Geschwindigkeit sind hauptsächlich eine Funktion der Porosität sowie des Porentyps, und weniger eine Funktion der mineralogischen Zusammensetzung. Zunehmende

Gesteinsdichte oder abnehmende Porosität führen normalerweise zu einer Zunahme der Geschwindigkeit. Einige Messungen weichen jedoch mit über 2500 m/s von den durschnittlichen Korrelationen ab. Diese Abweichungen können durch spezielle Porentypen erklärt werden, die sich während den verschiedenen Phasen der Diagenese bilden. Im Weiteren lassen die Labormessungen darauf schliessen, dass häufig gebrauchte Korrelationen wie das "Gardner's Law" (Vp - Dichte) oder die "time-average-equation" (Vp - Porosität) korrigiert werden müssen, da sie meistens zu tiefe Karbonat-Geschwindigkeiten liefern.

Geschwindigkeitsmessungen an unverfestigtem Karbonatschlamm im Zustand unterschiedlicher, künstlicher Kompaktion dokumentieren, dass die Geschwindigkeitszunahme durch reine Kompaktion geringer ist, als die Zunahme durch abnehmende Porosität in natürlich verfestigten Gesteinen. Diese Diskrepanz zeigt deutlich, dass diagenetische Prozesse, die vor oder während der Kompaktion stattfinden, die Schallgeschwindigkeit stärker als die Kompaktion bei zunehmender Überlast beeinflussen.

Die aus den Laboruntersuchungen stammenden Kenntnisse des Zusammenhangs zwischen Geschwindigkeit und Porosität können bei der Interpretation von kontinuierlichen Logdaten aus Bohrlöchern angewendet werden. Ein künstliches "Geschwindigkeits-Abweichungs" Log kann aus der Differenz zwischen der Geschwindigkeit des Sonic Logs und der von der Porosität zu erwarteten Geschwindigkeit des Neutron-Porosität Logs berechnet werden. Diese Differenzen, entweder positive oder negative Abweichungen, zeigen Zonen auf, in denen die Geschwindigkeit höher oder tiefer ist, als die Geschwindigkeit, die von der Porosität erwartet wird. Wie durch die Laboruntersuchungen gezeigt wurde, stehen diese Zonen im Zusammenhang mit konstruktiven oder destruktiven diagenetischen Prozessen, die anhand des Geschwindigkeits-Abweichung Logs kontinuierlich im Bohrloch vefolgt werden können.

Eine weitere Anwendung der Ergebnisse der Laboranalysen sind die seismischen Modellierungen eines gut aufgeschlossenen Karbonatplattformrandes und des dazugehörenden Abhangs (Montagna della Maiella, Italien). Die resultierenden synthetischen seismischen Linien erklären das seismische Reflexionsmuster von Karbonatplattformrändern, doch zeigen sie gleichzeitig die Limiten auf, die bei der Zuordnung von seismischen Sequenzen zu Ablagerungssequenzen entstehen.

Die Geschwindigkeiten und Dichten der wichtigsten aufgeschlossenen Lithologien wurden gemessen, um damit ein geschichtetes Impedanzmodel zu definieren. Dieses Impedanzmodel wird mittles einer computergestützten Modellierung in synthetische

seismische Daten verwandelt, wobei die Methode des "normal incidence raytracing" mit variablen Frequenzen, Verstärkungen und Lärmpegeln angewendet wird.

Die synthetischen seismischen Linien bilden eine seismisch transparente Plattform ab, welche an der Plattformwand durch eine Abfolge von starken Abhang-Reflektionen angelagert wird. Die verschiedenen Reflektivitäten von Plattform und Abhang stimmen gut mit dem engen Bereich von Impedanzwerten in Plattformkalken und dem weiten Impedanz-Bereich von Abhang- und Beckenkarbonaten überein. Dieses seismische Muster, mit einer inkoherenten bis transparenten Plattform, einem gut reflektierenden Abhang und den erkennbaren progradierenden Einheiten, ist dem Muster auf echten seismischen Profilen von steilen Plattformrändern sehr ähnlich (z. Bsp. Great Bahama Bank).

Sieben Supersequenzen konnten im Feld kartiert werden, die durch Diskordanzen voneinander getrennt sind. Ein Vergleich mit den synthetischen seismischen Profilen zeigt, dass lediglich fünf der sieben Supersequenzen bei einer dominierenden Frequenz von 20 Hz durch seismische Diskordanzen erkannt werden können. Erhöht man die Frequenz, erhöht sich auch die Anzahl der erkennbaren seismischen Diskordanzen. Bei 60 Hz können schliesslich sämtliche sieben Sequenzen aufgelöst werden. Einige der erkennbaren Diskordanzen sind jedoch Pseudo-Diskordanzen und bilden falsche oder nicht existierende Geometrien ab. Die unterschiedliche Anzahl seismischer Sequenzen bei verschiedenen Frequenzen, sowie die Pseudo-Diskordanzen, zeigen die Problematik des seismischen Abbildens von Ablagerungssequenzen auf. Eine falsche Anzahl Sequenzen kann erkannt werden, je nach dominanter seismischer Frequenz. Diese Limitierung sollte bei der Anwendung der Sequenzstratigraphie in Betracht gezogen werden, falls sie ausschliesslich auf der Interpretation von seismischen Daten beruht.

RIASSUNTO

La relazione esistente fra l'immagine di riflessione sismica e le variazioni in litologia dei sedimenti carbonatici ha due implicazioni: (1) le proprieta' fisiche delle roccie, ed in particolare la velocità sonica e la densità costituiscono la connessione fra la documentazione sismica e la litologia dei carbonati. Grazie ad un dettagliato studio di laboratorio sono stati studiati i fattori che controllano la velocità sonica ed e' stato possibile ricondurre le caratteristiche immagini ai differenti stadi diagenetici di una roccia. (2) La immagine sismica di una roccia carbonatica e' funzione dei parametri tecnici

utilizzati dal servizio di riflessione sismica. L'influenza di tali parametri sismici viene studiata utilizzando delle sezioni sismiche sintetiche modellate al computer.

La velocità delle onde compressive e di taglio (Vp e Vs) di 295 minicarote di rocce carbonatiche provenienti da diverse aree e di diversa età sono state misurate sotto condizioni variabili della pressione confinante e dei fluidi presenti nei pori. I campioni presentano una ampia gamma di variazioni, da fango inconsolidato fino a una roccia carbonatica completamente litificata. I risultati delle misurazioni mostrano che per una roccia carbonatica pura, contrariamente a quanto si verifica per i sedimenti terrigeni o argillosi, esiste una minima correlazione diretta fra le proprietà acustiche (Vp and Vs) ed il grado di seppellimento od età della roccia. Pertanto le inversioni di velocità con la profondità si verificano comunemente. La velocità sonica nelle rocce carbonatiche è piuttosto controllata dagli effetti combinati di litologia deposizionale e di un insieme di processi post-deposizionali, quali la cementazione e la dissoluzione.

Ad una pressione effettiva di 8 MPa, la Vp varia fra 1700 to 6500 m/s e la Vs varia fra 700 to 3400 m/s. Questa variabilità è causata principalmente da variazioni fra la quantita' di porosità piuttosto che da variazioni in mineralogia. In generale, le velocità misurate mostrano una correlazione positiva con la densità ed una correlazione negativa con la porosità, anche se deviazioni da questo andamento generale possono raggiungere fino 2500 m/s. Queste deviazioni si possono spiegare con l'occorrenza di diversi tipi di pori che si formano durante specifiche fasi diagenetiche. L' insieme dei dati suggerisce che correlazioni normalmente utilizzate, quali la legge generale di Gardner (Vp - densità) o la "time-average-equation" (Vp - porosità), debbano essere modificate, dal momento che esse risultano in velocità troppo basse per le litologie carbonatiche.

Misurazioni della velocità di fango carbonatico inconsolidato a diversi stadi di compattazione sperimentale indicano che gli aumenti di velocità dovuti alla compattazione sono piu' bassi degli aumenti dei velocità osservati a pressioni decrescenti in rocce naturali. Questa differenza mostra che i cambiamenti diagenetici, quali i processi di cementazione-dissoluzione, che possono verificarsi sia prima che dopo la compattazione, influenzano la velocità piu' della semplice compattazione dovuta ad un aumento progressivo della pressione di carico.

La conoscenza di questa relazione fra velocità e porosità derivata da campioni discreti viene applicata alla interpretazione di una documentazione continua di wireline logs lungo pozzo. Un log sintetico della "deviazione della velocità" puo' essere calcolato dalla differenza fra le velocita' dal log sonico e le velocità previste dal valore della porosità derivata dal log neutron-porosity. Queste differenze, sia positive che negative, marcano nelle carote delle zone nelle quali la velocità é maggiore o minore di quanto ci si aspetterebbe dal valore della porosità. Come discusso per i campioni misurati, l'origine

di queste zone puo' essere attribuita a processi diagenetici costruttivi o distruttivi, che possono essere tracciati lungo pozzo grazie all'uso di un log della deviazione della velocità.

I risultati delle analisi di laboratorio sono state anche applicate ad uno studio di modellizzazione sismica di un margine di piattaforma carbonatica e dell'adiacente bacino (Montagna della Maiella, Italia). Le risultanti sezioni sismiche sintetiche illustrano le facies sismiche di un sistema di margine di piattaforma carbonatica, ma in piu' mostrano le limitazioni che esistono nel mettere direttamente in relazione le sezioni sismiche alle sequence deposizionali.

In modo da definire un modello di impedenza a livelli, sono state determinate le velocità e la densità di tutte le principali litologie osservate sul terreno. Il modello di impedenza e' stato convertito in dati sismici sintetici utilizzando dei procedimenti che utilizzano il metodo "normal incidence raytracing" a frequenze variabili, aumenti di amplitudine, e livelli di disturbo del segnale. Le risultanti sezioni sismiche sintetiche mostrano una piattaforma prevalentemente trasparente, che viene onlappata sulla scarpata da una successione di riflettori di pendio ad alta amplitudine. Le diverse riflettività di piattaforma e pendio concordano con la bassa variabilità dei contrasti di impedenza in una piattaforma carbonatica rispetto alla alta variabilità dei contrasti di impedenza nei carbonati di pendio e bacino. La immagine sismica di una piattaforma da incoerente a trasparente, con riflettori di pendio ad alta amplitudine e con riconoscibili unità progradanti, è molto simile ai dati osservabili in altri margini di piattaforma ripidi, quali i dati di sottosuolo del Great Bahama Bank.

In affioramento, sono state riconosciute sette supersequenze delimitate de discontinuità. Un confronto con la sezione sismica sintetica mostra che, utilizzando la comune frequenza di 20 Hz, solo cinque delle sette sequenze deposizionali possono essere riconosciute grazie a discontinuità sismiche. Con un aumento della frequenza, un numero sempre maggiore di discontinuità diventa visibile e, utilizzando una frequenza di 60 Hz, tutte le sette supersequenze appaiono sulla linea sismica sintetica. Tuttavia, alcune delle discontinuità sismiche sono pseudodiscontinuità e riproducono geometrie erronee o non esistenti. Il diverso numero di sequenze sismiche a differenti frequenze, in addizione alla apparizione di pseudodiscontinuità, documentano il problema della rappresentazione sismica delle sequenze deposizionali. A seconda della frequenza dominante, è possibile interpretare erroneamente il numero di sequenze deposizionali riconoscibili. E' necessario tenere conto di questa limitazione quando interpretazioni di stratigrafia sequenziale sono basate unicamente sulla informazione sismica.

Leer - Vide - Empty

OVERVIEW

Geologists commonly use geophysical methods to gain insights into the types, geometries and structures of rock formations that cannot be observed in outcrop at the earth's surface. The obtained geophysical images of the subsurface have, however, no straightforward relationship with the stratigraphical or structural parameters, but are rather determined by the physical properties of the rocks. For instance, a seismic reflection pattern, aside from being a function of some technical parameters of the seismic survey, is mainly a function of acoustic impedance, which is the product of the sonic velocity and bulk density of the rock. As a result, physical properties form the link between the geologic rock record and the image of a geophysical survey (Figure 1). A knowledge of the range, controls and evolution of sonic velocity and density is thus essential to understand the relation of a seismic image with its geologic background.

The presented study concentrates on the acoustic properties of carbonate sediments from the moment of deposition through burial, and demonstrates how they affect seismic reflection patterns. This relation is of particular interest because reflection seismic surveys are a standard method in scientific, engineering and economical investigations of the subsurface. Despite the extensive use of seismic methods, the manner in which seismic rock properties are related to the lithology of the rocks and how they affect the seismic image are not well known. In addition, the relatively young concept of seismic stratigraphy is based on the recognition of rock units on a seismic section and is therefore dependent directly on the physical properties of the rocks.

The main purpose of this study was therefore to analyze the relation between the lithology and seismic response of carbonate rocks. This was achieved in two ways:

(1) The physical properties of carbonate sediments and rocks were measured in the laboratory on discrete samples. This allowed for the direct comparison of the measured values with the observable lithologies (Part A). Compressional wave and shear wave velocity, density, porosity and other physical parameters were determined on a total of 295 samples from (1) recent carbonate mud from Florida Bay, (2) platform and periplatform carbonate sediments from cored deep drillholes on Great Bahama Bank, and (3) limestones from an exhumed carbonate platform in Central Italy (Montagna della Maiella). These rock samples provided an extensive database that allowed for the

recognition of the factors controlling the acoustic properties in carbonates. As a result, characteristic impedance values can be assigned to every category of carbonate sediment, including unlithified sediments and lithified rocks at different stages of diagenesis. In addition, the different ages of the measured carbonates, which range from Cretaceous to recent, allow the tracing of the evolution of physical properties, especially of sonic velocity, from deposition to compaction and diagenesis. The laboratory measurements can be used to improve interpretations of other velocity datasets, such as velocities obtained from sonic wireline logs (Part B).

(2) The data and results of the laboratory analyses were applied to a study of seismic modeling (Part C). The main purpose of this modeling was to establish the seismic response of the platform-to-basin transition outcropping in the Montagna della Maiella (Italy). Field observations and measured impedance values from the laboratory were used to create a two-dimensional impedance model that was transformed into synthetic seismic sections through computer simulations. This provided the opportunity to compare directly outcropping rock sections with their modeled seismic image. The seismic properties, such as frequency, polarity and amplitude gain were varied during the modeling so as to mimic as closely as possible the conditions and problems of a real seismic survey. The effects of the physical rock properties on the seismic image as well as the effects of the seismic parameters can be observed on the synthetic sections. These sections were compared with real seismic data from similar geologic settings.

The results and conclusions of this multidisciplinary study of field observations, laboratory analyses and computer simulations were integrated and summarized in Part D.

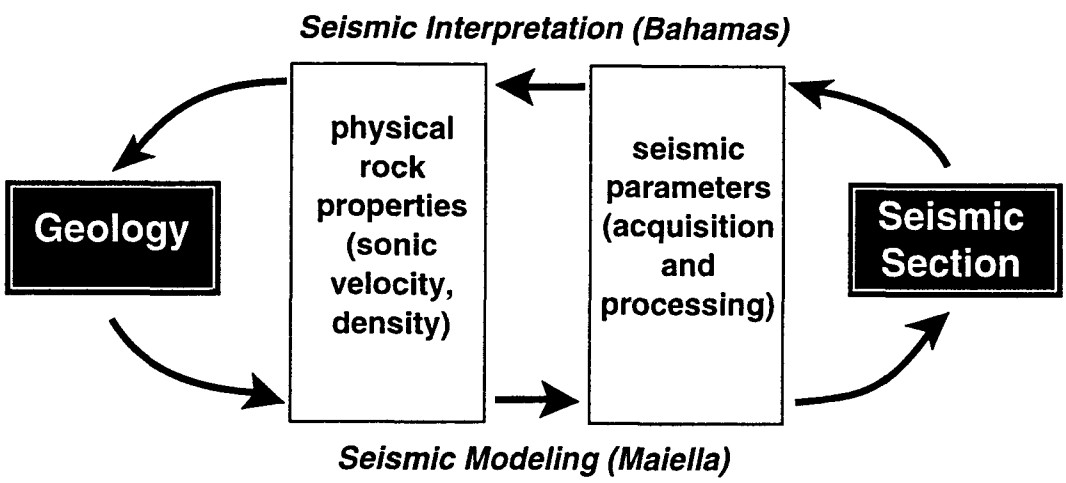

Figure 1: Schematic relationship between the geologic rock record and equivalent seismic reflection pattern. The physical properties of the rocks, in particular sonic velocity and bulk density, form the link between the geology and seismic data. These rock properties have to be taken into consideration for any study of forward seismic modeling or for interpretations of seismic sections.

PART A:

CONTROLS ON SONIC VELOCITY IN CARBONATE SEDIMENTS AND ROCKS

A.1. INTRODUCTION

Knowledge of the relation between sonic velocity in sediments and lithology is one of the keys to interpreting data from seismic sections or from acoustic logs of sedimentary sequences. Reliable correlations of rock-velocity with other petrophysical parameters, such as porosity or density (Gregory, 1977; Bourbié et al., 1987), are essential for calculating impedance models for synthetic seismic sections (Fagin, 1991) or for identifying the origin of reflectivity on seismic lines (Sellami et. al., 1990; Christensen and Szymanski, 1991). Velocity is thus an important parameter for correlating lithological with geophysical data.

Recent studies have increased the understanding of elastic rock properties in siliciclastic or shaly sediments. The causes of variations in velocity have been investigated for siliciclastic rocks (Han et al., 1986; Vernik and Nur, 1992), mixed carbonate siliciclastic sediments (Christensen and Szymanski, 1991), synthetic sand-clay mixtures (Marion et al., 1992) and claystones (Japsen, 1993). The concepts derived from these studies are however only partly applicable to pure carbonates. Carbonates do not have large compositional variations that are, as is the case of the other sedimentary rocks, responsible for velocity contrasts. Pure carbonates are characterized by the lack of clay or siliciclastic content, and are mostly produced and deposited on the top or on the slope of isolated or detached carbonate platforms, which have no hinterland as a source of terrigeneous material (Wilson, 1975; Eberli, 1991). They consist mainly of the carbonate minerals calcite (low- and high-Mg), dolomite and aragonite. These minerals have very similar physical properties, which excludes compositional variation as a major reason for the large variability of velocity of carbonates.

Theories that describe sonic wave propagation in porous media (Gassmann, 1951, Biot, 1956; Toksöz et al., 1976) are hard to apply to the complex system of pure carbonates, because the carbonates form a variety of unique diagenetic rock fabrics with

specific elastic properties. In order to quantify the physical properties, sonic velocities of pure carbonate samples from three different areas that cover a wide range of depositional environments, lithologies and diagenetic histories, have been measured. Measurements of compressional wave velocity (Vp) and shear wave velocity (Vs) were performed under confining and pore fluid pressures, which accurately simulate in situ subsurface conditions. This study (Anselmetti and Eberli, 1993, 1994) includes carbonates at all stages of diagenetic alteration and complements studies on the velocity of carbonates from drowned Cretaceous guyots (Kenter and Ivanov, 1994), of highly lithified, low porosity carbonate rocks (Rafavich et al., 1984, Wang et al., 1991) and of pelagic, deep water carbonates (Schlanger and Douglas, 1974, Milholland et al., 1980, Urmos and Wilkens, 1993).

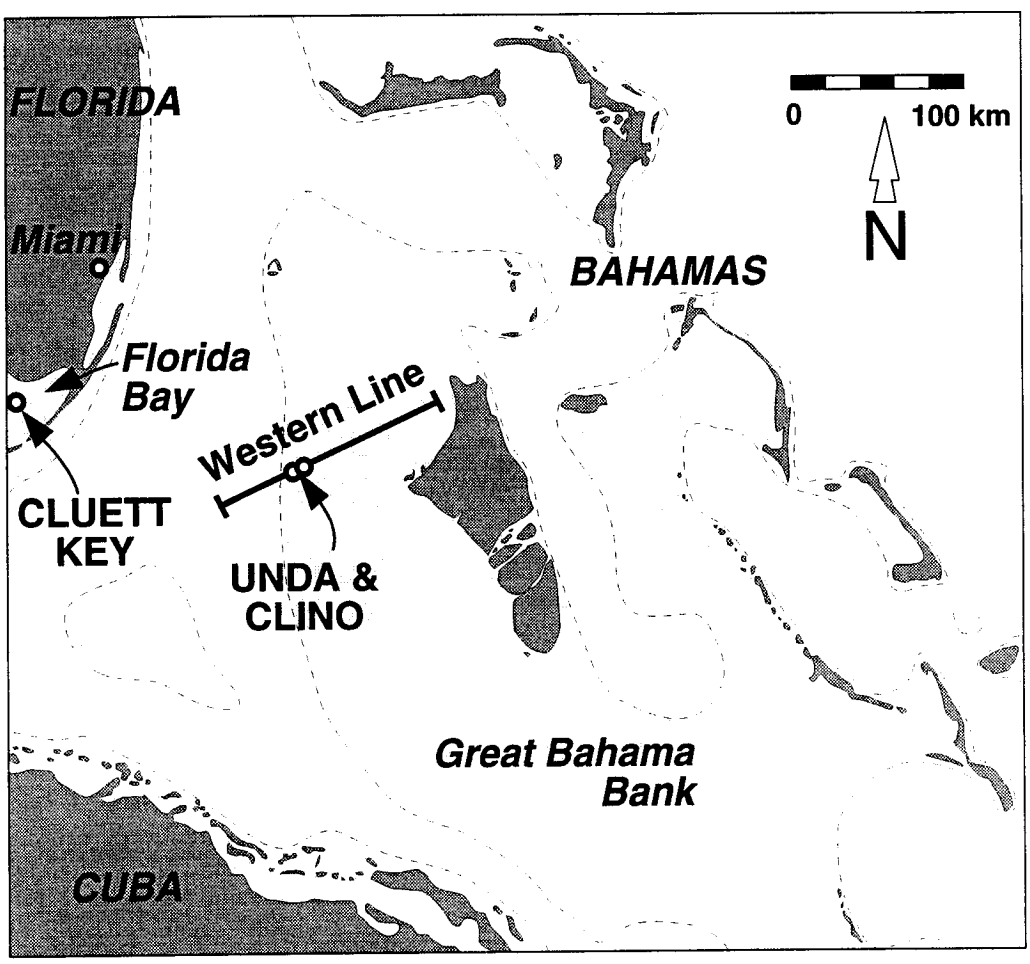

Figure 2: Location map showing the positions of the deep drillholes Unda and Clino along the Western seismic line on Great Bahama Bank and the location of Cluett Key in Florida Bay. Light shaded area is less than 20 m deep.

Sonic velocity measurements were performed in combination with a thorough lithologic and diagenetic examination of thin sections and XRD analysis. Porosities in the samples range from 0 to 60 % and the depositional environment varies from a protected shallow water platform over reefal and platform-marginal sediments to deeper slope deposits. The correlation of the velocity measurements with the lithological and mineralogical data enables characteristic velocities to be assigned to depositional and diagenetic stages. Furthermore, it allows the tracing of diagenetic evolution and velocity development from the time of deposition through different burial stages, recognizing that each diagenetic process alters velocity in a characteristic fashion.

A.2. SAMPLE AREAS

This study presents a correlation of physical rock properties with rock lithologies based on velocity analyses of 295 discrete samples from three different areas; (1) modern carbonate mud from Florida Bay, (2) two deep drillholes on Great Bahama Bank and (3) Montagna della Maiella, an exhumed carbonate platform margin in Central Italy. An understanding of the geological setting of the three areas is essential in order to relate the physical properties of the carbonates to the lithologies.

Velocity Samples from Modern Unconsolidated Carbonate Sediments: Artificially Compacted Carbonate Mud from Cluett Key, Florida Bay

The velocities of 20 carbonate mud samples were measured at various stages of artificial compaction in order to determine the increase of velocity caused by porosity reduction during pure mechanical compaction. The mud was collected with push cores of approximately 70 cm length from the interior pond of Cluett Key (Figure 2), a mangrove island in Florida Bay.

Florida Bay is a triangular-shaped shallow lagoon on the southern part of the Florida peninsula. This protected bay is subdivided by a series of mudbanks with several mangrove-fringed islands (Enos and Perkins, 1979). The Holocene sediments on the islands overlie Pleistocene bedrock and are up to 4 m thick. The base of the Holocene is often marked by a peat layer that is overlain by a succession of dominantly mud to wackestones with a few intercalations of shell-rich storm layers. Unconsolidated carbonate mud of the upper part of the Holocene section was used for the compaction-

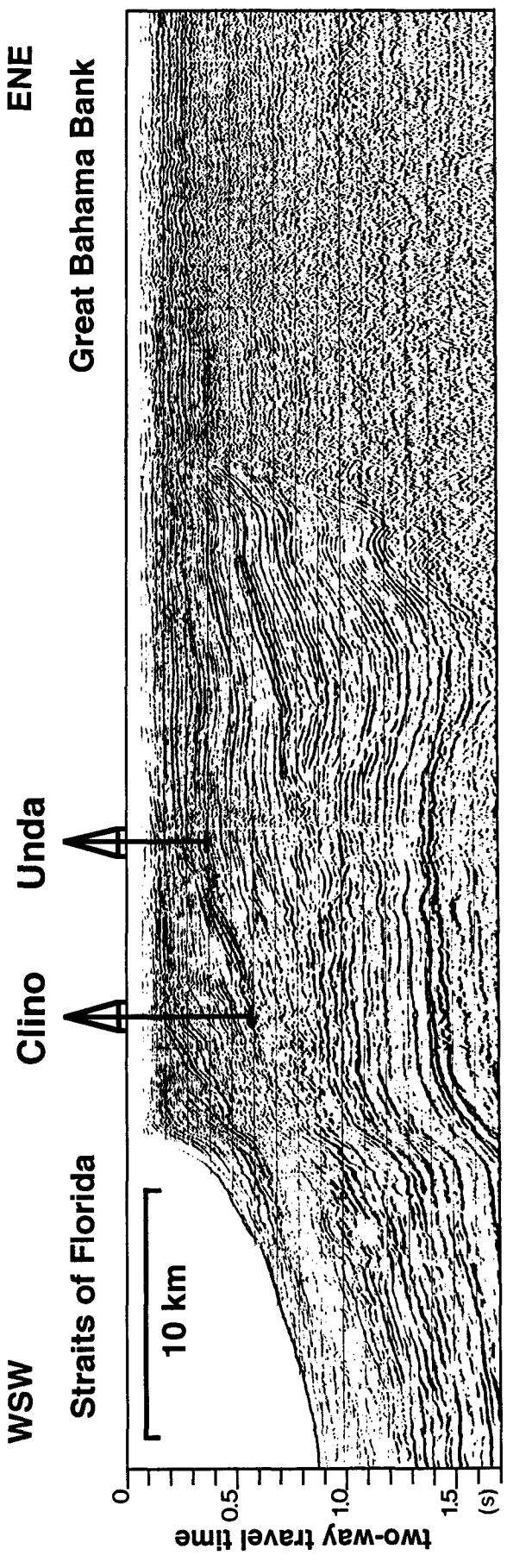

Figure 3: Part of the Western seismic line displaying a modern platform margin and the locations of drillsites Unda and Clino. The succession of inclined reflections below the modern shallow water platform document the progradation of the platform edge over inclined slope sediments for a distance of over 25 km (modified from Eberli and Ginsburg, 1987).

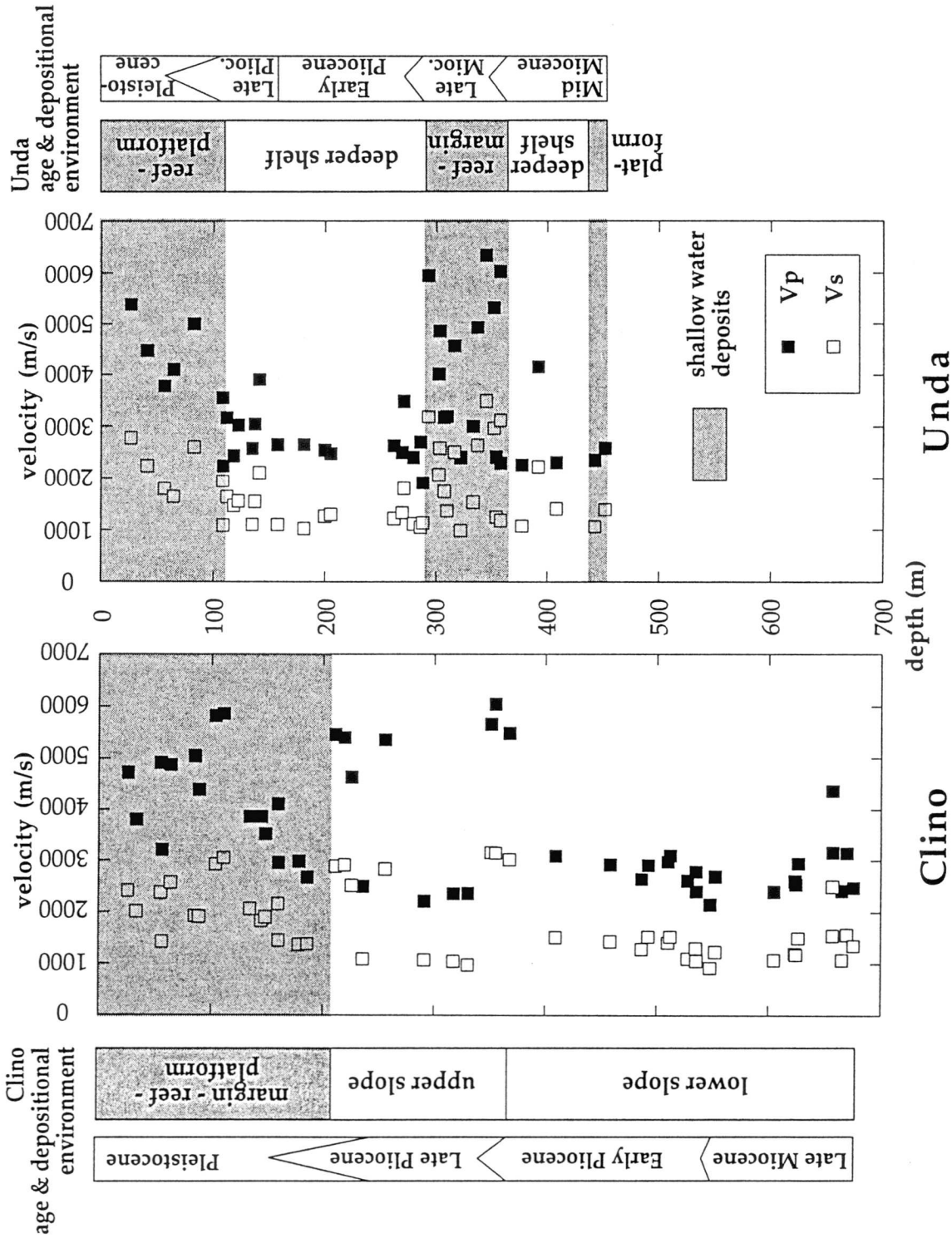

Figure 4: Correlation of Vp and Vs (at 8 MPa effective pressure) with depth, depositional environment and age of the drilled sediments from the two drillholes Unda and Clino on Great Bahama Bank. Velocity inversions are common in both holes and show that the effect of diagenetic alterations and sediment type dominate over the effect of depth. Velocities of carbonates that were deposited on the shallow water platform (shaded areas in graph) have larger variability and higher velocities than velocities from deeper water samples.

velocity experiments. The samples were taken from parts of the cores in which no roots or shell fragments disturb the homogeneous mud.

Mud from the islands and the mudbanks in Florida Bay have porosities that range from 61 to 78 % (Enos and Sawatsky 1981). Gamma ray attenuation measurements on cores from Cluett Key gave an average porosity for the Holocene sediments of 63 % (Vidlock, 1983). The mineralogical composition, determined on carbonate mud from Jimmy Key, an adjacent island, averages 65% aragonite, 20% high-Mg calcite and 15% low-Mg calcite throughout the whole Holocene section (Burns and Swart, 1992). No detectable diagenetic alterations occur and only traces (<5%) of dolomite are observed. However, variations in pore water chemistry indicate that early diagenetic processes such as dolomitization have already started (Burns and Swart, 1992).

Velocity Samples from Cores of Deep Drillholes: Pleistocene to Miocene Carbonates from Drillholes on Great Bahama Bank

Two continuous core borings from the Bahamas Drilling Project (Ginsburg, 1994), located along the multi-channel Western seismic line across Great Bahama Bank (Figures 2, 3; Eberli and Ginsburg, 1987, 1989) provide an excellent opportunity to correlate the physical properties of Miocene to Pleistocene carbonate sediments with their depositional lithologies and levels of diagenetic alteration. The multi-channel seismic data was shot by Western Geophysical with ten to twelve airguns of variable volumes (720-2280 $in.^3$) and recorded with a sampling interval of 2 ms. The shot- and receiver-point interval was mostly 25 m and occasionally 50 m. A "drag yo-yo cable" allowed the hydrophones to be lowered between each shot point on the sediment surface. Processing was performed using a F-K filter and a time-variant filter. Deconvolution was applied before stacking (Eberli and Ginsburg, 1989). Displayed sections are unmigrated.

The two drillholes (Unda and Clino, Figures 2, 3) penetrated to depths of 442 and 662 m below seafloor, respectively. The continuous cores had an average recovery of over 80%. A total of eighty-nine samples from the two drillholes were analyzed. Unlike older and exhumed outcrop samples, the young age of the drilled sediments allows for the measurement of sonic velocities of carbonates that are partly unconsolidated and that are not in their final stage of post-depositional alteration. The variety of diagenetic processes encountered has enabled the velocity evolution of different carbonate sediments to be traced under different diagenetic conditions through burial history and time.

The top of the rock section in both holes is of Pleistocene age (Kenter and Ginsburg, 1994). The oldest drilled sediments are dated as Middle Miocene at the bottom of Unda, whereas the bottom of Clino reaches carbonates of Late Miocene age (Figure 4). The retrieved lithologies range from platform-interior to platform-margin and slope carbonates; there is no siliciclastic sediment on this isolated carbonate platform.

Hole Unda, located 10 km from the modern platform edge, is characterized by three successions of shallow water platform sands and reefal deposits that alternate with fine sand and silt-sized deeper marginal deposits. The two intervals of deeper-water sediment record periods of rapid rise of sea-level and probable backstepping of the platform and reefal units. Hole Clino, 7 km closer to the modern platform edge, penetrated a single interval of shallow platform and reefal sediments overlying a thick succession of slope sediments. The nearly 500 m of fine sand to silt-sized slope sediments below 200 m have a variable amount of planktonic foraminifera and are, except for some intervals with coarse-grained, mainly skeletal sands, remarkably poor in coarser material.

This succession of depositional environments (Figures 3, 4) reflects the progradation of the platform top over the underlying slope sediments. The platform rim prograded over 25 km to the West into the Straits of Florida (Eberli and Ginsburg, 1989).

Not only the depositional lithology, but also the diagenetic overprinting changes several times downhole (Melim et al., 1994). The upper parts of both holes are characterized by early marine and subsequent intense freshwater diagenesis. Many samples show intense dissolution features, as well as extensive cementation, which led to rock-fabrics with characteristic elastic properties. In the lower part of Clino, the periplatform slope sediments show no major alterations. Characteristic for these zones of the cores are the dissolution of fine aragonitic components and the lack of cementation. Some parts of the cores have high micritic content and could preserve their aragonitic components due to low permeability, which inhibited high fluid-flow that would have been necessary for dissolution of the metastable grains (Melim et al., 1994). Only the coarser, platform-derived turbidite layers are more cemented. Little dolomite occurs in lower portions of the core and reaches 50% below a hardground at 536 m. Dolomitization in Unda is much more pervasive than in Clino - whole sections are completely dolomitized. Dolomite content increases below several hardgrounds and forms either a fabric-destructive sucrosic dolomite or a crystalline mimetic dolomite, depending on the precursor sediment (Dawans and Swart, 1988). For instance, the top of the lower reef-unit in Unda (293 m), a distinct lithological and rock-physical boundary, marks a change in dolomite type from sucrosic dolomite above the reef, to crystalline mimetic dolomite in the reef. Several layers of sucrosic dolomite appear

further below and are probably the result of more fine-grained lithologies within the coarser reefal units. In the lowest part of Unda, dolomite disappears and the rocks show again intense dissolution features.

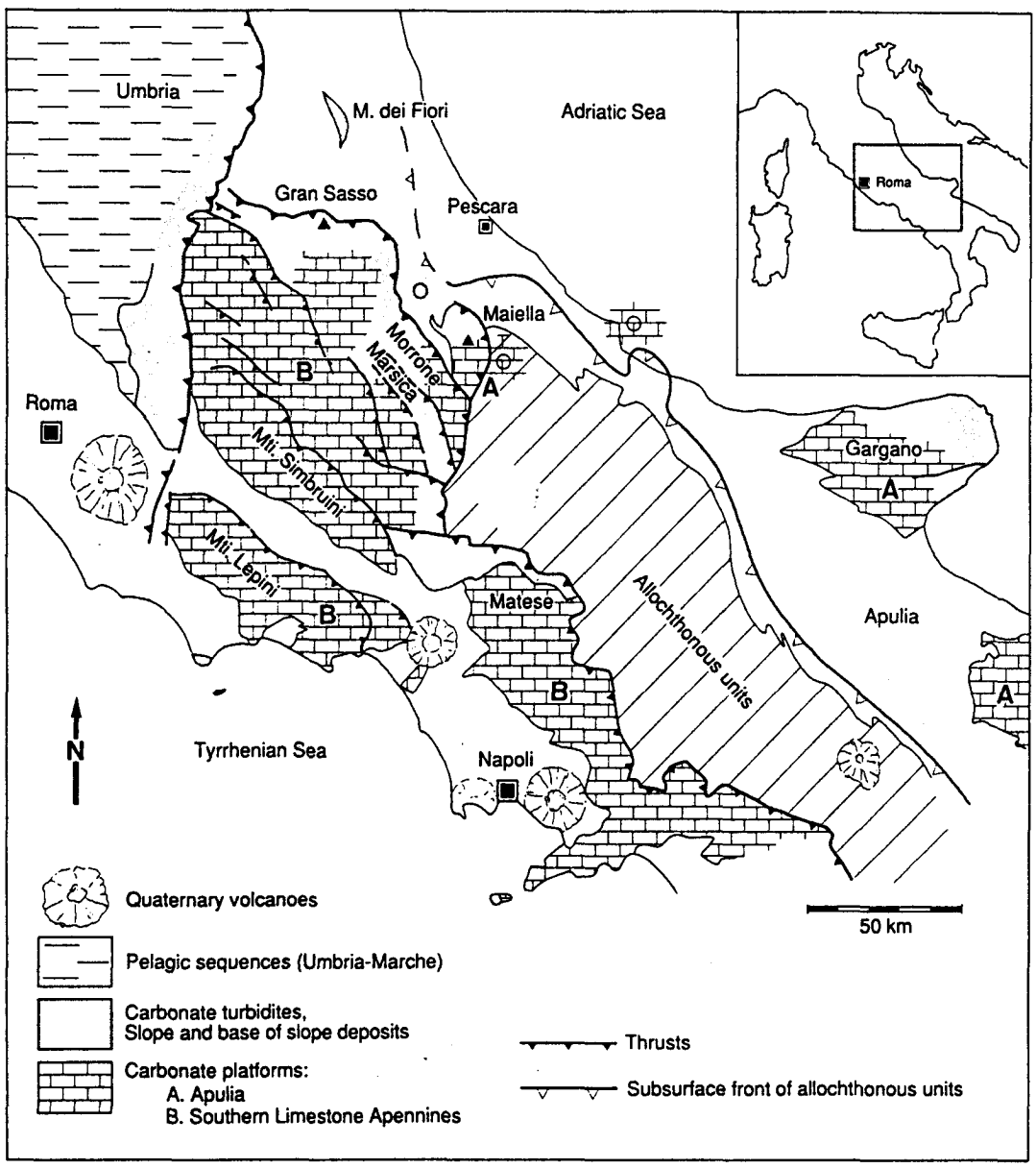

Figure 5: Location of the Montagna della Maiella in Central Italy and relative position of the carbonate platforms of Apulia (A) and of the Southern Limestones Apennines (B). The Apulian platform is partly covered by fore-land deposits and allochthonous units of the Southern Apennines and only marginally involved into Tertiary thrusting in the Montagna della Maiella. From Eberli et al., (1993).

Velocity Samples from Outcrops: Montagna della Maiella (Abruzzi, Italy)

186 samples for velocity measurements were collected in the Montagna della Maiella, Central Italy (Figure 5), which is a part of the Apulian carbonate platform. It is an uplifted and exhumed carbonate platform margin that is exposed in several valley flanks. The exposed platform and slope carbonates range in age from the Late Jurassic to the Late Miocene. The velocities of these carbonates, which underwent burial diagenesis, were determined for two purposes. One for the study what controls sonic velocity in carbonates; these Lower Cretaceous to Late Miocene samples provide data for completely altered and cemented examples. In addition, knowledge of the physical properties, in combination with an assessment of the large-scale geometrical pattern of outcropping rock-formations, will in a second study (Part D) be used to construct synthetic seismic sections (Anselmetti et al. 1991).

The Maiella carbonate platform margin was characterized by a steep escarpment during Early Cretaceous time that was buried during the Late Cretaceous and developed into a low-angle ramp in the Paleogene. In the Cretaceous, the sediments of the external platform are mostly rudist biostromes and carbonate sandbodies, whereas the platform interior is mainly made of limestones deposited in a shallow subtidal to supratidal environment, such as wackestones and fenestral mudstones (Crescenti et al., 1969; Bernoulli et al., 1992; Sanders, 1994). A distinct "mid"-Cretaceous, karstic unconformity separates the Cretaceous platform section into an upper and a lower unit. On the adjacent slope, several megabreccias onlap this platform margin (Accarie, 1988; Vecsei, 1991; Eberli et al., 1993;). They were deposited during sea-level lowstands that caused the exposure of the platform top and the erosion and downslope transport of platform fragments. These breccias are intercalated with calcareous turbidites and pelagic chalks that form the normal background sediments. The steep escarpment was infilled in the Maastrichtian. In the Paleogene, several sea-level fluctuations caused aggradation and subsequent erosion on the platform top and margin, followed by a relative deepening of the platform which resulted in a back-stepping of the platform margin in the Eocene. Finally, during the Late Eocene and Early Oligocene, reefal units of the platform margin prograded over the former deeper shelf and slope deposits and formed a wide and shallow shelf. This general evolution of backstepping and prograding of an isolated carbonate platform has striking similarities with the evolution of the modern Great Bahama Bank (Eberli et al., 1991).

Unlike the Great Bahama Bank, the Maiella platform margin shows almost no signs of dolomitization. This explains why, despite their older age, original lithologies

are generally better preserved than many dolomitized Bahamas carbonates. Some of the bioclastic sands of the Upper Cretaceous still have porosities of over 30 %, whereas most of the platform deposits are densely cemented (Mutti, 1994).

A.3. METHODS OF LABORATORY ANALYSES

Sampling Technique

The samples used for velocity determinations were cylindrical miniplugs 2.5 or 3.8 cm in diameter. The miniplugs of unconsolidated mud from Florida Bay were sampled from short push cores 7.6 cm in diameter. In order to avoid compaction and fabric destruction during sampling, a thin-wall tube with a diameter of 3.8 cm was used to cut the miniplugs vertically out of the cores. The 2 - 4 cm long cylinders were compacted longitudinally by a hydraulic press with a uniaxial pressure of up to 170 MPa. The velocities of the mud samples were measured at variable degrees of compaction. The maximum compaction attained was approximately 50%, so that the initial porosity of 63% was reduced to 26%. The samples from the Bahamas deep drillholes were cored horizontally, or occasionally vertically, into 7.6 cm diameter cores. Plugs from the Maiella were cored from hand samples collected from outcrops. All rock cores were trimmed to a length between 1.5 and 5 cm. The end surfaces were polished to make them flat and parallel in order to allow good transmission of the acoustic signal.

Velocity Measurements

The velocities of all Bahamas samples and from 114 (out of 186) Maiella samples were measured at the Petrophysics Laboratory at the University of Miami using a pulse transmission technique (Birch, 1960) with an apparatus shown in Figure 6. The samples were water saturated and jacketed in rubber or heat shrink tubing, which seals the pore fluid from the confining oil in the pressure vessel. Confining and pore fluid pressures were chosen independently to simulate in situ conditions of a buried sediment. Pore fluid pressures as high as 50 MPa can be obtained, but most experiments were run at 2 MPa. Confining pressure was varied between 3 and 100 MPa, resulting in an effective maximum pressure (confining pressure minus pore fluid pressure) of up to 98 MPa. However, many samples collapsed and failed at pressures below 100 MPa.

Within the end caps, piezoelectric crystals create a signal with a center frequency of 0.6 to 1.2 MHz. The same pair of transducers generates one compressional wave signal (Vp) and two orthogonally polarized shear wave signals (Vs1, Vs2). The transducers are arranged so that the waves propagate along the core axis. The electrical signal produced by the receiver crystal is amplified, filtered, and fed into a digital oscilloscope. The oscilloscope digitizes the ultrasonic signals and transfers the digitized waveforms to a Macintosh Quadra computer for display and time series analysis. A customized analysis software package collects the data as a function of effective pressure, and calculates the travel times of the signals as well as the three velocities (Vp, Vs1, Vs2) at every pressure step. The Vs used for the calculation of the Vp/Vs ratio is the mean Vs of the two measurements.

The velocities of the compacted mud from Florida Bay were measured with the same set of transducers but with a benchtop measuring system not under confining pressure. This measuring system allows recognition of compaction due to the axial pressure of the transducers during the measurement. The two transducers were pressed together with a piston at an axial pressure of 0.1-1 MPa. This relative low pressure allowed the transmission of the signal from the transducers into the mud, but did not compact drastically the still

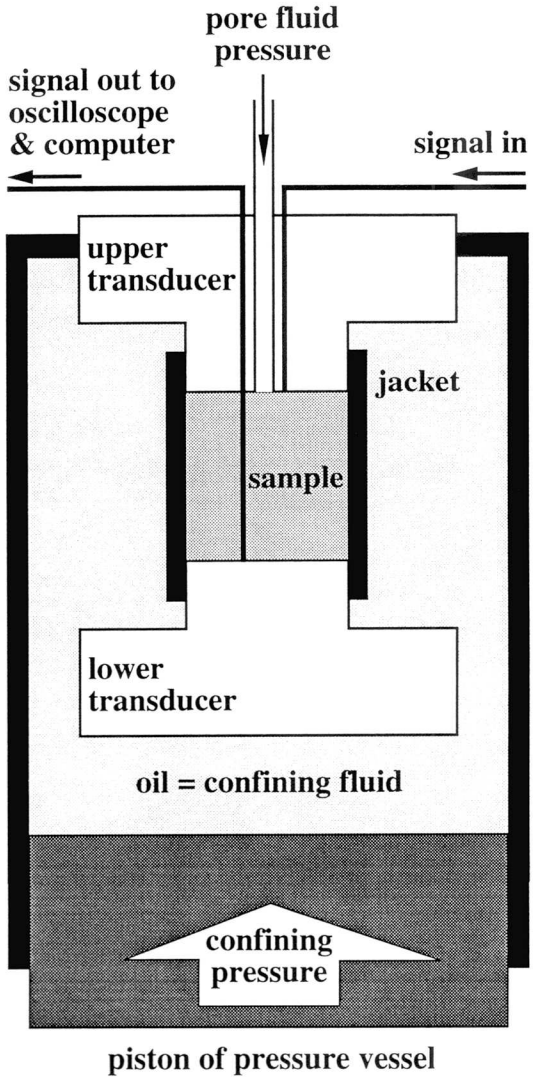

Figure 6: Schematic cross-section of ultrasonic velocity-meter at the petrophysics laboratory of the University of Miami. Confining pressure and pore fluid pressure can be chosen independently so as to simulate true in situ conditions of a buried sediment at any depth. An elastic jacket seals the pore space with the pore fluid from the confining oil. Maximum confining pressure is 100 MPa (1 kbar).

deformable mud samples. Some measurements were performed on uncompacted mud; however, the minimum required transducer pressure reduced the sample length by a few percent. Corrections for length change are made in order not to produce errors in the velocity determination.

A suite of the Maiella miniplugs (72 samples) were measured with a similar apparatus in the petrophysics laboratory at the University of Geneva, Switzerland. The transducer pair of this machine only creates a compressional wave signal. These measurements were performed under dry conditions without pore fluid pressure and under confining pressures varying up to 400 MPa.

The precision of the velocity measurements is mainly a function of the properties of the sample. In well-cemented, high-velocity samples, the lower transducer receives a clear peak as the first break, which allows measurements of velocity with an error of less than 1% to be made. Friable, unconsolidated samples tend to compact and reduce their sample length by up to 5 %. In addition, they sometimes produce only a moderate first break signal, especially for Vs, so that the error of velocity determinations in these difficult samples is probably approximately 5%.

Additional Properties

In addition to the velocity determinations, several other analyses were performed.

Petrography

X-ray diffraction analyses were performed on the cut-offs of the drilled plugs from the Bahamas samples. Calibration of these results with carbonate-standards allowed for the determination of the percentage of calcite, dolomite and aragonite in each sample. The cut-offs of the miniplugs were also used to make thin sections from all Bahamas samples and from most Maiella samples. Thin sections were examined in order to determine sediment-type, composition, grain size, porosity-type and diagenetic alterations. These observations enable the physical properties to be correlated with the lithological parameters.

Density

Dry bulk-densities were calculated by weighing the oven-dried rock plugs and calculating the volume by measuring the diameters and lengths. Because these almost pure carbonates consist dominantly (>95%) of three carbonate minerals, the percentage

of the minerals (XRD) determines a theoretical grain density (matrix density), which can be calculated using the plain mineral densities (Carmichael, 1989):

$$\rho\ grain = \frac{\%\ calcite \bullet \rho\ calcite + \%\ dolomite \bullet \rho\ dolomite + \%\ aragonite \bullet \rho\ aragonite}{100}$$

$$\rho\ calcite = 2.71 g/cm^3\ ;\ \rho\ dolomite = 2.87 g/cm^3\ ;\ \rho\ aragonite = 2.93 g/cm^3$$

This method does not work if the mineralogical composition of the sample is not limited to carbonate minerals. In this dataset, only samples from the karstic "mid"-Cretaceous unconformity in the Maiella contain a significant amount of non-carbonate minerals, such as aluminum and iron hydroxides. Some of the Miocene hemipelagic carbonates were expected to contain some clay minerals. To obtain the grain density of these lithologies, some samples were powdered and the grain density determined with a helium pycnometer at the Free University in Amsterdam. To compare the results, some pure carbonate samples were also measured there. In addition, carbonate content was determined on the same samples (Table 1).

sample #	lithology	grain density (g/cm^3)	$CaCO_3$ content (%)
FA139	carbonate (from platform)	2.732	100.0
FA196	carbonate (rudist sand)	2.719	100.0
FA183	hemipelagic carbonate	2.677	87.3
FA184	hemipelagic carbonate	2.673	86.6
FA147a	cemented bauxitic sand	3.008	35.6
FA147b	cemented bauxitic sand	3.014	
FA149a	cemented bauxitic nodules	3.182	28.2
FA149b	cemented bauxitic nodules	3.153	
FA150	breccia of bauxites and carbonates	2.887	54.4

Table 1: Grain density and carbonate content of selected samples from the Maiella (performed at Free University, Amsterdam). Grain densities were measured on powdered samples in a helium pycnometer. Sample FA196 and FA139 represent the vast majority of pure carbonates with a grain density close to the density of calcite. Note the slightly lower grain densities of the hemipelagic rocks and the extremely high densities of bauxites.

The grain density of the pure Maiella carbonates lie around the plain calcite value (2.715 g/cm^3), because no significant dolomite was found, whereas the hemipelagic carbonates have, probably due to some clay content, a slightly reduced grain density. The bauxitic samples show a significantly higher grain density, depending on the content of the iron and aluminum hydroxides. These high grain densities have to be taken into account for calculating the rock porosity.

Porosity

Rock porosity is calculated by comparing the grain density (matrix density) with the measured dry or saturated bulk density:

$$\rho\, bulk = \frac{\%\, porosity}{100} \cdot \rho\, fluid + \left(1 - \frac{\%\, porosity}{100}\right) \cdot \rho\, grain$$

or

$$\frac{\%\, porosity}{100} = \frac{\rho\, grain - \rho\, bulk}{\rho\, grain - \rho\, fluid}$$

This easy way of determing rock porosity was compared with the results from other techniques like helium densitometry and Archimedes principle. The porosity values obtained by the described method are systematically 0-3 % higher than porosities obtained by the other methods. The difference is caused by the fact that the helium densitometry as well as the Archimedes method require the complete penetration of a pore fluid or gas (water and helium respectively) into the pore space and therefore are a function of permeability. In addition, isolated and closed porosity is not penetrated by the pore fluid and is therefore not detected, whereas the method based on the density measurements and X-ray analyses considers this closed porosity.

A method of image analyses was applied to some samples. This method can document porosity and pore types by using a scanned color photomicrograph. The blue impregnated porosity is converted on the scanned image to black, whereas all non-blue sediment particles are converted to white. The black-and-white pattern can image the structure of the pore space and allows for the determination of pore types and total porosity. Micro-porosity however, is not detected by the scan.

Permeability

Klinkenberg and air permeabilities with nitrogen were determined on some minicores from parts of the Bahamas drillholes, where the drilled core allowed additional

sampling of miniplugs directly adjacent to the velocity samples. Permeability measurements on these minicores were performed by Marathon Oil Company, Houston. In addition to these permeability measurements, a handheld permeameter was used to measure permeability directly on the drilled cores. These data, which were not used in this study, allow for a more continuous investigation of variability and controls of permeability in the cores (Melim and Anselmetti, 1994).

A.4. VELOCITY DATA

All petrophysical and lithological data of the measured minicores are listed in the Appendix in Tables 5, 6 a+b (Maiella samples), Tables 7 a+b, 8 a+b (Bahamas samples), and Table 9 (Florida Bay samples).

Vp and Vs

In the following descriptions and correlations, velocities at a confining pressure of 10 MPa and a pore fluid pressure of 2 MPa are discussed. The resulting effective pressure of 8 MPa (10 MPa for dry samples) is high enough to allow good signal transmission but does not cause significant fracturing in the highly porous samples. The Vp measurements on dry samples are also presented here, because major differences between dry and saturated Vp are only expected in rocks with a dominant crack-porosity (Nur and Simmons, 1969), whereas the saturation of round-shaped pores, abundant in the samples of this study, does not influence Vp drastically.

Despite the limited variability in mineralogy, the measured carbonates have an extraordinary wide range in velocities. Vp varies between 1700 and 6500 m/s, and Vs between 700 and 3400 m/s. The three different datasets have different ranges of Vp and Vs (Figure 7). The unconsolidated mud-samples from Florida Bay have the lowest velocities with minimum Vp and Vs of 1700 and 700 m/s respectively. The Bahamas and the Maiella samples reach velocities of up to 6500 m/s (Vp) and 3400 m/s (Vs). Unlike siliciclastic sediments, where variations in mineralogy (e.g. clay-content) can cause large velocity contrasts, the different carbonate minerals, calcite, dolomite and aragonite, have very similar physical properties so that differences between them cannot be responsible for the large variability in velocities.

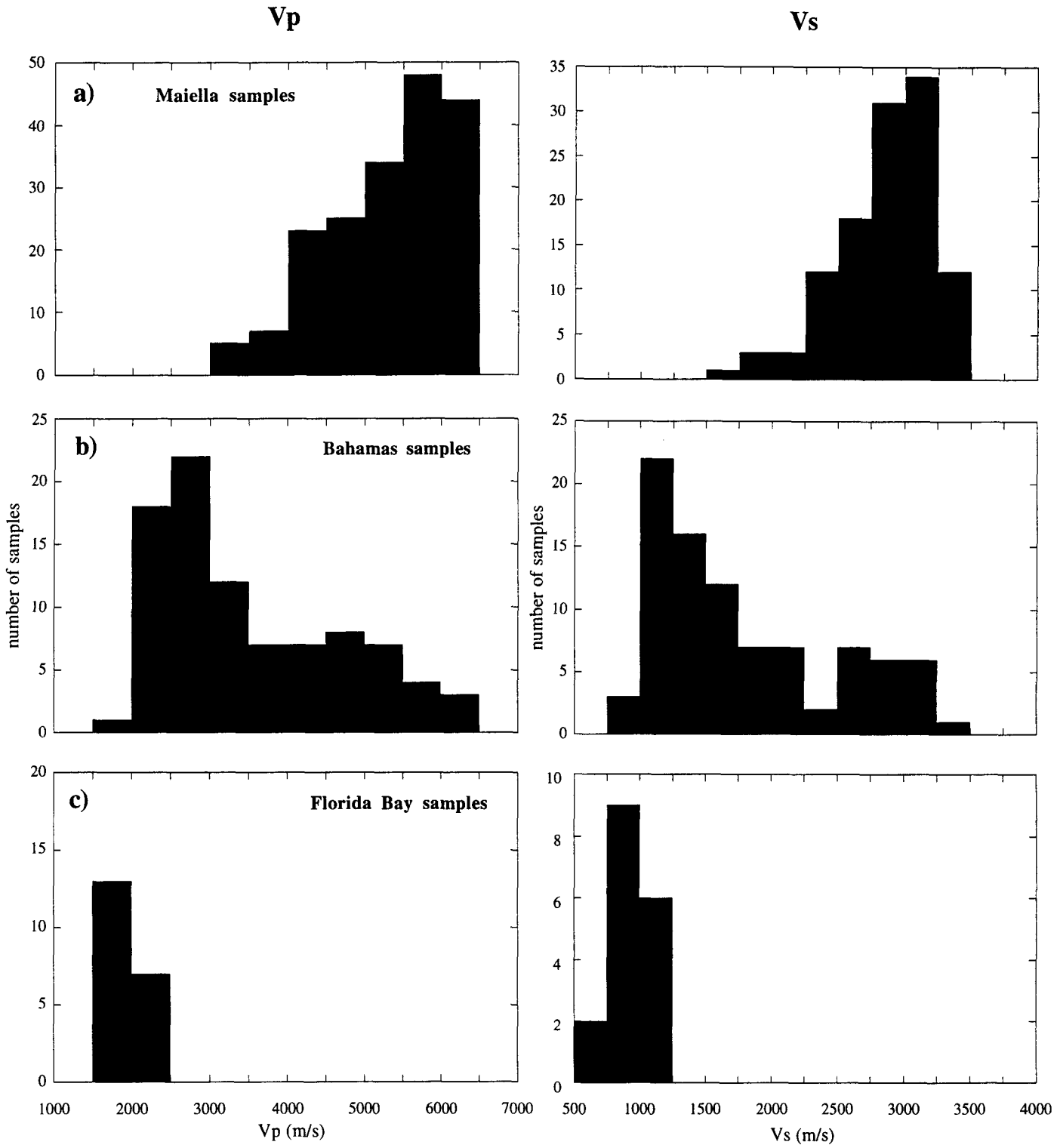

Figure 7: Range of Vp (left) and Vs (right) for all samples of the three investigated areas (at 8 MPa effective pressure). The Maiella samples (a) have higher average velocities than the Bahamas samples (b). The artificially compacted mud samples from Florida Bay (c) have, despite compaction of up to 50 %, only low velocities. The large range of velocity in all samples is remarkable for the restricted mineralogy of these pure carbonate sediments.

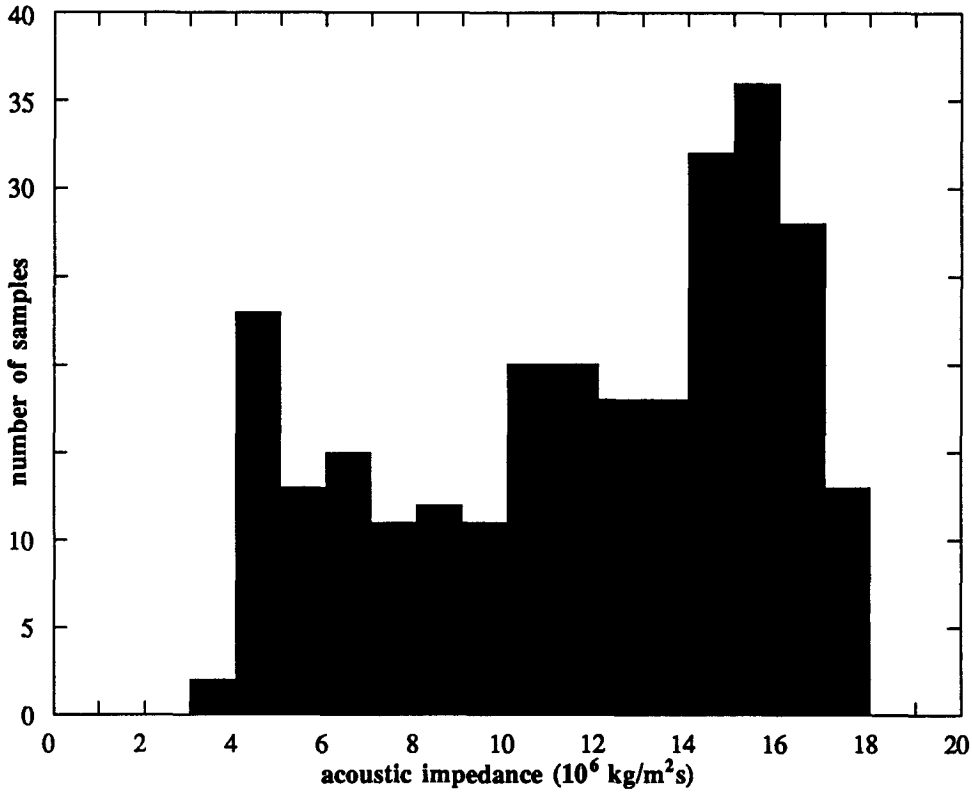

Figure 8: Range of acoustic impedance of the Bahamas and Maiella samples (at 8 MPa effective pressure). Impedances of high-velocity and dense rocks are over five times higher than impedances of low-velocity rocks. These impedance variations in the pure carbonates are caused by differences in fabric and not by differences in composition. The large range explains the good reflectivity observed in many seismic sections recorded over carbonate sediments (see Chapter C).

Acoustic Impedance

The observed ranges of Vp and Vs and therefore the large contrasts in acoustic impedance (Figure 8) can explain the excellent seismic reflectivity of many seismic sections recorded over pure carbonates. The two drillholes in the Bahamas for instance have acoustic impedance values that range from 3.8 - 17.4 10^6 kg/m^{2}s. As will be discussed in Parts B and C, the observed good reflections on seismic sections, often believed to be caused by intercalations of carbonate and non-carbonate sediments, can in fact be explained by variations in the fabric of the carbonates.

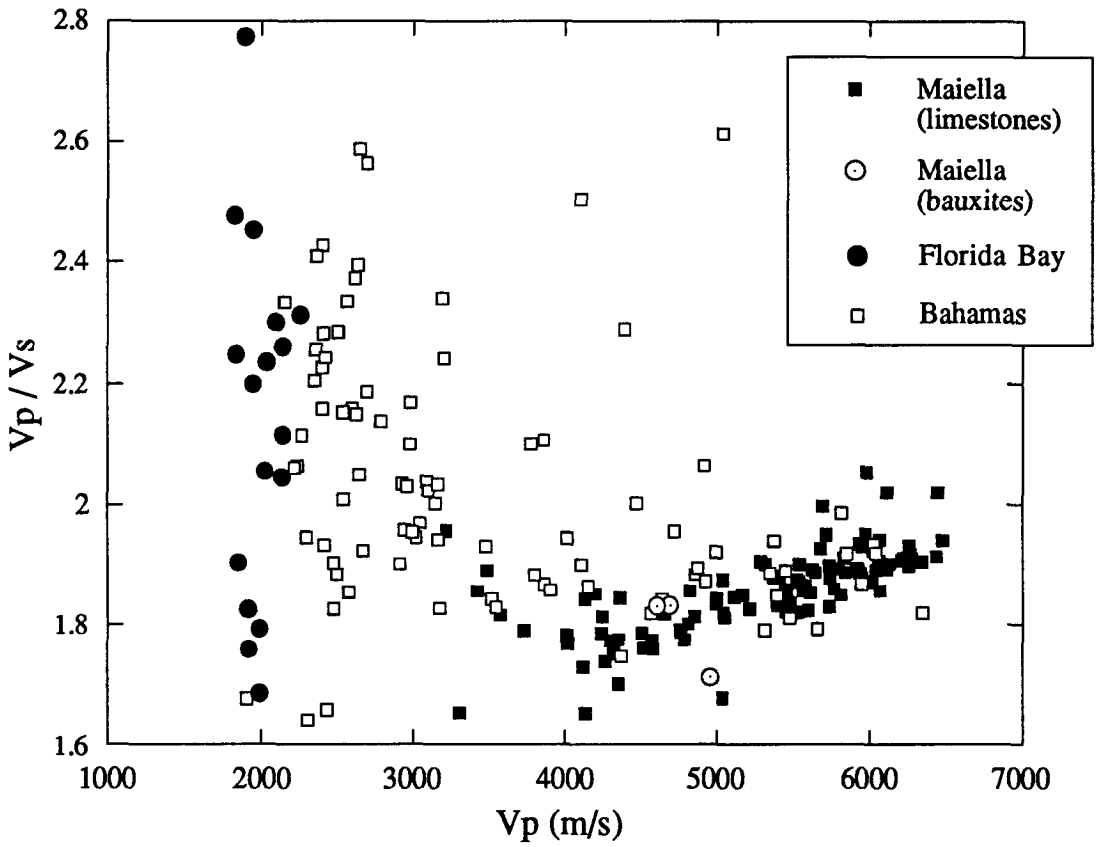

Figure 9: Vp/Vs as a function of Vp (at 8 MPa effective pressure). The wider range of Vp/Vs towards higher values in low-velocity rocks shows that shear waves are more affected by high-porosity fabrics than compressional waves. Some of the extreme low and high values might be caused by a questionable registration of the arriving Vs signal, in particular in high-porosity rocks.

Vp/Vs

Compared to other studies of Vp/Vs ratios in sedimentary rocks (Tatham, 1982; Rafavich et al., 1984; Wilkens et al., 1984; Johnston and Christensen, 1992, 1993), the Vp/Vs ratios of this study, which were only measured under saturated conditions, have a very wide range and reflect the large variety of encountered carbonate fabrics. The cross plot of Vp/Vs with Vp in Figure 9 shows that Vp/Vs in indurated, low-porosity rocks with high Vp normally falls between 1.8 and 2, which is in good agreement with the measurements of limestones and dolostones by Johnston and Christensen (1992). At lower Vp, the Vp/Vs ratio can reach much higher values of up to 2.8. These higher Vp/Vs ratios reflect the fact that, in general, Vs is more affected by the highly porous

fabric of the low-velocity carbonates than Vp. It also has to be taken into account that some readings of shear wave velocity, and thus the Vp/Vs ratio, might have large errors, due to poor Vs-signal quality, e.g. when low shear wave amplitudes are combined with high background noise. Therefore, some of the extreme Vp/Vs values might be unreliable; however, these few values do not change the general pattern of Vp/Vs values. The artificially compacted samples from Florida Bay have an extreme range of Vp/Vs values, varying from 1.7 to 2.8 over a narrow range of Vp from 1700 to 2300 m/s. The uncompacted mud, with a porosity of approximately 63 %, is not strong enough to sustain shear stresses (Laughton, 1957), thus inhibiting the transmission of shear wave signals. The slightly compacted mud samples have high Vp/Vs values of up to 2.8. With increasing compaction, the Vp/Vs of these Florida Bay samples approach more "normal" values of around 2.2.

A.5. FACTORS AFFECTING VELOCITY

In many sedimentary rocks, the concept of a grain- and matrix-supported fabric with a critical porosity is able to explain variations in velocity and to relate them to changes in sediment composition (Nur et al., 1991; Yin et al., 1993). However, diagenetic changes in carbonates cause cementation, dissolution and recrystallization-processes that form unique rock fabrics with associated velocity patterns that do not reflect simply the compositional variations of the sediment.

Velocity in carbonates is a complex function of several factors. It is possible to distinguish between rock-intrinsic and rock-extrinsic parameters. Intrinsic parameters, such as porosity, pore type, composition or grain size, are factors that are connected with the lithology and thus,

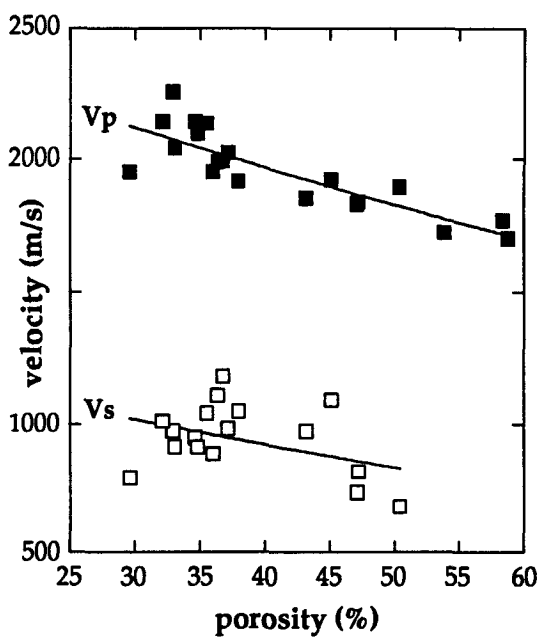

Figure 10: Increase of Vp and Vs at decreasing porosities in the Florida Bay samples measured at different stages of artificial compaction. The velocity increase results from pure compaction. Initial porosity of the carbonate mud is on average 63 %. The poorly compacted samples with porosities above 50-55 % did not allow Vs signals to be transmitted.

with the physical properties of the rock. Rock extrinsic parameters are factors that are not physically connected to the rock-fabric, but are determined by external boundary conditions. Examples of rock-extrinsic parameters are burial depth, confining pressure and age. It will be shown that for carbonates, the rock intrinsic factors are more important than the extrinsic ones.

Velocity as a Function of Rock-Extrinsic Parameters

Compaction

The compaction experiments and associated velocity measurements on modern carbonate mud from Florida Bay were performed in order to determine the manner in which velocity changes due to porosity reduction from purely mechanical compaction. The samples were pure carbonate mud, which is a special lithology that is rarely encountered in the other carbonate samples. However, most of the measured samples from other locations have, together with the coarser grain fraction, a large amount of micrite in the matrix. Therefore, compaction of the original sediments that comprise the other samples is likely to have a similar effect on velocity as in the compacted mud.

With an uniaxial pressure of 170 MPa, the porosity could not be reduced to less than 29 %, indicating that the microfabric of the rock, consisting of 65 % aragonite needles, is close to the densest packing that can be reached by mechanical compaction. This demonstrates that samples with porosities between 0 and 25 percent require diagenetic closing (cementation) of part of the pore space.

It is known that porosity has a major influence on velocity, with porosity decreases usually producing velocity increases. The Florida Bay samples show a relatively subtle increase in velocity with increasing compaction or decreasing porosity (Figure 10, Table 9). At porosities close to 60%, the poorly compacted samples have a Vp of 1700 m/s and no measurable Vs. The samples had to be compacted by 10-15% in order to allow the transmission of a Vs signal. This observation corresponds well with the measurements of Laughton (1957), who only detected shear waves in unconsolidated ocean sediments above a compacting pressure of 5 MPa. At maximum compaction with remaining porosities of 29 %, Vp increases to 2250 m/s and Vs lies around 900 - 1200 m/s. The gradient of measured increases in velocity of the compacted mud is significantly lower than observed gradients in the other Bahamas and Maiella samples (Figure 11). The mud samples show, due to their low shear modulus, a behavior similar to materials that have no rigidity (liquids) as suggested by Hamilton (1971). He showed that most unconsolidated marine sediments possess only little rigidity but nevertheless

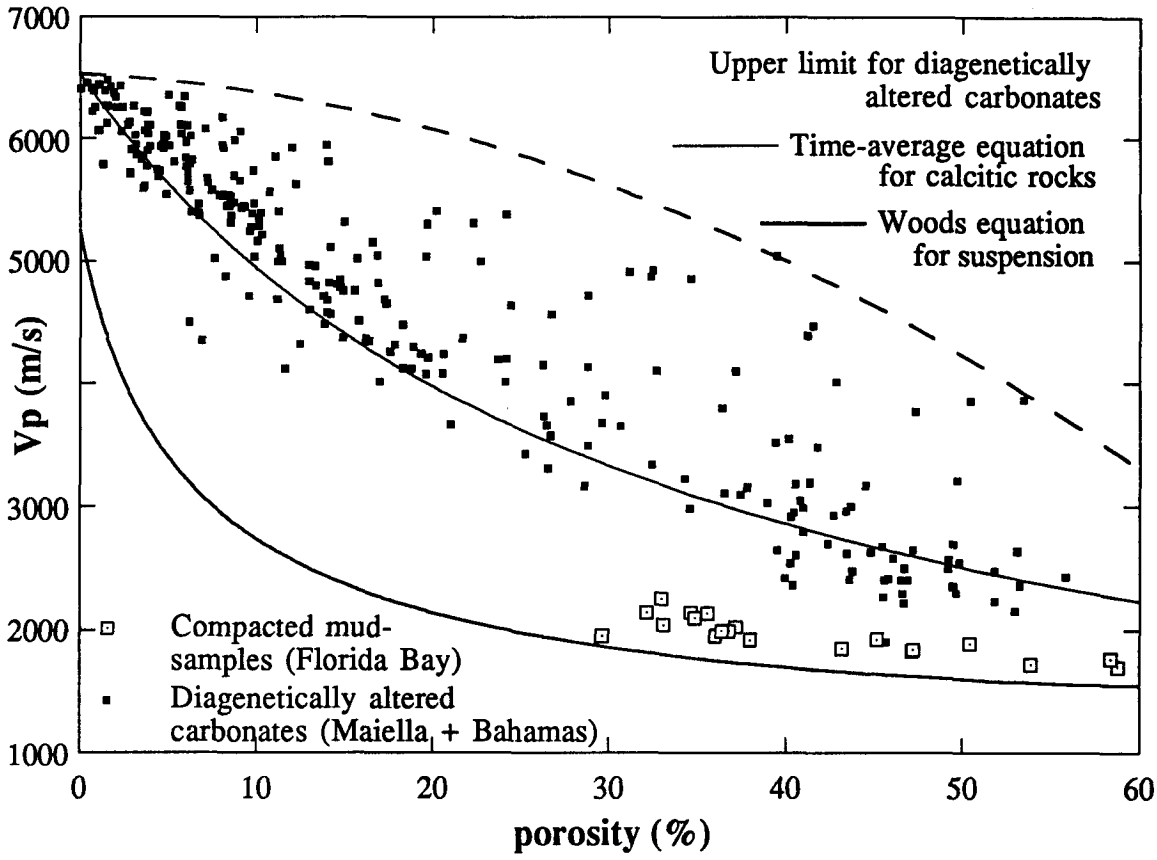

Figure 11: Velocity as a function of porosity for the three datasets. Vp and porosity show clearly an inverse correlation, but the gradient of increasing Vp at decreasing porosity is much lower in the compacted Florida Bay samples than in the natural rocks of the Bahamas and the Maiella. Velocities of the mud samples are only little higher than velocities of mediums without rigidity (suspensions), calculated using the Wood equation (Wood, 1941). This shows that porosity reduction due to mechanical compaction has only minor effect on Vp, whereas porosity reduction due to diagenetic processes (e.g. cementation) can increase rigidity which results in higher velocities. As a result of these diagenetic alterations, most carbonate rocks have higher velocities than predicted by the time-average equation (Wyllie et al., 1956).

have a shear modulus >0 and a definite structure. The Wood equation (Wood, 1941; Nafe and Drake, 1963), valid for media without shear modulus or rigidity, can be used to compare the observed porosity-velocity relation of the artificially compacted sediments with the values of liquids:

$$V_p = [(\Phi\beta_{fluid} + (1-\Phi)\beta_{solid})(\Phi\rho_{fluid} + (1-\Phi)\rho_{solid})]^{-1/2}$$

$$\Phi = \textit{fractional porosity};\ \beta = \textit{compressibility};\ \rho = \textit{density}$$

The Wood equation curve in Figure 11 was derived using compressibility values for water ($4.06 \cdot 10^{-10}$ m^2/N) and for calcite ($1.34 \cdot 10^{-11}$ m^2/N), because the elastic

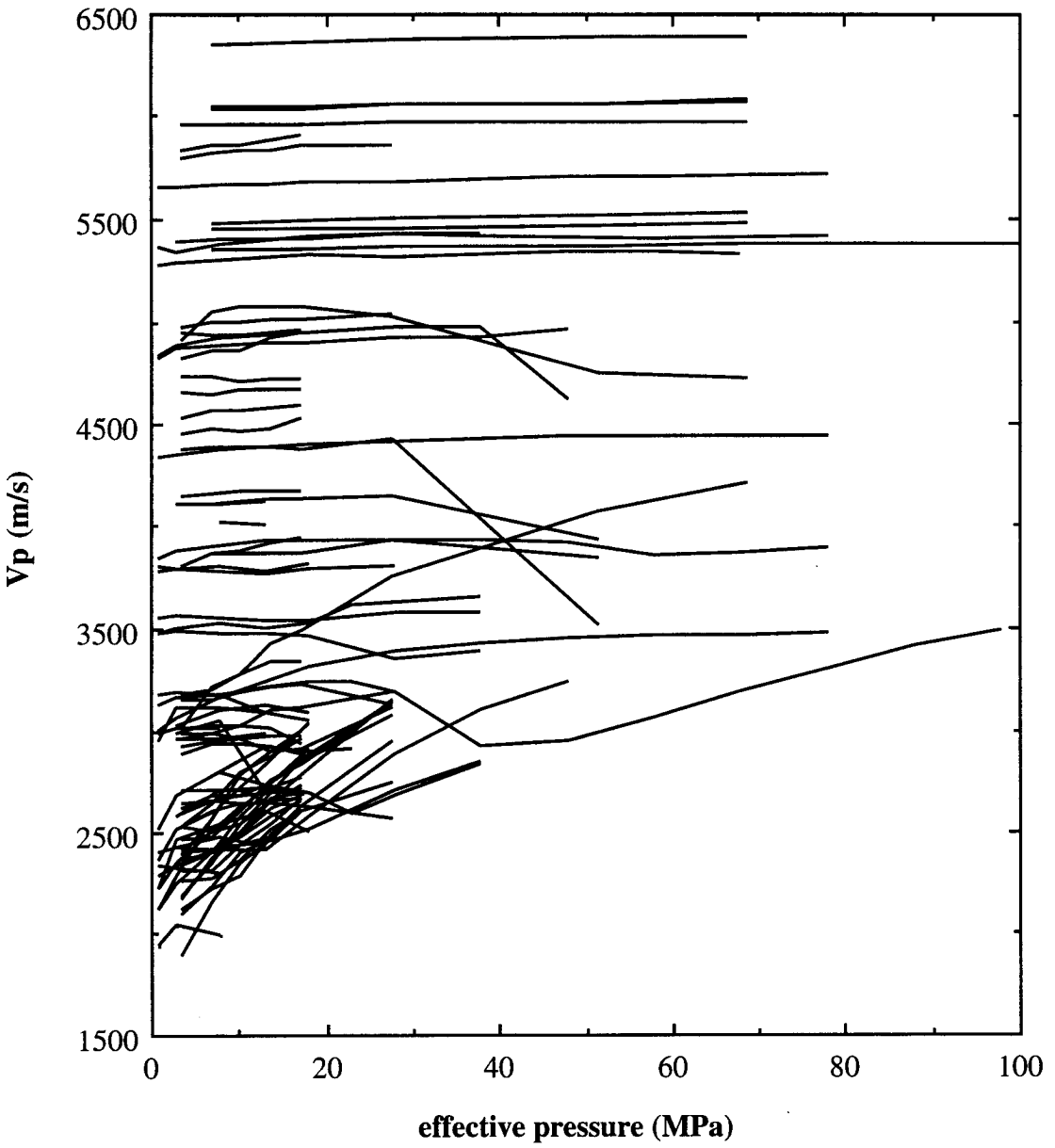

Figure 12 a: Velocity evolution of the Bahamas samples at increasing effective pressure. Each trace represents the velocities for one sample at different pressures. The gradients of the low-velocity samples are higher than those of samples with high velocities. Decreasing velocities at higher pressures mark a critical pressure at which the samples are intensely fractured and collapse. A minor part of the velocity increase is an artifact caused by decreased sample length.

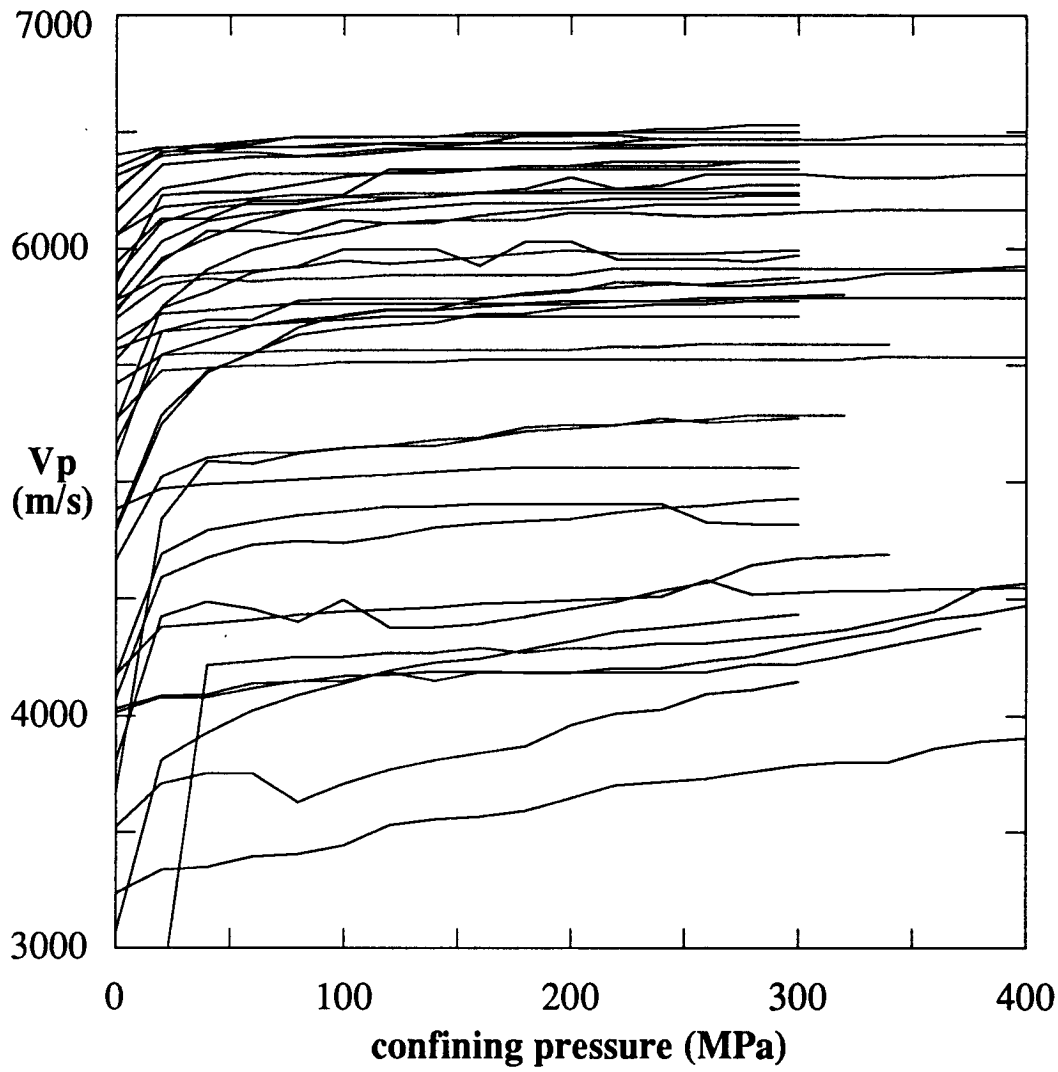

Figure 12 b: Velocity evolution of some Maiella samples at increasing effective pressure. Each trace represents the velocities for one sample at different pressures. Velocity-traces were only selected for this plot if confining pressures reached at least 300 MPa (these samples were measured without pore-fluid pressure). The velocity increases of the Maiella samples at lower pressures are similar to those of the Bahamas samples (Figure 12a). At high pressures above 300 MPa, velocities reach, in general, a plateau. The apparent velocity increase of a few samples at high confining pressures is likely to be caused by a reduction in sample length.

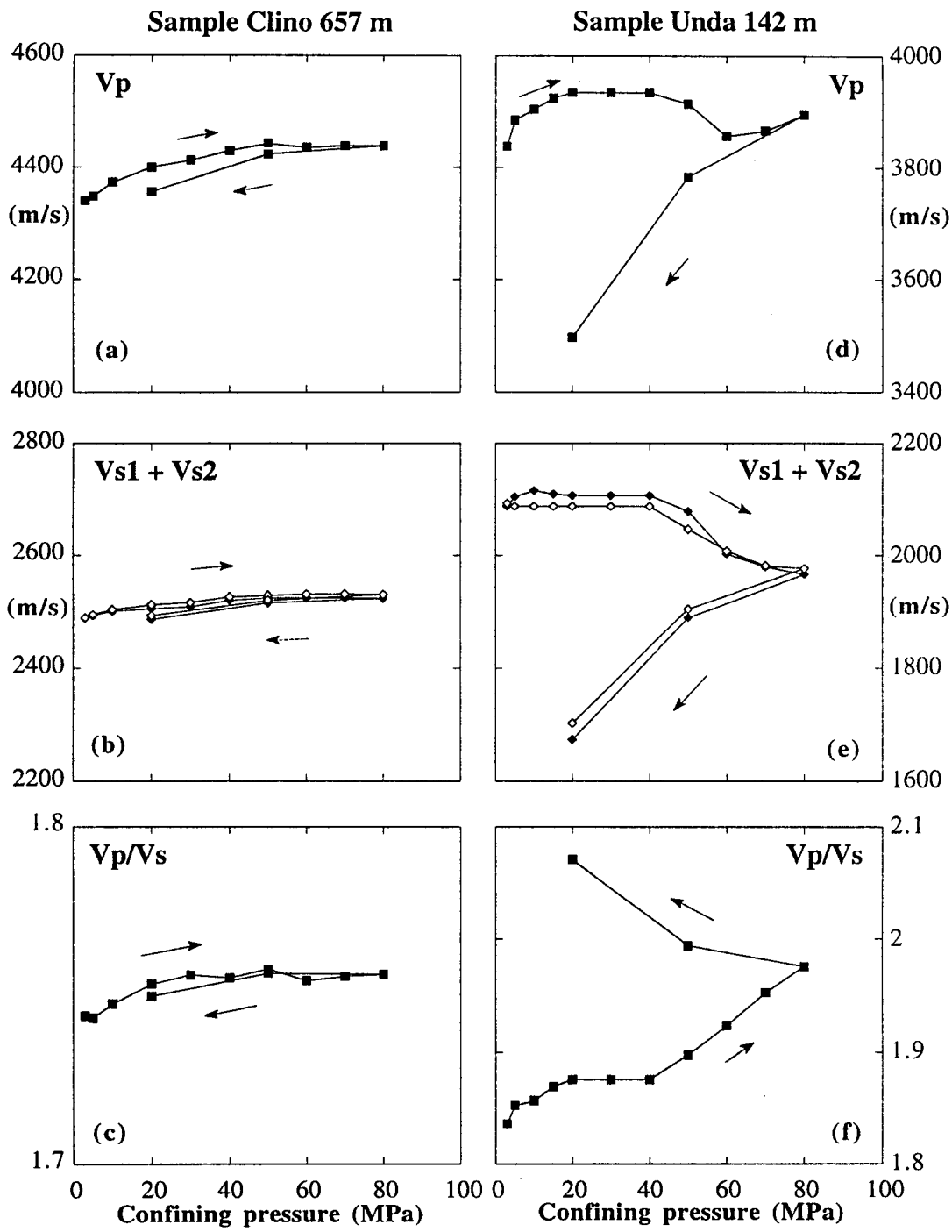

Figure 13: Two examples for elastic and non-elastic behavior of measured samples during changing confining pressures: Sample Clino 657 m shows a steady increase in Vp (a) and Vs (b); this increase is caused mainly by the closing of microcracks at elevated pressures. The increasing of Vp/Vs (c) shows that Vp increases more than Vs. The values reach a plateau at high pressures and approach starting conditions at the end of the hysteresis-loop. After the experiment, the plug shows no signs of damage. Sample Unda 142 m shows a similar increase in Vp at low pressures, but at a critical pressure of 40 MPa, Vp and Vs start to decrease (d+e). This decrease is the result of fabric destruction of the sample in the pressure vessel. The plug is fractured, and cemented grain contacts are destroyed, so that velocities decrease. Above 60 MPa, Vp starts to increase again (d), because the newly formed fractures are progressively closed. With the release of pressure, Vp and Vs decrease dramatically because the fractured plug disintegrates. The Vp/Vs increases remarkably above the critical pressure (40 MPa) and gets even higher at the end of the hysteresis-loop (f). Pore fluid pressure equals 2 MPa for all samples.

properties of aragonite are not well known. Comparisons of the calculated and measured velocities show that the measured velocities of the mud samples are only slightly above values predicted by the Wood equation, whereas all other samples, which were altered during diagenesis, show much higher values (Figure 11). The lower gradient of the mud samples can be explained by the absence of "additional" processes (e.g. diagenesis) that increase the rigidity of the rock and normally accompany the compaction of sediments. The artificial compaction experiments happen so quickly that no diagenetic alterations are initiated. Normally however, the effects of diagenetic processes, such as recrystallization or cementation, are superimposed on the effect of porosity reduction. The velocity, therefore, represents the combined effect of these different processes. The difference between the velocity-porosity relation in natural rocks and that in the artificial compacted rocks demonstrates how much diagenesis contributes to the observed velocity increases. The results shown in Figure 11 demonstrate that diagenetic alteration is more effective in increasing velocity than compaction, because it increases significantly the rigidity of the rock.

Burial Depth and Age

The samples taken from the two core borings in the Bahamas Drilling Project on the western margin of Great Bahama Bank show clearly that velocity is neither primarily a function of sediment age, nor of burial depth. In contrast to the usual assumption that velocity increases with depth (Hamilton, 1980; Japsen, 1993), the depth plots of Vp and Vs (Figure 4) from the two drillholes display velocity inversions that make velocity predictions, based only on depth, impossible. Both holes display a pattern of high variability of velocity in the carbonates that were deposited in shallow water environments (e.g. reef, platform margin or platform interior). The high-velocity zones, in Clino above 220 m and in Unda between 290 and 370 m and above 120 m, overlie zones of low velocity. The distinct jump to higher velocities at Unda 293 m, for instance, marks the transition from a fully dolomitized carbonate sand to a dolomitized reefal unit. Below the reefal unit, both Vp and Vs decrease again, resulting in a velocity inversion. Rocks of the low-velocity zones are mostly carbonates that were deposited in deeper water and which have undergone less diagenetic alteration than the shallow water carbonates. The trend of decreasing velocities at greater depths in part of the sections indicates that diagenetic processes other than simple compaction substantially control the velocity evolution. In the young sediments in the shallow parts of Clino and Unda, high velocities are attained due to intense diagenetic alterations that happen much faster than compaction due to increased overburden pressure.

The Maiella carbonates also demonstrate that depth, or in this case age, does not necessarily influence velocity. Some of the Upper Cretaceous rudist sands are among the oldest, but they also have the lowest velocities of the measured samples from this dataset. The Vp of 3300 m/s is remarkably low for Cretaceous carbonates, documenting again the insignificance of absolute age for velocity evolution in these samples. The reason for this low velocity is the preserved high porosity and the associated interparticle pore type (Mutti, 1994).

It is concluded that velocity predictions cannot be made from knowledge that a carbonate sediment has a certain age and/or is at a certain depth, but the acquisition of some additional, intrinsic rock parameters is necessary to give a reliable velocity estimation.

Effective Pressure

To investigate the pressure dependence of Vp and Vs in the consolidated rocks, sonic velocities of the Bahamas and Maiella samples were measured under varying confining and pore fluid pressures. Sonic velocity in rocks is a function of the differential pressure, or effective pressure, which is the difference between the confining and the pore fluid pressure. Minor departures from this relation are caused by changing pore fluid properties at different pressures (Coyner, 1984).

At low pressures, all samples show an increase in velocity with increasing effective pressure due to better grain contacts, changing pore shapes and closing of microcracks (King, 1966; Gardner et al., 1974). This increase is large for unconsolidated samples with low velocities (Figures 12 a, b, 13), whereas the velocities of indurated, dense samples are usually less affected by higher pressures. All velocity-pressure traces of the Bahamas samples (Figure 12 a) display a systematic pattern with higher gradients for low-velocity samples and lower gradients for fast samples. A minor part of the observed velocity-increase is an artifact, because compaction at increasing pressures reduces the sample length. Part of the Maiella samples which were measured at higher pressures than the Bahamas samples (up to 400 MPa) display a similar pattern (Figure 12 b): At low pressures, velocity increases significantly, resulting in a steep gradient. Higher confining pressure usually results in stagnating velocities, because most cracks in the rock were already closed at pressures below 100 MPa.

A characteristic of many samples is that both Vp and Vs reach a maximum during increasing pressure and suddenly decrease above a critical pressure. This velocity decrease is caused by disintegration and collapse of the sample in the pressure vessel, with progressive destruction of the partly cemented grain contacts that supported the transmission of the acoustic signal. Eventually, velocity may increase with further

increasing pressure (e.g. sample Unda 142 m, Figure 13 d) as the newly formed fractures that reduced the velocity close. In these samples, velocities that are measured under decreasing pressure at the end of a hysteresis loop (Figures 13 d, e) are much lower than at the same pressures in the first part of the loop, because the fractured plugs are irreversibly damaged to an unconsolidated fabric with loose fragments. Vp/Vs increases dramatically above the critical pressure (Figure 13 f) and continues to increase with decreasing pressure in the hysteresis loop. Shear wave velocity is affected in an extreme fashion by the destroyed fabric that results in non-elastic behavior. Similar behavior with decreasing velocity during increasing pressure was also observed in some Cretaceous samples from the Maiella, indicating that age or burial depth is not a guarantee for consolidation and lithification of a carbonate sediment.

In contrast to the non-elastic behavior described above, the hysteresis loops of fast, more lithified samples (e.g. sample Clino 657 m in Figures 13 a-c) show gentle increase in velocities with increasing pressure. Vp, Vs and Vp/Vs eventually reach plateaus at high pressures and almost return to the original velocities at decreasing pressures. In these cases, the plugs are perfectly intact when they are removed from the pressure vessel, documenting the elastic behavior of the high-velocity rocks under moderately increasing pressures.

The critical pressure at which the first velocity decrease occurs varies with lithology. Dense, indurated rocks display no evidence of fabric-destruction up to the highest measured pressures of 100 MPa (or even up to 400 MPa in some Maiella samples, Figure 12 b), whereas soft, unconsolidated samples show signs of velocity-decrease at pressures as low as 5 MPa. Under hydrostatic conditions, an effective pressure of 5 MPa is equivalent to a burial depth of less than 500 m, which is about the depth of the two drillholes on Great Bahama Bank. The cores of these two drillholes are in fact distinguished by open or partly cemented fractures that have a pre-drilling origin (Kenter and Ginsburg, 1994). The low critical pressures, at which fracturing occurs, demonstrate that some carbonates, especially the slope deposits or sucrosic dolomites, became buried without being progressively indurated. Another fact is, that many of the Bahamas samples show no signs of destruction of the fabric up to high pressures, demonstrating that relatively high porosity can be preserved even at pressures of 100 MPa. This pressure is equivalent to a depth of 5km, assuming an average rock density of 2 g/cm^3 (compare densities in Tables 7 a+b). If the pore-water network is open to the surface, the effective pressure of 100 MPa will be the equivalent of a burial depth of up to 10 km (since effective pressure = confining (lithostatic) pressure - pore fluid pressure).

Velocity as a Function of Rock-Intrinsic Parameters

Depositional Lithology

The lithology of a carbonate sediment at the time of deposition has a strong influence on the evolution of velocity, because it controls future alterations of the rock. At the time of deposition all unconsolidated sediments have velocities between 1550 and 1800 m/s. The different lithologies have, however, different susceptibilities to diagenetic alteration that will change with time the physical properties and thus the velocities of the sediments. The diagenetic susceptibility of certain sediments causes fast or slow alterations of the rock fabric, depending on the diagenetic potential of the sediment (Schlanger and Douglas, 1974) and on the diagenetic regime.

Bahamas

In the Bahamas cores, the velocities of the shallow water and deeper-water deposits have different ranges with an overlap of values in the low-velocity area (Figure 4). The majority of the Bahamian slope carbonates are unconsolidated and, thus, have low velocities, whereas the platform carbonates range from low to relatively high velocities. Therefore, not all platform deposits reach high velocities, but both the average velocity and overall velocity range are much higher for the platform samples than for the slope samples. Only turbidites in the slope section, which contain platform-derived material, have high velocities resulting in similar velocity variability as in the platform deposits (Figure 4).

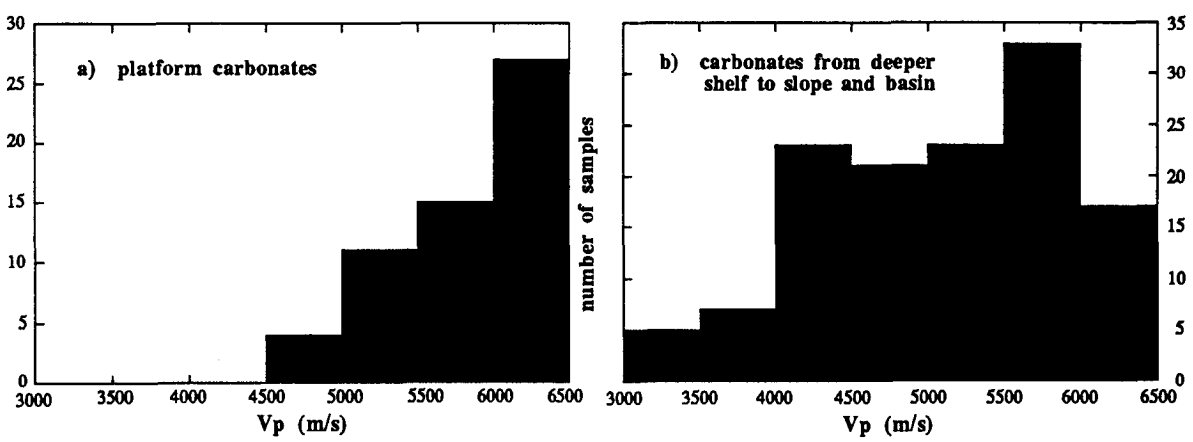

Figure 14: Ranges of Vp (at 8 MPa effective pressure) of different depositional environments from the Maiella. Carbonates deposited on the shallow water platform (a) have a narrow range with generally high velocities. Sediments from the deeper shelf, slope or basin (b) show a higher variability towards lower Vp, but maximum velocities are the same as in the platform rocks.

Maiella

Comparison of velocity ranges with depositional environments in the Maiella confirms the relationships described above. For example, if the Maiella samples are grouped into two categories of depositional environment, (1) platform deposits and (2) basin, slope and deeper shelf deposits (Figure 14), the velocity range of the two categories form two distinct clusters that only overlap in the high velocity area. The platform carbonates have a significantly higher average velocity than the basin, slope and deeper shelf carbonates.

Explanation for observed velocity variations

The diagenetic potential of a sediment is an important factor in the evolution of velocity. This potential is mainly a factor of the grain size and the amount of metastable minerals (Schlanger and Douglas, 1974). A high content of fine-grained micritic material, as found in mud- or wackestones, results in a low permeability. The resulting low rate of fluid flow inhibits or slows diagenetic alterations that rely on the transport of chemicals in water. In contrast to fine-grained rocks, sediments with a grain-supported fabric and a low content of micrite (grain- to packstone) have a higher permeability and, as a consequence, a higher fluid flow. This accelerates diagenetic processes such that the sediment is quickly altered and consolidated. Thus, original coarse-grained rocks may reach higher velocities after a relatively short time of burial, whereas fine-grained rocks tend to preserve their unaltered fabrics and their low velocities for longer burial durations. In addition to grain size, the amount of metastable minerals, such as aragonite or high-magnesium calcite, controls the diagenetic potential. A high amount of metastable components causes a high diagenetic potential, leading to rapid dissolution or recrystallization of the sediment. This alteration can enhance the elastic properties and increase permeability, resulting in accelerated lithification.

In the Bahamas as well as in the Maiella, the platform carbonates are usually high in coarse skeletal or non-skeletal grains (ooids, peloids). They consist predominantly of aragonite (ooids, peloids, corals, *Halimeda*, bivalves, etc.), which is metastable in sea water. On the other hand, slope or deeper water deposits are normally characterized by high micritic grain fractions, by higher contents of pelagic calcareous organisms (globigerinids, coccoliths) and by more stable low-Mg calcite shells. Shallow water carbonates fulfill thus both conditions for fast diagenetic alterations: coarse grain size and a high amount of metastable minerals. Some turbidites deposited on the slope contain many skeletal aragonitic fragments from the platform top and are therefore similar to the platform deposits and different from the normal slope sediments (Eberli, 1988). This explains the fast velocities in the generally low-velocity slope section of Clino (Figure 4).

In the Maiella samples, most of the platform carbonates had enough time for diagenetic alteration, allowing the sediments to reach their stable mineralogy and thus their final high velocities. As a consequence, the platform sediment velocities cluster at higher values than the slope sediment velocities (Figure 14). In the Bahamas cores, the velocities of shallow water carbonates are also higher than those of the slope sections and may reach the same maximum velocities as samples from the Maiella. However, due to their younger age and partially incomplete diagenetic alteration, they have a broader range that includes lower velocities.

These data suggest strongly that the depositional environment of a carbonate sediment determines the starting conditions for a sediment to undergo diagenetic alterations. This indirect influence controls rock-intrinsic parameters such as porosity, pore type, density and mineralogy.

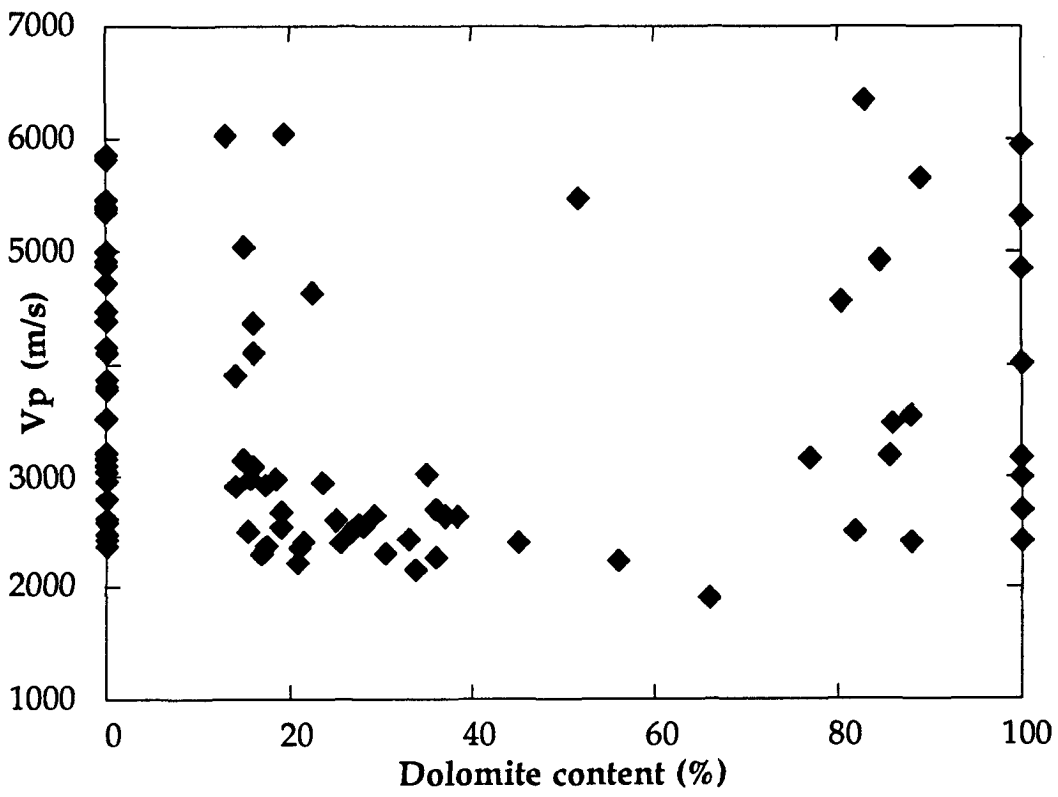

Figure 15: Velocity (at 8 MPa effective pressure) as a function of dolomite content in the Bahamas samples. There is no correlation between these two factors. However, different dolomite fabrics, such as sucrosic dolomite or dolomite-cement, have profound, but different effects on velocity. Therefore, dolomite content alone cannot be used as an indicator for velocity.

Mineralogy

More than 95% of the minerals in the measured samples from the Bahamas cores are calcite, dolomite and aragonite, and the Maiella carbonates consist almost totally of calcite. The difference between the velocities of the three carbonate minerals calcite (6.53 km/s), dolomite (~7.4 km/s), and aragonite (~5.8 km/s) (Simmons and Wang, 1971; Carmichael, 1989) are high enough, so that, similar to siliciclastic rocks, some control of mineralogical composition on the velocity might be expected. In siliciclastics, the physical variety of minerals is very large (e.g. quartz and clay) and mineralogy has strong influence on sonic velocity (Christensen and Szymanski, 1991). However, as shown below, the data of this study suggest that changes of mineralogical composition in pure carbonates have no major influence on velocity.

A plot of dolomite content versus velocity of the Bahamas samples clearly shows no correlation (Figure 15). This lack of correlation is apparent in two measured plugs from Unda only 7 m apart. Both are composed of 100% dolomite: sample Unda 286 m has a Vp of 2697 m/s and a Vs of 1052m/s, whereas sample Unda 293 m has a Vp and Vs of 5953 m/s and 3187 m/s. The high-velocity sample is a "reefal" dolomite with a fabric preserving dolomitic cementation resulting in a total porosity of 14%, whereas the low-velocity sample is a sucrosic dolomite with a high interparticle/intercrystalline porosity of 49%. This suggests that the effect of mineralogy is insignificant compared to the effect of porosity and fabric. Velocity depends more on the type of dolomite and thus the associated fabric, porosity, and pore type. Mineralogy alone is thus not a critical parameter for the determination of velocity in carbonates.

While the mineralogical composition in carbonates has little direct influence on velocity, the processes, however, that alter mineralogy have a strong influence. These processes, such as sucrosic dolomitization or dolomitic cementation, also alter, in concert with changing mineralogy, porosity and porosity type. For example, fabric-destructive dolomitization also destroys most of the earlier cementation, creating an under-cemented and loose dolostone with petrophysical characteristics similar to a semi-lithified carbonate sand.

Porosity and Pore types

Velocity is strongly dependent on rock-porosity (Wang et al., 1991, Rafavich et al. 1984). A plot of porosity versus velocity displays a clear inverse trend; an increase in porosity produces a decrease in velocity (Figure 16). Using the following relationships,

the general trend of the Bahamas and Maiella samples have correlation coefficients of 0.94 for Vp and 0.92 for Vs.

$$Vp\ (m/s) = 6393 \cdot e^{-0.0180 \cdot \text{porosity}\ (\%)}$$

$$Vs\ (m/s) = 3527 \cdot e^{-0.0206 \cdot \text{porosity}\ (\%)}$$

Nevertheless, the measured values display a large scatter around these best-fit exponential curves. Velocity differences at equal porosities can exceed 2500 m/s, especially at high porosities. For example, rocks with porosities of 40 % can have velocities between 2100 m/s and 5000 m/s, which is an extraordinary range for rocks with the same chemical composition and the same porosity. It will be shown that this variation is caused by the ability of carbonates to form cements and particular fabrics that, though highly porous, can enhance the elastic properties of the rock without filling the pore space. The high elastic moduli result in velocities that are higher than velocities predicted by theoretical equations, such as the time average equation (Wyllie et al., 1956), as shown in Figure 16.

In other datasets, such as from artificial sand-clay mixtures (Marion et. al, 1992) or siliciclastic sediments (Vernik and Nur, 1992), similar scattering in the velocity-porosity diagram is observed. But unlike carbonates, the scattering in these rocks can be explained by compositional variations, in particular by changes in clay content. Wilkens et al. (1991) noticed that velocities of low-porous basalts are very dependent on the pore shapes. Samples containing pores with low aspect ratios (cracks) are associated with lower velocities than samples with round pores or high aspect ratios. As a result, high velocity contrasts without large variations in total porosity are observed between rocks.

The pores in the high porosity carbonates generally have high aspect ratios. In this case, the high velocity contrasts between rocks with similar total porosity can be related to specific pore types resulting in characteristic and very different elastic properties. Based on thin section observations, the Bahamas samples can be grouped into five categories of predominant pore types all of which have characteristic clusters in the velocity-porosity diagram (Figure 17). The five dominant pore types that can be distinguished are:

(1) Interparticle and intercrystalline porosity (Figure 18): The pore space between the components of a sediment is interparticle porosity. This porosity predominates after deposition of a sediment when grains form a loose package with little cementation. Intercrystalline porosity develops at a later stage during diagenesis, when newly crystallized minerals such as dolomite rhombohedra form a loose aggregate - it has a similar petrophysical behavior as interparticle porosity. The accumulation of

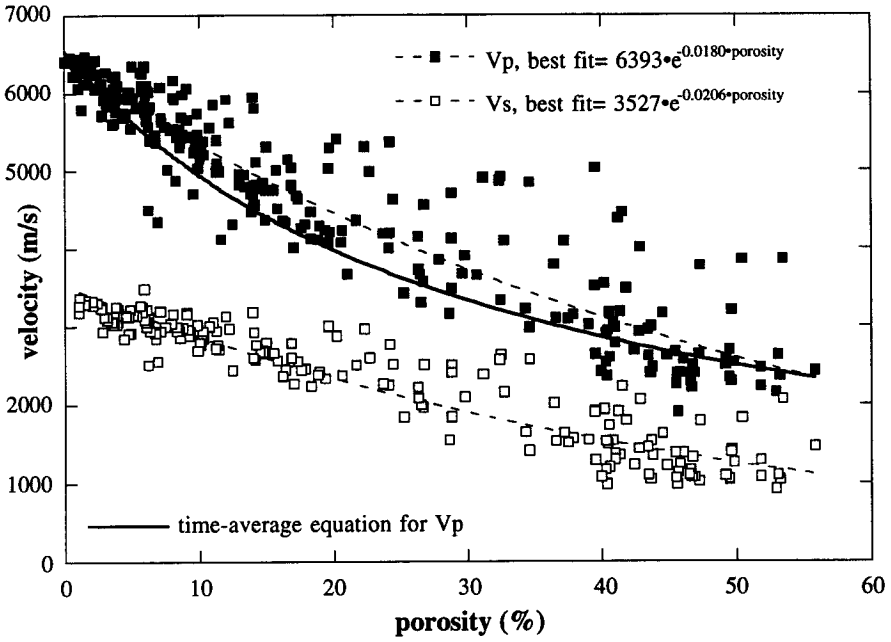

Figure 16: Vp and Vs from the Bahamas and the Maiella samples (at 8 MPa effective pressure) as a function of porosity with exponential best-fit equations. Both Vp and Vs demonstrate the trend of decreasing velocities with increasing porosities, but scatter, especially at higher porosities, is observed around the dashed best-fit lines. The scattering is a result of certain fabrics and pore types that enhance the elastic moduli of the rock without filling the pore space. As a consequence, measured Vp are higher than Vp predicted by theoretical equations, such as time-average equation (solid line, Wyllie et al., 1956).

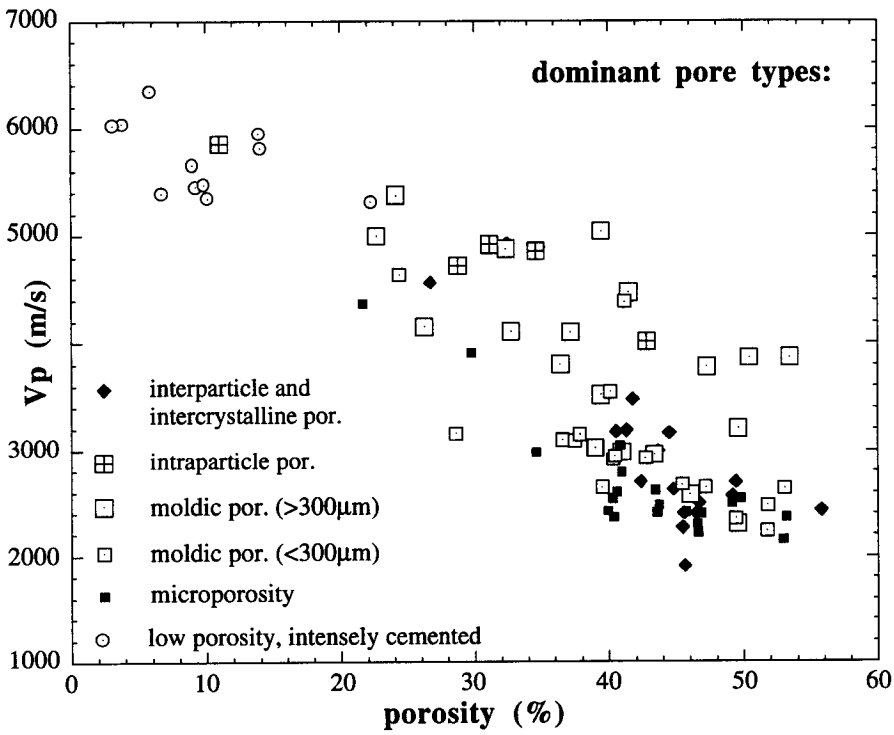

Figure 17: Velocity vs. porosity diagram for the Bahamas samples, with observed categories of different pore types. The large scattering (e.g. velocities from 2200 to 5000 m/s at porosities of 40 %) is a result of different predominant pore types in the analyzed samples. Rocks with moldic or intraparticle porosity have positive departures from the general trend, whereas rocks with interparticle, intercrystalline, or micro-porosity have relatively low velocities, and show thus negative departures. Velocities are taken at an effective pressure of 8 MPa. (Compare with Figure 24).

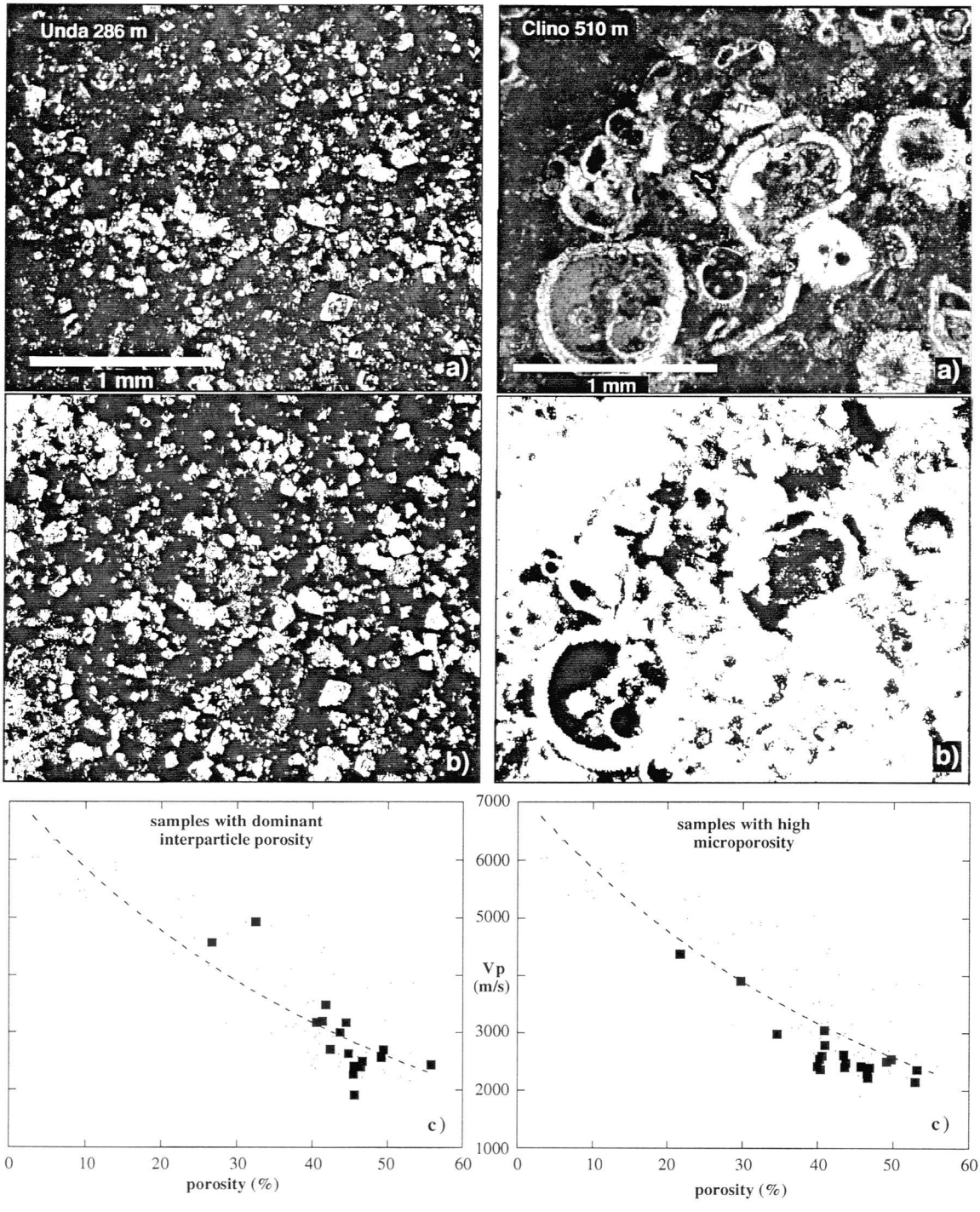

Figure 18 a: Photomicrograph of a sample with interparticle (intercrystalline) porosity: Unda 286m - The sediment is completely altered to micro-sucrosic dolomite. Plug-porosity is 49%. **b:** Computerscan of thin section above (porosity black, particles white) with characteristic pattern of interparticle porosity. Loose grains are surrounded by connected pore space. **c:** Velocity-porosity diagram of all samples with dominant interparticle or intercrystalline porosity; Velocities are in general below the average velocity-porosity trend (dotted line).

Figure 19 a: Photomicrograph of a sample with high micro-porosity: Clino 510m - Slope deposit rich in globigerinids and micritic matrix. Almost no diagenetic alterations and only little compaction are visible. Plug-porosity is 35%. **b:** Computerscan of thin section above (porosity black, particles white). Due to the fine pore size, only part of micro-porosity is detected by the scan. **c:** Velocity-porosity diagram of all samples with high micro-porosity. Velocities are in general below the average velocity-porosity trend (dotted line).

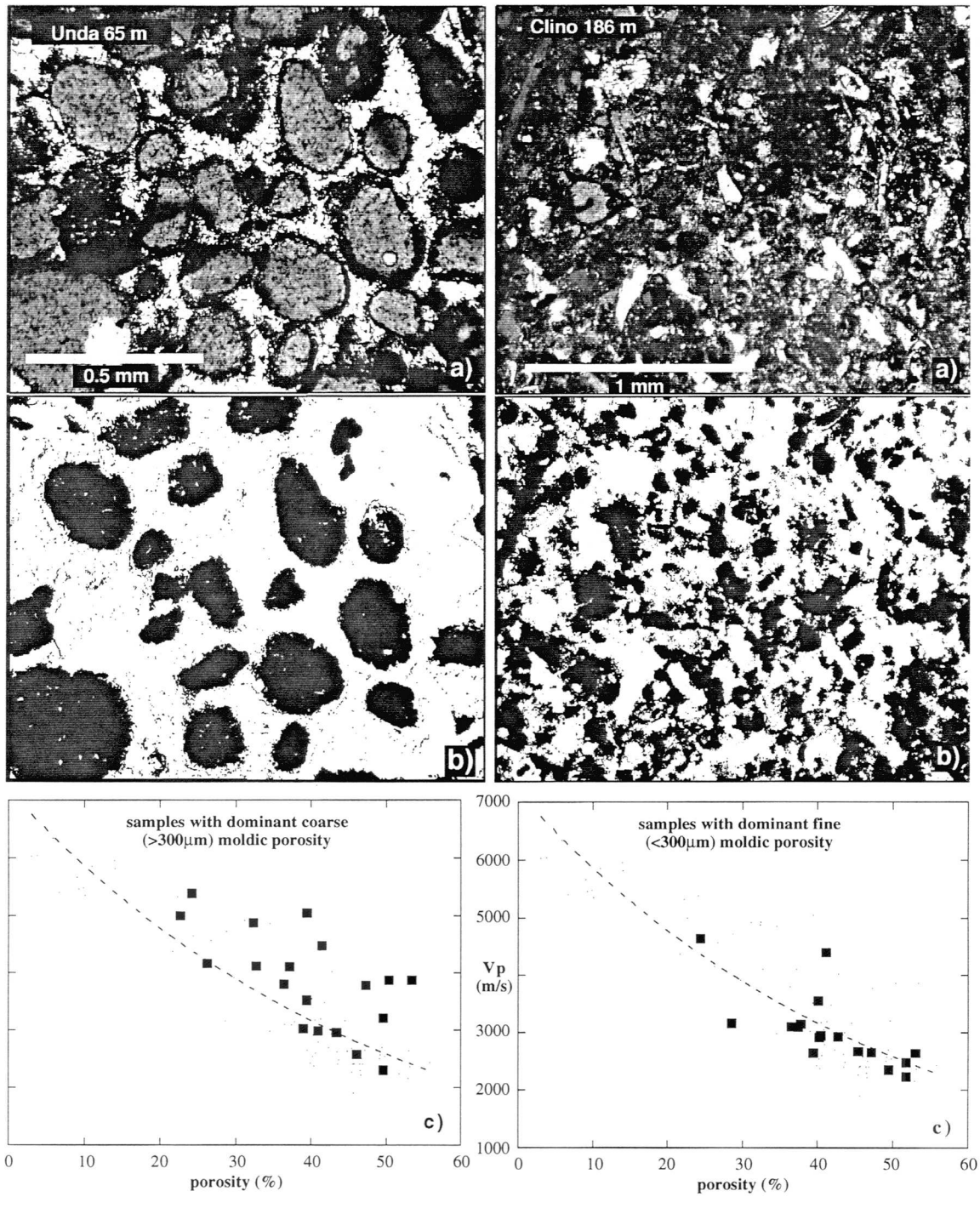

Figure 20 a: Photomicrograph of a sample with coarse (>300µm) moldic porosity: Unda 65m - All components of this grainstone were dissolved during and after cementation of the interparticle pore space. Plug-porosity is 37%. **b:** Computer-scan of thin section above (porosity black, particles white). The non-connected molds are integrated in the frame of sparry cement. **c:** Velocity-porosity diagram of all samples with dominant coarse moldic porosity. Velocities are significantly above the average velocity-porosity trend (dotted line).

Figure 21 a: Photomicrograph of a sample with fine (<300µm) moldic porosity: Clino 186m - Most skeletal to non-skeletal grains are dissolved. Plug-porosity is 45%. **b:** Computer-scan of thin section above (porosity black, particles white). The fine molds are embedded in a frame of micrite, cement and remaining grains. **c:** Velocity-porosity diagram of all samples with fine molds as dominant pore type. Vp are lower than in coarse moldic rocks (Figure 20) and form a cluster along or slightly below the average velocity-porosity trend.

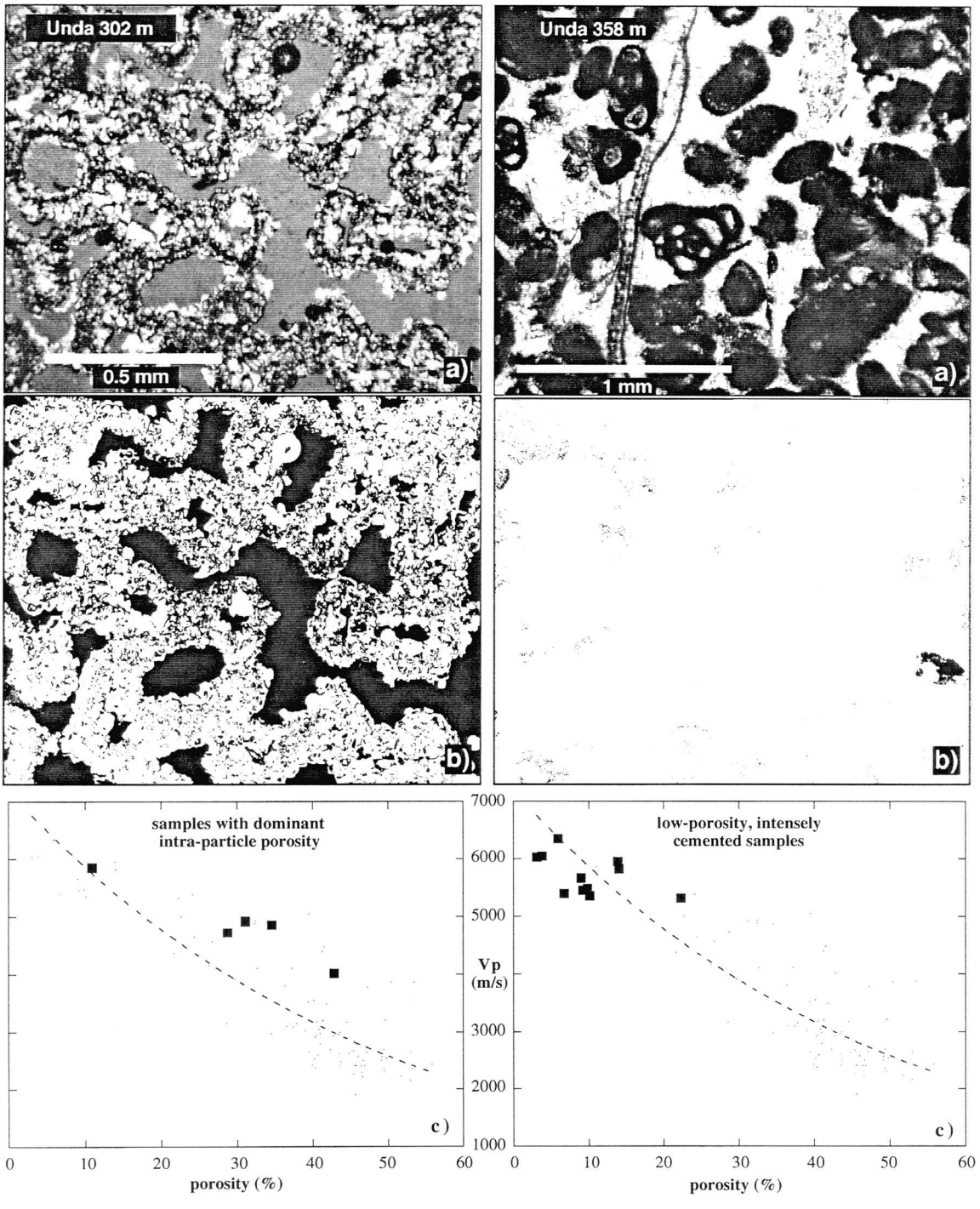

Figure 22 a: Photomicrograph of a sample with intraparticle porosity: Unda 302m - The coral has a porosity which is integrated in the construction of the framestone. Plug-porosity is 43%. **b:** Computerscan of thin section above (porosity black, particles white). The porosity is part of the constructional framework of the coral. **c:** Velocity-porosity diagram of all samples with dominant intraparticle porosity (mainly frame- and boundstones). Velocities are, similar to coarse moldic rocks (Figure 20), higher than the average velocity-porosity trend.

Figure 23 a: Photomicrograph of a sample which is densely cemented and has low porosity: Unda 358m - The mainly skeletal grainstone is cemented with a blocky calcite that completely filled the former interparticle pore space. Plug-porosity is 3%. **b:** Computer-scan of thin section above (porosity black, particles white). Almost no porosity is detected by the scan. **c:** Velocity-porosity diagram of all samples with intense cementation and low porosity. These samples form a cluster at the upper end of the correlation line with high velocities and low porosities.

unconnected grains without cement or matrix results in low velocity, because without a rigid framework, the rock has low elastic moduli. Most of these samples show a negative departure from the average velocity-porosity exponential curve (Figure 18).

(2) Micro-porosity (Figure 19): Micro-pores (<10μm) are abundant in carbonate mud, either in a micrite grain or in the micritic matrix. High micro-porosity is thus expected in carbonates with a high micritic content. Due to the lack of cementation that results in an unconnected grain fabric, micro-porosity has a similar effect on velocity as fine-grained, interparticle porosity. It shows a negative departure from the average velocity-porosity trend.

(3) Moldic porosity (Figures 20, 21): Moldic porosity develops by dissolution of grains with a metastable mineralogy (e.g., grains of aragonite and high-Mg calcite). Selective dissolution can occur before, during, or after cementation of the interparticle pore space. After dissolution, the rock consists mainly of molds and the partially cemented former interparticle pore space which is a fabric type with high values of the elastic parameters. Samples in which moldic porosity predominates have higher velocities than expected from their total porosities, and therefore a positive departure from the best fit curve (Figures 20, 21). These high velocities are caused by the self supporting framework comprising cement and micrite surrounding the molds. The travel time through this framework is faster than through grains that are only connected by point contacts, as found in rocks with interparticle porosity. In addition, velocity is dependent on the diameter of the molds. Velocities are higher in coarse moldic rocks, whereas fine-moldic samples are relatively slower.

(4) Intraparticle porosity (Figure 22): Framestones and boundstones, formed by organisms such as corals or bryozoans, consist of a constructional framework with a porosity that is embedded in the solid frame. Therefore, these samples show a similar velocity-porosity pattern to coarse moldic porous rocks that also have a framework with high elastic rigidity, resulting in high velocities. The samples with predominant intraparticle porosity all show positive departures from the general trend in the velocity-porosity diagram.

(5) Low porosity samples with dense cementation (Figure 23): These samples show an extensive, blocky cementation with porosities of 20 % or less. They are close to the final stage of diagenetic evolution. Velocities are high and close to the intrinsic velocities of the minerals calcite (6500 m/s) and dolomite (6900 m/s). These samples form the upper part of the velocity-porosity correlation line.

As discussed above for the Bahamas samples, the variety of pore types explain why rocks with the same porosity can have extremely different velocities. The most significant velocity contrasts at equal porosities are measured between coarse moldic

rocks and rocks in which interparticle porosity predominates (Figures 17, 20). Moldic rocks with 40-50 % porosity can have velocities up to 5000 m/s, whereas rocks with interparticle or intercrystalline porosity have velocities of about 2500 m/s with the same porosities. This relationship between pore type and velocity can also be seen in the samples measured from the Maiella (Figure 24). The Cretaceous rudist sands consisting of individual, non-connected rudist fragments with only little cementation, have a predominant interparticle porosity and therefore have very low velocities of around 3000 m/s.

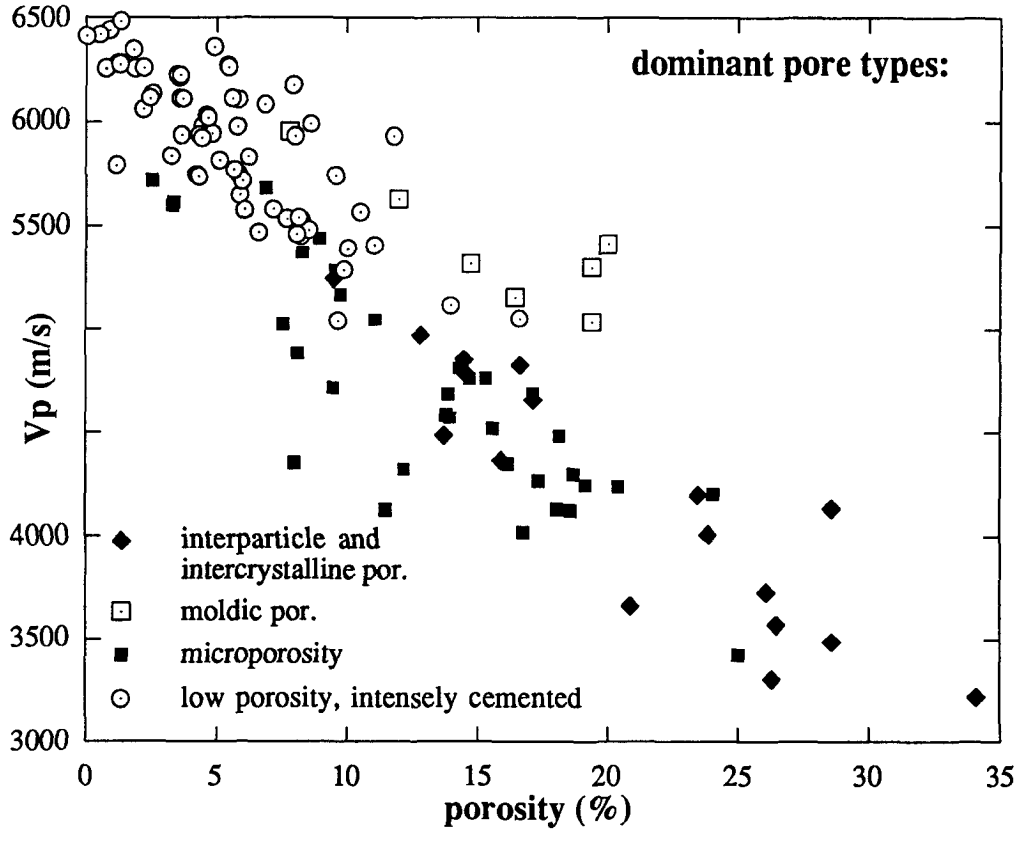

Figure 24: Velocity vs. porosity diagram for the Maiella samples, with observed categories of different pore types. Although the range of porosities is smaller than in the Bahamas samples, these samples show similar clusters of velocity-porosity values as a function of the dominant pore type (Figure 17). At the same total porosities, moldic porosity generally results in higher velocities than does micro-porosity or interparticle porosity.

Velocity estimation for a given carbonate sample should not be attempted using only the porosity values, but in combination with an assessment of the pore type. The observed complicated velocity-porosity patterns, which cause matching impedance-porosity patterns, imply that an impedance contrast between two layers can occur even without a porosity change, due only to different pore types.

The reason for the lack of strong correlation between velocity and mineralogy is the described dominant role of porosity on the velocity determination. The combined relationships between these factors are documented in Figure 25, which compares the influence of mineralogy (calcite versus dolomite) with the influence of porosity, without consideration of the different pore types. It can be clearly seen that the different carbonate minerals (calcite and dolomite) have an insignificant effect on velocity when compared with porosity.

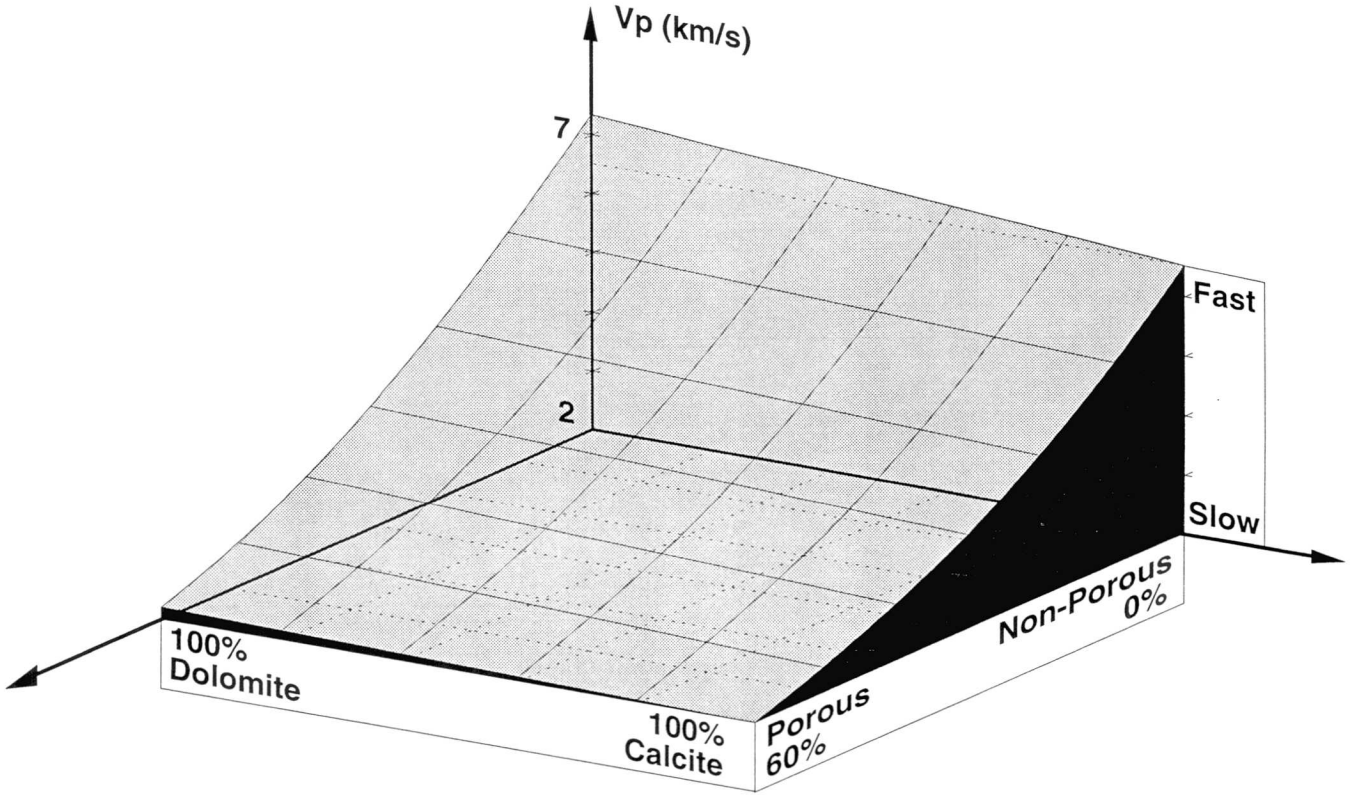

Figure 25: Schematic diagram showing the relationships of mineralogy and porosity to sonic velocity in carbonates, without consideration of different pore types. Curved porosity-velocity relation is empirical (from measurements), linear mineralogy-porosity relation is caused by velocity-differences in plain minerals calcite (6500m/s) and dolomite (7400m/s). This diagram shows why mineralogy has only a minimal influence on velocity as compared to the influence of porosity.

Density

Seismic reflection patterns are a function of acoustic impedance contrasts. In many case studies, only one parameter, either velocity or density, is known and the other has to be estimated using empirical functions or formulae. Because density is closely related to

porosity, velocity shows a good correlation with density (Figure 26). Despite the good correlation coefficients of 0.94 for Vp and 0.93 for Vs, the data in a plot of velocity vs. density scatter around a best-fit curve that reflects the carbonate specific pore types. The velocity-density trend from our dataset can be used to calculate the velocity-density formula for pure carbonate rocks. Hitherto, most empirical formulae, such as the general Gardner's Law (Gardner et al., 1974), are mainly applicable for siliciclastic rocks. Gardner's Law is an empirical equation for sedimentary rocks relating Vp to density:

$$\text{density (g/cm}^3\text{)} = 0.23 \cdot [\text{Vp (ft/sec)}]^{1/4}$$

or

$$\text{Vp (m/s)} = 108.9 \cdot [\text{density (g/cm}^3\text{)}]^4$$

This formula is used mainly to calculate impedance values from either density data alone or velocity data alone. However, the laboratory measurements resulted in velocities that are all higher than the velocities predicted by Gardner's Law (Figure 26). This deviation implies that Gardner's Law, which is an average formula for all sedimentary rocks, requires a modification for carbonates towards higher velocities. Based on the data from the Bahamas and Maiella samples, the following empirical formulae are suggested:

$$\text{Vp (m/s)} = 524 \cdot [\text{density (g/cm}^3\text{)}]^{2.48} \qquad \text{Vs (m/s)} = 199 \cdot [\text{density (g/cm}^3\text{)}]^{2.84}$$

The proposed formula for Vp fits well another dataset shown in Kenter and Ivanov (1994) and fits well the special Gardner correlation for limestones [density (g/cm^3) = 1.493 • Vp(km/s) $^{0.324}$] plotted in a figure by Gardner et al., (1974) and graphically depicted by Kenter and Ivanov (1994).

Pore Fluid

Experimental and theoretical studies have shown that the state of saturation and the type of pore fluid are strong influences on acoustic properties of porous rocks (Nur and Simmons, 1969; Wang et al., 1990; Batzle and Wang, 1992). The investigated samples with maximum porosity values of over 50 % in this study are expected to have velocities that are sensitive to changes in pore fluid properties.

The effect of different pore fluids however has not been addressed in this study. The measured velocities have been applied to a seismic interpretation and to seismic modeling of carbonate deposits that have exclusively brine as pore fluid and that require thus no measurements with different pore fluids. Except for a few measurements of

selected Maiella samples, which were measured under dry conditions, all velocities from this study were determined on minicores that were saturated with brine or water and that were set under independent confining and pore fluid pressures.

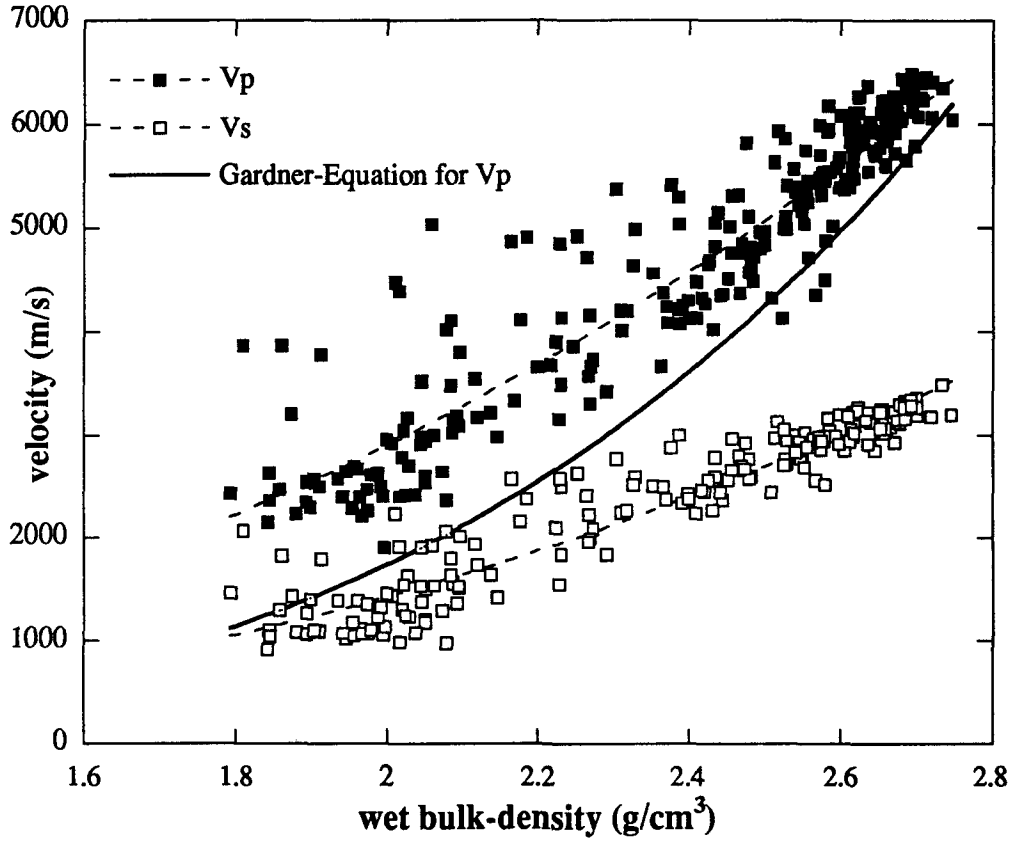

Figure 26: Velocity as a function of density in the Bahamas and Maiella samples (at an effective pressure of 8 MPa). The solid line represents Vp calculated by the general "Gardner's Law" [density (g/cm^3) = 0.23 Vp $(ft/sec)^{1/4}$], an empirical formula for all sedimentary rocks, which is often used to calculate impedance values from only velocity or only density data (Gardner et al., 1974). The velocities of the measured carbonates are all higher than the Gardner equation velocities. The equation thus has to be modified towards higher velocities in order to produce more reliable velocity-density pairs in carbonates (for suggested equations see text).

Permeability

Permeability of 32 samples from the Bahamas boreholes was determined by measuring the flow of nitrogen gas through plugs of known dimensions (Tables 7 a, b). Permeability is highly variable in the porous carbonates of Unda and Clino; values range from 0 to 678 millidarcies (md). The highest permeabilities were measured on two sucrosic dolomites with fully connected intercrystalline porosity that allows high fluid-flow. The low permeability samples consist either of densely-cemented rocks or have a

high content of micro-porosity (wacke- or packstones). The logarithmic plot of the available Klinkenberg permeability data with porosity (Figure 27 a) shows a wide range in permeability values and a general positive correlation. Permeabilities far from the average trend can be related to samples with special pore types and pore-sizes that have characteristic effects on permeabilities. Very low permeabilities at high porosities are observed in samples with high amounts of micro-porosity, such as sample Clino 1503 ft/458 m (<0.01 md permeability at 43% porosity), or sample Clino 955 ft/291 m (0.9 md at 47 %). Samples with a connected, coarse porosity, such as in a coral boundstone (Clino 365 ft/111 m; 63 md permeability at 11 % porosity), show high permeability values, despite their relatively small amounts of porosity (Figure 27 a, Tables 7 a, b).

The number of permeability measurements is limited and does not allow a statistically-provable correlation. Nevertheless, the scatter suggests that the different pore types not only cause different velocities but also variable permeabilities. The crossplot of velocity with permeability (Figure 27 b) shows only a moderate correlation. Based on this limited dataset, it does not to seem reasonable to make permeability predictions directly from velocity analyses.

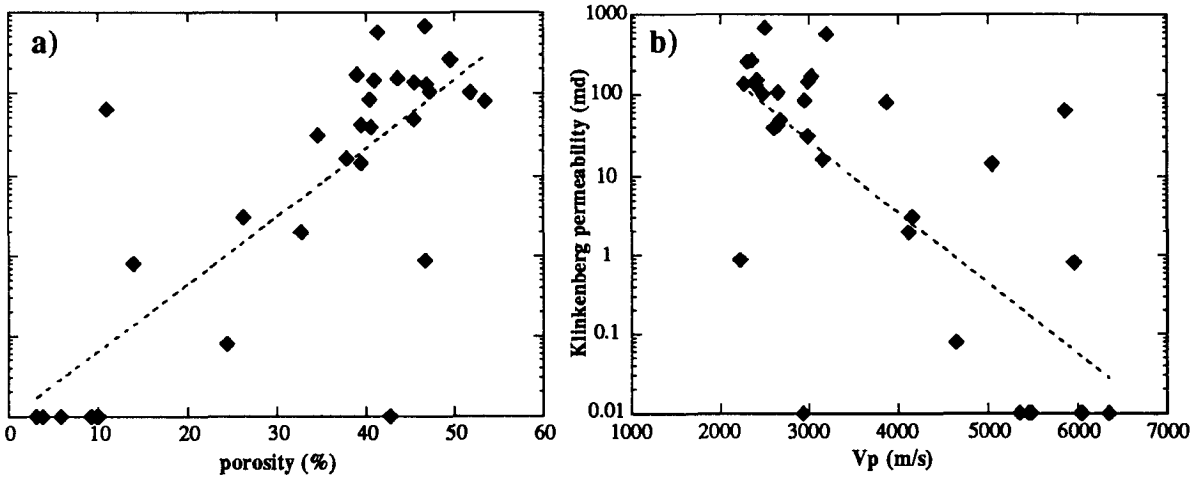

Figure 27: Crossplot of Klinkenberg permeability with porosity (a) and velocity (b). The scatter around the general trend in (a) might be caused by different pore types, but the permeability dataset is too limited to relate closely all variations to changes in lithology. The moderate correlation in the permeability-velocity diagram (b) suggests that velocities cannot be used to predict permeability.

A.6. VELOCITY-EVOLUTION DURING DIAGENESIS

Diagenesis is a very important process in carbonates that can transform a lithified sediment into a rock with completely different physical properties. These post-depositional processes alter porosity and cause transformations to different fabric and pore types that produce characteristic patterns in the velocity evolution. The different ages of the analyzed samples, which cover almost continuously the period from Cretaceous to recent times, offer the special opportunity to measure velocities at the different stages of the various diagenetic processes. In particular, the samples from the Bahamas cores document in detail the evolution of the porosity-velocity relations for carbonate sediments under varying diagenetic stages, because most of these samples are caught in the act of ongoing diagenetic alterations. The development of porosity and pore types can be determined by analyzing the original composition and the subsequent suite of diagenetic events. This development can then be correlated to the measured physical properties.

The Concept of Velocity-Porosity Paths

The correlation of lithologies with velocities and porosities shows that the different diagenetic processes affect the evolution of porosity and velocity of a sediment much more than compaction does. Several stages of dissolution and cementation can be distinguished during the diagenetic history of the investigated samples (Melim et al., 1994). These stages lead to different pore types that have characteristic patterns in the velocity-porosity diagram. The effect of diagenetic evolution, in particular the effect of the transformation of pore types, can be described by a velocity-porosity path (Figures 28-30). During burial, every sediment follows a velocity-porosity path, which starts at deposition and ends at the time, when velocity-porosity values are measured. This diagenetic path can be complicated, depending on the number of diagenetic stages and the related pore types. The different clusters of these pore types in the velocity-porosity diagram (Figures 17-24) make the velocity-porosity paths of the sediments rather to be curved paths than straight lines, depending on the timing of the diagenetic events.

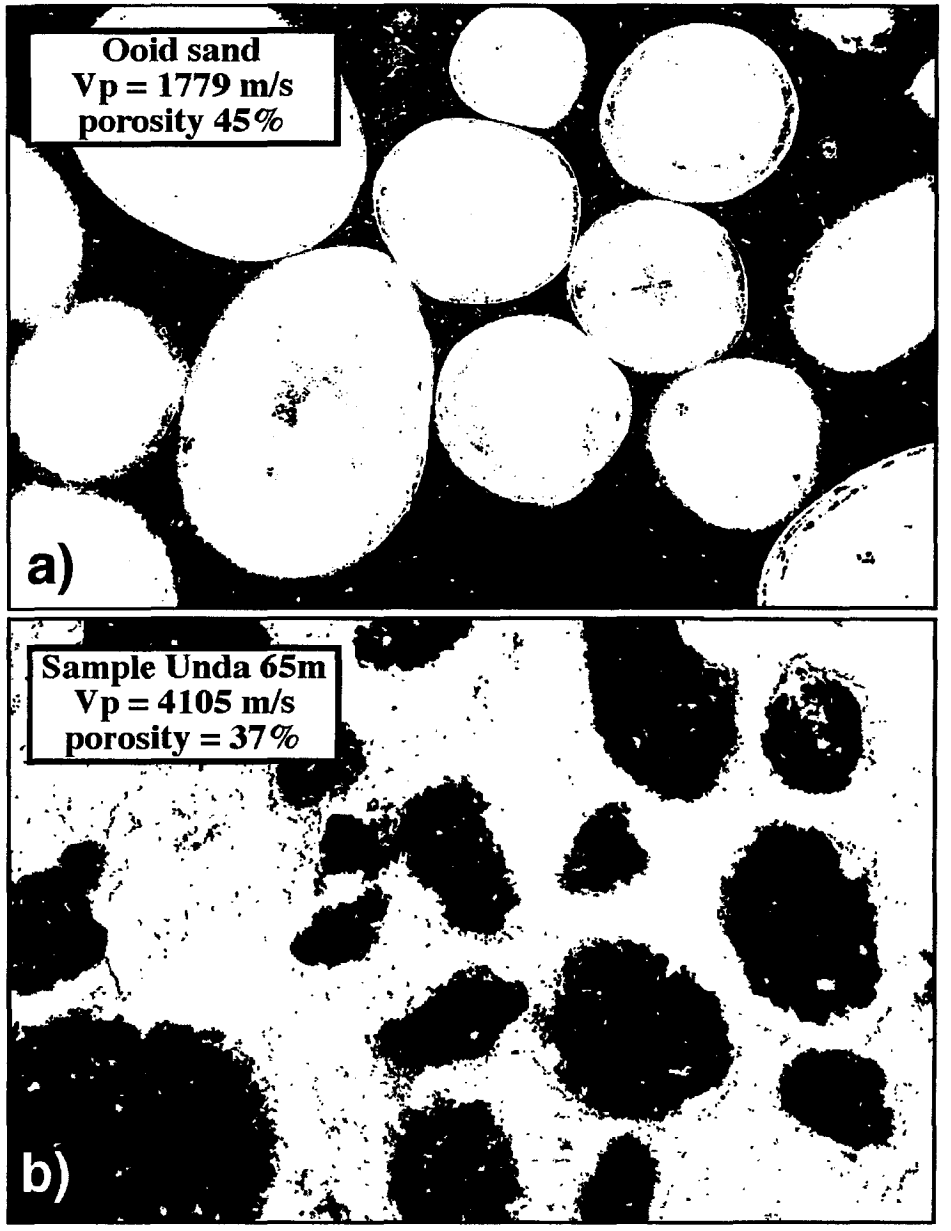

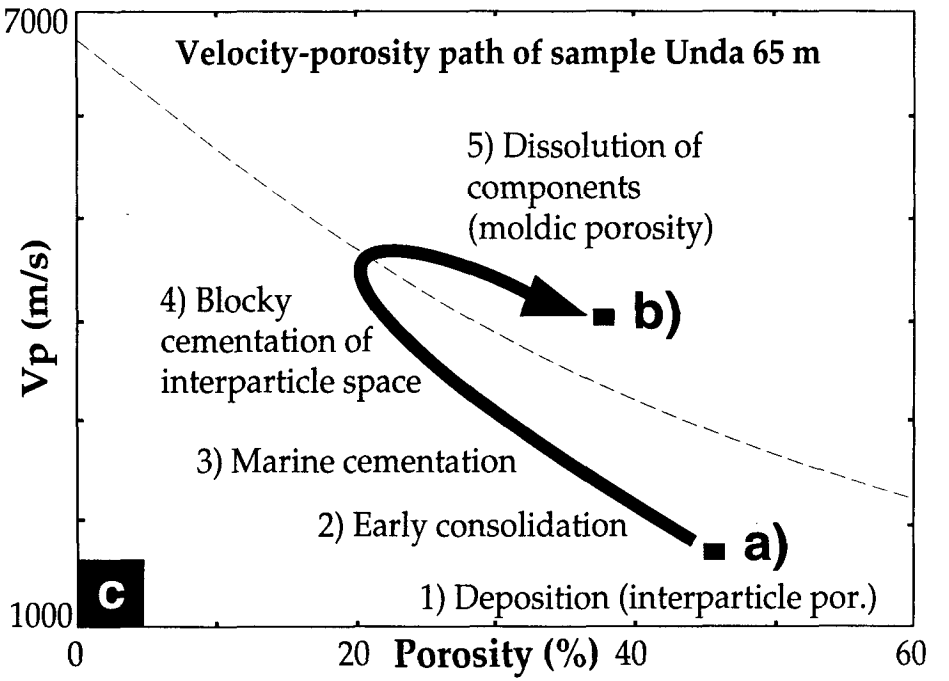

Figure 28: Example of reconstruction of a porosity-velocity path. Figures a and b are porosity scans (porosity=black; particles=white) of photomicrographs, short side equals 1mm. **a)** Ooid-grainstone at time of deposition (Cat Cay, Bahamas) with interparticle porosity, representing starting conditions of the path; por.=45%, Vp=1779 m/s. **b)** Sample Unda 65 m (photomicrograph shown in Figure 20 a, por.=37%, Vp=4105 m/s, Vs=1640 m/s. Former ooid(?)-grainstone with coarse moldic porosity. After alterations in marine waters and intense blocky cementation, all grains were dissolved leaving molds behind (black). **c)** Reconstructed velocity-porosity path for a non-skeletal grainstone from deposition (a) to the observed diagenetic stage (b). The transformation of pore types, together with the dissolution of grains, which happened mainly after cementation, led to a fabric inversion. This succession of diagenetic processes resulted in a characteristic loop of the path. The moldic framework (b) provides high elastic rigidity and thus high velocity at high porosity.

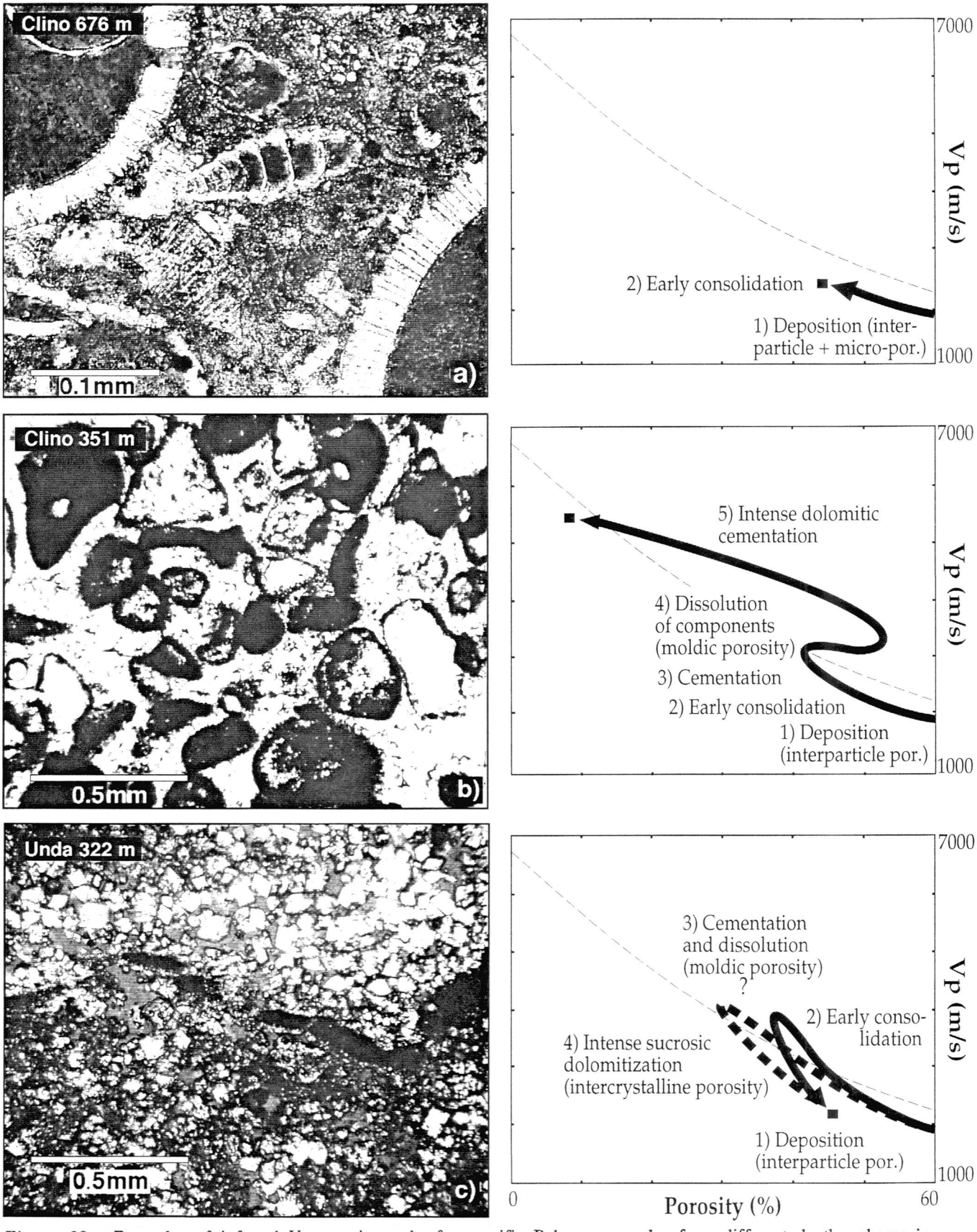

Figure 29: Examples of inferred Vp-porosity paths for specific Bahamas samples from different depths, shown in photomicrographs (left). The black square in the Vp-porosity diagram (right) marks the measured values. The path is constructed by observing the different diagenetic stages of the sample and by relating them to Vp-porosity values. **a:** Clino 676 m, por.=44%, Vp=2478 m/s, Vs=1356 m/s. Periplatform slope sediment with globigerinids. Despite the burial depth (deepest sample of both cores), only little compaction and matrix recrystallization can be observed. The Vp-porosity path is thus a short, straight line from conditions at deposition to present times. **b:** Clino 351 m, por.=9%, Vp=5661 m/s, Vs=3158 m/s. Densely cemented grainstone. Similar evolution as in sample of Figure 28, but an additional cementation after dissolution filled the earlier created moldic pore space, resulting in reduced porosity and increased velocity. **c:** Unda 322 m, por.=46%, Vp=2405 m/s, Vs=991 m/s. Sucrosic dolomite with few relics of redalgaes. The sedimentary fabric has been completely destroyed by sucrosic dolomitization that created a dominant intercrystalline porosity.

An example for such a velocity-porosity path is the fabric inversion of a grainstone to a coarse moldic rock. A clean unconsolidated ooid sand from Cat Cay (Bahamas), which has a depositional, mainly interparticle porosity of 40-50 % (Enos and Sawatsky, 1981) was measured in its unconsolidated and unaltered state (Figure 28 a). The resulting Vp equals 1779 m/s at 8 MPa effective pressure. This rock type can be considered as the potential precursor of a sample encountered in the Bahamas cores (sample Unda 65 m), which is characterized by interparticle cement and moldic porosity (Figures 20 a, b, 28 b). The fact that only the former interparticle pore space is cemented, so that the molds are still open and not filled with cement, indicates that the interparticle pore space became cemented mainly before the dissolution of the ooids or peloids. As a consequence, the rock has a completely inverted fabric compared to the original ooid sand. It has a porosity of 37 % (mainly moldic) and a Vp of 4105 m/s. During fabric inversion, the rock must have gone through a stage with much lower porosity. This stage marks a turning point in the loop in the velocity-porosity path (Figure 28 c) documenting the interference of two processes with different effects on porosity and sonic velocity. This evolution demonstrates how diagenetic processes can invert the fabric and change the elastic properties of the rocks, even without changing total porosity. The velocity-porosity path is useful for describing such an evolution, which would not be recognized by laboratory measurements alone. Other examples of such inferred velocity-porosity paths are shown in Figures 29 a-c and are described in the following paragraphs.

Figure 29 a describes a path that is the result of early compaction, which is usually one of the first processes to affect a sediment. Early compaction results in initial consolidation, dewatering and grain rearrangement, but no diagenetic reaction, cracking or breaking of the components. Initial values of approximately 50-60% porosity and 1600 m/s for Vp change during this first consolidation stage to values close to 40-50% and 2000 m/s respectively. At this early stage, the sediments are characterized by an interparticle porosity (grainstones) or a high micro-porosity (mud to packstones). Sample Clino 676 m (Figure 29 a) is an example of a carbonate sediment that hardly shows any other diagenetic alteration than a little compaction. Interestingly, it is the deepest sample from both drillholes in the Bahamas and its velocity-porosity path is a simple short, straight line. The great burial depth of this sample and the absence of any major alteration document again the insignificant effect of burial depth alone on the velocity of carbonates. In this case, the fine grained, low-aragonite lithology inhibited the initiation of diagenetic reactions that would have indurated the rock and increased the elastic properties.

Some samples undergo after an early dissolution stage, a subsequent intense cementation of the newly created moldic pore space (Figure 29 b, sample Clino 351 m).

The relics of the stage with a dominant moldic porosity can be recognized by the abundance of former molds that are filled with a blocky spar and surrounded by a micritic rim that mimics the former grain shape. The beginning of the velocity-porosity path towards the moldic stage might be the same as in the example described in Figure 28 and describes a clockwise loop. In addition the last stage of cementation reduces porosity, increases velocity and creates a much denser rock fabric. The resulting velocity-porosity path is a z-shaped curved line. If the rock had not undergone a stage of dominant moldic porosity, the final high velocity and low-porosity values would have been reached along a relatively straight line path.

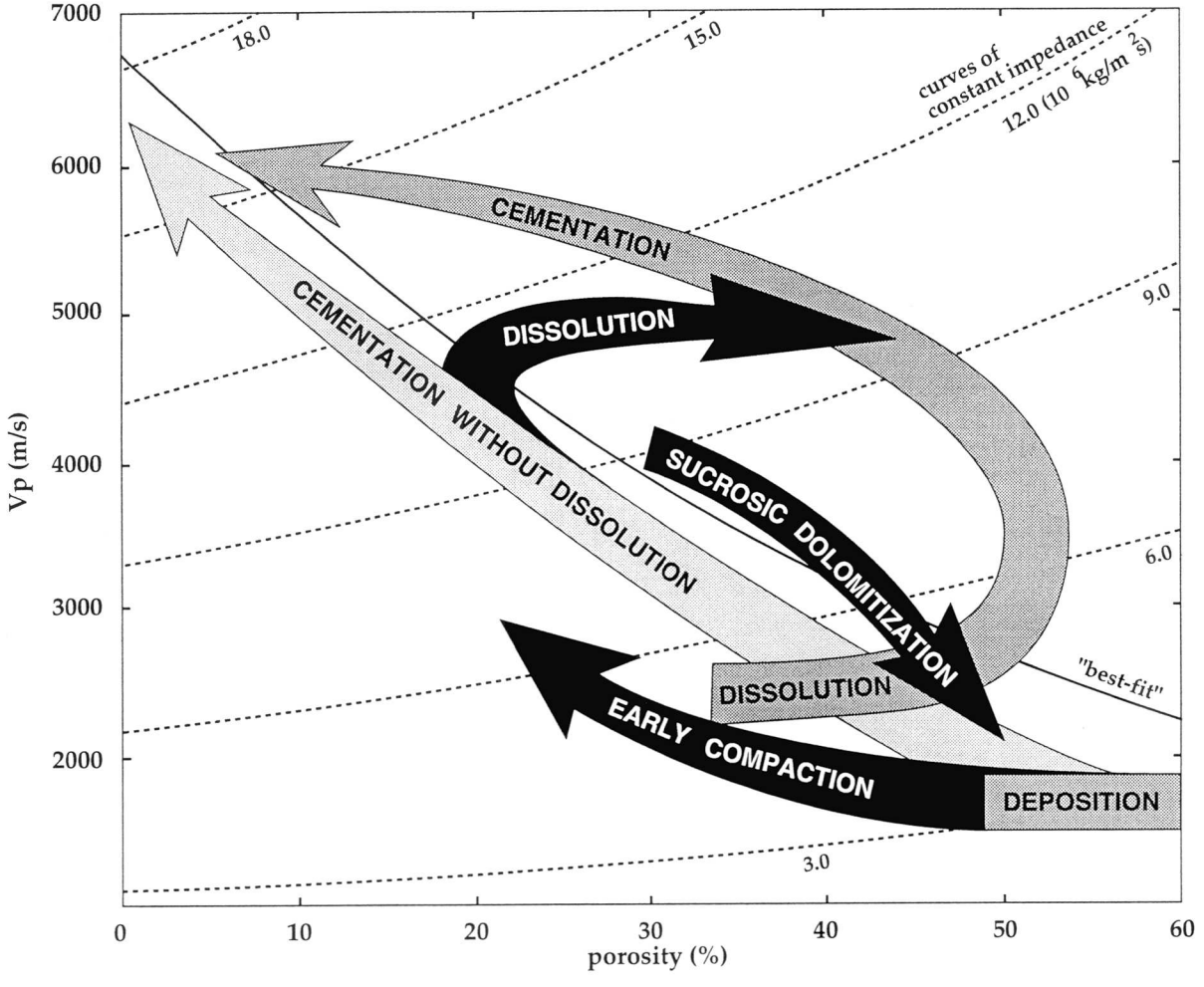

Figure 30: Velocity-porosity paths of different diagenetic processes in carbonate sediments. The same process may have different positions in the diagram, depending on the timing of the diagenetic events, but the trend (= direction of arrow) should be the same for a given process. Dolomitization can have opposite effects: fabric-destructive dolomitization decreases velocity, whereas fabric-preserving dolomitic cementation increases velocity. Dissolution can follow lines of equal impedance and has, therefore, only little influence on acoustic impedance, though it increases porosity significantly. The solid line is the exponential best-fit line through all data points measured in this thesis; dashed curves are lines of equal impedance (calculated with the density of calcite).

In contrast to the constructive process of cementation, fabric destructive processes, for example sucrosic dolomitization, can decrease velocity and increase porosity of an already altered sediment. Figure 29 c shows the characteristic evolution of such a destructive diagenetic process as seen in sample Unda 322 m. Except for few relics of red algae, no original components or textures can be recognized in the thin section of this sample. Therefore, it is difficult to reconstruct the beginning and the intermediate stages of the velocity-porosity path, but it is likely that some marine or freshwater environment led to cementation and dissolution before sucrosic dolomitization started. As a result, the path might have a loop shape which, due to the destructive nature of this dolomitization process, points downward towards lower velocities and higher porosities.

All described velocity-porosity paths can be summarized in a graph (Figure 30) that displays the effects of the various diagenetic processes. Each process has its characteristic direction in the velocity-porosity diagram (= direction of arrow), but the absolute position within the diagram is dependent on the succession and timing of the different processes. The path for all sediments starts at deposition. The subsequent evolution is mainly dependent on the depositional lithology (diagenetic potential) and the succession of diagenetic processes. It is remarkable that dissolution only has a minor effect on impedance, because dissolution follows, to a certain extent, the lines of equal impedance. This leads to preservation of elastic properties during selective dissolution, during which the rock maintains a framework with relatively high elastic stiffness.

Apart from purely calcitic pelagic oozes (Schlanger and Douglas, 1974), most carbonate sediments are characterized by a high diagenetic potential and all the described diagenetic processes happen much faster than compaction. Consequently, carbonates are quickly dissolved, cemented and recrystallized. In siliciclastic or shaly sediments, the diagenetic potential is much lower than in carbonates, and increasing burial pressure leads to an increase in velocity at greater depth (Hamilton, 1980; Japsen, 1993). In carbonates, the diagenetic processes control and alter the velocity before compaction can play a significant role. The dominance of lithification by chemical diagenesis over lithification by compaction is the reason why the velocities of carbonates show no clear correlation with increasing depth. Before burial pressure compacts the rock fabric, the sediment is already altered and the cemented fabric as well as part of the porosity can survive the increasing overburden to considerable depth.

PART B:

VELOCITY DATA FROM SONIC WIRELINE LOGS

B.1. INTRODUCTION

The results of velocity analyses from laboratory data (Part A) can be compared to other velocity datasets, such as velocities determined from sonic wireline logs of drillholes. The results of this comparison and calibration can be used as a reference to other drillholes that are not cored and where the geophysical wireline logs are the only available source of petrophysical information.

The excellent recovery of over 80% of core from the two holes from the Bahamas Drilling Project allows the direct comparison of rock-lithologies observed in the drilled cores with their geophysical response in the wireline logs. The velocities from the sonic logs can be calibrated and compared with the velocities from laboratory measurements on discrete samples from the cores.

Using the wireline logs from the two cored drillholes on Great Bahama Bank (Figures 2, 3), it is possible to make comparisons between velocity and carbonate lithology down a continuous rock section. First, the differences between the two velocity datasets are determined, so that the results from the laboratory measurements may be applied to the interpretation of the log data. Knowledge of the relation between velocity and porosity is then applied to (1) improve the interpretation of the wireline logs and (2) to calculate synthetic seismograms of the two holes. The drill sites are positioned directly on the Western seismic line, a seismic reflection line that was shot across Great Bahama Bank, so that the two synthetic seismograms may be compared with the observed seismic reflection data.

B.2. LABORATORY VELOCITIES VERSUS VELOCITIES FROM SONIC LOGS

Velocity Dispersion

The velocities in the laboratory study were measured with a broadband ultrasonic pulse with frequencies between 600 kHz and 1.2 MHz. Due to dispersion (frequency dependence of velocity), the measured velocities are likely to be higher than the seismic or log velocities in the same rocks. Seismic frequencies (20-200 Hz) are significantly lower than frequencies used for sonic logs (1 kHz-100 kHz) or laboratory studies (600 kHz - 1.2 MHz).

It is difficult to measure acoustic velocities on the same rocks using different frequencies, because the associated different wavelengths require different sample sizes. In addition, theoretical approaches for estimations of dispersion in fluid-saturated porous media are very complex and velocity dispersion is not yet fully understood (Wang and Nur, 1990). Nevertheless, some studies have shown that dispersion in water-saturated rocks is usually below 3-5% and is a function of several parameters, such as the elastic moduli of the pore fluid and rock frame, as well as the density, temperature, pressure, saturation, porosity, pore-size and pore shape (Goetz et al., 1979; Wang and Nur, 1990). It is difficult to estimate by how much the experimental laboratory velocities have to be reduced in order to match the lower seismic frequencies. Nevertheless, the estimated dispersion <3-5% is relatively low compared to the large range of measured velocities in the investigated samples. The effects on velocity by dispersion can thus be neglected in this dataset. This conclusion is supported by the close agreement between the lab- and log velocities in homogeneous parts of the cores (Figure 31). Even if dispersion significantly affected the absolute velocity values, the velocity contrasts, which are crucial for seismic interpretations and modeling, would be mostly preserved.

Observed Differences in Log- and Laboratory-Velocities

In the holes of the Bahamas Drilling Project, a sonic log was run after drilling operations were completed. In two intervals of hole Clino, from 0-650 ft/0-198 m and from 1050-1150 ft/320-350 m, logging data are missing because parts of the casing

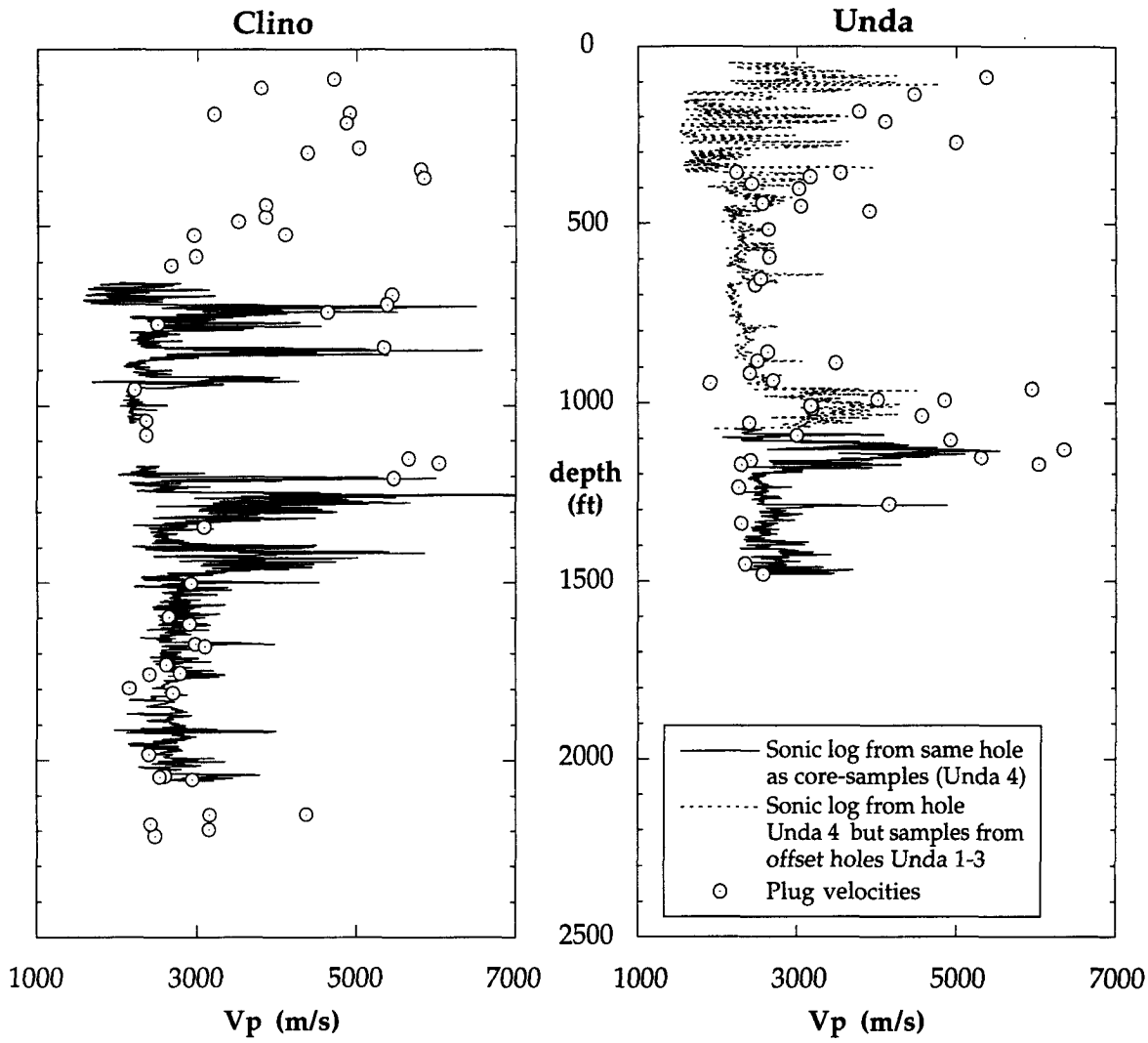

Figure 31: Comparison between ultrasonic lab-velocities (circles) and velocities obtained by the sonic wireline log in the two drillholes on Great Bahama Bank. Dashed logs indicate an offset between holes for coring (Unda 1-4) and the hole used for logging operations (Unda 4). Due to the better resolution of the ultrasonic measurements (length of sample = 2-5 cm, compared to the 20 cm log spacing), lab-velocities display usually higher maxima and lower minima. Thin beds are not well detected by the wireline tool, but in the more homogeneous parts of the holes, as in lower Clino, the differences between the results of the two techniques are minimal. This coincidence shows that the two methods produce similar velocity values. The continuous recording of the sonic log can complete the lab-velocities dataset, so that downhole changes in velocity can be related better to changes in lithology.

remained in the hole (Figure 31). At Unda, the cores above 1050 ft/320 m were taken from the Unda holes 1-3, 25 m away from the Unda hole 4, which was used for logging operations. This offset does not allow a direct comparison between log and lab-velocities in Unda above 1050 ft/320 m, because the individual layers show a significant lateral variation. However, general trends do not change over 25 m and the overall velocity pattern remains approximately the same (Figure 31).

In general, the new data agrees well with the findings of Rafavich et al. (1984), who showed that velocities from laboratory measurements and wireline logs are comparable. In homogenous parts of the core with low variability of sonic velocity, (e.g., Clino: 1500-2000 ft/457-609 m and Unda: 500-960 ft/152-292 m), there is a very good correlation between laboratory-determined velocity and sonic log velocity. This good fit between the two velocities shows that dispersion, due to the different frequencies of the acoustic signal, is not significant.

In zones with a high variability of velocity, the laboratory data has higher and lower velocities than the respective sonic log velocities. These differences between log and laboratory velocities are interpreted to be caused primarily by the different resolutions of the two methods: the lab-velocities have a resolution of 2-5 cm (sample size), whereas the sonic log has a source-receiver spacing of 20 cm. Thin beds are not detected with the wireline tool, explaining the differences between the higher maxima and the lower minima in laboratory velocities relative to the log values.

Another cause of differences between the velocities are fractures that are larger scale than the measured minicores. Large fractures might lower the velocity of the whole rock formation, especially at shallow depths (Guadagno and Nunziata, 1993). Due to the sampling procedure, most minicores are sampled in unfractured parts of the cores and thus represent the more ideal rock conditions.

In addition to these factors, differences in the velocities are caused in part by the karstic and cavernous nature of the upper parts of both drillholes and by the uncertainty in the depths of the sampled plugs due to the incomplete recovery. It can be assumed that the measured contrasts in ultrasonic velocities for the different lithologies do not change their signatures at the lower log frequencies or seismic frequencies. Only the absolute velocity values of the discrete samples have to be shifted slightly towards slower values.

B.3. THE VELOCITY DEVIATION LOG: A COMBINATION OF POROSITY LOG AND SONIC LOG

In addition to the sonic log, a full set of wireline logs were taken in both holes on Great Bahama Bank. Warzeski and Ginsburg (1994) have discussed in detail the lithologic calibration and interpretation of the different logs (caliper, gamma, velocity, neutron, density, neutron-porosity).

The laboratory analyses of discrete samples showed that different velocities at the same porosities can be related to particular diagenetic fabrics and pore types in the

carbonates. A direct application of this knowledge is to evaluate the pore type-velocity relationship of the logs, in order to detect the effect of diagenetic overprint continuously downhole. By combining the sonic log with the porosity log, special zones in the cores can be mapped, where velocities deviate from standard values expected from the measured porosities. Applying the results of laboratory analyses to wireline log data can provide a first assessment of the pore type distribution downhole.

Method

The velocity deviation log involves the conversion of the neutron porosity log to "standard" velocities and a comparison of these velocities with those determined from the sonic log. Because in fully saturated pure carbonates, porosity is related directly to density, a similar procedure could have also been performed based on a combination of the density and sonic logs.

The general trend of velocity versus porosity in carbonates can be described by following equation, which is the best-fit exponential formula based on an analyses of the 272 miniplugs of carbonates from the Bahamas cores and the Maiella outcrops (Figure 16):

$$Vp\ (m/s) = 6393 \bullet e^{-0.0180 \bullet porosity\ (\%)}$$

This equation converts the porosity values that are obtained from the neutron-porosity log (Figures 32 b, f) to a standardized velocity log (Figures 32 c, g). Due to the small expected frequency dispersion (see discussion above), the exponential equation was not corrected for lower log frequencies. This new velocity log displays velocities that would be expected from the measured log porosities.

This standardized velocity log can be compared with the sonic log (Figures 32 a, e), and the difference between the two logs defines the deviation of the measured velocity from the value expected from the porosity.

velocity deviation = (sonic log velocity) - (standardized velocity from porosity log)

This deviation can be plotted versus depth as a log (Figures 32 d, h). To better visualize the trend of the velocity deviations in the different zones of the cores, the area between the positive or negative departures and the zero-deviation line is blackened.

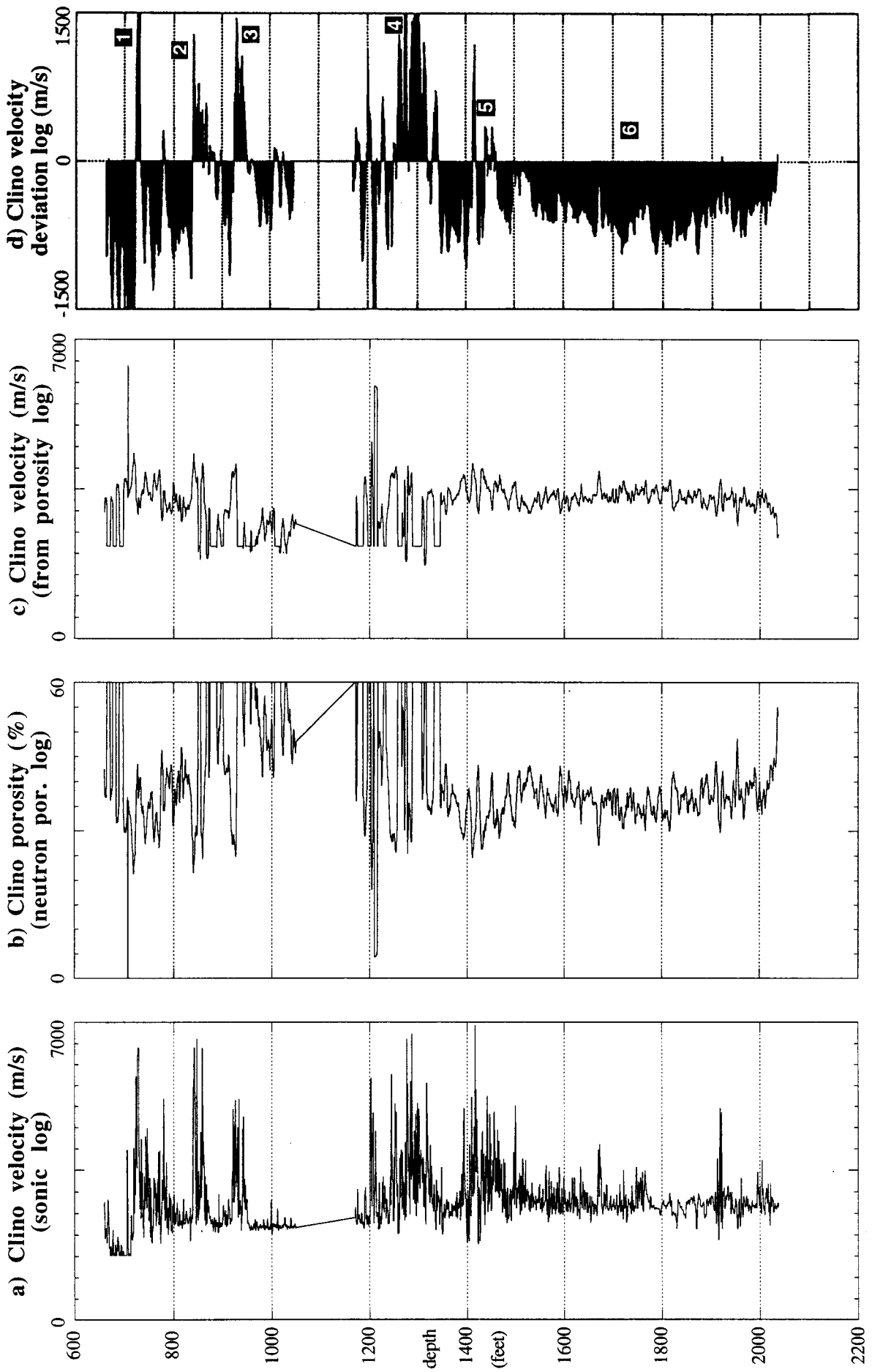
d) Clino velocity deviation log (m/s)
1500
0
-1500
1
2
3
4
5
6
c) Clino velocity (m/s) (from porosity log)
7000
0
b) Clino porosity (%) (neutron por. log)
60
0
a) Clino velocity (m/s) (sonic log)
7000
0
600
800
1000
1200
depth
1400
(feet)
1600
1800
2000
2200

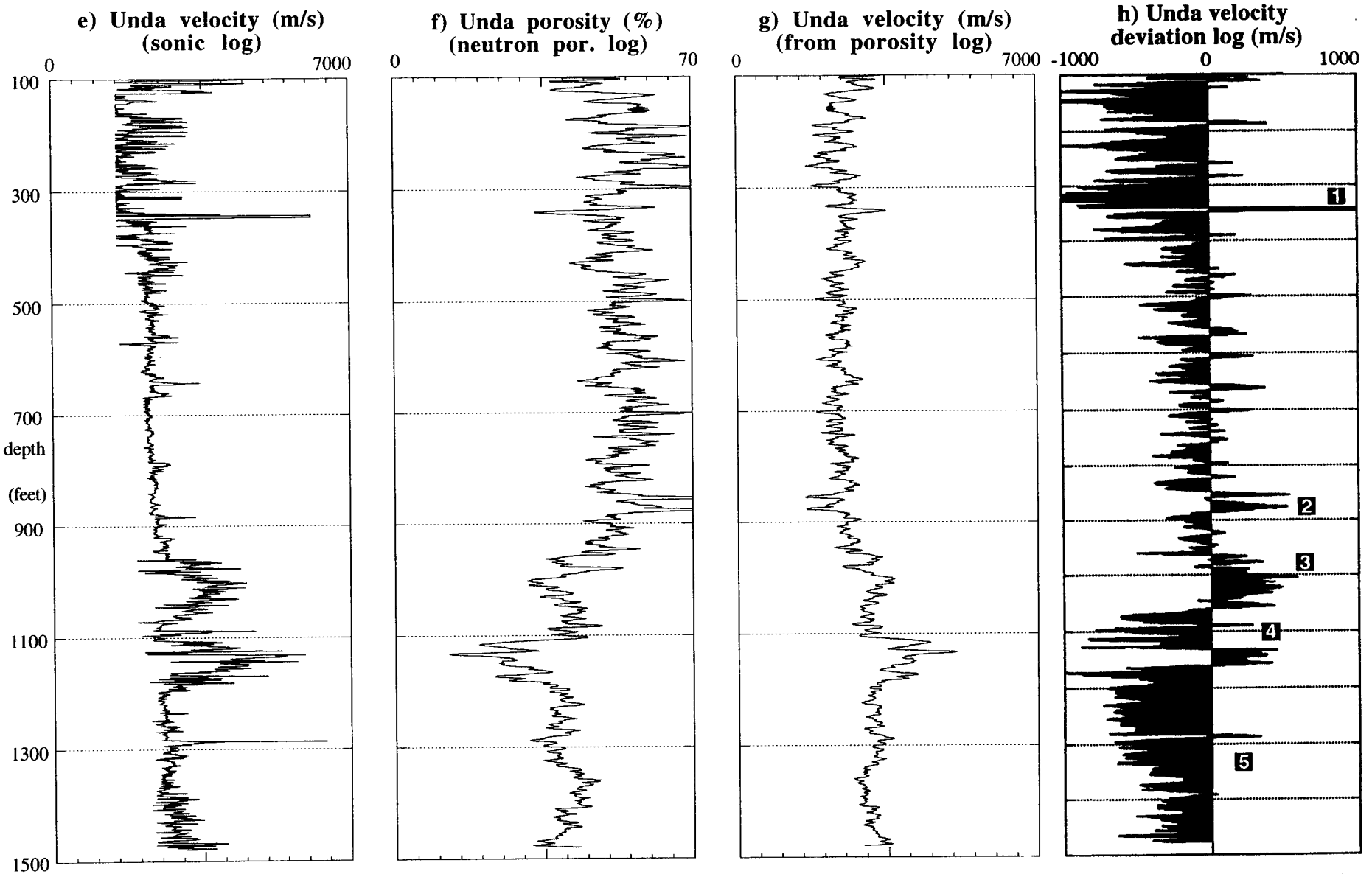

Figure 32: Log data of holes Unda and Clino on Great Bahama Bank. In two intervals of Clino, from 0-650 ft, and from 1050-1150 ft, logging data are missing because casing remained in the hole. **a+e:** Sonic log with a source-receiver spacing of 40 cm. **b+f:** Neutron-porosity log. The upper part in Clino is disturbed by the irregular borehole wall, resulting in cycle skips and artificially high porosities. Porosities values were clipped above 60 %. **c+g:** Calculated velocity log, based on conversion of the neutron-porosity log to velocity. Conversion equation is best-fit relation of 272 laboratory measurements. The velocities represent "standard" values that would be expected from measured porosities. **d+h:** The velocity deviation log is calculated by subtracting the velocity log converted from porosity (Figures c, g) from the sonic log (Figures a, e). Deviations indicate where velocities are too high or too low compared with porosity-estimates (numbers referred in text). Positive deviations are caused by intra-frame porosity (moldic or intraparticle porosity). Negative deviations are the result of high interparticle or micro-porosity. The log can thus be used to trace diagenetic zones with characteristic elastic properties.

Interpretation of Velocity Deviation Logs

Figures 32 d, h display the calculated velocity deviations for the holes Unda and Clino respectively. The final curve was smoothed over ten data points (equals 5 ft/1.5 m) so as to eliminate small scale errors and cycle-skips. Although the velocity deviation log mimics in some zones the shape of the sonic log (Figures 32 a, e), it does not show the trend of velocity so much as the existence of special fabrics that are created by specific diagenetic processes. Positive deviations from the zero-line indicate zones where velocity is higher than expected from the porosity value. Negative deviations indicate zones in which velocity is lower than expected from the porosity value. The plug analyses (Part A) show that velocities are higher than expected in rocks that have a porosity embedded in a stiff frame, such as in rocks with moldic or intraparticle porosity. Lower velocities than expected were measured in samples with dominant interparticle porosity or high micro-porosity. Consequently, the velocity deviation is a function of the elastic properties of the rock fabric, which is related to diagenesis. The calculated log can be used to trace pore types or their related diagenetic processes downhole. Although the neutron-porosity log of the two drillholes that was used is not of high quality (Figure 32 b, Warzeski and Ginsburg, 1994), the resulting velocity deviation log reflects the velocity-porosity relation in carbonates (Figures 32 d, h).

In hole Clino, the velocity deviation log displays clearly the peaks of the well-cemented firmgrounds at 720, 840, and 920 ft (219, 256, and 280 m), which are marked with "1" to "3" in Figure 32 d (Kenter and Ginsburg, 1994; Melim et al., 1994; Warzeski and Ginsburg, 1994). Below 1500 ft/457 m in Clino, the deviation log is characterized by uniformly negative velocity deviations ("6" in Figure 32 d). This deviation pattern agrees well with the encountered lithology in the lower part of Clino, which is dominated by hemipelagic carbonates that lack extensive diagenesis or cementation and have high interparticle and micro-porosity. Two zones of positive excursions with similar shape on the sonic log in the middle part of Clino (Figure 32 a, 1200-1300 ft/366-396 m and 1400-1500 ft/427-457 m) produce two different images on the deviation log ("4" and "5" in Figure 32 d). The upper zone produces strong positive deviations, whereas the lower one gives only low positive values. This difference can be explained by a relatively higher amount of intra-frame porosity, such as moldic or intraparticle porosity, in the upper section, whereas the lower zone shows less of these features.

The uppermost parts of the velocity deviation log of hole Unda shows some peaks with high positive departures that are indicative of abundant intra-frame porosity (e.g. at 340 ft/104 m, marked with "1" in Figure 32 h). These zones of the cores are

characterized by intense freshwater cementation, a suite of exposure horizons, and high moldic porosity (Kievman and Ginsburg, 1994). At a depth of 960 ft/293 m, which is the upper boundary of the lower reef, the deviation log is characterized by a strong positive departure ("3" in Figure 32 h). In this zone, fabric-preserving dolomitization creates a cemented frame (Melim et al., 1994). At places, this frame is replaced by microsucrosic dolomite, which results in negative departures on the velocity deviation log ("4" in Figure 32 h). Hardgrounds within fabric-destructive microsucrosic dolomites, (e.g. at 880 ft/268 m, "2" in Figure 32 h), result in positive deviations, reflecting constructive diagenetic processes. The lower parts of Unda show strong negative deviations ("5" in Figure 32 h) that are caused by the abundance of interparticle and micro-porosity, similar to the lower part of Clino.

The velocity deviation log demonstrates how physical property data, obtained by laboratory measurements on discrete minicores, can be used to improve interpretations of wireline logs. The velocity deviation tool is especially useful when geophysical logs have to provide the main lithological information, as is the case in drillholes that are not cored continuously and for which cuttings are the only direct source of lithologic information.

B.4. SYNTHETIC SEISMOGRAMS OF THE DRILLHOLES ON GREAT BAHAMA BANK

Correlation of seismic reflections to the cores can be achieved by two means: (1) by a vertical seismic profile (VSP) and (2) by the calculation of synthetic seismograms. In this study, the VSP is used for a correct depth-to-time conversion of the wireline log data, so that the synthetic seismograms can be calibrated to match the seismic line. The data from sonic and density logs can be used to calculate one-dimensional synthetic seismograms that allow observed seismic reflection information to be compared with the observed lithologies in the logged section of the cores.

Method

The calibration of well log data to travel times is achieved by using first-arrival times from a vertical seismic profile survey. VSP surveying is a technique that includes the recording in the borehole of waves generated by an airgun detonated above the sea floor at the drill site. A series of geophones is lowered into the hole and registers the

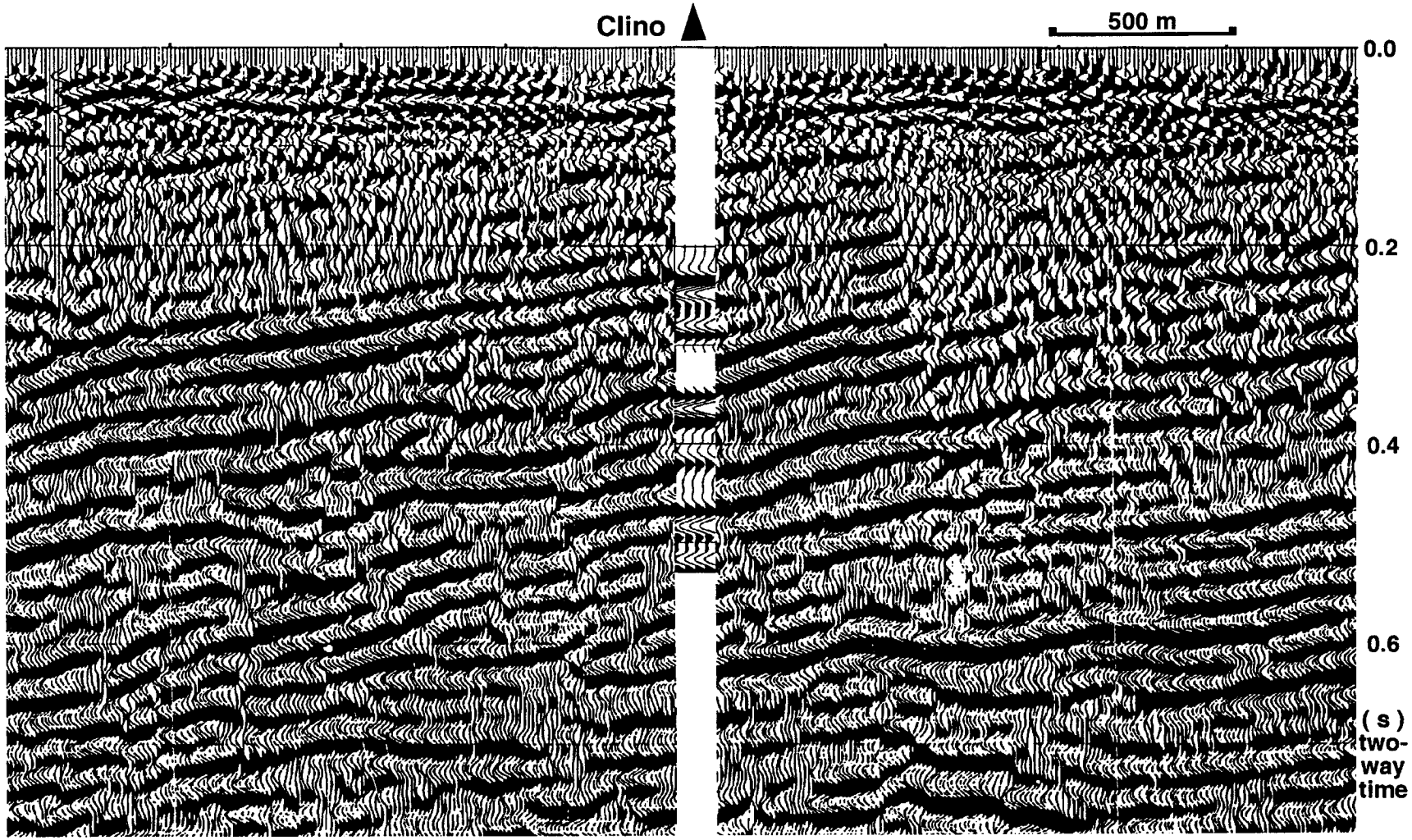

Figure 33 a: Synthetic seismogram of drillhole Clino, spliced into the Western seismic line at the appropriate drillsite. The missing parts of the seismogram at 0-0.2 s and 0.3-0.35 s two-way time are caused by casing, which remained in the hole and inhibited complete logging operations. The seismogram was calibrated by check shots originating from first-arrival data of the vertical seismic profile (VSP). The synthetic seismogram is calculated with a zero-phase Ricker wavelet of 30 Hz, negative polarity and with multiple reflections. An automatic gain control with a 100 ms window was applied. The match between the synthetic seismogram and observed seismic data is good: in the modeled section, every reflection has its equivalent on the seismic section at the correct two-way times.

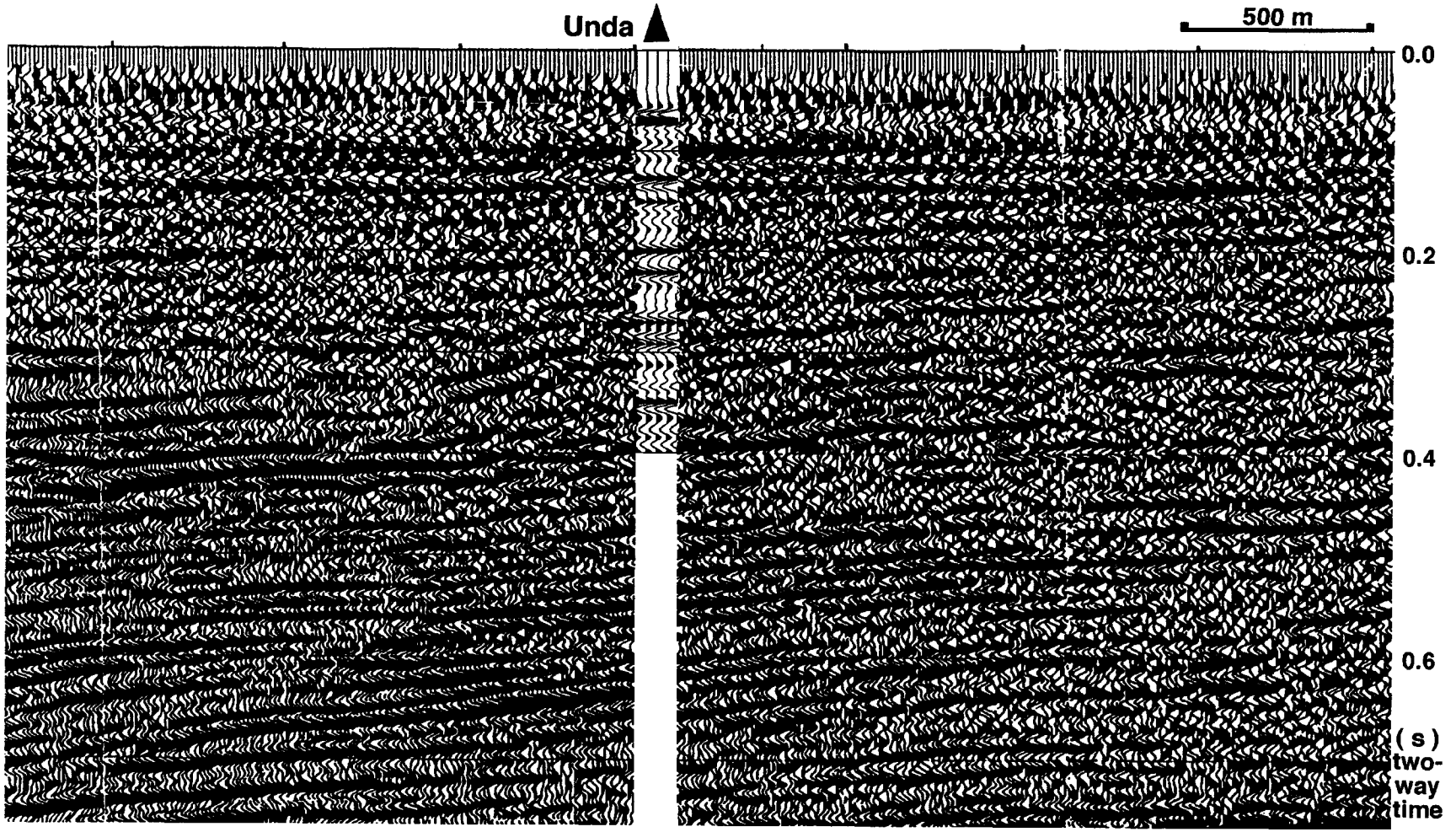

Figure 33 b: *Synthetic seismogram of drillhole Unda, spliced into the Western seismic line at the appropriate drillsite.* The synthetic seismogram is calibrated by check shots originating from first-arrival data of the vertical seismic profile (VSP) data. The synthetic seismogram is calculated with a zero-phase Ricker wavelet of 50 Hz, negative polarity and with multiple reflections. The frequency of 50 Hz is higher than that used for Clino (30 Hz, Figure 33 a), because the part of the Western seismic line containing the drill site of Unda was reprocessed and shows higher frequencies. An automatic gain control with a 100 ms window was applied. Especially in the shallow part, the match between the synthetic section and the observed seismic data is only moderate; most shallow reflections on the seismic line are not properly simulated, whereas the deeper reflections below 0.25 s show a better coincidence (e.g. top of the lower reef unit at 0.29 s).

waves of the downgoing and upcoming acoustic signal at varying depths. The first-arrival times converted to two-way travel times by performing several corrections (water depth, offset of source, etc.) allow for reliable time-to-depth or depth-to-time conversions.

The Landmark ITA™ software package (*LOGEDIT* program) is used to calculate synthetic seismograms for both drillholes from the wireline logs. The values from sonic log and density log are multiplied to calculate an acoustic impedance log. The used sonic log had a spacing between source and receiver of 40 cm. The program converts the downhole impedance data to a series of reflection events with positive or negative reflection coefficients. These downhole successions of reflection events are convolved with wavelets of different dominant frequencies and positive and negative polarity. Before convolving the well-log data with the wavelet, several check shots from the VSP survey with correct depth-time values are entered into the ITA™ program. This places the reflections at correct travel times so that the synthetic seismograms can be compared with the observed seismic line. The calculation of the seismogram includes multiple reflections.

Comparison of Synthetic Seismograms with Seismic Section

Figures 33 a, b show the calculated synthetic seismograms for the two boreholes superimposed on the Western seismic line across Great Bahama Bank. Five identical traces of the synthetic seismograms are spliced into the seismic section at the drilling locations, thus allowing a direct comparison with the observed seismic reflection data. Both, the Western seismic line and the synthetic seismograms are plotted with negative polarity. The part of the seismic section that crosses near the drillhole Clino has a dominant frequency of approximately 30 Hz. Drillhole Unda lies in a part of the section that was reprocessed, resulting in a higher frequency of approximately 50 Hz. Therefore, the two displayed synthetic seismograms are calculated with frequencies of 30 and 50 Hz respectively. The best fit between the Western seismic line and the synthetic seismograms was reached when an automatic gain control (AGC) with a window length of 100 ms was applied.

Due to partly casing of the hole, the synthetic seismogram of Clino covers only part of the drilled sections. Nevertheless, the match between the synthetic and the observed data is good (Figure 33 a). Except for one weak low-amplitude reflection at 0.4 s, every observed reflection in the seismic section has its equivalent on the synthetic trace. The comparison of the synthetic and the observed seismic data with the sonic log

(Figures 32 a, e) reveals the influence of lateral continuity and AGC on the amplitude of seismic reflections. High amplitude reflections are seen on the seismic data between 0.4 and 0.5 s (Figure 33 a). These high amplitude reflections originate from rocks that have very low acoustic impedance contrasts. This facts suggests that the lateral continuity of impedance variation may be more important for the recognition of a reflection than the absolute impedance contrast, because the amplitude of a coherent reflection can be increased easily with an automatic gain control function. This amplitude gain over-accentuates the significance of these weak reflections, which are likely to be interpreted as a product of major changes in acoustic impedance and lithology if "true" amplitude data are not available. In reality, the weak reflections are the result of minor changes in lithology that are widespread, resulting in continuous reflections.

The match between the synthetic and the observed seismic data in hole Unda is not as good as that for the hole Clino (Figure 33 b). Not all reflections are imaged by the synthetic trace, and some synthetic reflection events do not have equivalents on the Western seismic line. The top of the reef, the most prominent impedance contrast in Unda, is imaged clearly at 0.29 s, although it is not the most prominent reflection.

The lack of agreement in the upper part of Unda might be explained by (1), most likely, the moderate quality of the sonic and density logs, which results in a synthetic trace that does not mimic the real seismic section, (2) by errors in the VSP data, which would result in a wrong depth-to-time conversion, or (3) by a moderate quality of the seismic data resulting in artifacts in the seismic reflection pattern.

Correlation Between Depositional, Diagenetic and Seismic Sequences

It was demonstrated in Part A that sonic velocity measured in the carbonate minicores is the combined product of depositional lithology and diagenetic alterations. The quasi-continuous velocity records provided by the sonic logs from the two drillholes on Great Bahama Bank confirm and complete the trend of velocity values that was recognized in the analyses of the discrete samples (Figure 31). Extrapolating the knowledge of the control of velocity from the laboratory to the whole rock section, it can be assumed that the downhole distribution of velocity in the cores of the Bahamas drillholes is as well controlled by the distribution of depositional lithologies and by the suite of diagenetic events.

Based on variations of depositional lithologies in the cores, several depositional successions could be recognized (Kenter et al., 1994, Figure 34). The boundaries of these successions are marked by variations in depositional style, grain composition and

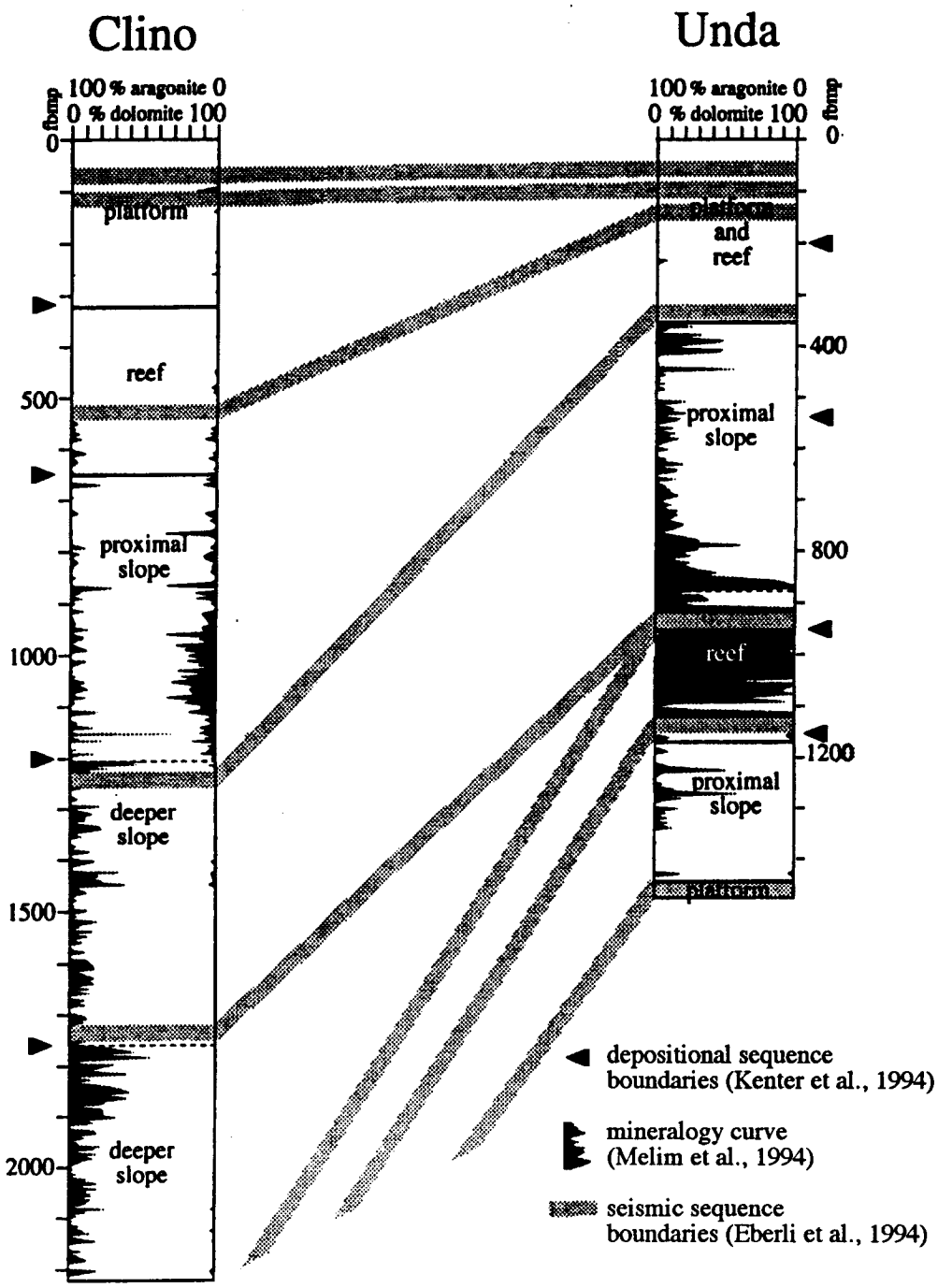

Figure 34: Correlation between the seismic sequences with depositional sequences and mineralogical content in the two drillholes on Great Bahama Bank. Many seismic sequence boundaries coincide with depositional sequence boundaries and with a change in mineralogy. In the slope section of Clino two diagenetic horizons separate packages of similar mineralogical assemblages. These diagenetic horizons are correlated with seismic sequence boundaries (modified from Eberli et al., 1994).

accumulation rates. These variations are interpreted to be caused by fluctuations of sea-level (Kenter et al., 1994). The successions of depositional lithology thus represent depositional sequences.

Many of the depositional sequence boundaries mark not only boundaries between sediment types, but are also boundaries between diagenetic zones that can be recognized on the downhole mineralogy curve (Melim et al., 1994, Figure 34). It can be seen that most depositional sequences have characteristic patterns in mineralogy, which documents that the effects of diagenetic alterations are also tied to the depositional lithology. This correlation between depositional lithology and diagenetic signature implies that sea-level fluctuations do not only control sedimentary processes, but also control the diagenetic regime and thus the successions of diagenetic alterations.

The observed coherence of the two velocity-controlling factors, depositional lithology and diagenetic alterations, explains the good correlation between seismic sequence boundaries, identified as unconformities and correlated conformities on the seismic section (Eberli et al., 1994), with depositional sequences and paragenetic sequences from the cores (Kenter et al., 1994; Melim et al., 1994, Figure 34). In fact, all onlapping packages on the seismic section correlate well (within the limits of seismic resolution) with parts of the cores that were interpreted to be lowstand deposits (Eberli et al., 1994). This match between depositional lithology, diagenesis and seismic response confirms that sequence stratigraphic units can be recognized on seismic profiles and that seismic sequence analyses may be a useful tool for making depositional, stratigraphical or even diagenetic interpretations based on seismic data.

However, the sometimes moderate match between synthetic seismograms and seismic section (e.g. Figure 33 b) suggests that the relation between seismic reflection pattern and lithology is not straightforward. It is dependent on more factors than just the distribution of physical properties. Part C of this study will thus focus on the seismic modeling of carbonates. This modeling will demonstrate how geologic and seismic parameters together influence the seismic image of a rock section with a characteristic impedance distribution.

Leer - Vide - Empty

PART C:

SEISMIC MODELING OF CARBONATES

C.1. INTRODUCTION

The connection between the geologic rock record and its seismic response is not a simple and straightforward relationship. Seismic profiles are physical images of rock sections and do not necessarily image the geological relevant characteristics of the rocks. The links between the geology and the seismic image are the physical properties of the rocks, in particular the acoustic impedance. An understanding of the controlling factors of these properties is essential for interpreting seismic sections. These factors were discussed in Part A of this thesis.

Part C focuses on the influence of the physical properties on the seismic data. To evaluate this complicated relationship, several factors have to be considered; (1) the geologic boundary conditions, (2) the petro-physical characteristics of the rocks, and (3) the technical parameters of a seismic survey. Different seismic methods with different seismic parameters that are applied to the same rock section can result in different seismic images. Therefore, the physical properties of a geologic section alone do not guarantee a certain seismic reflection pattern.

In order to evaluate the imaging capabilities of seismic survey methods, two different approaches can be adopted (Figure 1):

(1) One is the direct method, which compares real seismic data with the rocks and their physical properties. Such a comparison was performed on sediments from the Bahamas, where a multichannel seismic line (Western seismic line) offers the opportunity to observe the seismic image of the prograding carbonate platform margin of the Great Bahama Bank (Eberli et al., 1994). The geologic information is provided by two continuously cored deep drillholes that are located directly on that seismic line. The lithology and physical properties of the drilled cores were analyzed. Results were discussed in Parts A and B.

(2) The second method uses a known geologic section, such as that found in mountain outcrops, as the starting point for a forward model to produce synthetic seismic

sections. Two- and three-dimensional geologic information can be obtained through field work and may be of an extent that cannot be achieved by one-dimensional drillholes located on seismic profiles. In this study, forward modeling was applied to the carbonate platform-to-basin transition outcropping in the Montagna della Maiella in Italy. This approach is described in the following chapters.

C.2. OBJECTIVES OF THE SEISMIC MODELING

The purpose of seismic modeling is to evaluate the seismic response of a geologic setting by computer-simulating a seismic survey. The basic principles and techniques of such seismic modeling and applied case studies are discussed in Neidell and Poggiagliolmi (1977) and Fagin (1991). Galloway et al. (1977) and Meckel and Nath (1977) discuss applications of seismic modeling in the context of seismic stratigraphy. Several examples of modeling describe the relationship between observed outcrop geology and associated synthetic seismic sections (Rudolph et al., 1989; Biddle et al., 1992; Schlager et al., 1991; Campbell and Stafleu, 1992; Stafleu and Schlager, 1993; Stafleu et al, 1994; Stafleu and Sonnenfeld, 1994) or model subsurface data so as to better interpret existing seismic lines (Middleton, 1987; Rudolph and Greenlee, 1991). Synthetic seismic sections are useful in areas that cannot be surveyed by a real seismic campaign. In addition, seismic modeling can improve the interpretation of real seismic lines. For example, three-dimensional (3D) modeling can show the origin and position of out-of-plane reflections so that they can be identified on two-dimensional (2D) seismic sections (Fagin, 1991; Stäuble and Pfiffner, 1991).

The disadvantage of some outcrops in mountain ranges is that they cannot be easily seismically surveyed. However, this disadvantage is outweighed by the advantage that outcrops can offer insight into lithology, heterogeneities and geometry of rocks and depositional sequences that are not available on seismic lines. The quality of this information cannot be obtained from actual seismic profiles or from cored drillholes. Therefore, seismic models provide useful insights into the seismic response of outcropping rock sections that are already studied from a geological point of view, especially if they can be compared to real seismic data in the same area.

In this study, seismic modeling is performed in 2D to simulate the seismic response of the transition from the isolated carbonate platform to the adjacent pure carbonate slope of the Montagna della Maiella (Central Italy). The objectives of this study are:

(1) Evaluation of the seismic facies of escarpment-bounded platforms and their slopes. So far, it is not well known, why many carbonate platforms show an incoherent to chaotic seismic facies. It was speculated that pervasive dolomitization or strong karstic overprints may be responsible for the low seismic reflectivity of platforms. This modeling will show that the low range in impedance, as measured in platform samples, is not sufficiently high to result in high seismic reflectivity. In addition, the steep carbonate platform escarpment is believed to be either a fault- or a growth structure. The characteristics of the seismic image of an escarpment, as seen on the modeled synthetic seismic sections, may help to interpret other seismic sections, where similar escarpments are visible.

(2) Testing the concept of seismic sequence stratigraphy in a carbonate platform-to-basin setting. The concept of sequence stratigraphy, performed on seismic sections, is often used in geologic interpretations of seismic data. This study of modeling addresses the problems that origin in the limited seismic resolution, which may not be sufficient to image correctly the depositional sequences. It will be shown that several misinterpretations can be made by performing sequence stratigraphic analyses solely with seismic data, in particular at low seismic frequencies.

The Montagna della Maiella is characterized by excellent outcrops on a seismic scale, which make the area suitable to approach the mentioned objectives.

C.3. METHODOLOGY AND APPROACH

A synthetic seismic section is calculated by establishing a petrophysical model of the rock section and by converting this model into seismic data by using computer simulations (Figures 35 a-f). The second step is here discussed first, because knowledge of the computer program is essential to construct the impedance model of the rocks. The *Sierra™ system* software, installed on a VAX 8600 computer, is able to simulate a seismic survey for a given model. The software consists of the *MIMIC™* software, which creates the impedance model, and the *QUIK™* software, which performs the raytracing and convolves the reflectivity section with a wavelet (see below). A geometrical impedance model that consists of several layers with characteristic geometries and impedances is the initial input to the program.

The program uses standard laws of reflection seismology to calculate the synthetic sections. A contrast in acoustic impedance is required for the reflection of a seismic

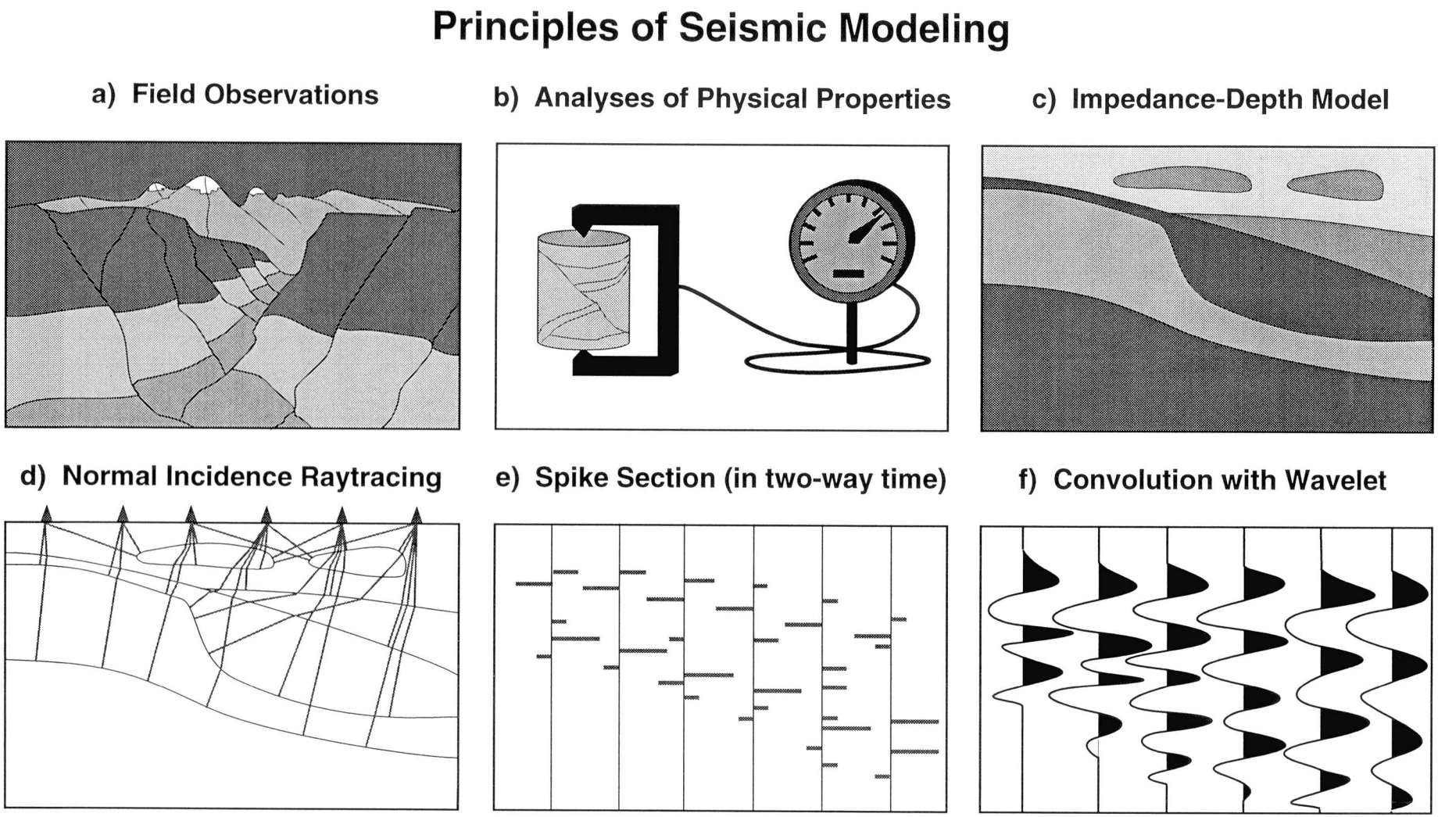

Figure 35: Schematic steps of a study in seismic modeling, combining observations and sampling in the field (step a) with laboratory analyses of physical rock properties (step b) and computer simulations (steps c-f).

signal. At an interface at which impedance changes, part of an arriving acoustic signal is reflected and part is refracted. Both reflected and refracted rays obey Snell's law (see below). The amplitudes of the reflected and the refracted signals are functions of the arriving signal and the contrast in impedance. The following formulae are used to calculate the angle, polarity and amplitude of a reflected and refracted acoustic signal, which passes through a boundary between two layers with contrasts in Vp and/or Vs and density (ρ)(Figure 36):

$$\frac{\sin \alpha_i}{Velocity_i} = constant \ (Snell's \ Law)$$

$$Amplitude_{reflected} = Amplitude_{arriving} * \underbrace{\frac{r_2V_2 - r_1V_1}{r_2V_2 + r_1V_1}}_{Reflection\ coefficient}$$

$$and$$

$$(Amplitude_{transmitted})^2 = 1 - (Amplitude_{reflected})^2$$

Strictly, the formula for the reflection coefficient and amplitudes are only valid for normal incidence waves. The amplitude of a reflected or a refracted ray, which passes through a layer boundary at an angle other than normal, is a little lower, because part of the arriving compressional wave is converted to reflected and refracted shear waves (Figure 36).

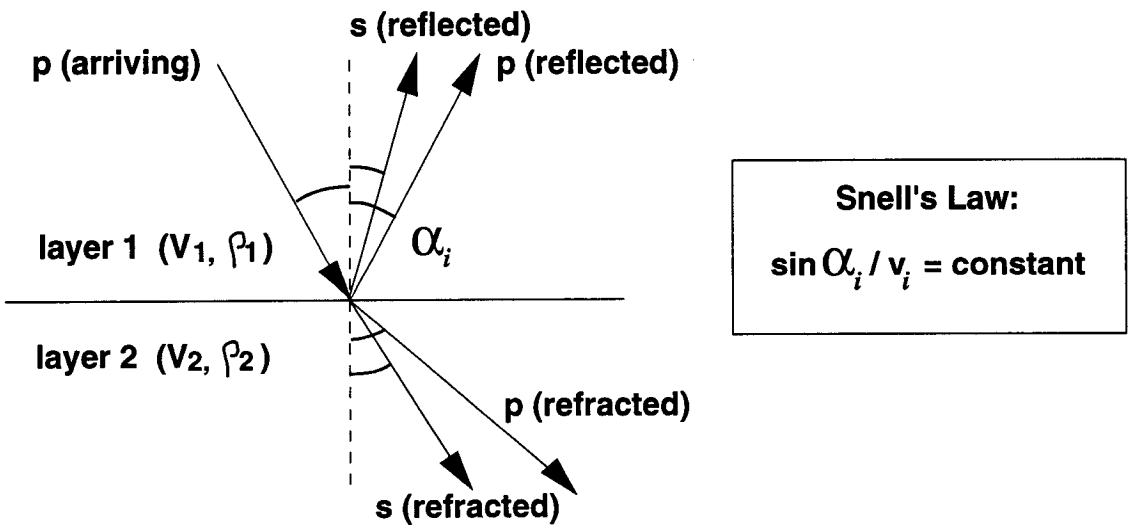

Figure 36: Path of a reflected and refracted seismic ray (formulas in text). Part of an arriving compressional wave will be transformed into a reflected and refracted shear- and compressional wave. If ray path has normal incidence ($\alpha i = 0$), no shear wave will be created.

A program that uses these formulae may also amount for shear waves, but due to the size of the model, which was close to the limits of the software, they were not included in the calculations. For reflection seismic surveys, the compressional wave is more significant, because it travels faster than the shear wave and has more energy to travel back up to the surface, where it is recorded by the geophones.

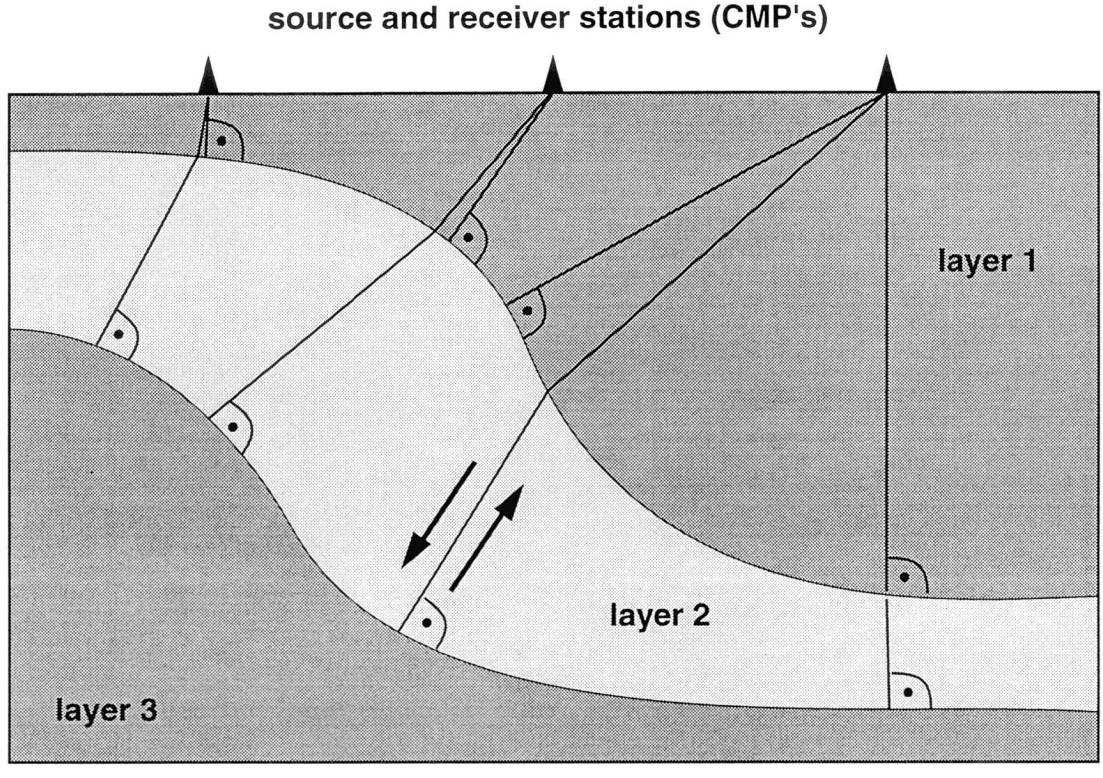

Figure 37: Principles of normal incidence raytracing. For every source and receiver station a search is made for all rays that are reflected at normal angle to the various layers. Downgoing and upcoming rays are therefore identical. Several rays from the same surface may be received at a any station. The resulting synthetic seismic section represents at stacked, but unmigrated, seismic section.

Normal Incidence Raytracing

Synthetic seismic sections were calculated by simulating the refraction and reflection of seismic signals that are initiated at the top surface of the model. The ray paths are constructed through the layers of the model employing the normal incidence raytracing method (Fagin, 1991). This ray tracing method uses only rays that arrive and

are reflected at a 90 degree angle to the reflecting target surface (Figure 37). Downgoing and upcoming rays are thus identical and the resulting seismic data represents a stacked section. This normal incidence raytracing method is effective in simulating traces of a CMP-stacked seismic survey (Yilmaz, 1987). Unlike the often used *vertical* incidence method, which only uses vertical rays, the *normal* incidence raytracing method calculates the true trace of a ray, which is influenced by the two-dimensional geometries of the layers. The signals of all rays that arrive at one station are added to the final seismogram of that station. In some cases, several reflections from the same target horizon are recorded at a same geophone station. This focusing of rays is a characteristic pattern of irregularly dipping surfaces and can be simulated with the normal incidence method (Figure 37).

Virtual geophones record the upcoming signal as reflection events (spikes) as a function of two-way travel time at previously defined common mid-points (CMP's). A reflected signal is detected at the surface of a model if it arrives within a capture radius around the virtual geophone. As default, the modeling software uses a capture radius that equals 15% of the CMP spacing. This value of the radius ensures the separation of rays into adjacent groups and produces reasonably accurate travel times, while preserving execution speed of the simulation. After raytracing, the program creates a spike-section for every CMP (Figure 35 e). For every trace, this spike seismogram includes information on the two-way travel time, reflection-coefficient and polarity of the reflection events.

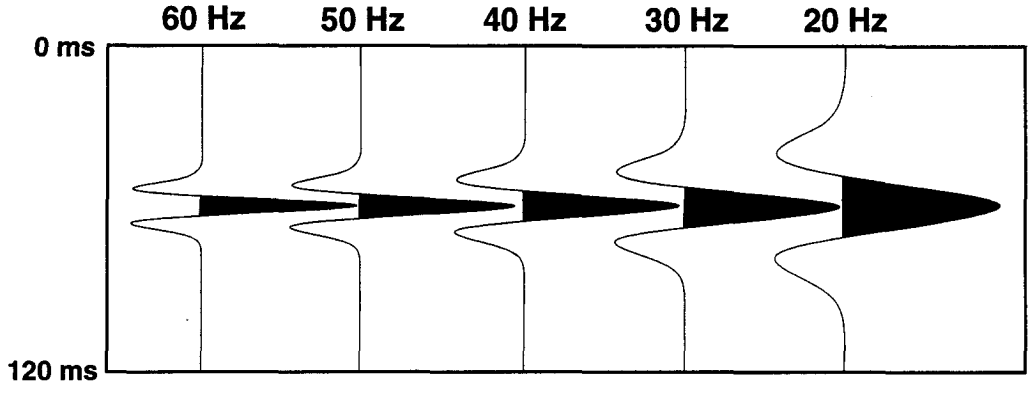

Figure 38: Zero-phase Ricker wavelets of different frequencies that were used in this study. With positive polarities, a boundary with an increase in impedance results in a reflection with a black peak centered on the reflecting surface.

Wavelet Type and Noise

In the next step, the spike seismogram is convolved with a seismic wavelet. To investigate the effects of different frequencies, wavelets with dominant frequencies of 20, 30, 40, 50 and 60 Hz were selected. The lower frequencies of 20 - 30 Hz are common in hydrocarbon exploration, whereas the higher frequencies of up to 60 Hz can in reality, only be reached with high-resolution and high-quality surveys. A zero-phase Ricker wavelet was chosen to allow the highest possible resolution (Schönberger, 1974). This wavelet type has an amplitude peak in the center of the wavetrain (Figure 38). The resulting reflected wavelet from a layer with a contrast in impedance has its main peak centered on the two-way travel time to that layer.

To make the synthetic seismic section and the interpretation more realistic, the seismograms were disturbed by adding background noise at 10 % of the average registered amplitudes. Unlike *structural modeling* studies (Fagin, 1991), in which the main purpose is the identification and origin of out-of-plane reflections, *stratigraphical modeling,* as performed in this study, is likely to be improved by added noise, because the main purpose of such modeling is the realistic imaging of reflection patterns from sedimentary sections. Such imaging is dependent on the interference of several reflections with variable amplitudes. Low-amplitude reflections are very sensitive to the signal-to-noise ratio and might only be visible on clean, undisturbed sections, but remain undetected in more realistic sections with added background noise. Such more realistic synthetic sections are needed for the test of seismic sequence analysis, which are in particular dependent on the resolution and amplitude of reflections. Added background noise can thus be very significant.

Gain Control

The final seismic image is also dependent on the type and amount of amplitude gain that is applied to the seismograms (Yilmaz, 1987). In addition to the automatically adjusted amplitude loss due to geometrical spreading, the program offers two options to control the gain at increasing travel times: (1) an automatic gain control (AGC) amplifies the signal to keep the sum of amplitudes constant within a time window of desired length. This window is moved along the seismograms with the result that low amplitude events are amplified; (2) a time ramp scaling with a power function that amplifies the amplitudes at longer travel times. A comparison of the two methods (see Figure 47)

shows the differences. For the interpretations of the synthetic seismic sections from this study, the second method with time-ramp scaling and an exponent of 1.2 was chosen. In contrast to the AGC approach, this method produces pseudo-true amplitudes and seems more realistic for simulating the pattern of low-amplitude reflections from interfaces with low contrasts in impedance.

C.4. SEISMIC MODELING OF MONTAGNA DELLA MAIELLA

The carbonate platform margin of the Montagna della Maiella in Central Italy, a part of the Apulian carbonate platform (Figure 5), is an ideal example of an outcropping platform margin that can be transformed through computer simulations into synthetic seismic data. The excellent outcrops that are exposed over an area several kilometers in width and length allow a detailed study of rock lithologies and geometries to be made, which includes the mapping of depositional sequences (Vecsei, 1991; Eberli et al., 1993; Sanders, 1994). Rough topography, with elevation differences of up to 2500 m do not allow a seismic survey to be performed. In such an environment, seismic modeling provides the only tool that can explore the potential seismic response of the rocks.

Platform/Basin Architecture

In the Jurassic/Cretaceous, the platform-to-basin transition of the Maiella carbonate platform is characterized by a steep, non-depositional escarpment (Figures 39, 40 a, 41; see also Chapter A.2.). During that time, the deeper-water deposits on the adjacent slope are detached from the time-equivalent layers on the platform and form an onlap onto the escarpment. In the Upper Cretaceous, the relief between platform and slope becomes infilled so that the layers can reach continuously from the slope on the platform top. Instead of an only aggrading sedimentation, at this point the platform is able to prograde over the former slope deposits. During the Oligocene and Eocene, this evolution results in reefal units with a distribution that reaches basinward of the buried Cretaceous escarpment. In the Miocene finally, the Maiella platform forms a gentle ramp, which is characterized by bioclastic sedimentation. During all that time, no terrigeneous source provides detritic material so that the sediments consists almost exclusively of carbonate minerals.

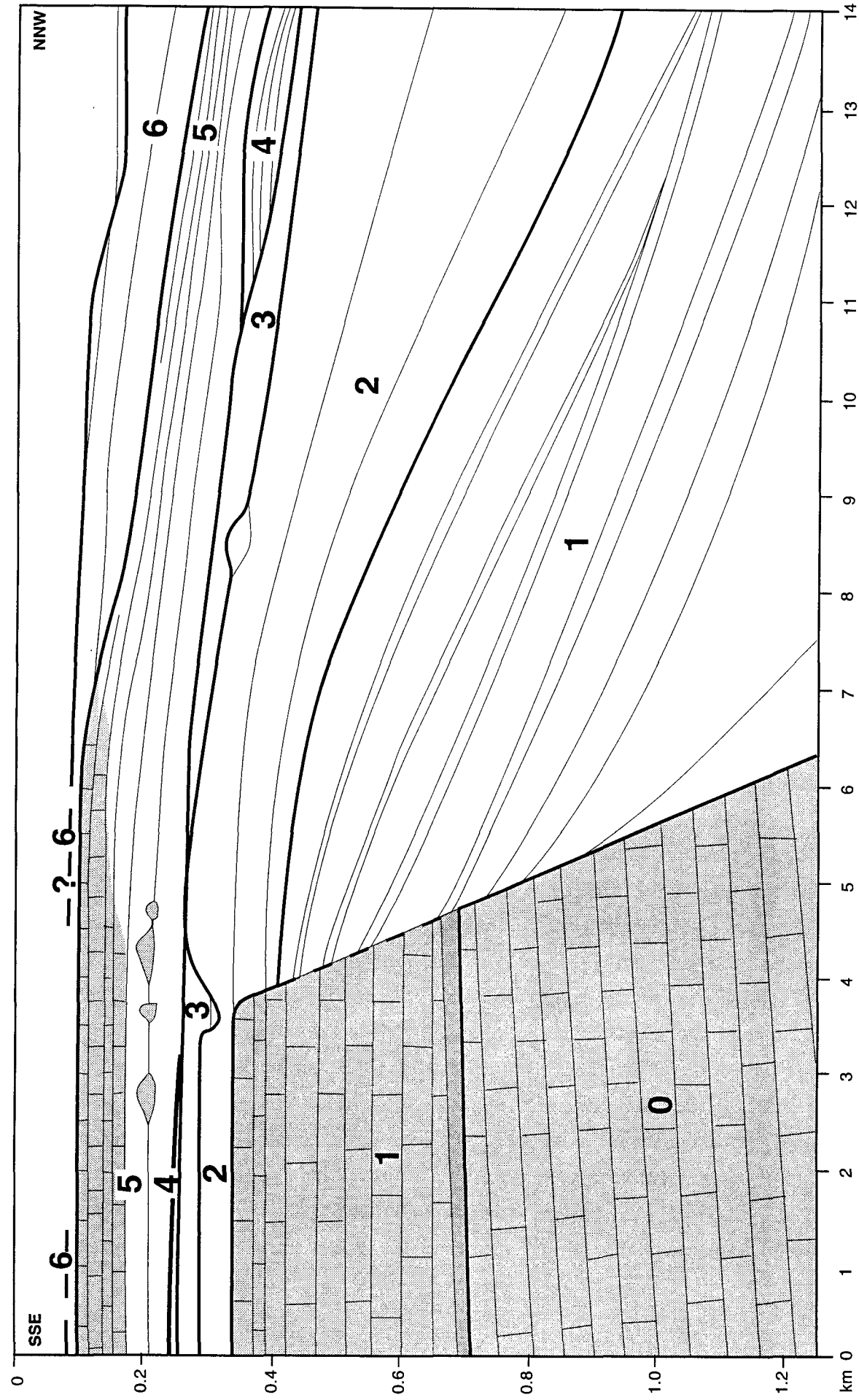

Figure 39: Schematic cross-section of the Maiella carbonate platform. Seven second-order supersequences (sensu Haq et al., 1988) can be distinguished (Vecsei, 1991). On the platform, the Upper Jurassic-Lower Cretaceous substrate (Supersequence 0) and Supersequence 1 represent the aggrading stage with an escarpment that is onlapped by slope sediments. Upper Cretaceous Supersequence 2 infills the relief between platform and slope and shows the first progradation of the platform margin. Paleogene Supersequences 3-5 are characterized by erosion and repeated flooding of the platform, by redeposited megabreccias (Supersequences 3 and 4), by progradation of reefal units (Supersequence 5) and by resedimented and pelagic carbonates on the slope. Miocene Supersequence 6 was deposited on a wide and shallow shelf basinward of the former platform. Bold lines are supersequence boundaries; shaded areas mark shallow water carbonates.

Supersequences of Montagna della Maiella

Next to the investigation of the seismic facies of the different carbonate environments, one of the main goals of seismic modeling of the Maiella outcrops is to compare the seismic sequences from synthetic seismic sections with the depositional sequences determined in the field. This comparison allows the testing of the concept of seismic stratigraphy in a pure carbonate setting (Mitchum et al., 1977; Vail et al., 1977a; Kendall and Schlager, 1981; Sarg 1988; Schlager, 1992). A good agreement between seismic sequences and depositional sequences would support the assumption that seismic sequence analyses can be used for stratigraphic and sedimentologic interpretations. The partitioning of the sedimentary record into sets of depositional sequences and their sedimentologic content and geometry, which is here of particular interest, is described in more detail in this chapter.

Depositional sequences have been defined as relatively concordant successions of genetically related layers separated by unconformities and their equivalent conformities (Van Wagoner et al., 1988). In the Montagna della Maiella, seven second-order depositional sequences (including their substrate with unknown lower boundary) can be distinguished based on field observations of geometrical and lithological characteristics (Figure 39) (Vecsei, 1991; Bernoulli et al., 1992; Eberli et al., 1993; Sanders, 1994). The six sequence boundaries which partition the rocks into these seven supersequences are recognized in the field by geometrical unconformities and by prominent changes in the sedimentary systems. In proximal areas, the signatures of subaerial exposure are an additional characteristic of these boundaries. The durations of the observed sequences vary between 7 and 21 million years (Vecsei, 1991), which suggests that the sequences are second-order and are the equivalent of supersequences, sensu Haq et al. (1988). These supersequences can be subdivided into several smaller scale sequences, possibly of third-order, which themselves consist of smaller-scale, fourth-order parasequence sets.

The model represents an attempt to image seismically the seven supersequences and the related geologic features. It is tested if the observed unconformities and bedding planes can be seen on synthetic seismic data. The third-order depositional sequences were not completely simulated in the petrophysical model, because the thickness of these sequences is mostly beyond the seismic resolution and their inclusion would have increased the size of the computer model above the limitations of the modeling software. In other sedimentary environments, specifically in siliciclastic rocks, third-order sequences, which are the base of the global sea-level curve (Haq et al., 1988), seem to have, in general, higher sedimentation rates and therefore greater seismic significance.

Under very favorable conditions, even fourth-order sequences can be recognized on seismic sections (Fulthorpe, 1991). However, the modeled platform margin-to-slope transition of the Maiella is characterized by relatively low bulk sedimentation rates and the third-order sequences are therefore thin.

Lithologic Composition of Supersequences

The following description of the nomenclature of formations and the separation of the rocks into supersequences is based on Vecsei (1991). Figure 39 shows a general cross-section of all depositional supersequences.

Upper Jurassic - Lower Cretaceous ("Supersequence" 0)

Upper Jurassic and Lower Cretaceous platform rocks form the oldest outcropping formations of the Montagna della Maiella (Morrone di Pacentro Formation). Even though the sequential development and its lower boundary is not known, this substrate which underlies the six supersequences above, will be named in the following chapters as Supersequence 0, because its mapped upper boundary marks the top of this oldest supersequence. In the modeled section, Supersequence 0 consists of Lower Cretaceous carbonates that were deposited in restricted, shallow water. On the platform this supersequence is truncated by the "mid"-Cretaceous unconformity, whereas it is cut basinwards by the escarpment and onlapped by slope sediments of Supersequence 1.

Figure 40: Outcrop photographs of the different architectural elements of the Maiella impedance model shown in Figure 42. Figures 40 a-c show rock formations that are easily included in the impedance model, due to clear seismic-scale geometries and characteristic impedance distribution. Figure 40 d documents a section that is difficult to model, because thin layering forms no impedance pattern on a seismic scale. **a)** Platform escarpment (from lower left to upper right) with onlapping megabreccias at Monte d'Ugni (breccia onlaps marked by arrows). Horizontal width of picture ~ 1.5 km. The megabreccias of Supersequence 1 form an onlap geometry onto the Lower Cretaceous platform ("Supersequence 0") and have higher impedances than intercalated rocks (Figure 46 c). **b)** Patch reefs (Supersequence 5) at Pesco Falcone. Two high-velocity coral buildups are surrounded by low-velocity carbonate sands (Figure 46 f). The height of the larger patch reef is ~ 40 meters. **c)** Succession of cliff-forming Bryozoan Limestones (Supersequence 6) with intercalated hemipelagic marls in Valle San Bartolomeo. The marls (40 m thick) form the grassy slope between the vertical cliffs of Lower Bryozoan Limestone (50 m thick) and Upper Bryozoan Limestone (20 m thick). Vp of marls range between 4300 and 4900 m/s, whereas Vp of limestones are significantly higher and vary between 5500 and 6200 m/s (Figure 46 g). **d)** Slope sediments (Supersequences 4 and 5) in Valle dell'Orfento near Decontra (height of cliff ~ 100 m). The section consists of alternating pelagic limestones, turbidites and breccias. The breccias cut the underlying beds and mark the base of higher-order depositional sequences. Small-scale layering provides no clear impedance distribution, though the layers have characteristic individual impedance values (Figure 46 e).

Figure 41: View of western side of Valle dell'Orfento displaying all major elements of the impedance model of Figure 42. In foreground is the Cretaceous platform, which is onlapped at the escarpment by Cretaceous base of slope sediments. The overlying uppermost Cretaceous sediments infill the relief between platform and slope. The top of the mountain is formed by Upper Eocene and Lower Oligocene reefal units, which prograde over slope and shelf deposits. (Vertical relief from escarpment at lower right corner to mountain top is approx. 1200 m).

Figure 40:

Figure 41:

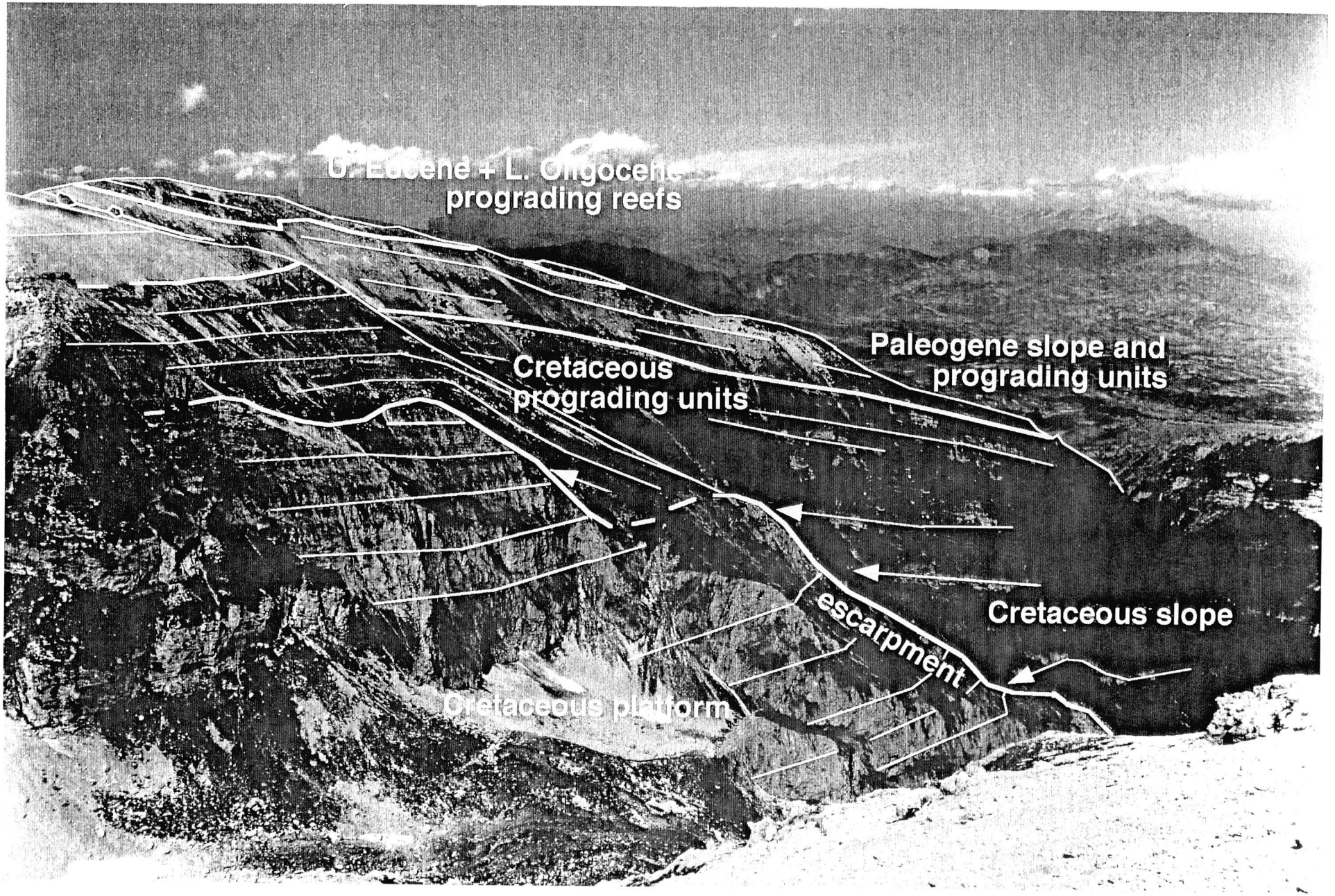
U. Eocene + L. Oligocene
prograding reefs
Cretaceous
prograding units
Paleogene slope and
prograding units
escarpment
Cretaceous slope
Cretaceous platform

Supersequence 1

On the platform, the base of this supersequence (Cima delle Murelle Formation) is the "mid"-Cretaceous unconformity, a distinct exposure horizon. This is a very irregular surface with numerous karstic features such as speleothems, breccias and bauxitic accumulations. The overlying successions of platform sediments are dominated by peritidal carbonates and grainstones that alternate with rudist biostromes. The abundance of the biostromes increases upsection and towards the escarpment, but as in proximal Supersequence 0, no massive rim facies or reef has been observed.

In the basin, Supersequence 1 can be subdivided into two units (Figure 39). The lower one, at the base of the escarpment, is the Valle del Inferno Unit, which is a succession of breccias and bioclastic grainstones that form an internally cross-bedded onlapping wedge. The upper unit is the Tre Grotte Formation, an alternation of carbonate turbidites and periplatform ooze ("Scaglia" of Italian authors) with intercalated megabreccias. The breccias form an onlap onto the platform sediments along the escarpment, are often amalgamated and contain lithified blocks and pebbles eroded from the shallow water platform. They are interpreted to be deposited during lowstands of sea-level (Vecsei, 1991). Consequently, each megabreccia is considered as the base of a third-order sequence.

Escarpment

The Cretaceous platform was separated from the slope sediments by a non-depositional escarpment that reached a height of up to 1000 m. The escarpment was probably an inherited feature from the Early Jurassic rifting phase of the continental margin, i.e. the edge of a fault block (Bernoulli and Jenkyns, 1974; Eberli et al., 1993). The average inclination of the escarpment is around 30-35 degrees. In the upper part, where the declivity can be 50 degrees or steeper, several niches form concave structures in the platform wall. Sediments produced on the platform bypassed the upper escarpment and were deposited as an onlapping wedge at its foot (Figures 39, 40 a, 41). The irregular and undulating surface of the escarpment and the lack of a pronounced rim facies in the preserved platform sediments indicate that the escarpment periodically eroded and dismantled by gravitational collapse. This is supported by the appearance of older cemented components of the platform in the onlapping megabreccias. The main events of platform erosion are interpreted to have happened during sea-level lowstands (Vecsei, 1991). During the latest Cretaceous (Supersequence 2), the aggrading slope and basin sediments continuously infilled the high relief and transformed the steep escarpment into a gradual ramp-like margin.

Supersequence 2

The escarpment separating the platform from the adjacent basinal sediments was buried during deposition of Supersequence 2 (Orfento Formation) comprising first aggrading, then prograding units deposited on the Upper slope, which finally led to a gentle ramp-like platform-to-basin transition. The Maiella platform margin therefore changed during the Campanian-Maastrichtian from aggradation to progradation.

The most typical lithology of Supersequence 2, called "Calcari Cristallini", is characterized by well-sorted bioclastic sands of mainly rudist debris with high porosities and almost no cementation. They overlay a karstic surface at the top of the platform (Mutti, 1995). Within this supersequence, several horizontally and vertically stacked breccia bodies can be recognized in proximal positions that define lower-order depositional sequences (Mutti et al., 1994). Unlike the underlying megabreccias, these breccias do not extend far into the basin. The distal sediments of the Orfento Formation are very well sorted, fine rudist sands, which have an average porosity of approximately 30 percent.

Supersequences 3-5 (slope)

The slope deposits of these supersequences consist of alternations of thin-bedded pelagic carbonates ("Scaglia" of Italian authors), turbidites and breccias (Figure 40 d, Santo Spirito Formation). The breccias appear in bundles and can be amalgamated. Lithoclasts in many of these breccias are the products of erosion of the exposed platform top or along the slope. Meteoric cements in these clasts indicate that they were eroded during sea-level lowstands (Sanders, 1994). Thus they are interpreted to be the base of third-order (?) sequences (Vecsei, 1991). The turbidites consist mainly of skeletal grains with abundant nummulitids in a micritic or sparitic matrix. The "Scaglia" is a fine grained pelagic lime mudstone with abundant planctonic foraminifera.

Supersequences 3-4 (platform)

On the platform, these two supersequences occur only as relics. The weakly indurated rudist sands of Supersequence 2 are on the platform locally covered by massive breccias of Supersequence 3. These breccias are intercalated with pelagic limestones and were deposited in channels that incised the platform. The breccias were deposited mainly by processes of mass-flows primarily during two phases, one in the uppermost Maastrichtian and one in the Paleocene (Vecsei, 1991, Sanders, 1994).

On the platform, Supersequence 4 is preserved only as discontinuous and thin Alveolina limestones (Sanders, 1994).

Supersequence 5 (platform)

During the Priabonian, the platform was repeatedly flooded, which resulted in the deposition of progradational units of skeletal sands. Several small patch-reefs developed on these sands (Figure 40 b). They are characterized by upward convex shapes and contain large corals and hydrozoans. The surrounding bioclastic sands are grain-to-packstones that contain benthic foraminiferas, algae, bryozoans and other skeletal fragments (Vecsei, 1991).

In the Lower Oligocene, coral reefs (Pesco Falcone Formation) bloomed and eventually prograded approximately 4 km basinwards over these fine sands (Eberli, et al., 1993). South of the former escarpment, where relics of younger sediments from Supersequence 6 above are only locally preserved (Sanders, 1994), the reefal units of the Pesco Falcone Formation usually form today the mountain crests and thus the upper limit of the outcropping section (Figure 41).

Supersequence 6

In the Miocene, the Maiella was characterized by a wide and shallow shelf on which Supersequence 6 was deposited (Bolognano Formation). Rocks belonging to this supersequence are found mainly overlying the former slope. On top of the prograding reefs of sequence 5, they are only occasionally preserved. The lower part of Supersequence 6 is formed by two higher-order sequences. Both contain one bioclastic grainstone unit (bryozoan limestone), overlain by marly limestones, indicating deeper water deposition (Figure 40 c). The top of the supersequence is not continuously preserved. Where present, it is made of Lithothamnium limestones and a marly interval (Vecsei, 1991).

This supersequence is onlapped by the evaporitic sediments of the Gessoso-Solfifera Group of Messinian age (Crescenti et. al, 1969). These sediments were deposited during the evaporitic drawdown of the Mediterranean Sea and are part of the next supersequence.

Impedance Model

The most crucial step in seismic modeling is to establish a realistic petrophysical model of the geometrical distribution of acoustic impedance. This model will be converted to a synthetic seismic section. The complex structure and sedimentological architecture of the Maiella has to be simplified to an impedance model that represents all

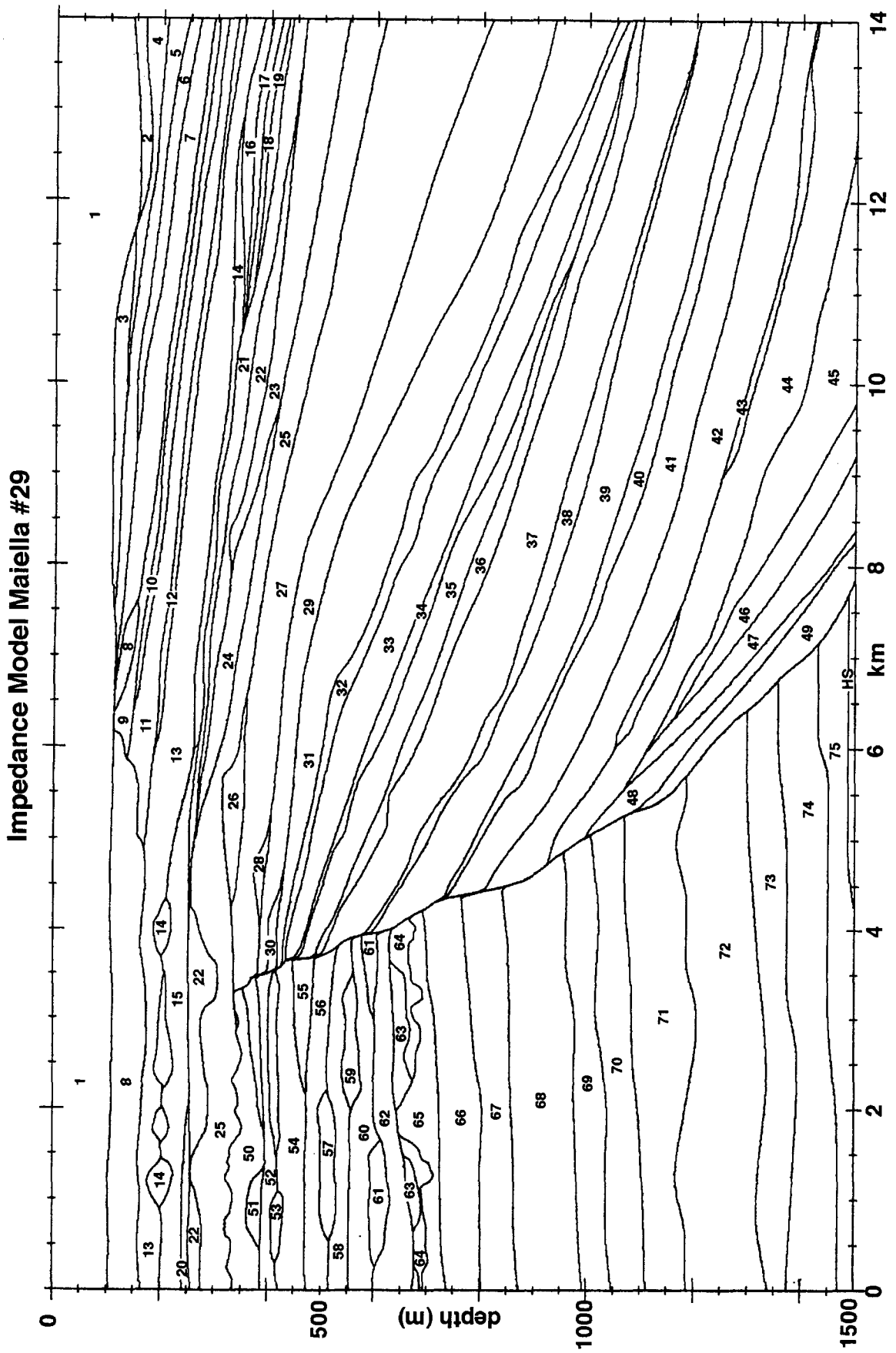

Figure 42: Plot of impedance model Maiella #29 (6 times vertical exaggerated). This model is 14 km in width and 1.5 km in depth and consists of 75 layers and the halfspace below it. All layers have characteristic geometries and impedance values. The layer numbers refer to Table 3, in which detailed information on the individual layers are displayed (supersequence, lithology, velocity, density, impedance and reflection coefficient). All major elements of the model can be seen on the photographic view of the western side of Valle dell'Orfento (Figure 41) and in the schematic cross-section (Figure 39).

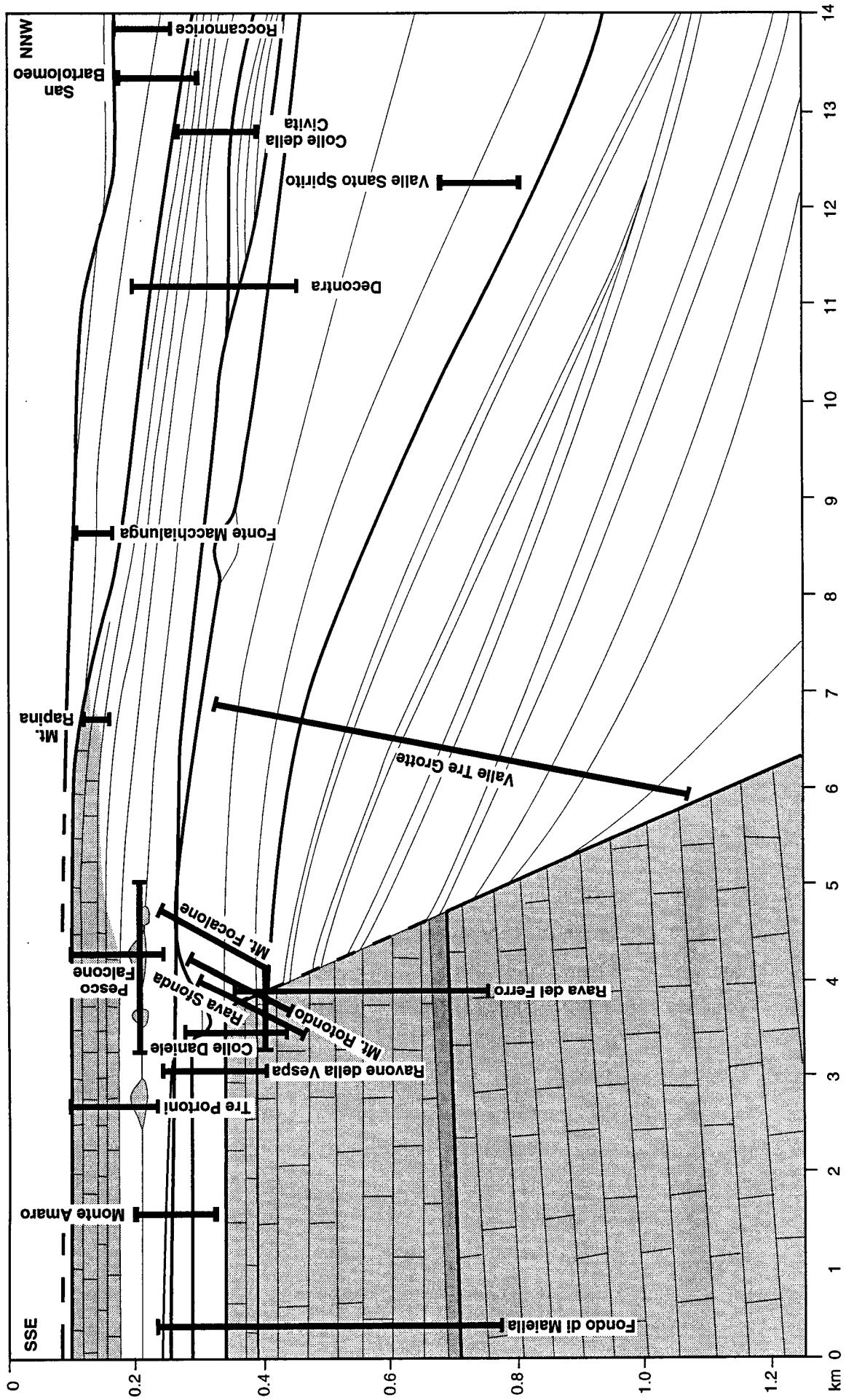

Figure 43: Schematic cross-section of the Maiella showing the relative positions of sample locations. The locations are projected into the plane of the cross-section that is used to define the geometries of the impedance model (Figure 42). Projection is performed parallel to the general direction of the platform margin. For sample numbers, data and locations, compare with Table 5. Bold lines are supersequence boundaries (see Figure 39); shaded areas mark shallow water carbonates.

of the major lithological units. It is evident that the model can only represent a simplified version of the true impedance distribution of the rock section, which in reality consists of countless fine layers with distinct impedances. Considering the seismic resolution, which is limited to approximately a quarter of the signal's wavelength (Sheriff, 1977, 1985), one cannot resolve all details of the true geologic section, but it is nevertheless feasible to simulate on a seismic scale the physical properties with a simplified model.

The impedance model used to calculate the synthetic sections was the 29th in a series of stepwise improved models. It measures 14 km in width, 1.5 km in depth and consists of 75 layers with characteristic geometries (Figure 42) and impedances (Tables 2, 3). The layers were defined by grouping rocks with characteristic velocity and density pairs. Ideally, the thicknesses of the layers should be comparable to, or thinner than the resolution of the seismic section. However, due to the variety of impedances in the different parts of the Montagna della Maiella, the thicknesses of the layers are very variable. Homogeneous parts of the rock column can be simulated by fewer layers than parts which are physically more variable.

Figures 41 and 42 compare on a large scale the model with the valley outcrop on the western side of the Upper Valle dell'Orfento. In outcrop, most of the modeled layers have a distinct appearance (Figures 40 a-c). The platform escarpment, the onlapping breccias, and the prograding reefs can be easily recognized. However, not all of the layers defined in the model are obvious in outcrops (Figure 40 d). The following paragraphs describe the layers of the impedance model and the criteria and methods that were used to select the different layers.

Impedances of the Modeled Layers

Knowledge of the impedance distribution of the Maiella carbonates were derived from laboratory measurements of velocity and density of 186 samples. The complete data are listed in Table 5. The samples were collected on several vertical measured sections and cover all major units. Relative positions of the sampled sections are displayed in a schematic cross section in Figure 43. Due to the fairly large scattering of velocity and density data within a given unit, a statistical averaging of measurements within each unit was necessary to define the acoustic properties of the modeled layers. The average velocity and density values of the mappable lithological units are given in Table 2. These average values provided the basis for assigning velocity-density pairs to the individual layers of the impedance model. Table 3 displays the chosen velocity-density pairs for the 75 layers of the final impedance model.

No corrections were made to convert the measured ultrasonic velocities into velocities at seismic frequencies. The velocity dispersion, as discussed in Part B, is

assumed to be insignificant compared to the wide range of measured velocities. A general correction for dispersion would lower all velocity values of the model and would have thus only a minor impact on the seismic reflection pattern, which is influenced mainly by the impedance contrast between layers rather than by absolute impedance values. Furthermore, the decision to take the velocities at ultrasonic frequencies results in a negligible error compared with other assumptions that are made, such as sample selection or layer definition.

Lithology (Formation after Vecsei, 1991)	super-sequence #	# of samples	average porosity (%)	average density (g/cm^3)	average Vp (m/s)
Lower Cret. platform (Morrone di Pacentro Form.)	0	4	1.6	2.69	6315
"mid"-Cretaceous unconformity (breccias)	1	6	3.7	2.70	6160
"mid"-Cretaceous unconformity (bauxites)	1	3	12.5	2.81	4754
Up. Cretaceous platform (Cima delle Murelle Form.)	1	21	4.6	2.64	6044
Up. Cret. rudist biostromes (Cima delle Murelle Form.)	1	5	14.2	2.48	5566
Valle del Inferno Unit	1	3	6.7	2.60	5600
Up. Cretaceous megabreccias (Tre Grotte Form.)	1	5	7.5	2.59	5713
Up. Cretac. turbidites and Scaglia (Tre Grotte Form.)	1	9	12.7	2.50	5021
Calcari Cristallini (Orfento Formation)	2	27	19.6	2.38	4283
Calcari Cristallini breccias (Orfento Formation)	2	3	11.2	2.53	5217
Paleogene reefs and patch-reefs (Pesco Falcone Form.)	5	15	9.0	2.56	5618
Paleogene nummulitid sands/silts (Santo Spirito Form.)	5	5	16.1	2.44	4509
Paleogene breccias (Santo Spirito Formation)	3-5	12	5.9	2.62	5929
Paleogene turbidites (Santo Spirito Formation)	3-5	26	7.2	2.59	5602
Paleogene Scaglia (Santo Spirito Formation)	3-5	19	10.0	2.55	5128
Bryozoan limestone (Bolognano Formation)	6	10	4.4	2.64	5817
Hemipelagic marls (Bolognano Formation)	6	6	10.6	2.53	4598
Lithothamnium limestone (Bolognano Formation)	6	6	21.9	2.35	4186
total samples	0-6	186	10.1	2.55	5321

Table 2: Statistically averaged values of porosity, density and compressional wave velocity for different lithologies and formations. These values were used to assign impedance values to the layers of the model (Table 3).

Geometries of the Modeled Layers

The overall geometries of the layers are based on the observed geometries of the seven supersequences of Vecsei (1991). The selected cross section represents a cut

Layer #	Superse-quence #	Lithology	Vp (km/s)	Density (g/cm^3)	Impedance $10^6 kg/m^2s$	Refl. Coeff.
1		top of model (=average values of all samples)	5.32	2.55	13.57	0.132
2		evaporites (gypsum)	6.10	2.90	17.69	-0.285
3	6	lithothamnium limestone	4.19	2.35	9.85	0.083
4		upper marl unit	4.60	2.53	11.64	0.138
5		upper bryozoan limestone	5.82	2.64	15.36	-0.138
6		lower marl unit	4.60	2.53	11.64	0.138
7		lower bryozoan limestone	5.82	2.64	15.36	-0.033
8	5	reefs / build-ups	5.62	2.56	14.39	0.004
9		turbidites	5.60	2.59	14.50	0.035
10		breccias	5.93	2.62	15.54	-0.086
11		scaglia	5.13	2.55	13.08	0.086
12		breccias	5.93	2.62	15.54	-0.171
13		nummulite packstone	4.51	2.44	11.00	0.134
14		(patch) reefs / breccias	5.62	2.56	14.39	-0.134
15		nummulite packstone	4.51	2.44	11.00	0.171
16	4	breccias	5.93	2.62	15.54	-0.086
17		scaglia	5.13	2.55	13.08	0.086
18		breccias	5.93	2.62	15.54	-0.035
19		turbidites	5.60	2.59	14.50	0.035
20		breccias	5.93	2.62	15.54	-0.086
21	3	scaglia	5.13	2.55	13.08	0.064
22		breccia	5.79	2.57	14.88	-0.128
23	2	calcari cristallini (rudist sand)	4.70	2.45	11.51	0.069
24		calcari cristallini (rudist sand)	5.22	2.53	13.21	-0.173
25		calcari cristallini (rudist sand)	4.00	2.33	9.32	0.173
26		calcari cristallini (rudist sand)	5.22	2.53	13.21	-0.069
27		calcari cristallini (rudist sand)	4.70	2.45	11.51	0.069
28		calcari cristallini (rudist sand)	5.22	2.53	13.21	-0.173
29		calcari cristallini (rudist sand)	4.00	2.33	9.32	0.173
30		calcari cristallini (rudist sand)	5.22	2.53	13.21	-0.026
31	1 (basin)	scaglia / turbidite	5.02	2.50	12.55	0.082
32		megabreccias	5.71	2.59	14.79	-0.082
33		scaglia / turbidite	5.02	2.50	12.55	0.082
34		megabreccias	5.71	2.59	14.79	-0.082
35		scaglia / turbidite	5.02	2.50	12.55	0.082
36		megabreccias	5.71	2.59	14.79	-0.082
37		scaglia / turbidite	5.02	2.50	12.55	0.082
38	1 (basin)	megabreccias	5.71	2.59	14.79	-0.082
39		scaglia / turbidite	5.02	2.50	12.55	0.082
40		megabreccias	5.71	2.59	14.79	-0.082
41		scaglia / turbidite	5.02	2.50	12.55	0.082
42		megabreccias	5.71	2.59	14.79	-0.082
43		scaglia / turbidite	5.02	2.50	12.55	0.082
44		megabreccias	5.71	2.59	14.79	-0.082
45		scaglia / turbidite	5.02	2.50	12.55	0.012
46		Valle del Inferno unit	5.04	2.55	12.85	0.046
47		Valle del Inferno unit	5.48	2.57	14.08	-0.046
48		Valle del Inferno unit	5.04	2.55	12.85	0.136
49		Valle del Inferno unit	6.28	2.69	16.89	-0.029
50	1 (plat-form)	platform limestones	6.04	2.64	15.95	-0.072
51		rudist biostromes	5.57	2.48	13.81	0.072
52		platform limestones	6.04	2.64	15.95	-0.072
53		rudist biostromes	5.57	2.48	13.81	0.072
54		platform limestones	6.04	2.64	15.95	-0.072
55		rudist biostromes	5.57	2.48	13.81	0.072
56		platform limestones	6.04	2.64	15.95	-0.072
57		rudist biostromes	5.57	2.48	13.81	0.072
58		platform limestones	6.04	2.64	15.95	-0.072
59		rudist biostromes	5.57	2.48	13.81	0.072
60		platform limestones	6.04	2.64	15.95	-0.072
61		rudist biostromes	5.57	2.48	13.81	0.072
62		platform limestones	6.04	2.64	15.95	-0.089
63		bauxite concretions and sand	4.75	2.81	13.35	0.109
64		bauxitic limestone breccias	6.16	2.70	16.63	0.019
65	"0"	platform limestones	6.40	2.70	17.28	-0.016
66		platform limestones	6.25	2.68	16.75	0.016
67		platform limestones	6.40	2.70	17.28	-0.016
68		platform limestones	6.25	2.68	16.75	0.016
69		platform limestones	6.40	2.70	17.28	-0.016
70		platform limestones	6.25	2.68	16.75	0.016
71		platform limestones	6.40	2.70	17.28	-0.016
72		platform limestones	6.25	2.68	16.75	0.016
73		platform limestones	6.40	2.70	17.28	-0.016
74		platform limestones	6.25	2.68	16.75	0.016
75		platform limestones	6.40	2.70	17.28	0.009
HS	halfspace	model base = platform limestones	6.50	2.71	17.61	

Table 3: Lithologic descriptions, velocity-density pairs, resulting impedances and reflection coefficients of layers in the model Maiella #29. The impedance values of the different lithologies are average values from Table 2, which are based on the measurements of 186 samples (Table 5). The reflection coefficient were calculated with respect to the underlying layers (=layer with next higher number), which may not necessarily be an impedance contrast in the model, due to variable bed terminations.

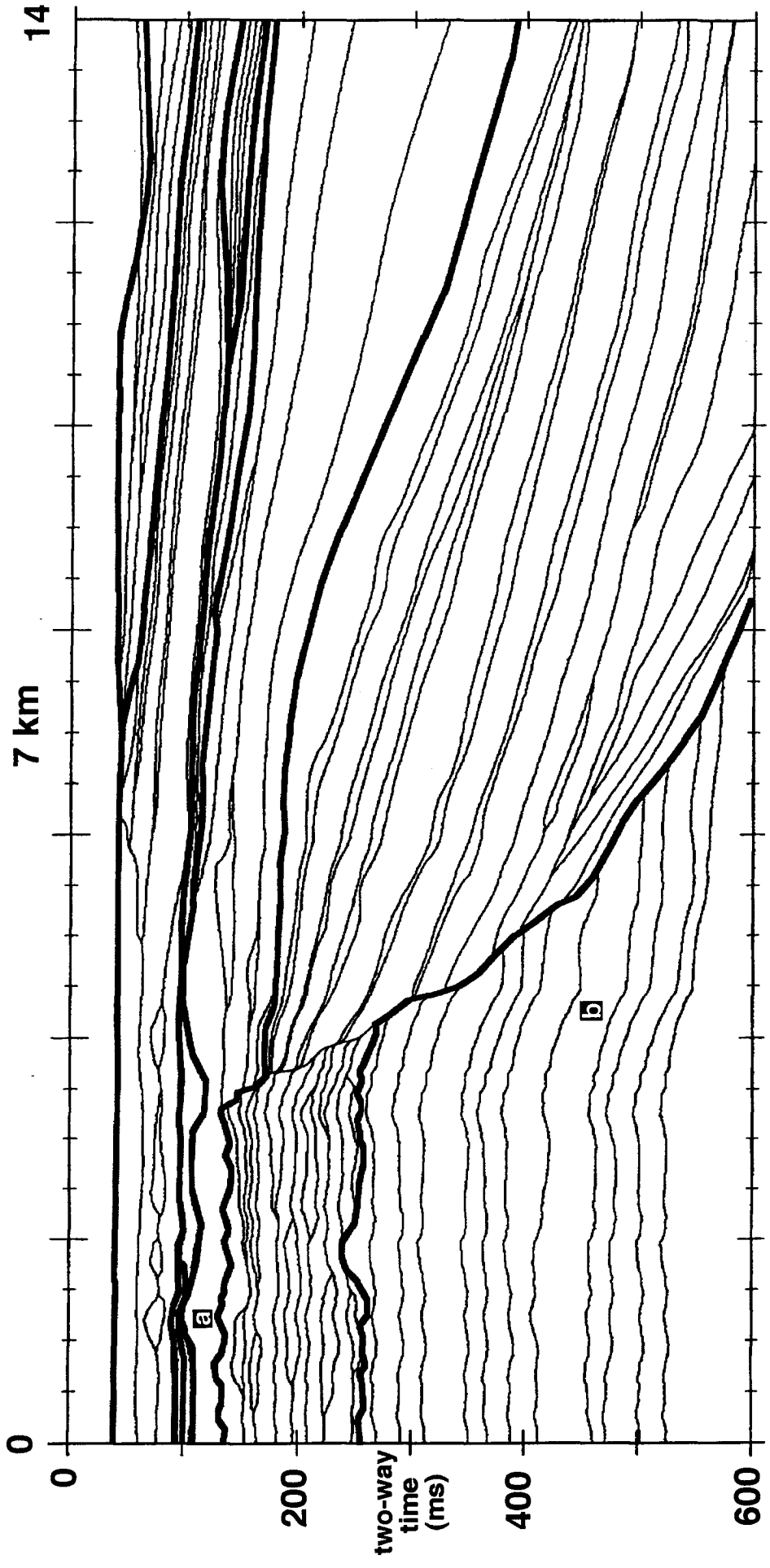

Figure 44: Maiella impedance model #29, converted from depth (Figure 42) to two-way travel time. This conversion is computed in vertical direction only, and does not consider dipping layer-geometry, as normal incidence raytracing does. Nevertheless, the resulting time-section can be used to identify the reflections on the seismic sections of Figures 48 - 50. Note the effects of velocity pull-up below patchreefs (a) and of push-down below the escarpment (b). Bold lines mark supersequence boundaries.

through the platform-basin transition that parallels the western side of Valle dell'Orfento (Figure 41). Several profiles were projected orthogonally into the plane of the cross-section (Figure 43). Faults and tectonic dips were corrected, so that the resulting geometry represents the geometrical relations at the end of deposition.

The model was generated using the *MIMIC*™ program and consists of a succession of layers, all of which have characteristic geometries and impedances. A pre-condition of the modeling program is that all layers are present across the entire model width of 14 km. The layers that wedge out or are truncated have to continue to both sides of the model as 'zero-thickness layers' that do not affect the seismic response of the model. The final layer geometry is dependent on the chosen truncation characteristic of a layer (hard or soft) and on the order of entry into the model. This determines whether a layer cuts or is cut by another layer.

The final geometrical depth model (Figure 42) can be converted into a time model (Figure 44). The depth of a layer is converted to two-way travel time depending on the velocities and thicknesses of the layers above. A two-way travel time model is especially useful in identifying the reflection events on a seismic section because model and synthetic section can be plotted at the same scale.

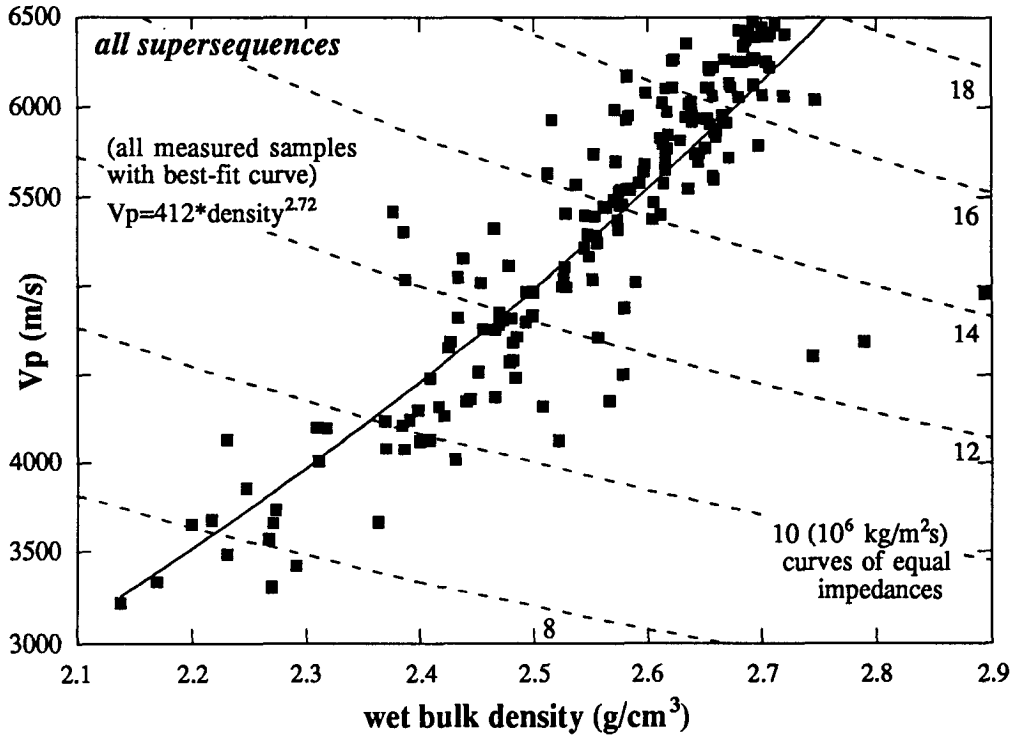

Figure 45: Velocity-density plot of 186 measured Maiella samples from all supersequences with best-fit equation (solid line). The dashed lines mark the curves of equal impedances (calculated for the density of calcite). These measurements are the basis for defining the velocity-density values for the layers of the impedance model. Figures 46 a-g show how these velocity-density pairs are grouped into lithologic categories within the individual supersequences.

The numbers following the titles in the next paragraphs refer to the numbering of impedance layers as marked in Figure 42 and shown in Table 3. Figures 45 and 46 display the measured velocity and density values of all samples of the individual lithologies in a series of cross plots. The average values taken to define the impedance values of the modeled layers are marked in these plots.

Layers of "Supersequence" 0 and Lower Halfspace (#65-75, HS)

In the modeled section, Supersequence 0 is only present as the Lower Cretaceous platform. All layers of the Lower Cretaceous platform and of Supersequence 1 end at the escarpment. Supersequence 0 forms the base of the model in the South. The lowest layer of the model is the lower 'halfspace' lithology. The expected lithology below the Lower Cretaceous platform is assumed to be a dense, well cemented platform limestone. Therefore, the selected velocity and density of the lower halfspace are the values for pure calcite, 6.5 km/s and 2.71 g/cm^3.

The measured velocity contrasts of the Lower Cretaceous platform samples are extremely small (Figure 46 a). All velocities lie within a narrow range between 6270 and 6450 m/s. The Lower Cretaceous platform is one of the units in the modeled section that shows no evident bedding pattern with physically different units on a seismic scale. Nevertheless, an arbitrary bedding system comprising eleven layers is assumed in order to simulate the maximum potential for reflectivity of such a section with low impedance variation. The physical properties of the modeled layers vary within the measured narrow range of impedance values. This arbitrary method of modeling, which is only applied in a minor part of the modeled section, has been used in several published modeling studies (Biddle et al., 1992; Stafleu and Schlager, 1993; Stafleu et al., 1994). This approach is the only way to simulate the seismic reflection pattern of rock units that comprise thin-bedded layers which cannot be grouped on a seismic scale into bundles of layers with characteristic impedances.

Layers of Supersequence 1 (#31-64)

Supersequence 1 consists of two parts (Figures 39, 42): (1) the Upper Cretaceous platform; and (2) the onlapping sediments of the slope and basin. The two units are separated by the escarpment.

The platform section of Supersequence 1 was modeled with 15 layers. The upper part consists of alternating peritidal carbonates with intercalated rudist biostromes. The graphic connections between the rudist biostromes in the stratal horizons in Figure 42 have no seismic significance, because they are zero-thickness layers that separate layers of equal impedances. Compared to the other platform sediments, the rudist biostromes have higher porosities and therefore lower densities (Figure 46 b). However, the

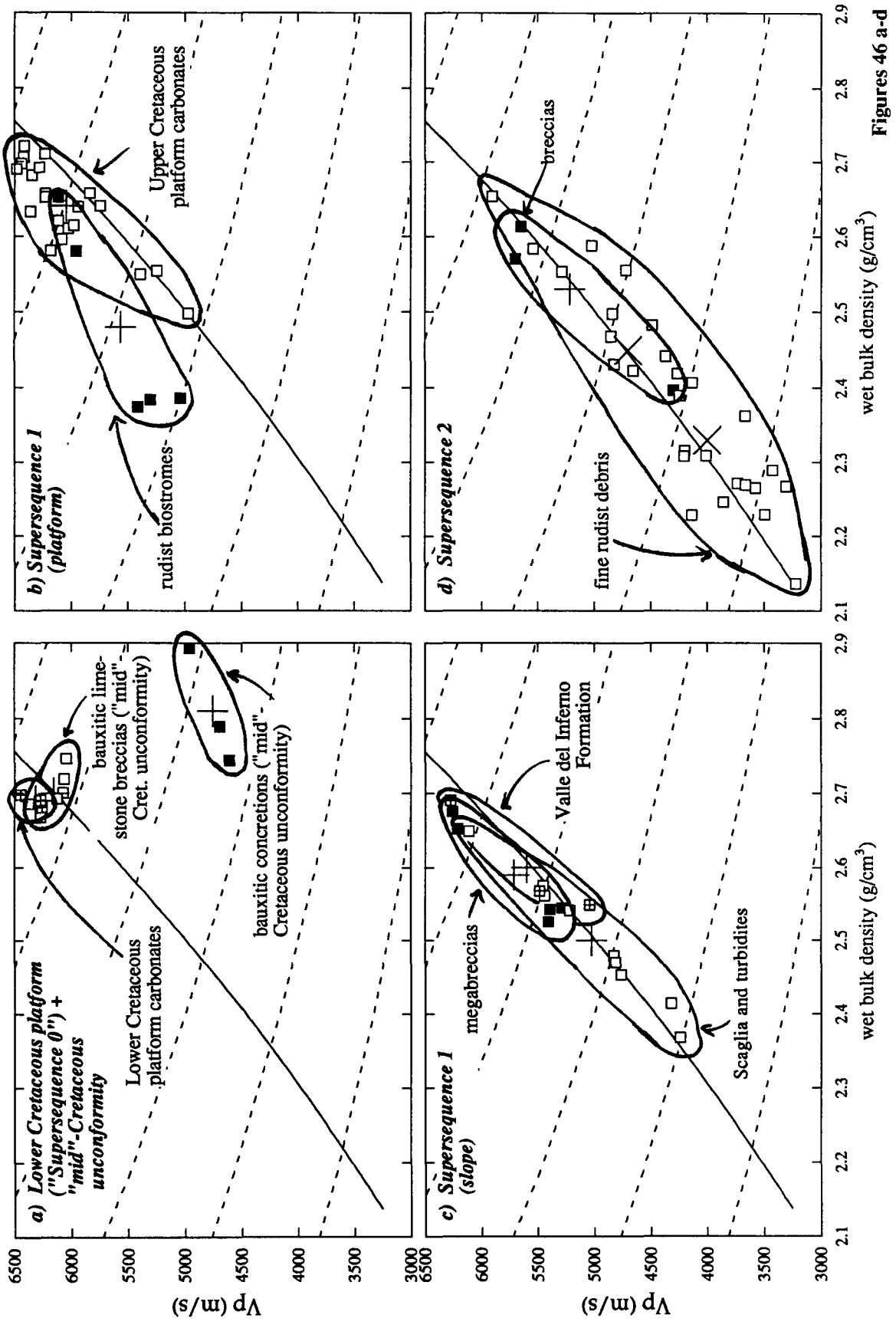

Figures 46 a-d

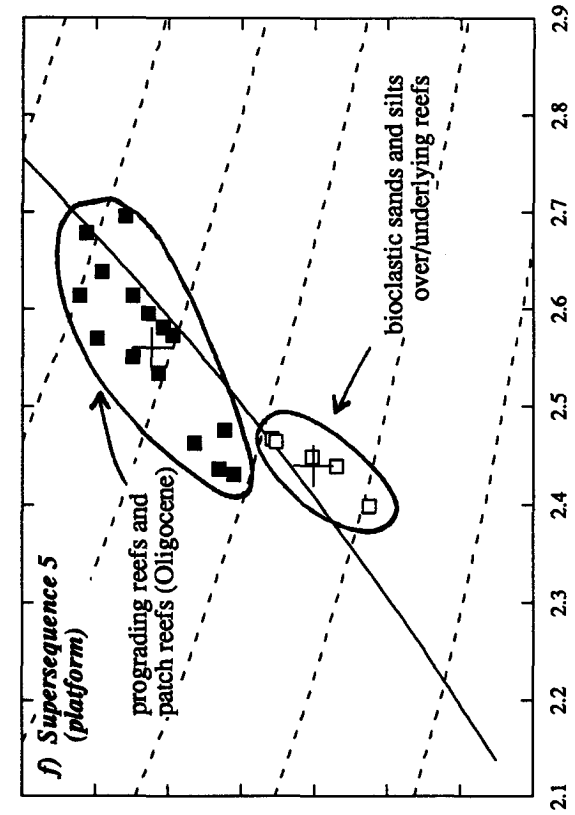

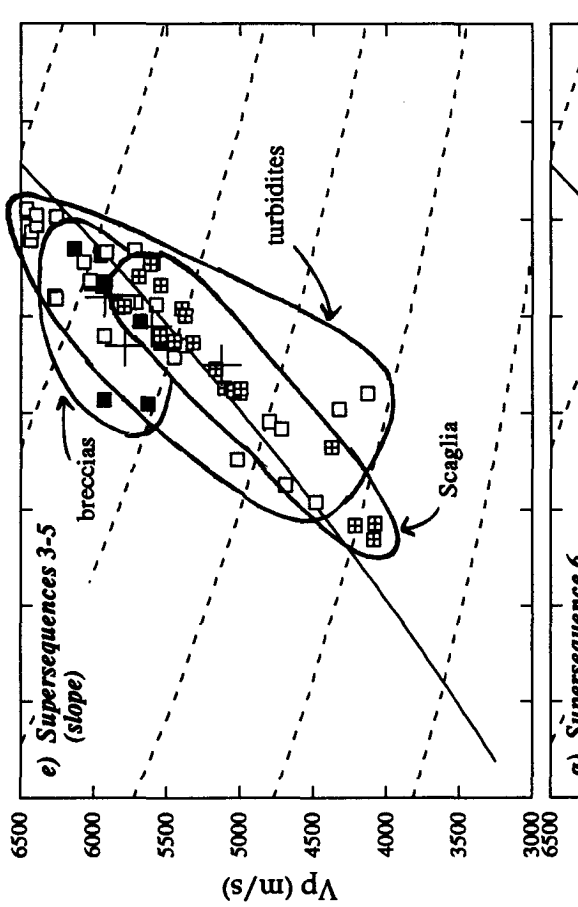

Figures 46 a-g: Velocity-density plots of sampled lithologies within Supersequences 0-6. The solid line is the general velocity-density trend of all samples; the dashed lines are curves of equal impedances for rocks with density of calcite (for values see Figure 45). The '+'-marks are the statistically averaged velocity-density values, which were used to define the impedance value of the individual lithologies in the impedance model (Table 2, 3, Figure 42). The two 'x'-marks in Figure 46 d) are the two arbitrarily chosen impedance values for the fine-grained Calcari Cristallini. These values represent the wide range of the measured samples. The Lower Cretaceous platform is also represented in the model by two arbitrarily chosen values within the measured range (Table 3). These two values lie very close to each other and were not plotted in Figure 46 a; only the average value is marked by a '+'.

measured average velocities are only slightly below normal velocities of the Upper Cretaceous platform limestones, ranging between 5 and 6 km/s. The relatively high velocities at the high porosities of the rudist biostromes can be related to the rigid frame fabric of the biostromes which build a constructional framework with enclosed porosity that results in high elastic properties. A similar relationship was observed in certain carbonate samples from the drillholes on Great Bahama Bank (Part A, Anselmetti and Eberli, 1993). Consequently, the observed impedance contrasts between the platform carbonates and rudist biostromes are not as high as would be expected from consideration of porosity contrasts alone. This is documented by the comparison of the measured velocity-density pairs with the curves of equal impedances in Figure 46 b.

On the platform, the basal sequence boundary of Supersequence 1 is a karstic horizon, the "mid"-Cretaceous unconformity. This unconformity is an irregular accumulation of bauxite-rich limestone breccias and pockets of bauxitic sand. The breccias have velocities similar to the overlying and underlying limestones, whereas the bauxitic sands have completely different acoustic properties. Due to the high grain density of the aluminum and iron hydroxides, the unconsolidated sands may have very high bulk densities of more than 3 g/cm^3. The measured velocities, however, can be as low as 4500 m/s, so these samples form a cluster in the velocity-density diagram that is far from the average trend of the carbonates (Figure 46 a). The rocks of the unconformity were modeled with two layers; one represents the limestone breccias and one the bauxitic sands. Both layers have an irregular geometry in reality and in the model; they wedge out, form pockets or are sometimes completely absent.

The basinal time equivalent deposits of the Valle del Inferno Formation is modeled with four layers, whereas the overlying succession of onlapping breccias and background sediment of the Tre Grotte Formation is represented by 15 layers (Figure 46 c). The impedance values of the Valle del Inferno Formation are, due to a low number of measurements, not very reliable as in other groups, but above the lower halfspace, this formation forms the deepest unit north of the escarpment and is thus not very important for the general picture. The impedances of the overlying Tre Grotte Formation are well established. The cluster in the velocity-density diagram of the megabreccias (Figure 46 c) partly overlies the data of the background sediments (Scaglia and turbidites). However, the mean velocities of the two groups show a clear impedance contrast. The irregular geometries of the megabreccias, particularly the cut and fill structures at the base of the breccias, were also used in defining the layer geometries in the model.

Layers of Supersequence 2 (#23-30)

The Orfento Formation (Supersequence 2, Figure 39) forms a unit that is very difficult to incorporate in an impedance model. The dominant interparticle porosity

results in extremely low velocities. Rapid dissolution of the aragonitic part of the rudist shells, which probably occurred in the marine environment (Mutti, 1995), resulted in rocks exclusively composed of well-sorted calcitic rudist fragments and having a low diagenetic potential. Despite the generally low average velocities, the overall range of velocities in this unit is still high (3100 to 5800 m/s). No general pattern of impedance distribution can be recognized in the measured samples, although the breccias have a slightly higher average velocity than the other samples (Figure 46 d). The calcarenite samples on the platform show velocity values similar to those of the lithologies that onlap the escarpment. The extremely low values (slightly above 3000 m/s) are limited to the distal, homogeneous, and fine-grained part of the slope.

The model represents, therefore, only an estimate of the general impedance distribution in this stratigraphic unit. In the model, four breccias form sigmoidal units with relatively high velocities. They represent the breccia units close to the platform edge (Figure 42). The remaining rocks were modeled with four layers with impedances that range between the measured values of the analyzed samples (Figure 46 d). One layer reaches the top of the platform (Figure 42, layer #25). It covers the platform and forms an extreme impedance contrast with the underlying platform sediments. This contact of the Orfento Formation with the Upper Cretaceous platform, either on top of the platform or along the surfaces of the escarpment, can be seen in the field and marks the most distinct impedance contrast throughout the whole section.

Layers of Supersequence 3 (#21-22)

The slope sediments of Supersequence 3 comprise alternations of pelagic limestones (Scaglia), turbidites and breccias, similar to the slope parts of Supersequences 4 and 5. Figure 46 e shows that the velocity-density pairs of the sediments of these three sequences overlap and that there is no unique impedance distribution that correlates with the sediment type. However, the average velocity of the breccias is higher than that of the turbidites. The Scaglia samples have the lowest average velocity. In this case, average velocity can be correlated directly with the grain size.

Above the platform, Supersequence 3 is composed of massive breccias that cover the Orfento Formation and produce a high impedance contrast, because the breccias are significantly faster (5790 m/s) than the underlying rudist sands (4700 m/s). Since Supersequence 3 is thinner on the slope than the overlying two supersequences, it was modeled with only two layers: (1) a breccia layer, which has a discontinuous geometry from the platform to the basin; and (2) a Scaglia layer, which overlies the breccia.

Layers of Supersequence 4 (#16-20)

Supersequence 4 is found as an onlapping wedge on the lower slope and as a thin interval on the platform. The slope section was modeled with a succession of two breccia layers and interbedded Scaglia and turbidite layers. Supersequences 3-5 consist of similar rocks and therefore the impedance values were taken from slope samples of these three slope sequences (Figure 46 e). For the thin breccia and Alveoline limestone layers (Vecsei, 1991) on top of the platform, only one model layer was employed with an impedance equal to the average breccia value.

Layers of Supersequence 5 (#8-15)

The velocities of the prograding reef and the patch-reefs of Supersequence 5 lie between 5300 and 6100 m/s. They are significantly higher than the velocities of the underlying and overlying sands, which only reach velocities between 4100 and 4800 m/s. The two groups form separate clusters in the porosity-velocity diagram that do not overlap (Figure 46 f). The fact that the velocities of the reefs are higher than those of the sands, which have equal porosities and densities, reflects the frame-like fabric and the intra-frame porosity of the reefal rocks. The characteristic geometries and distribution of patch-reefs in the field (Figure 40 b) are represented in the model by five patch-reefs of different size, including the most basinward reef at Monte Rapina (Vecsei, 1991).

In the basin, Supersequence 5 consists of alternations of breccias, turbidites and Scaglia much like Supersequences 3 and 4. It is modeled by a succession of six layers. To simplify the model, the layer with the patch-reefs extends into the basin, where it reappears as breccia at the base of the sequence (Figure 42). This is possible because the average velocity of the breccias (5930 m/s) is very similar to the average velocity of the reefal sediments (5620 m/s). The graphic connection between the reefs and the breccia (Figure 42) is a zero-thickness layer that in fact separates two layers of equal impedance, which has therefore no seismic effect.

Layers of Supersequence 6 (#3-7)

The Lithothamnium Limestone and the twofold succession of bryozoan limestone and hemipelagic beds in Supersequence 6 make up five prominent units. These successions are represented by five layers in the seismic model. The bryozoan limestones have high velocities (5500-6100 m/s) that are significantly higher than those of the hemipelagic beds (4300-4900 m/s). Both units have small scatters in the velocity-porosity diagram (Figure 46 g) and can thus be modeled by reliable impedance values. The overlying Lithotamnium Limestone shows a wider range of velocities between 3300 and 5400 m/s and, therefore, cannot be modeled with equal confidence.

In the distal parts of the basin, where the layers overlie the slope sediments of Supersequence 5, the total thickness of Supersequence 6 amounts to 160 m. The two hemipelagic layers wedge out towards the platform, so that the two bryozoan limestones are in direct contact with each other in the proximal areas. Since Supersequence 6 is very thin or eroded on top of the prograding reefs of Supersequence 5, it is not well known in which extent Supersequence 6 was deposited over the former platform (Vecsei, 1991, Sanders, 1994). As a consequence, the two bryozoan limestones show, in the field and in the model, an onlap geometry in front of the slope and prograding reefs of Supersequence 5 (Figure 42).

The only layer above Supersequence 6 (layer #2) is a unit of Messinian evaporites that belongs to an overlying, younger supersequence (Vecsei, 1991). No petrophysical analyses were performed on evaporitic samples - the impedance value for this layer is taken from the average value for anhydrite (Gardner et al., 1974).

The top of the model is an arbitrary layer (#1) that only defines the zero timeline of the synthetic section and has no geological significance. The impedance value for this layer is taken to be the average value of all measured samples.

Synthetic Seismic Sections

The synthetic seismic sections are displayed in Figures 47-50. The impedance model, 14 km in width and 1.5 km in depth, was covered by a virtual survey of 400 shot points that are identical with 400 common mid-points (CMP's) and 400 receiver points. The resulting CMP distance equals 35 m, which is a reasonable value for true seismic lines. The time sample interval for all synthetic sections is 2 ms. All figures are displayed with all CMP traces and with two-way travel times between 0 and 0.6 s. Figure 44 shows a depth-to-time conversion of the impedance model, which is plotted at the same horizontal and vertical scale as the synthetic seismic section, so that it can be used directly to compare the geologic layers with their seismic responses.

The geological details that can be recognized on the seismic sections are discussed first, followed by an evaluation of the seismic reflection patterns, which define the geometries and terminations of the reflections. These two points are of particular interest because they influence directly sequence analyses, which will be performed on the synthetic seismic section.

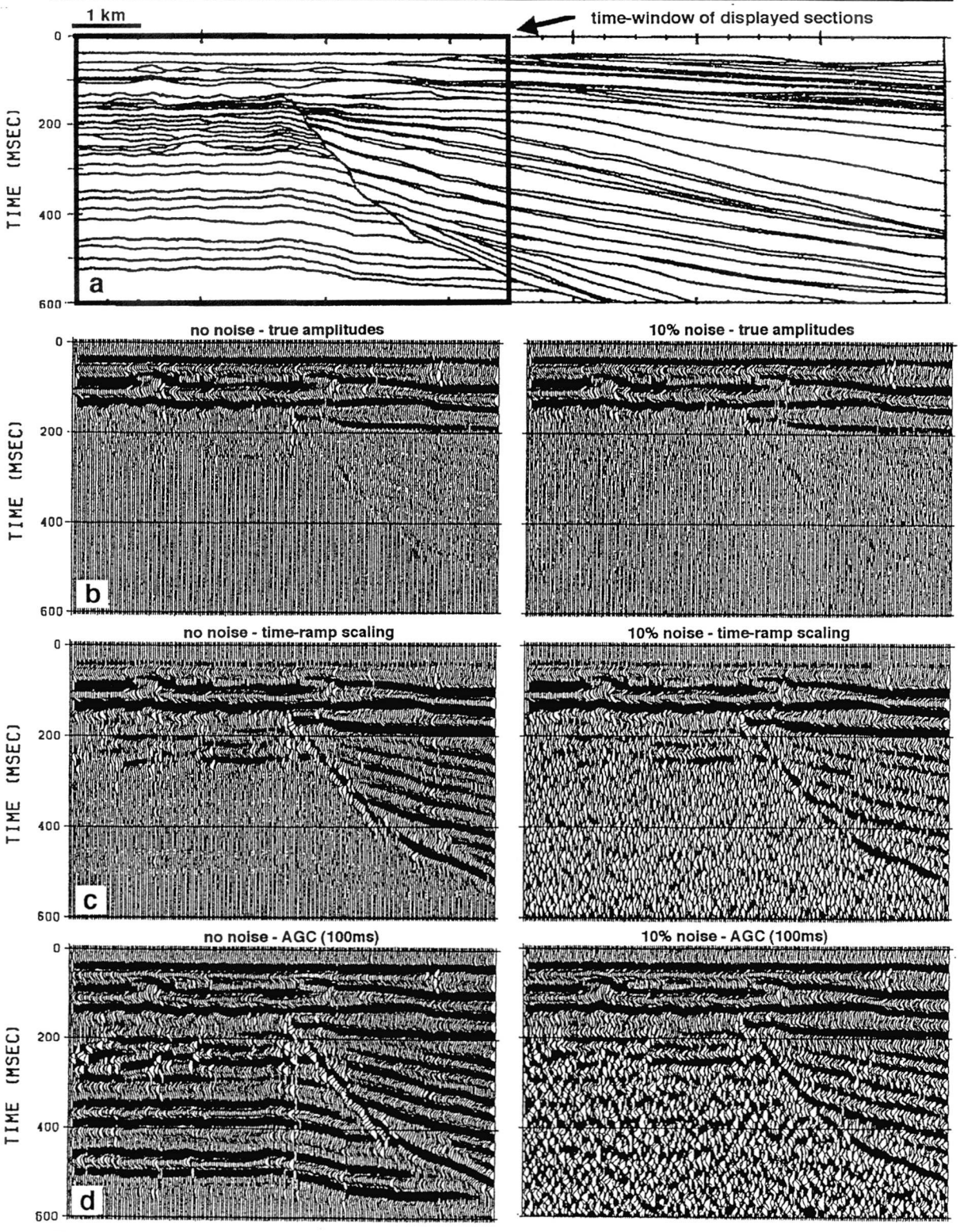

Figure 47: Comparison of different noise and amplitude gain options. **a)** Impedance model converted to time (as shown in Figure 44). The frame marks the displayed synthetic sections of Figures b-d. The sections on the left are the pure seismograms with no noise, whereas those on the right are disturbed by randomly added noise (10 % of average amplitude). **b)** True amplitude sections without amplitude gain. Both synthetic sections are similar, and only shallow reflections can be recognized. **c)** Sections with time-ramp scaling. The power function with an exponent of 1.2 results in a realistic image; the high-amplitude reflections on the slope are well displayed, whereas the Lower Cretaceous platform is relatively transparent, with or without added noise. The Upper Cretaceous platform shows some internal structure (rudist biostromes). **d)** Sections with applied automatic gain control (AGC) of 100 ms. The AGC keeps the total amplitude within a time window constant. Without noise, the extremely low impedance contrasts of the Lower Cretaceous platform (R=+/- 0.016) are amplified distorting the seismic image. All amplitudes are equalized, so that amplitude information is lost.

Seismic Imaging of Geologic Features

Two of the most important factors for the recognition of a geologic feature on a seismic section are: (1) the contrast of acoustic impedance relative to the surrounding rocks, and (2) the vertical and lateral extent of the geologic element. These two factors determine together with the processing and display parameters (amplitude gain, signal-to-noise ratio, frequency) which parts of the rock record are imaged on a seismic section.

Required Impedance Contrast

Recognition of a reflection through the noise requires a certain amplitude level. Patterns of reflections with high coherency may be recognized at lower amplitudes than reflections with low coherency. It was shown earlier that the variation of velocity in the modeled layers is remarkably high. This variability causes the carbonates to have impedance contrasts between the individual layers that result in high reflection coefficients with an average value of approximately 0.1 (Table 3). Jones and Nur (1982) assume that a reflection coefficient higher than +/-0.05 causes a reflection with an amplitude that can be seen on most seismic sections. Modern seismic techniques with high signal-to-noise ratios might even image layer boundaries with a coefficient of only +/-0.02 (A. Green, pers. comm.). Most layers in the Maiella model have reflection coefficients that are far higher than required (Table 3), so they should be imaged on the synthetic sections.

However, some layers do not have sufficiently high impedance contrasts to create reflections. For example, the Lower Cretaceous platform section shows a succession of layers with velocity values that vary between 6250 and 6400 m/s, resulting in reflection coefficients of +/-0.016. These low impedance contrasts and reflection coefficients cause reflections with very low energy. As a consequence, the layers cannot be detected when noise is present on the synthetic sections. The result is a seismically transparent Lower Cretaceous platform (Figures 47 b, c), which demonstrates how layers with considerable vertical and lateral extent may not be resolved on a seismic section due to insignificant contrast in acoustic impedance. A modeling procedure without added noise and with an applied automatic gain control would have distorted the seismic image by showing a platform with high seismic reflectivity (Figure 47 d). In contrast to the often made assumption, that added noise does not contribute more insight into seismic modeling (Stafleu et al., 1994), this comparison shows, that artificial noise is useful to investigate the significance and the pattern of low-amplitude reflection events.

Horizontal and Vertical Resolution

The limit of vertical resolution is determined by the wavelength, which is a function of velocity and frequency (wavelength = velocity / frequency). Every layer produces at its top and base reflections, which may be superimposed to create the resulting signal. Reflections from the top and base of a layer may have opposite polarities resulting in destructive interference if the layer has a thickness of less than a quarter wavelength (Sheriff, 1977, 1985). A layer thicker than a quarter wavelength produces two reflections that interfere to two separate and thus detectable signals on a seismic section. Table 4 displays the limits of resolution for the different frequencies used and for two examples of sonic velocity.

frequency	v = 4 km/s		v = 6 km/s	
(Hz)	wavelength	wavelength/4	wavelength	wavelength/4
20	200	50	300	75
30	133	33	200	50
40	100	25	150	38
50	80	20	120	30
60	67	17	100	25

Table 4: Wavelength of an acoustic signal at frequencies used and at velocities of 4000 and 6000 m/s. The limits of vertical seismic resolution are taken to equal a quarter of the wavelength (Sheriff, 1977, 1985). Any layer that is significantly thinner than a quarter wavelength produces at its top and base reflections that destructively interfere and cannot be resolved seismically.

Horizontal resolution on unmigrated sections is limited by the Fresnel zone (Sheriff, 1977, 1985). The Fresnel zone is the circular part of a reflector from which all reflected energy arrives at the surface within a half wavelength and is therefore in constructive interference. The size of the Fresnel zone is dependent on (1) frequency, (2) depth of reflector, and (3) velocity of the layers. For a two-way travel time of 0.5 s, a frequency of 40 Hz, and a velocity of 4000m/s, the diameter of the Fresnel zone is approximately 220 meters. Elements that are smaller than this value may still be recognized on a seismic section but by a diffraction rather than by a reflection. On migrated sections, horizontal resolution is more limited by other factors, such as noise and spatial sampling, than by the diameter of the Fresnel zones (Sheriff, 1985). For the model used in this study, most layers have lateral extents that are far larger than the Fresnel zones. Only the patch-reefs have widths that are close or below the size of the Fresnel zones. However, the method of normal incidence raytracing does not simulate

the effects of Fresnel zones. The main limiting factor of horizontal resolution in this study is the spacing of the detectors, which equals 35 m in most used sections. A layer with little horizontal extent nevertheless produces a reflected signal when it is "hit" at a normal angle by a synthetic ray that arrives at the surface within the capture radius of a virtual geophone.

Because most of the modeled layers are characterized by thicknesses close to or below the seismic resolution and by widths that are considerably larger than the geophone spacing, the vertical resolution in this study is much more critical than the horizontal one. In reality, however, a rock section is made up of a countless number of physical layers, which also have a wider lateral extent than vertical thicknesses, resulting in a reflection pattern that is a product of interference from several thin layers.

Seismic Image of Platform Escarpment

Despite its irregular and steeply dipping geometry, the platform escarpment is imaged clearly on all resulting synthetic sections (Figures 48-50). Regardless of the chosen frequency, polarity, or gain, the escarpment produces its own reflection and is also recognized by the termination of onlapping slope reflections. It separates high-velocity platform rocks from lower-velocity slope sediments and is thus characterized by a high-amplitude reflection on the positive polarity plot (Figures 48 a-e). Because of the nature of the zero-phase Ricker wavelet (Figure 38), the reflection from the escarpment forms a trough bounded by two low-amplitude reflections on the negative polarity plot (Figures 50 b, d).

The raytracing of all reflections from the escarpment is shown in Figure 51. A CMP spacing of 60 m was chosen for this plot, so that the individual rays may be distinguished. For the synthetic seismic sections of Figures 48-50, the CMP spacing was 35 m, i.e. more rays are actually used for calculation of the synthetic sections than are displayed in Figure 51. This plot, which shows true angles, shows that most of the escarpment is imaged by rays that have angles of incidence between 10 and 45 degrees to the vertical. The irregular surface produces bundling and divergence effects, in particular at concave and convex niches in the platform wall. In reality, the escarpment is likely to be the origin of numerous diffractions, which are not simulated properly with the *QUIK*™ program. The oblique nature of the ray paths results in a relatively large offset between the position of the escarpment on the unmigrated seismic section and its true position (Figure 48 a-e). The true position of the escarpment in the two-way travel time plot (Figure 44) is calculated using a vertical depth-time conversion of the individual layers and, unlike on the synthetic sections, represents a perfectly migrated section. In reality, correct migration of such a setting would be rather difficult, because the relief of

the steep escarpment is quite complicated. It is a steep discontinuous surface that separates horizontal to gently dipping beds which are imaged close to their true positions on both migrated and unmigrated sections. However, the offset between the reflection of the escarpment and its true position does not change the general picture and is not a major source of error in seismic interpretations.

---

on following pages:

Figure 48 a: Impedance model plotted in two-way time and displayed at the same scale as the synthetic seismic sections in Figures b-f. For identification of individual layers in the model see Figure 42, 44, and Table 3. Unlike with normal incidence raytracing, the depth-time conversion of the model does not consider dipping layers. The plotted model represents thus a migrated section. This plot can be used to identify reflection events on the synthetic sections. **b-f:** Synthetic seismic sections of impedance model shown in Figure a, at dominant frequencies of 20 to 60 Hz. The modeling was performed with a zero-phase Ricker wavelet (Figure 38) using the normal incidence raytracing method (Figure 37). A time ramp power function with an exponent of 1.2 was used as the amplitude gain. No automatic gain control was applied, and the sections are displayed with positive polarity. For seismic interpretation see text and Figures 49 and 52.

Figure 49 a: Impedance model plotted in two-way time and displayed at the same scale as the synthetic seismic sections in Figures b-f. For identification of individual layers in the model see Figure 42, 44, and Table 3. This plot can be used to identify reflection events on the synthetic sections. **b-f:** Interpreted synthetic seismic sections of the impedance model shown in Figure a, at dominant frequencies of 20 to 60 Hz. Uninterpreted sections are shown in Figures 48 b-f. The red lines mark interpreted seismic sequence boundaries, which were mapped by tracing reflection terminations and resulting unconformities on the synthetic sections. The line drawings of Figures 52 b-f show the characteristics of the reflection terminations and the interpreted unconformities.

Figure 50: Comparison of synthetic seismic sections with different polarities (positive and negative). **a:** Synthetic seismic section with a dominant frequency of 20 Hz and positive polarity (shown in Figures 48 b and 49 b). **b:** Same section as in Figure a, but displayed with negative polarity. **c:** Synthetic seismic section with a dominant frequency of 40 Hz and positive polarity (shown in Figures 48 d and 49 d). **d:** Same section as in Figure c, but displayed with negative polarity. A switch in polarity does not only change the black-white pattern, but it can also change the characteristics of the unconformities, because reflection terminations are recognized more easily with reflections forming a black peak than a white trough.

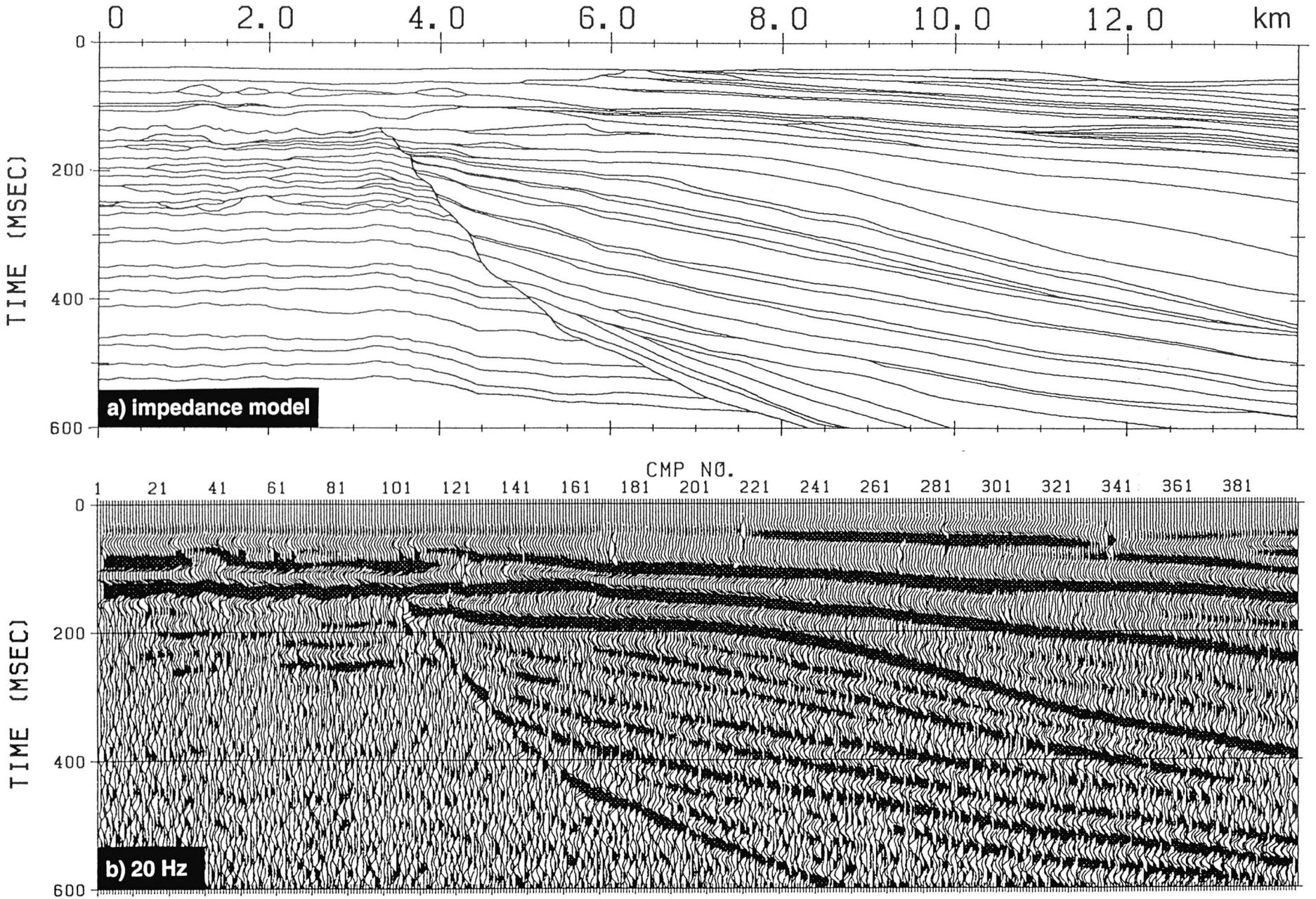

Figures 48 a-b

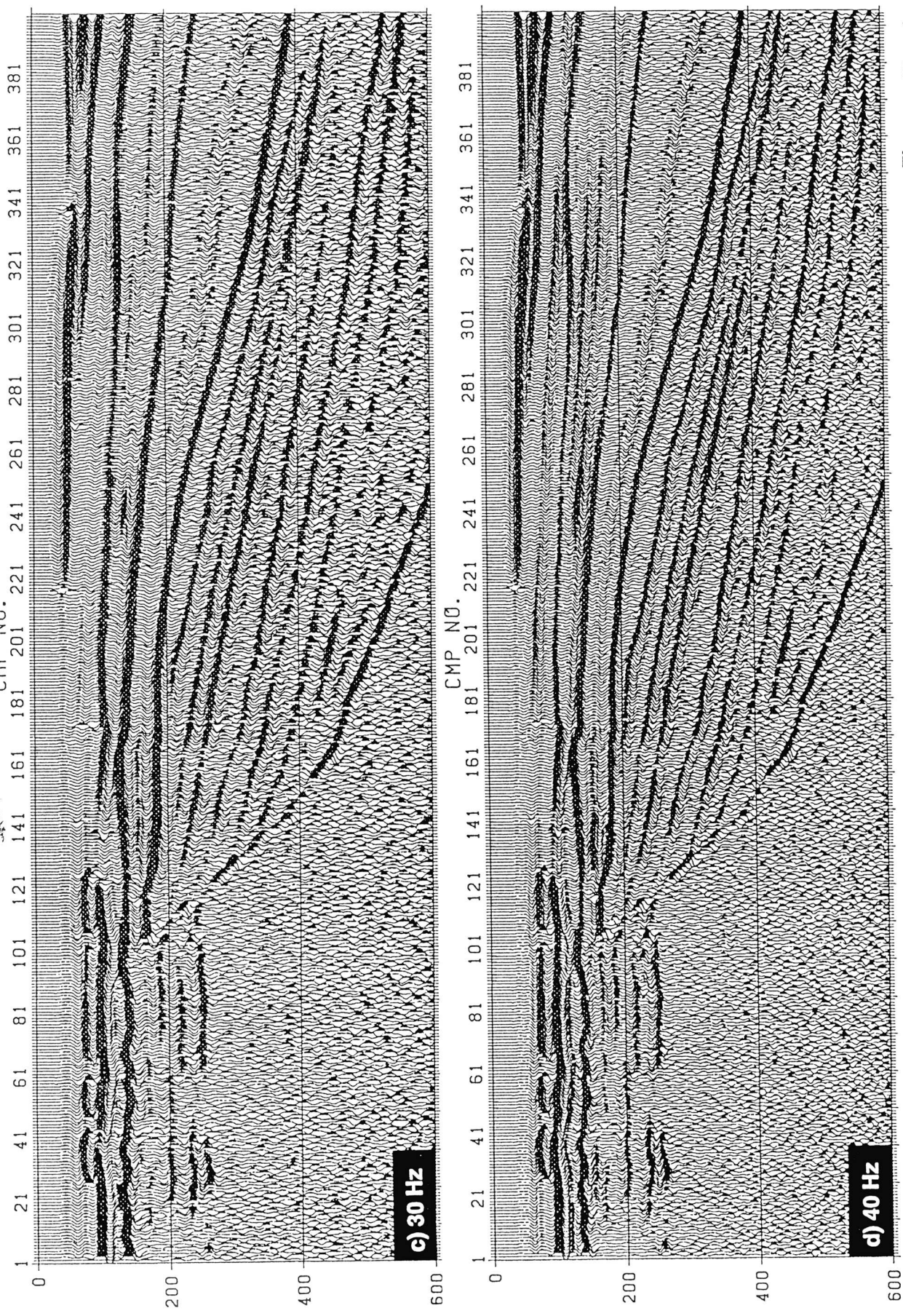

Figures 48 c-d

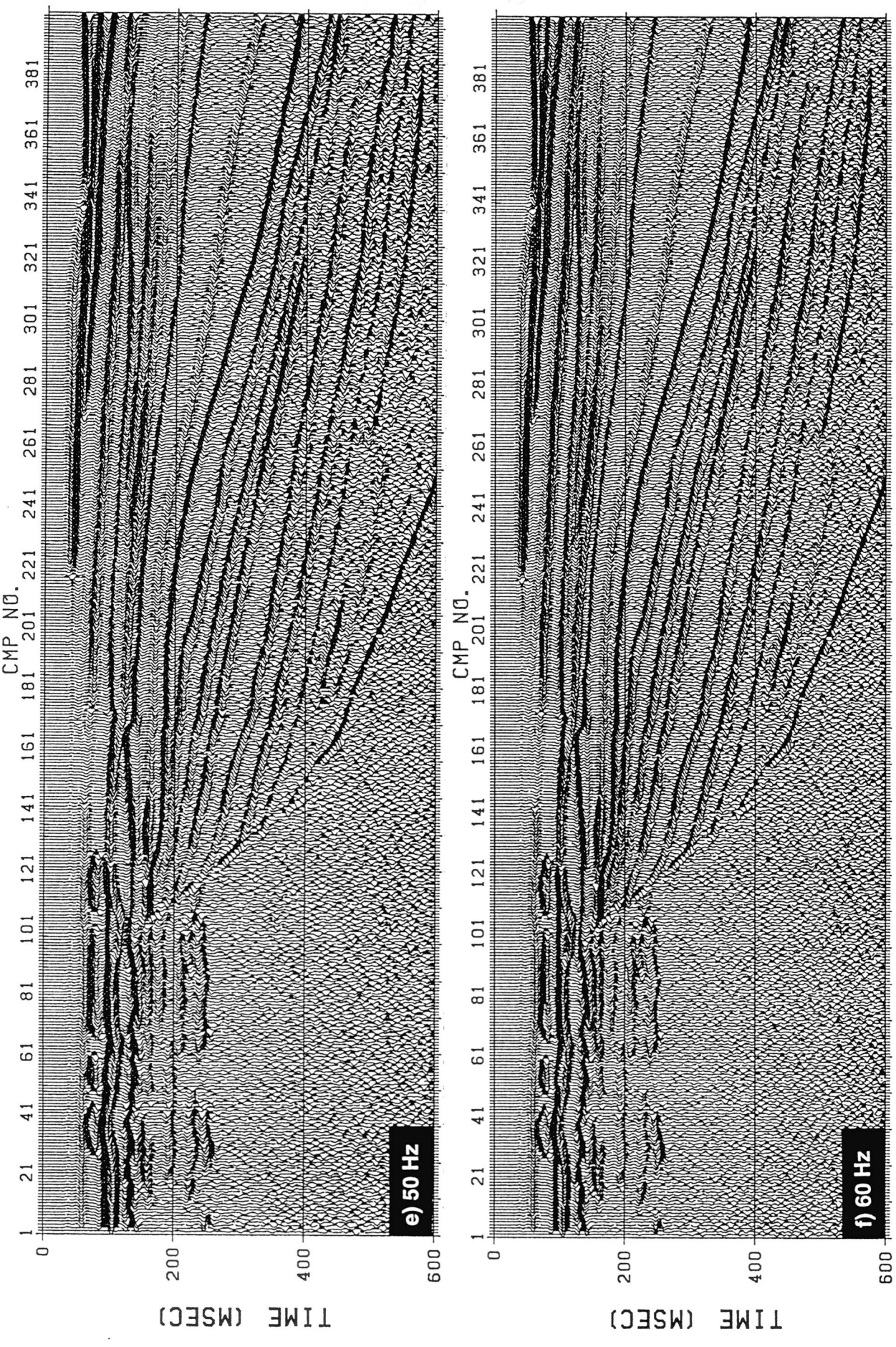

Figures 48 e-f

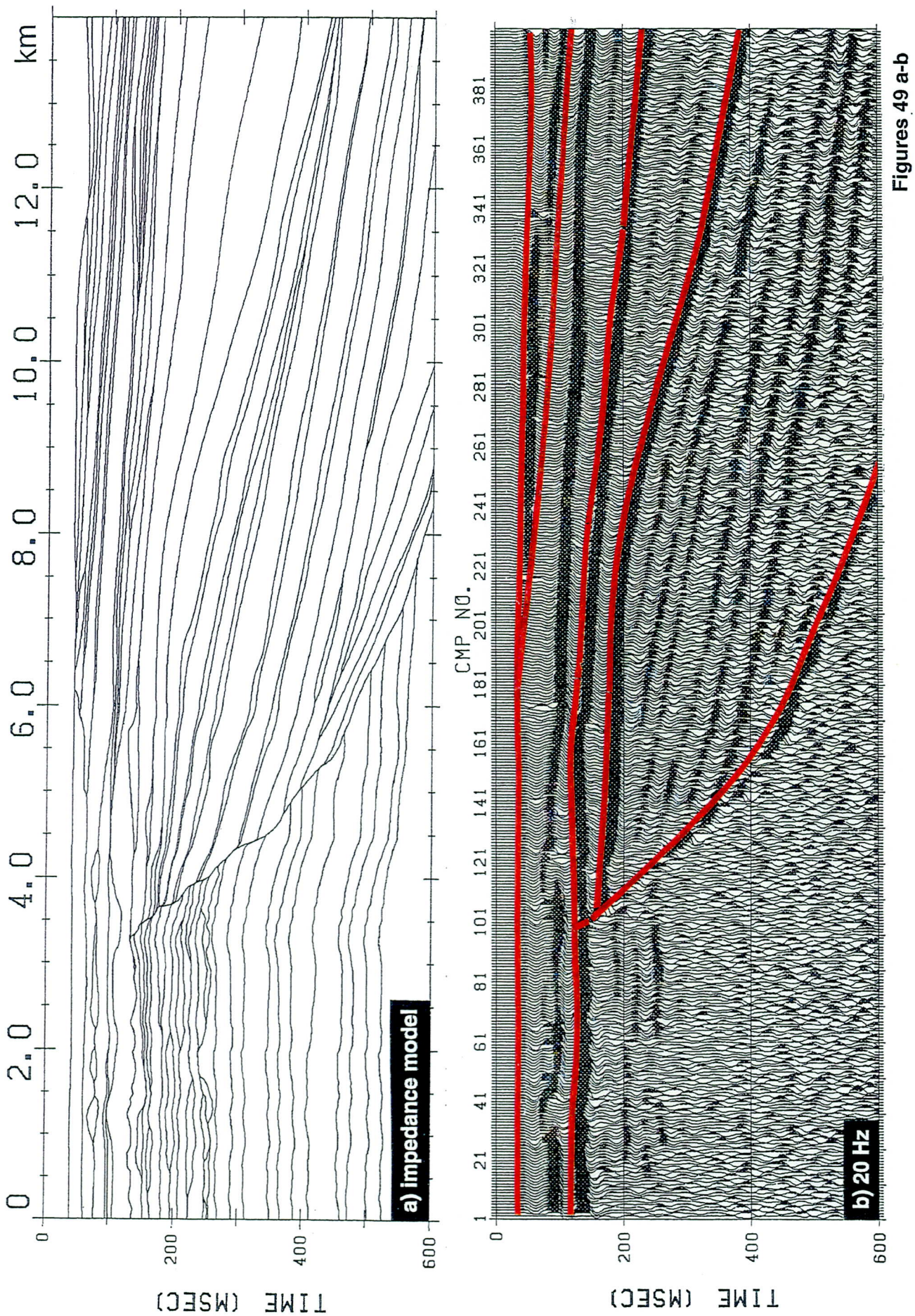

Figures 49 a-b

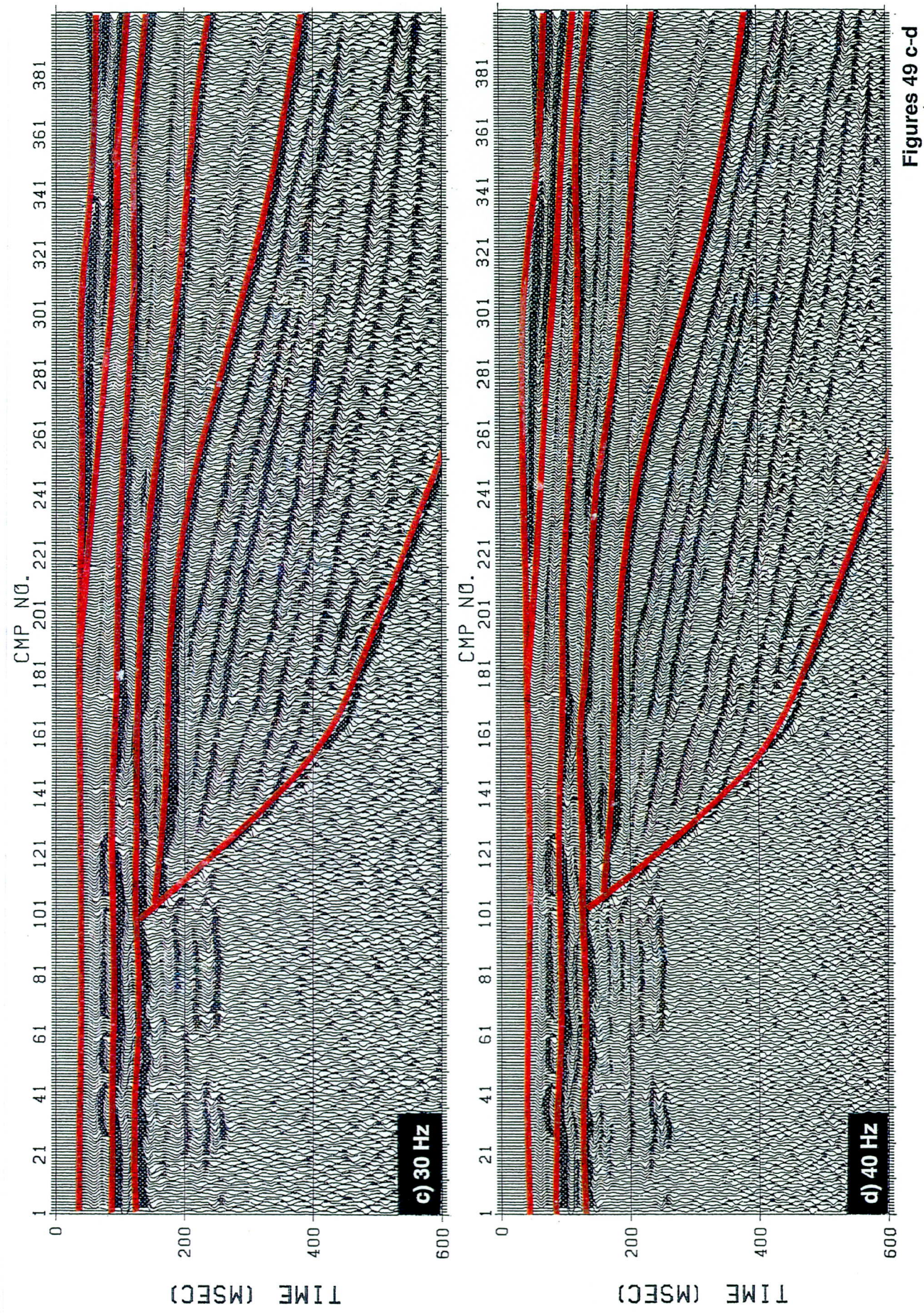

Figures 49 c-d

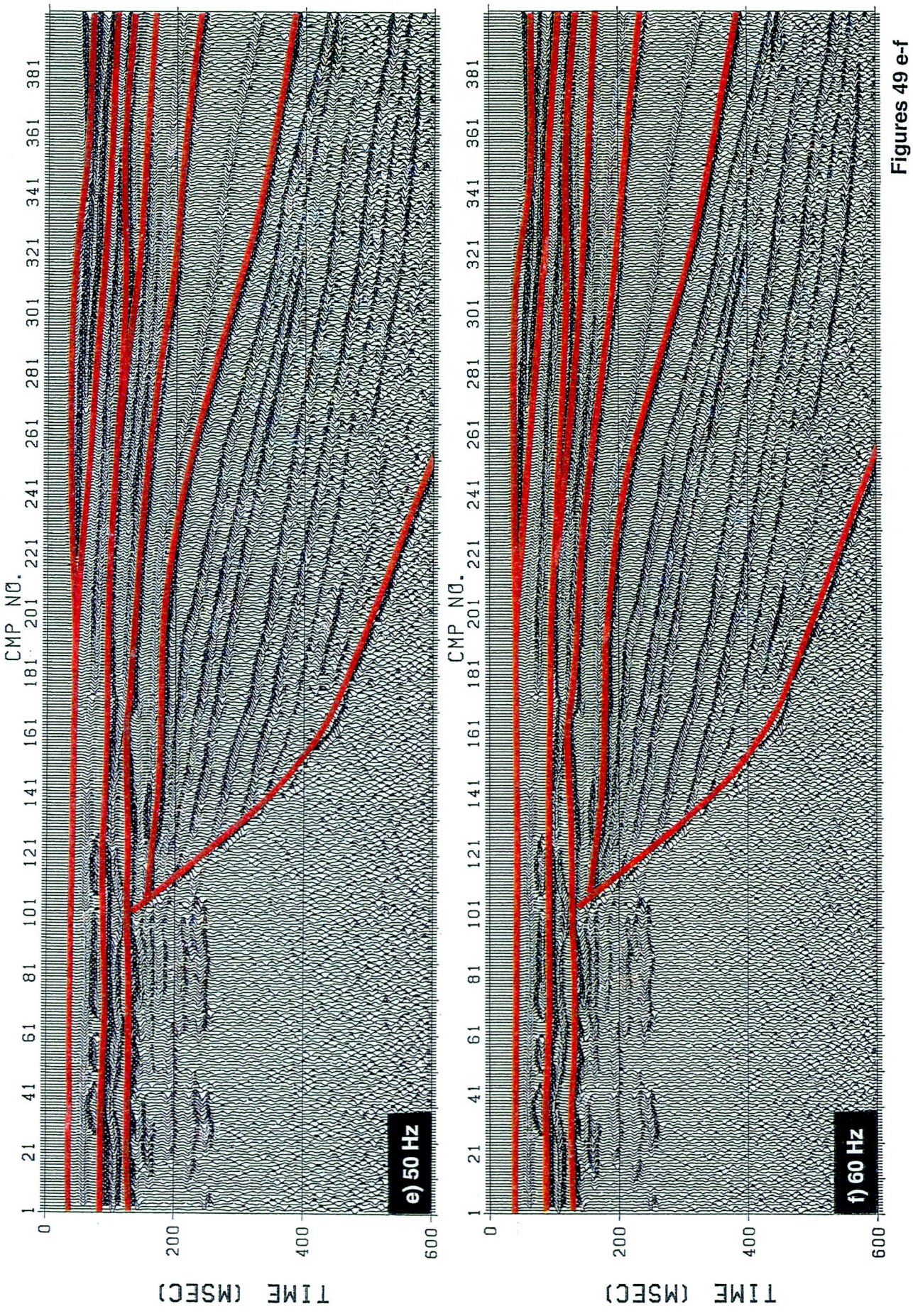

Figures 49 e-f

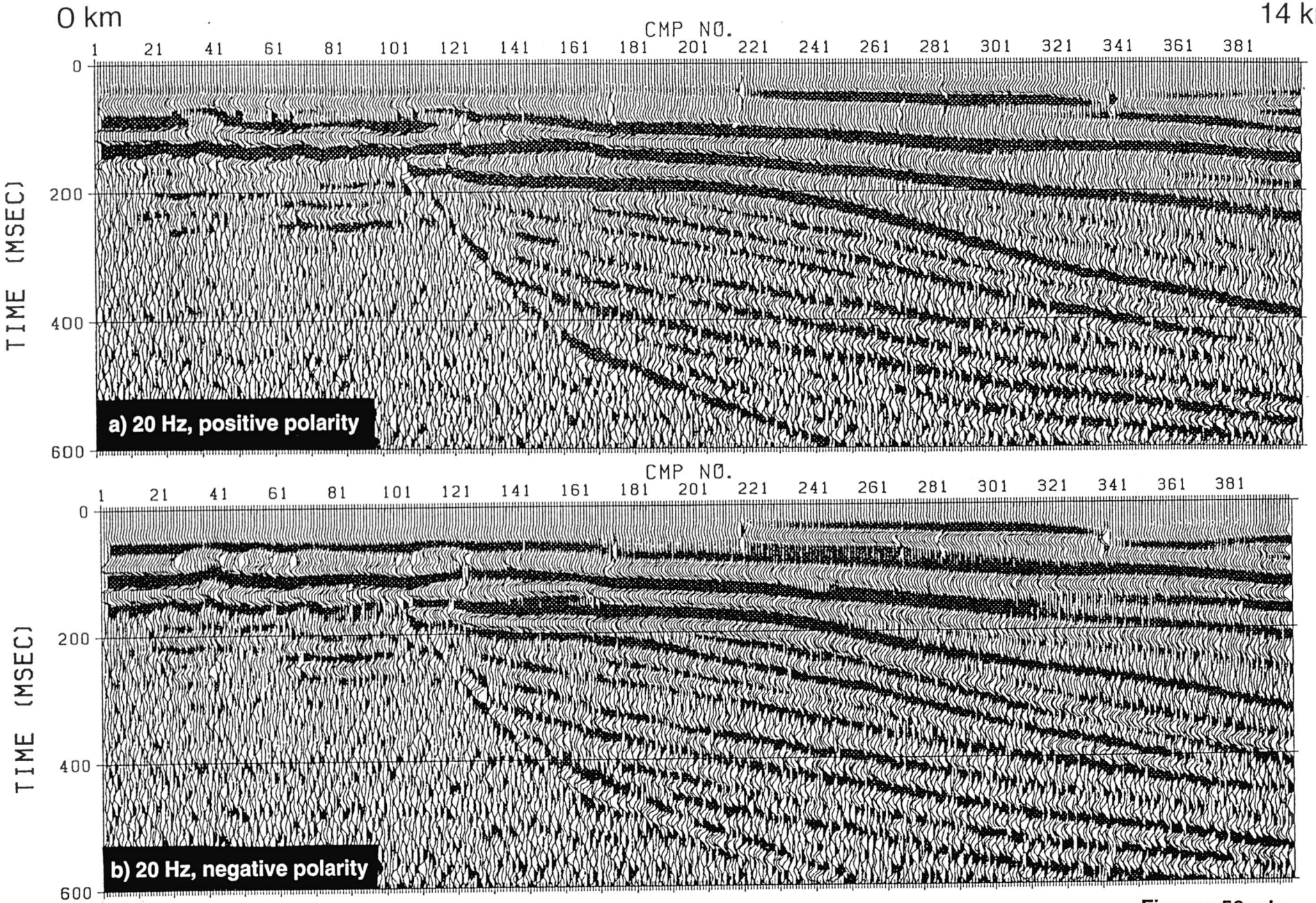

Figures 50 a-b

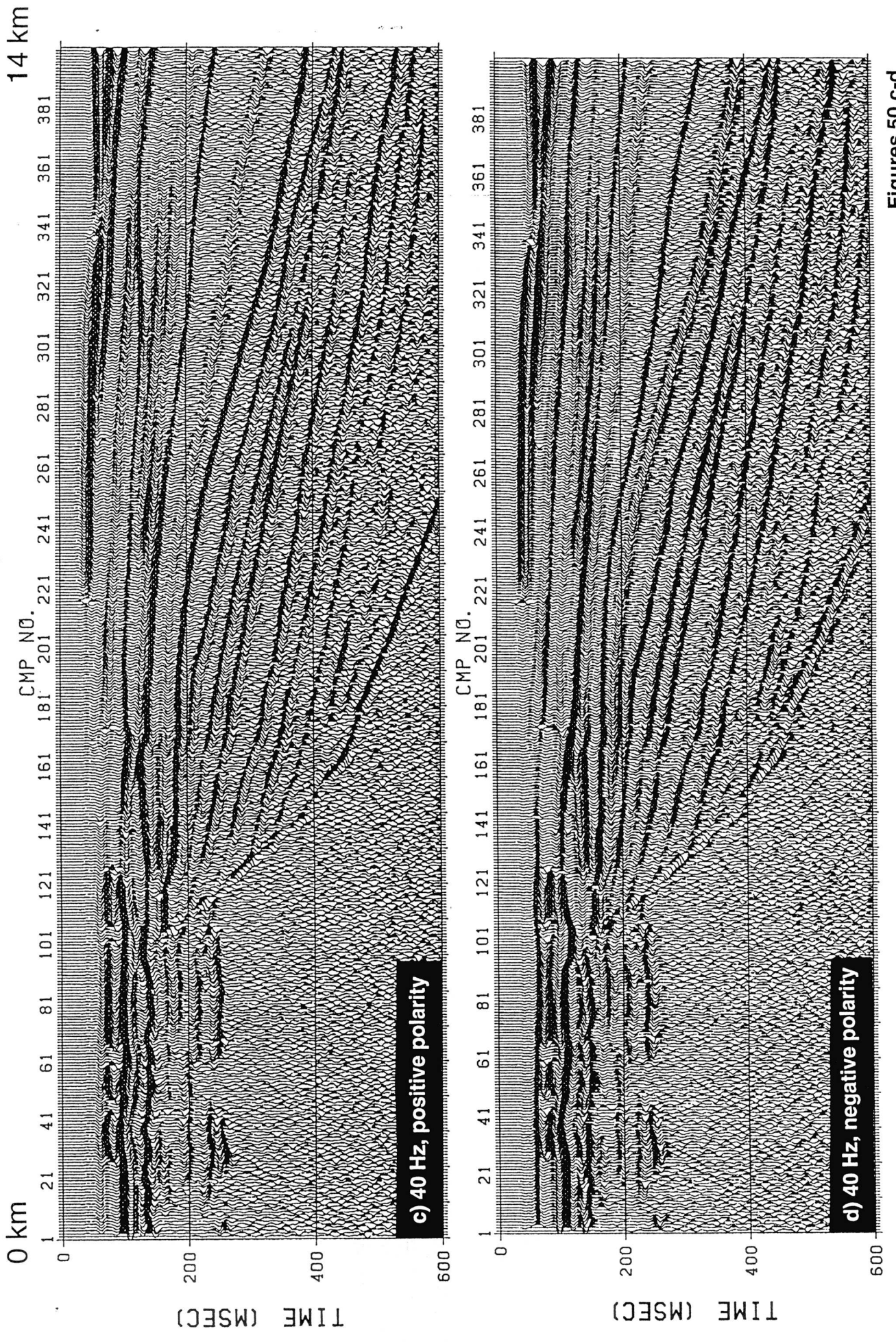

Figures 50 c-d

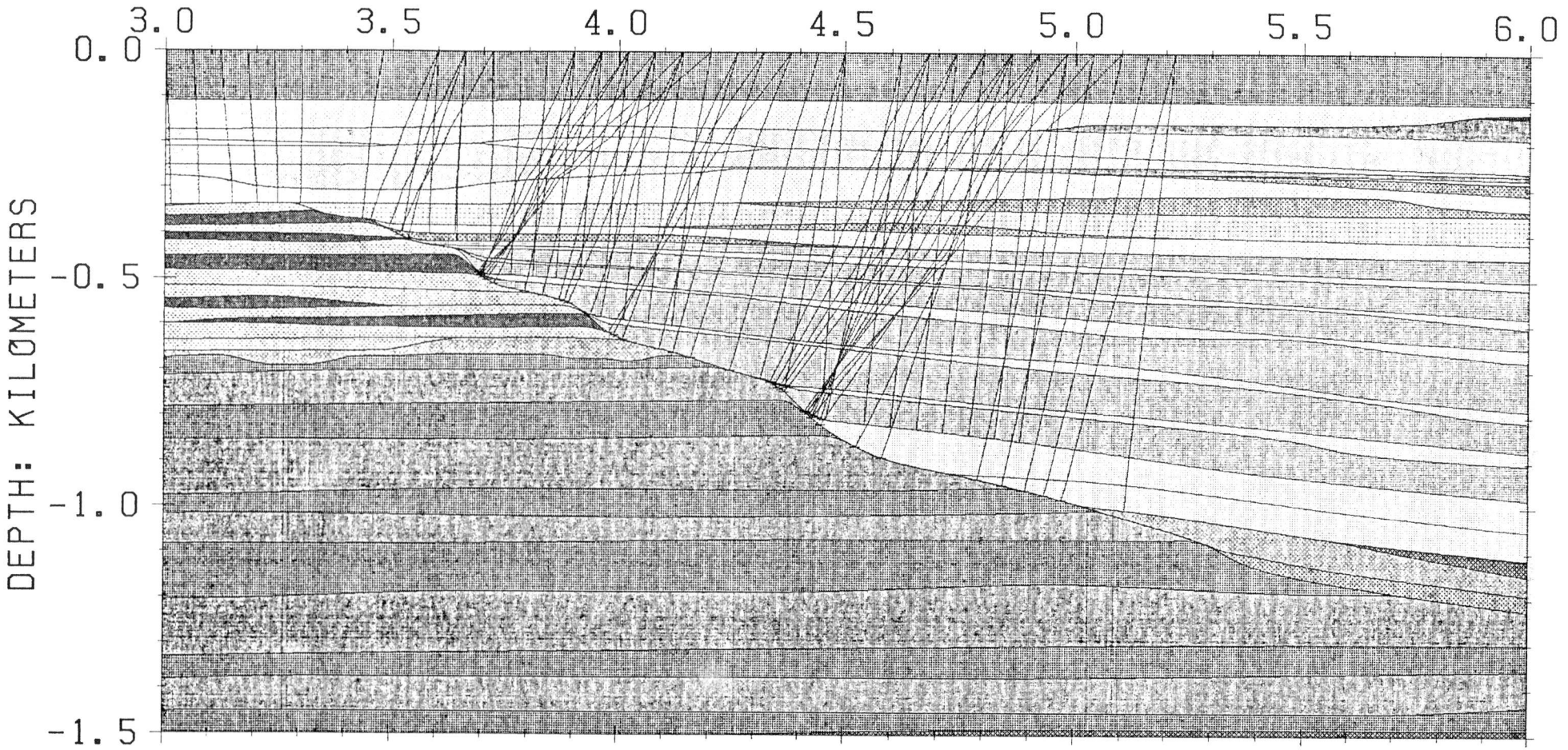

Figure 51: Raytracing of reflections originating from the platform escarpment. The displayed part of the impedance model is not vertically exaggerated, and shows true angles. The rays are calculated by the normal incidence raytracing method, which only considers rays that arrive with a normal angle on the target surface (Figure 37). Downgoing and upcoming ray are thus identical. Due to the limited display options of the program, some rays, which originate from other interfaces than the escarpment, had to be included in the plot. To separate individual rays, a CMP spacing of 60 m was chosen, which is higher than the spacing of the synthetic section (35 m). Therefore, not all rays are displayed that are relevant for calculated synthetic sections. The irregular surface of the escarpment has an average dip of 30 degrees. It forms some niches which are steeper and which are the result of erosion and collapse processes along the platform wall. These convex and concave structures result in bundling and divergence of the rays. The raytracing demonstrates that most of the escarpment is imaged with seismic rays, even if some rays have angles of 45 degrees to the vertical.

Seismic Image of Cretaceous Platform and "mid"-Cretaceous Unconformity

The top of the platform, which is overlain by the low-velocity Orfento Formation (Calcari Cristallini), forms a major contrast in acoustic impedance. This contact yields a high amplitude reflection on the synthetic sections. The modeled karstic nature of this contact is visible on the seismic section by a wavy, but still continuous reflection (Figures 48 b-f, CMP#1-100/0.15s). Across this surface, very little acoustic energy penetrates to the underlying layers of platform rocks, because the high impedance contrast results in most of the energy being reflected back to the surface.

Compared with the seismic facies of the slope, the platform has only a moderate seismic reflectivity and is imaged by low-amplitude reflections that barely exceed the noise levels. The Upper Cretaceous platform, which has little higher impedance contrasts due to the rudist biostromes, produces some low-coherent reflections that are partly visible through the randomly generated noise. The "mid"-Cretaceous unconformity, marked by pockets of low-velocity rocks, is also imaged by non-continuous reflections that have a reflection pattern similar to that of the biostromes above (Figure 48 b, CMP#1100/0.25 s). At low frequencies, the "mid"-Cretaceous unconformity cannot be distinguished from the biostromes. At dominant frequencies above 40 Hz, the reflection from this unconformity has a significantly higher amplitude than reflections from the rudist biostromes (Figures 48 e-f, CMP#1100/0.25 s) and can therefore be recognized.

The angular unconformity between the Upper Cretaceous and the Lower Cretaceous Platform rocks (Sanders, 1994) cannot be recognized on the seismic sections, because the Lower Cretaceous rocks do not produce reflections that have a high enough amplitude to be seen through the added noise. The extremely small impedance-contrasts in the Lower Cretaceous platform result, therefore, in seismic transparency. For instance, the synthetic sections with added noise do not image the layering of the Lower Cretaceous platform carbonates. This layering is only imaged with reflections if no noise is added *and* if an automatic gain control (AGC) with a small time-window (less than 100 ms) is applied to the data (Figures 47 c, d).

The transparent seismic facies of the platform with only few low-coherent reflections correlates well with the seismic facies of platforms on observed seismic lines across the Bahamian platform margins (Figures 54, 55 b) or across the Apulian platform margin (de Alteriis and Aiello, 1993, Figure 56).

Seismic Image of Slope Carbonates

Unlike the platform carbonates, the slope deposits show excellent reflectivity on the seismic sections due to their wide range of acoustic impedance. This is seen clearly on

the modeled synthetic sections, where the slope reflections onlap the transparent core of the platform (Figures 48 a-e).

Measurements of physical properties show that breccias have significantly higher impedances than the pelagic background sediments and turbidites. The resulting synthetic sections image these breccias because their thicknesses and lateral distribution are above the limits of seismic resolution. The unconformities, which are observed in the modeled slope sequences are not necessarily real, since several "pseudo"-unconformities (Schlager et al., 1991; Biddle et al., 1992) are created when breccia beds or intercalated background sediments thin below seismic resolution.

One of the most important characteristics of the seismic image is that the major slope breccias are thick enough and have sufficient impedance contrasts to be imaged. In fact, these breccias control the reflection pattern. This is in accordance with real seismic lines, which show that slope carbonates have similar reflectivity as the modeled synthetic sections.

Seismic Image of Prograding Reefs and Patch-Reefs

Using a signal with a dominant frequency of 20 Hz and a positive polarity plot, only two of the four modeled patch-reefs are recognized clearly on the synthetic seismic section (Figure 48 a, CMP#40+120/0.1 s). With negative polarity (Figure 50 b), the reflection at the top of the reefs is hardly distinguishable from reflections of the breccias that overly the platform below the patch-reefs. Using dominant 30 and 40 Hz signals (Figures 50 c, d), all reefs can be seen at both polarities - the vertical resolution allows the reefs to be imaged as separate reflections that do not overlap with the strong reflections from the underlying top of the platform. Increasing the dominant frequency does not change this pattern significantly. In contrast to the isolated patch-reefs above the platform (Figure 40 b), the most distal reef at Monte Rapina is not seen clearly on all the sections (Figures 40 b-f, CMP#200/0.05 s). This invisibility is mainly the result of the small thickness of the reef and its lower impedance contrast relative to the surrounding rocks.

Comparison of Sequence Stratigraphy in Outcrop and on Synthetic Sections

One of the goals of this seismic modeling study is to compare depositional sequences in outcrops with seismic sequences on synthetic seismic sections. The depositional supersequences that could be determined in the field, numbered 0 to 6, are the basis for the impedance model that is convolved with different wavelets. Sequence stratigraphic analysis have been performed on the resulting synthetic sections following

the procedure described by Mitchum and Vail (1977). The first step of such an analysis is to determine where reflections terminate or where two reflections merge into one. In the next step, unconformities are defined by the positions of these reflection terminations. These unconformities are examined in regards to their geometrical characteristics, i.e., surfaces of onlap, downlap, toplap, or truncation. On a seismic section, the presence of an unconformity was the only criteria to define a seismic sequence boundary .

The seismic sequence analyses were performed on the sections with the different input signals for both positive and negative polarities. The results are shown in Figures 49 a-e, 52 a-f, and are discussed in the following paragraphs.

Chronostratigraphic Significance of Reflections

An important assumption for applying the concept of seismic sequence stratigraphy is that seismic reflections do not cross stratigraphic time lines and have, therefore, chronostratigraphic significance (Vail et al., 1977b). Though other seismic modeling studies have indicated that this assumption is not automatically fulfilled (Tipper, 1993), a comparison of the Montagna della Maiella impedance model with the synthetic sections shows that no reflection cuts significantly the stratigraphic time lines. A violation of the assumption would be expected if the transition zone between two facies is shifted horizontally during a transgressive or regressive cycle. If the different facies have different acoustic impedances, the created reflection may follow the diachronous boundary between the lithofacies or it may represent the stratal pattern, depending on bed thicknesses and geometrical characteristics of the facies transition zone (Tipper, 1993). However, the Maiella model is characterized by layers that are laterally continuous and that terminate at a distinct unconformity (i.e. at the escarpment), rather than at a gradual transition zone.

The low-coherent to transparent seismic facies of platform deposits make it difficult to detect time lines on a seismic section. On all synthetic sections with varying frequencies and polarities, the platform cannot be separated into a Lower and a Upper Cretaceous part. That the upper part of the Upper Cretaceous platform belongs to the same sequence as part of the slope sediments that onlap the escarpment, can also not be detected. The relationship between the platform and slope cannot be resolved due to the lack of physical connections between the separated time-equivalent layers of the slope and platform - the onlap surface of the escarpment is interpreted as a seismic sequence boundary, even where it separates sediments belonging to the same supersequence (dashed line in Figure 52 a). This apparent seismic sequence boundary crosscuts time lines; however, this is not a result of the limits in resolution of the different wavelets, but is rather a problem with the geometry of the layers. A seismic interpreter who is aware

of the nature of platform escarpments will know that the seismic section provides no information as to how much the time lines are displaced across the unconformity of an escarpment. Except from this escarpment reflection, no diachronous reflection can be observed and the requirement of chronostratigraphic reflections is, in this case, fulfilled.

Effect of Frequency

The interpreted seismic sections with dominant frequencies of 20, 30, 40, 50 and 60 Hz and normal polarity are shown in Figures 49 a-e. Figures 52 a-f show a simplification of the interpretation that characterizes the observed seismic sequence boundaries.

At a frequency of 20 Hz and positive polarity, only five of the seven supersequences identified in the field are recognized on the synthetic section (Figures 49 a, 52 b). The oldest sequence that can be separated by seismic unconformities, is the Cretaceous platform core. Its apparent upper boundary is marked by the onlap of slope Supersequence 1 (Figure 49 b, CMP#100-250/0.15-0.6 s). The slope sequence represents the true depositional Supersequence 1 on the slope, whereas its platform equivalent cannot be separated from the Lower Cretaceous platform (see above). The lower boundary of the slope sequence is characterized by an onlap on the escarpment which is real, whereas at this low frequency its upper boundary is seen as a pseudo-toplap surface (Figure 49 b, CMP#150-220/0.2 s), that is neither part of the model nor observed in reality. These "pseudo"-surfaces are the result of layers that thin below the limits of seismic resolution so that the reflections appear to terminate far from the true termination of the layers (Schlager et al., 1991). In this case, the two uppermost megabreccias of Supersequence 1 merge towards the platform and become thinner, so that the reflections terminate far from the escarpment, though in reality, the thinned breccias form an onlap on the escarpment. The toplap unconformity is an artifact and is therefore called a pseudo-toplap.

The third seismic sequence that can be distinguished at 20 Hz is the equivalent of Supersequence 2 (Orfento Formation). The lower boundary of this seismic sequence is imaged by an onlap surface that is also a pseudo-unconformity. Supersequence 2 forms an overall wedge, such that the layer thicknesses reach the limits of resolution and their reflections terminate with an onlap geometry on top of the pseudo-surface of Supersequence 1 (Figure 49 b, CMP#220-340/0.2-0.3 s). The upper boundary of seismic sequence 2 is onlapped by the overlying sequence that is the equivalent of the three depositional Supersequences 3, 4 and 5. Though an onlap occurs in reality by wedging-out of some of the breccias, the surface appears too low on the profile and marks a horizon within the Orfento Formation (Figure 49 b, CMP#300-350/0.18-

0.22 s). This low horizon is an effect produced by the extremely low velocity of the Calcari Cristallini of the Orfento Formation, which form a negative impedance contrast that is displayed too low in the positive polarity section due to the reversed shape of the reflected signal. On the negative polarity plot the unconformity appears at its true location (Figures 50 b, d). The very thin platform equivalents of Supersequences 3 and 4 are not detected at 20 Hz because they are far below the vertical resolution at this frequency. In addition, they form layers that are conformable with the overlying and underlying beds.

The boundaries between depositional Supersequences 3,4 and 5 on the slope cannot be resolved using the 20 Hz signal, because they are too thin to produce a succession of reflections; the vertical resolution at 20 Hz lies between 50 and 75 meters (Table 4). The seismic sequence above sequences 3-5 onlaps the slope and matches well depositional Supersequence 6 (Figure 49 b, CMP#200-360/0.05-0.1 s). The onlap is real, being the onlap of bryozoan limestones and hemipelagic marls onto the underlying slope sediments. The succession of two high-velocity bryozoan limestones with the two interbedded low-velocity marls form a package with sufficient impedance contrast and layer thickness to be imaged with reflections and an associated unconformity at the lowest frequency (20 Hz).

With increasing frequencies the appearance of the lowest two sequences on the seismic sections does not change significantly (Figures 49 c-f). The pseudo-toplap at the upper boundary of slope sequence 1, however, becomes a true onlap: the pseudo-toplap terminations of the two upper megabreccias move from distal positions at low frequencies toward more proximal positions at the escarpment with increasing frequencies. At 60 Hz, both reflection terminations are true onlaps (Figure 49 f, CMP#110/0.17-1.2 s). This evolution demonstrates how increasing resolution at higher frequencies changes not only the existence, but also the type of a seismic unconformity.

Figure 52: Comparison of the depositional supersequences, which are the basis for the impedance model, with the seismic sequences, that are recognized on the synthetic seismic sections (Figures 49 b-f). **a:** Plot of the input impedance model with seven depositional supersequences. The depth model was converted to two-way travel time, and can thus be compared directly with the seismic line-drawings (Figures b-f). **b-f:** Seismic line-drawings derived from the synthetic seismic sections at positive polarity and different frequencies (Figures 48-49). The black arrows mark observed reflection terminations with their termination character (onlap, toplap, downlap, truncation). These terminations were used to constrain the seismic sequence analyses; unconformities define seismic sequence boundaries (bold lines), which can be compared with the depositional supersequences (Figure a). The "mid"-Cretaceous unconformity (Figure a, at 0.25 s) cannot be recognized on the synthetic sections, because the Upper Cretaceous platform is conformable with the Lower Cretaceous platform. The Upper Cretaceous platform and slope carbonates are not recognized as time-equivalent units, because they are separated by the onlap surface of the escarpment. At a frequency of 20 Hz, only five of the seven supersequences are recognized. The total number of recognized unconformities, and thus sequences, increases with increasing frequency. At 60 Hz, seven seismic sequences can be mapped. Especially at the low seismic frequencies, many observed unconformities are "pseudo"-unconformities, whose geometries are in error or are non-existent patterns in reality.

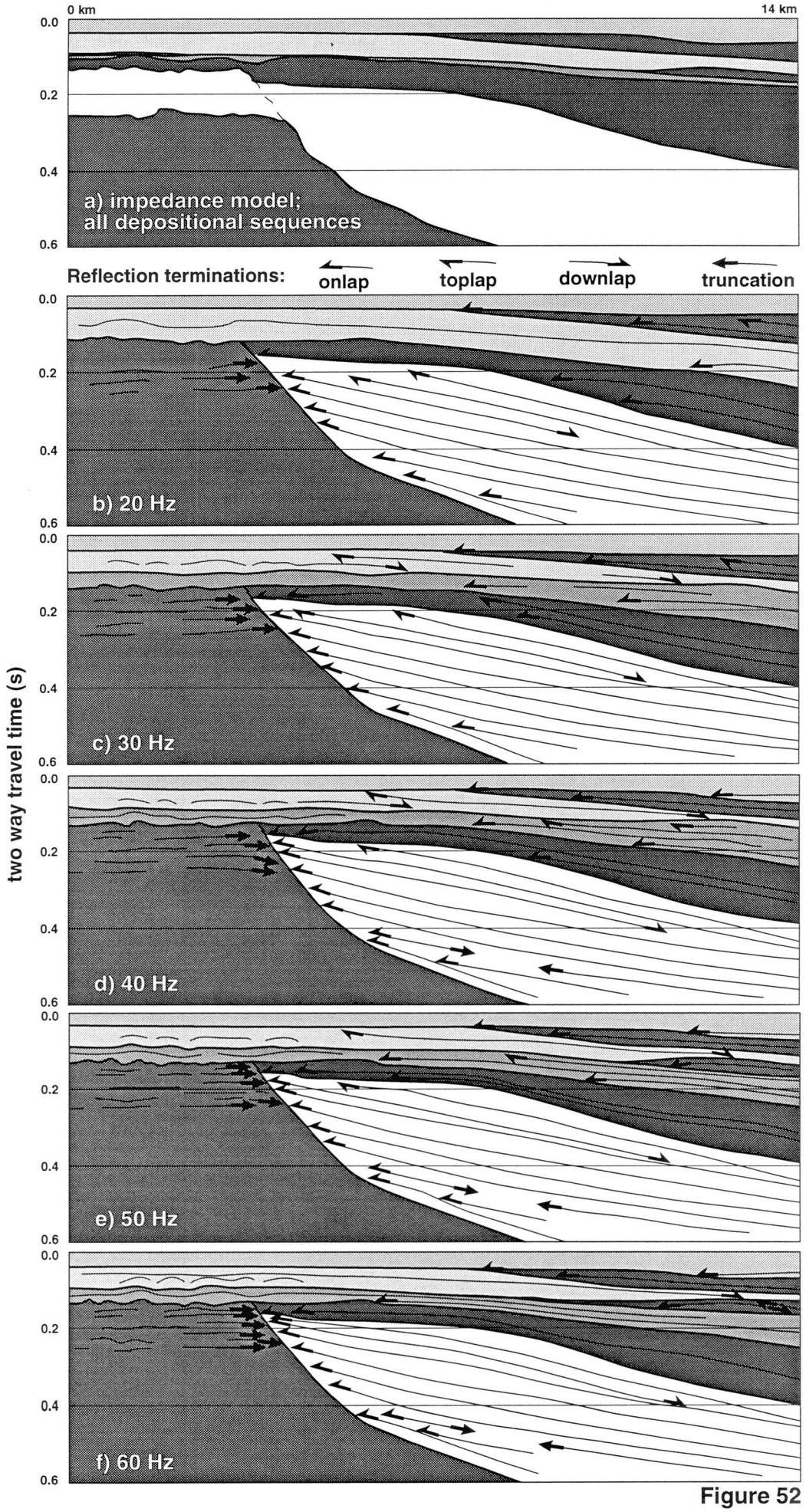
0 km
14 km
0.0
0.2
0.4
0.6
a) impedance model;
all depositional sequences
Reflection terminations:
onlap
toplap
downlap
truncation
b) 20 Hz
c) 30 Hz
d) 40 Hz
e) 50 Hz
f) 60 Hz
two way travel time (s)

Figure 52

The positions of the two reflection terminations that define the pseudo-onlap at the base of sequence 2 (Orfento Formation) also move updip with increasing frequencies, but continue to form an onlap geometry (Figures 49 c-f, CMP#120-250/0.18-0.22 s). At higher frequencies, these two reflections merge to one because they are only formed by the negative impedance contrast of a single horizon; a wavelet without the two negative lobes of the zero-phase Ricker wavelet (Figure 38) would not have produced two reflections. Thus the onlap geometry is independent of the chosen wavelet.

The main differences at increasing frequencies concern the sequence that is the equivalent of depositional sequences 3 to 5. At 30 Hz, a subtle downlap surface is observed within this sequence (Figure 49 c, downlaps at CMP#170/0,08 s and CMP#340/0.12 s). The surface is not necessarily a sequence boundary, but could represent an intra-sequence horizon, such as a maximum flooding surface.

No additional unconformities can be recognized at 40 Hz. However, a subtle reflection on the lower slope seems to form an onlap just below the sequence defined on the 30 Hz plot (Figure 49 d, CMP#340/0.15 s) . At 50 Hz, this onlap appears stronger and a new seismic sequence can be distinguished. The upper boundary of this sequence is now the downlap surface of the next overlying sequence. This sequence represents depositional Supersequence 4, which forms a limited onlapping wedge with breccias, turbidites and pelagic carbonates on the lower slope. At 60 Hz, this sequence is imaged clearly with a subtle additional intra-sequence reflection.

The onlap of the Gessoso-Solfifera evaporites on the top of Supersequence 6 is imaged at frequencies higher than 30 Hz (Figures 49 c-f, CMP#370/0.06 s). This sequence is not included into the interpretation because it was not part of the analyses of physical properties and was only modeled with a single layer as the upper limit of the modeled section.

The succession of sequence analyses at the different frequencies document clearly that seismic images do not mimic in a simple fashion true geologic conditions. Only five of the seven supersequences are recognized at low frequencies. Using signal with increased frequencies allows the remaining two supersequences to be resolved. In addition, the geometrical criteria that allow individual sequences to be discerned are often artifacts produced by pseudo-unconformities. Furthermore, the position of seismic sequence boundaries may be different from the positions of geologic sequence boundaries, especially if such boundaries are characterized by negative impedance contrasts.

That the total number of sequences increases from five to seven with higher frequencies demonstrates the limitations of performing stratigraphic sequence analyses on seismic sections with low dominant frequencies.

Positive versus Negative Polarity of Seismic Display

The zero-phase Ricker wavelet has a positive center peak with two low-amplitude lobes (Figure 38). A reflection from an interface with increasing impedance results in a black peak flanked by two white troughs on a positive polarity plot. The same reflection, plotted with negative polarity, is characterized by a white center trough flanked by two black peaks. Therefore, such a surface is seen on a negative polarity section as two parallel low-amplitude reflections, instead of the single, high-amplitude reflection with positive polarity.

Because a change of polarity changes neither the shape of the seismogram nor the convolution calculations, it seems to be only a minor parameter with no great importance. However, a comparison of seismic sections with positive versus negative polarity shows that seismic interpretations can vary significantly according to the chosen polarity. Both polarity plots were analyzed by tracing the black peaks of the seismograms. Figures 50 a-d display two comparisons of the same sections with different polarities. The 20 and 40 Hz synthetic sections were selected to be displayed with positive and negative polarities.

The analyses at 20 Hz results in the same total number of sequences (five) at both polarities. The Cretaceous platform sequence and the lowest slope sequence do not change their seismic appearance significantly. The onlap of the megabreccias of Supersequence 1 on the escarpment and the escarpment itself appear to be shifted slightly to the left at negative polarity, which is closer to the true position. The pseudo-onlap surface on top of sequence 1 and at the base of sequence 2 appears higher in the section with negative polarity, because the sequence boundary is now created, not by the true supersequence boundary, but by a surface within sequence 2 that, with its negative impedance contrast, dominates the negative polarity reflection pattern. This reflection dominates over other reflections that originate from surfaces with positive impedance contrast, since the negative polarity plot emphasizes surfaces with downward decreasing impedance. The onlap surface on top of seismic sequence 2 is imaged at its correct position on the negative polarity plot. It appears at the right-hand limit (CMP# 400, Figure 50 b) of the negative polarity section at 0.2 seconds, whereas it is apparently displayed at 0.25 s on the positive polarity section (Figure 50 a). The true position of this onlap surface in the time-converted impedance model is 0.18 s. Another difference between the polarity plots is that the patch-reefs are imaged better with positive polarity, because they have positive impedance contrasts with the overlying and underlying rocks.

The interpretation at negative polarity and 40 Hz frequency (Figure 50 d) is not as straightforward as it is with the positive polarity at the same frequency (Figure 50 c).

The shift in two-way time of the seismic sequence boundaries observed at 20 Hz remain, but some complications concerning the interpretations of recognizable unconformities occur in the 60 Hz plot. Within slope sequence 1, a new sequence boundary may be mapped, assuming that the reflection termination at 0.2 s near CMP#160 (Figure 50 d) is interpreted to be an onlap surface. Alternatively, it could be considered a toplap, which would then not mark the base of another sequence. The same situation can be seen higher in the section (Figure 50 d, CMP#220-260/0.15 s), where two reflections terminate in a manner that could also be interpreted as an onlap or as a toplap. Depending on these interpretations, the total numbers of sequences varies between 5 and 7, compared to the 6 observed sequences at positive polarity.

These examples demonstrate that a change of polarity does not simply change the position of the peak reflection, but may also influence the general reflection pattern. This difference can result in different interpretations of the geometries and may lead to different sequence analyses.

The discussed comparison between the rock record and the seismic response of a carbonate platform margin showed that in such a setting, the performance of seismic sequence analyses can result in correct stratigraphic interpretations. However, several limitations of the seismic imaging capabilities may lead to errors in sequence interpretation, in particular at lower dominant frequencies. The correctly scaled overlay of the synthetic seismic section over a photograph of the valley-flank outcrop (Figure 53, see also Figure 41) demonstrates that, already at low seismic frequencies, all major elements of the modeled rock section can be well imaged by a seismic survey. Nevertheless, the overlay in Figure 53 also reminds any field-geologist that the geological information, which can be observed in outcrops on a micro-scale, has drastically higher resolution than the macro-scale seismic image.

Comparison of Synthetic Section with real Seismic Data

A good way to test the credibility of seismic models is to compare the synthetic data with real seismic sections from the same or similar geologic environments. Such a comparison can refine and improve the interpretation of observed seismic data (e.g., Middleton, 1987; Rudolph and Greenlee, 1991; Stäuble and Pfiffner, 1991) or the synthetic sections of outcropping rocks units may be compared with true seismic data from a similar geologic environment to see the seismic response of a particular geologic setting (Stafleu and Sonnenfeld, 1994; this study). In this model of a carbonate platform-to-basin transition, the synthetic sections are compared with seismic data

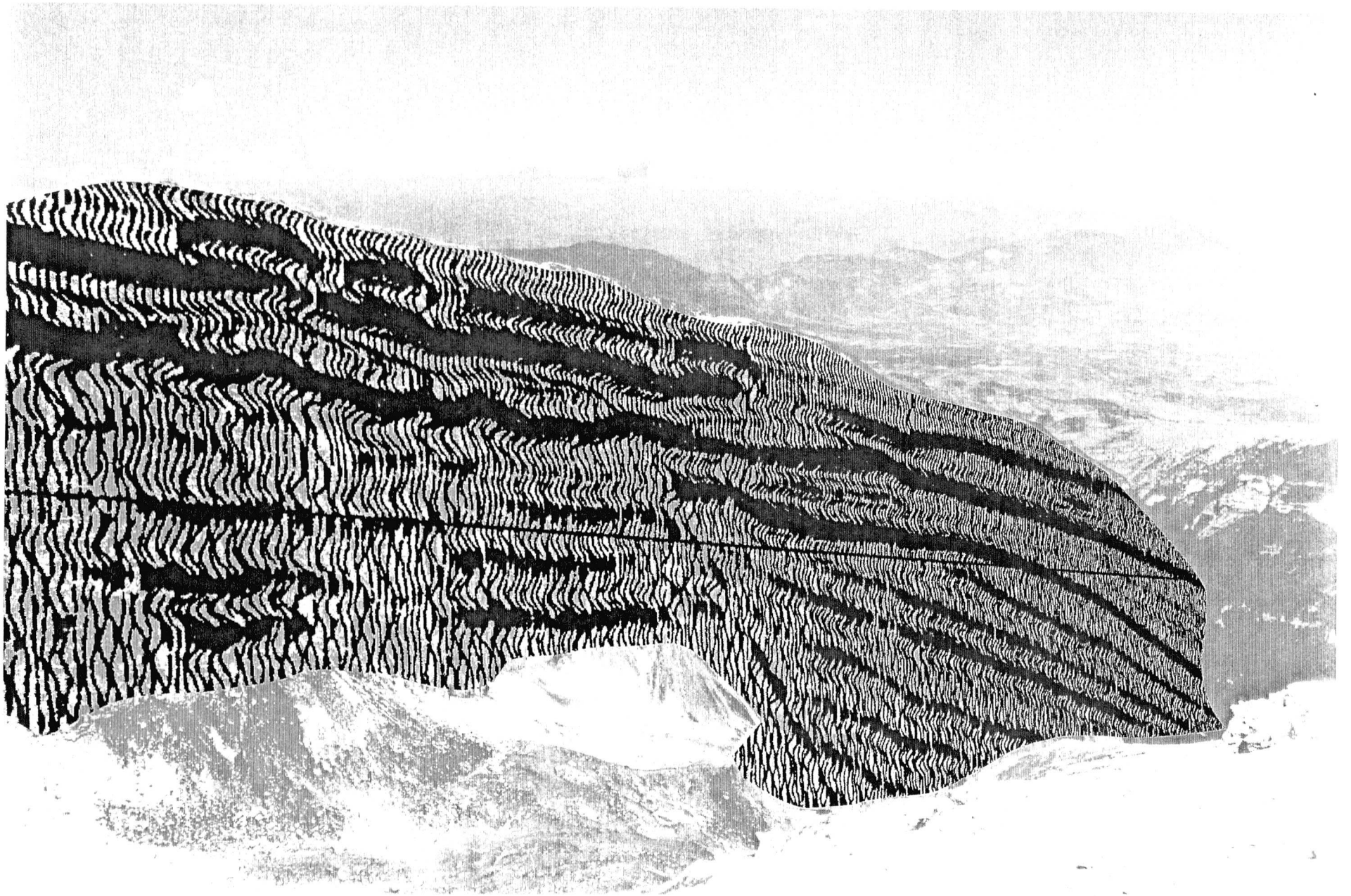

Figure 53: Plot of synthetic seismic section (30 Hz, Figure 48 c) over the modeled valley-flank outcrop (Valle dell'Orfento, Figure 41). This overlay, distorted and plotted at approximately correct scale and position, demonstrates that all major elements of the geologic section, such as escarpment, megabreccias or reefs, are well imaged. However, seismic resolution is not comparable with detailed geological information that can be obtained from outcrops.

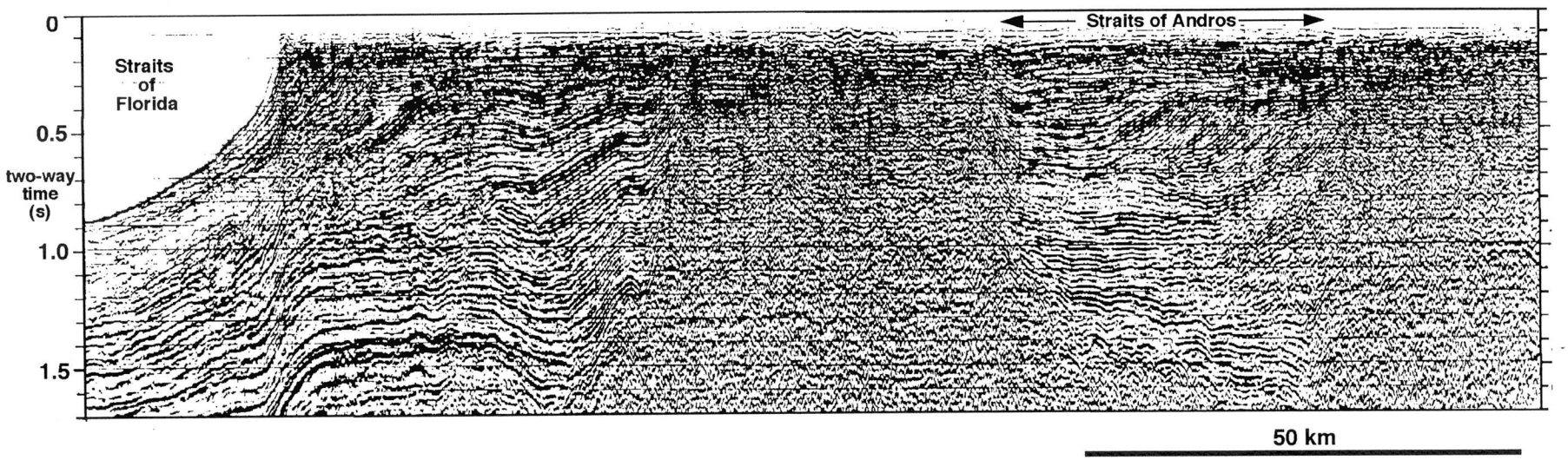

Figure 54: The Western seismic line from Great Bahama Bank (east to the right-hand side, see also Figures 2, 3). The modern Great Bahama Bank consists of old platform cores, characterized by seismic transparency, and by slope carbonates, which show inclined high-amplitude reflections. The slope carbonates could infill seaways (Eberli and Ginsburg, 1987). Such a former seaway, the Straits of Andros, can be recognized in the right third of the displayed section by the succession of inclined high-amplitude reflections. The observed difference in seismic reflectivity between slope and platform is in good concordance with the performed laboratory analyses of platform carbonates (narrow impedance range) and slope carbonates (wide impedance range).

originating from two similar geological settings. Two seismic datasets were available from pure carbonate environments characterized by a sharp transition from platform sediments to slope deposits: (1) the Western seismic line from Great Bahama Bank and (2) a seismic section of the eastward continuation of the Maiella escarpment, which plunges into the subsurface beneath the Adriatic Sea. Despite the difference to the Late Cenozoic evolution of the Maiella, both compared sections show striking resemblance with the modeled section. Some differences can be related mainly to differences in the geologic environment.

Comparison with Western Seismic Line from Great Bahama Bank

The subsurface of Great Bahama Bank, which was imaged by the Western seismic line (Eberli and Ginsburg, 1987, 1989, Figures 2, 3, 54, 55 b), represents a similar geologic environment as seen in the Montagna della Maiella. Both settings represent an aggrading and subsequent prograding carbonate platform margin system. The multichannel seismic line across Great Bahama Bank images a buried modern platform margin and a succession of aggrading and prograding carbonate sequences and shows many elements comparable to the synthetic sections from the Maiella.

Below the modern flat-top platform, the Western seismic line images clearly a buried slope section prograding into the Straits of Florida. An infilled intra-platform seaway, the Straits of Andros, can be seen in the eastern part of this section (Figure 54, Eberli and Ginsburg, 1987, 1989). The slope carbonates can be recognized on the seismic section by their inclined geometry, displaying the depositional slope angle, and by a succession of high-amplitude reflections that contrast sharply with the seismically transparent platform cores.

These seismic facies can be recognized in a similar way on the modeled Maiella sections. In Figures 55 a and b, the Western seismic line is plotted with the same scale as the synthetic sections of the Maiella to allow for direct comparison. Despite the moderate quality of the available paper copy of the Western seismic line, the general pattern of inclined, high-amplitude reflections that onlap a transparent platform is seen clearly. In addition, both sections image the geometries of the prograding units by coherent high-amplitude reflections, so that several prograding sequences can be recognized. Thus, the Maiella model and the Western seismic line show a similar seismic pattern of an aggrading and subsequent prograding carbonate platform margin. However, the geometries of the slope sediments of Great Bahama Bank appear to be more complicated than the slope geometries on the synthetic section of the Maiella. The slope reflections of the Bahamas line show irregularities in dip, which can be explained partly by velocity pull-ups of the overlying and prograding high-velocity reefal sections.

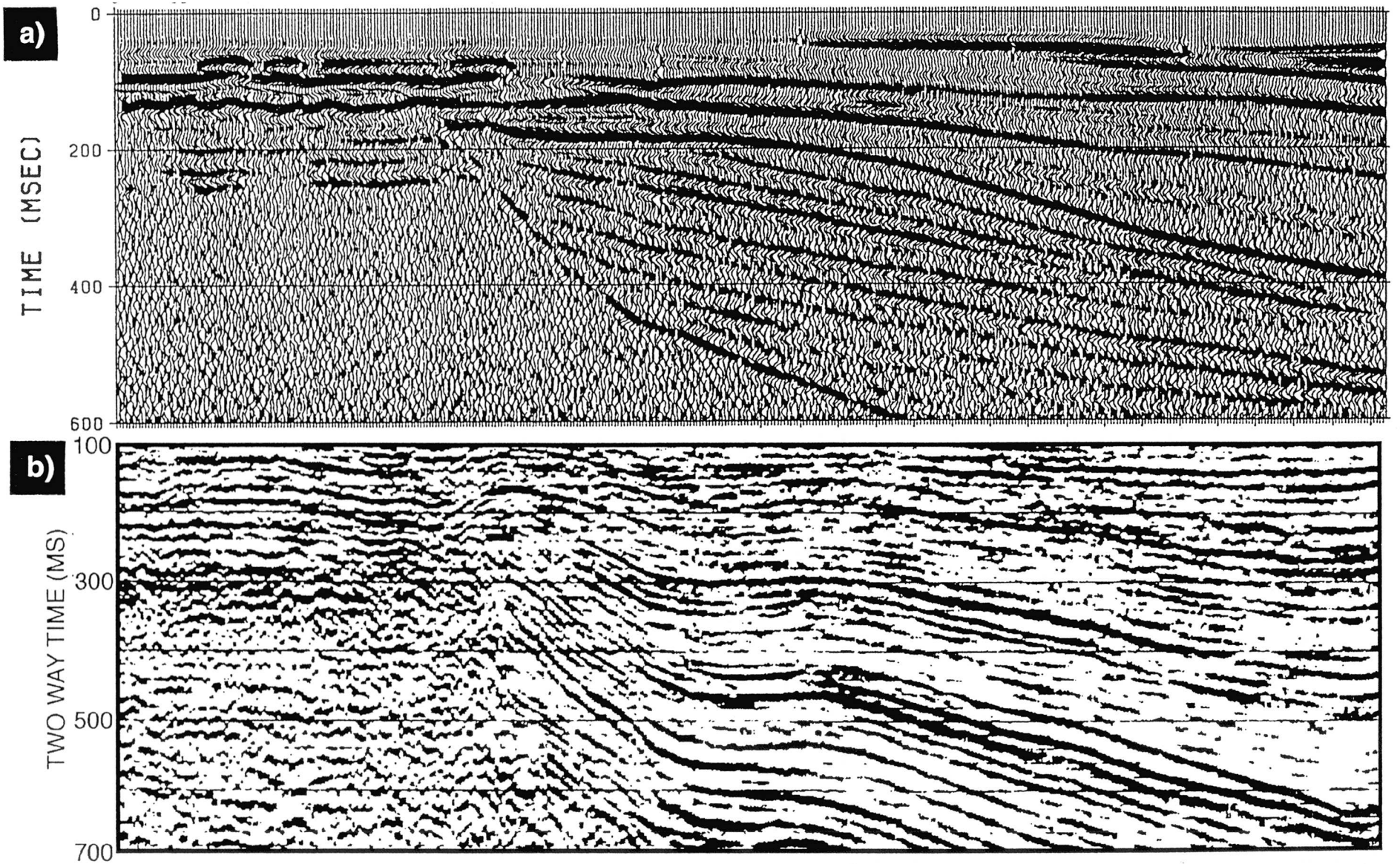

Figure 55: Comparison of two seismic sections originating from similar geologic environments. They are plotted at equal horizontal and vertical scales; total width of displayed sections is 14 km. **a:** Synthetic seismic section across the platform-to-basin transition in the Montagna della Maiella (30 Hz, positive polarity). **b:** Part of Western seismic line from Great Bahama Bank (Eberli and Ginsburg, 1987+1989). The displayed section was flipped about a vertical axis to match the synthetic section (platform on the left, slope on the right). The general reflection pattern is similar in a and b, confirming the differences in seismic facies of platform and slope. Furthermore, the resemblance of geometry and characteristics of the steep onlap surface suggest a Maiella-type non-depositional escarpment in the subsurface of the Bahamas, which also became buried at a later stage. Carbonate sequences that prograde over former slope deposits can be recognized on both sections.

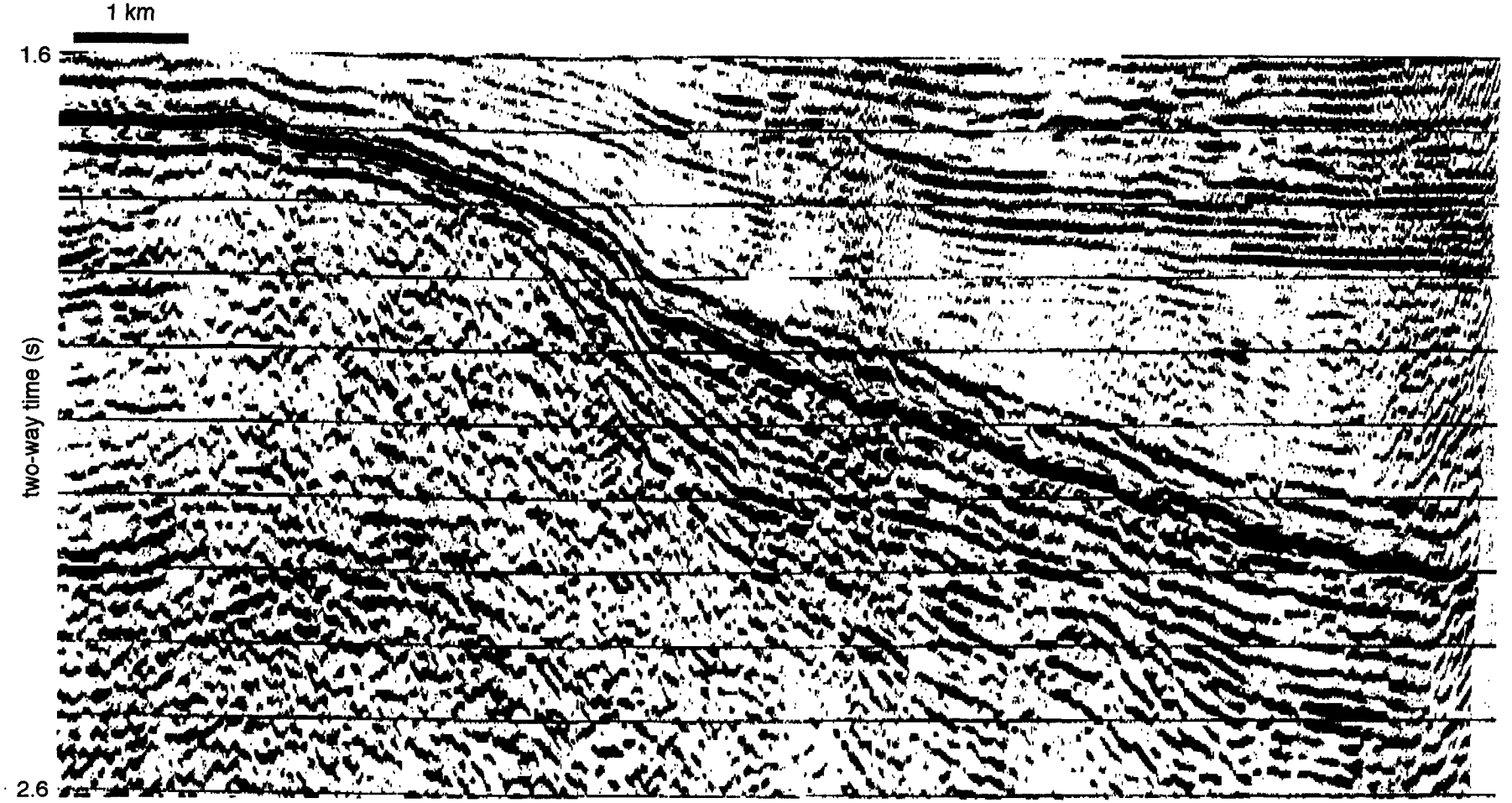

Figure 56: Seismic section imaging the eastward continuation of the Maiella platform margin (Apulian platform). This section is located approximately 40 km to the east of the Maiella, where the platform margin plunges into the subsurface beneath the Adriatic Sea (Figure 57). Horizontal width equals 14 km, horizontal and vertical scale as in Figures 55 a, b. Similar to Figures 55 a, b, the reflection pattern is characterized by a transparent platform, which is onlapped by a wedge-like succession of high-amplitude reflections. The similar geometries of the boundary between platform and slope suggest the existence of an equivalent escarpment in the Adriatic subsurface. As in the Maiella (Figure 55 a), the relief across the escarpment is buried and the platform-to-basin transition becomes gentle. Despite the similarities, the time-frame of the two settings is different, because the Maiella was involved into the eastward directed Apennine thrusting, while at the same time, the Adriatic area in the east became the foredeep of the Apennine thrust belt (thick Plio-Pleistocene section).

Comparison with Seismic Line from the Subsurface of the Adriatic Sea

Several published seismic sections across the margin of the Apulian platform in the subsurface of the Adriatic Sea show similar reflection patterns as the modeled Apulian platform margin in the Montagna della Maiella (De Alteriis and Aiello, 1993). They display similar seismic facies of slope and platform carbonates and have comparable onlap geometries.

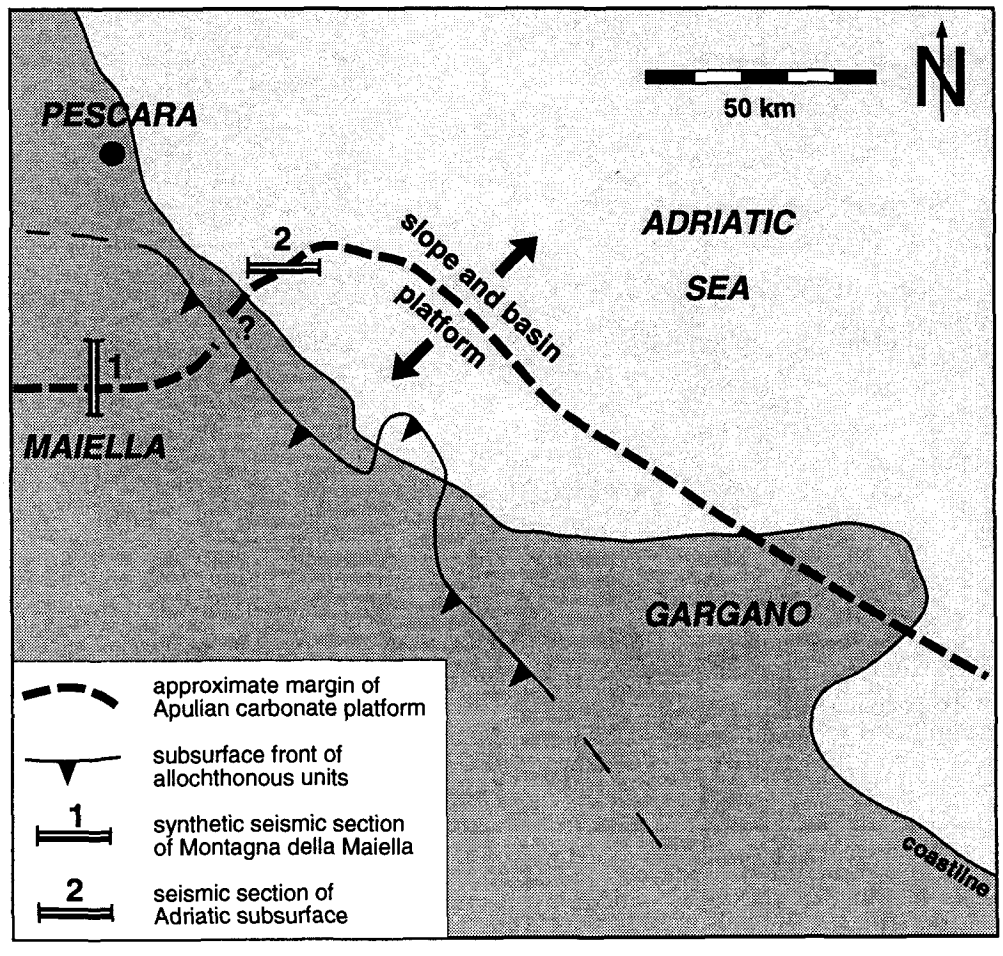

Figure 57: Location map of seismic section displayed in Figure 56. This seismic line of the Adriatic subsurface (#2 on Figure, courtesy of ELF Italiana) images the same Apulian platform margin as the synthetic seismic section of the Montagna della Maiella (#1). The geologic characteristics of both settings are similar. Differences in evolution are caused by the involvement of the Maiella in the Apennine thrustbelt, while the Adriatic zone became the foredeep during Apennine orogeny.

In addition, a multichannel seismic line offshore in the Adriatic Sea (Figures 56, 57) images the buried continuation of the Apulian platform margin only 40 km away from the Maiella outcrops (seismic data courtesy of ELF Italiana). Figures 56 shows a window from this line. A copy of the seismic section was scanned and horizontally squeezed, so that this Adriatic section and the seismic model from the Maiella (Figure 55 a) are displayed with the same horizontal (distance) and vertical (two-way time) scale. Consequently, the seismic images and geologic structures (dip, size, etc.) can be directly compared. The dominant frequency of the Adriatic line is approximately 30 Hz and no automatic gain control was applied.

Similar to the Maiella and the Bahamas sections (Figures 55 a, b), the Adriatic line shows a more or less transparent platform core that is onlapped by high-amplitude slope reflections. Due to the deeper burial, the thick slope-to-basin sediments between 1.6 and 2.2 s (Plio-Pleistocene) might have higher velocities than the slope sediments of the Maiella and might thus represent a thicker rock section than the modeled slope. The buried platform section cannot be significantly faster than the Maiella, since the Maiella platform was modeled with velocities between 5500 and 6500 m/s. The fact that the Adriatic section shows on the slope steeper inclined reflections might be explained by a velocity push-down of the overlying thick basinal sediments.

The Maiella and the Adriatic section (Figures 55 a, 56) display both sharp boundaries between the transparent platform zone and the high-reflectivity slope section. These boundary-surfaces are steep at the top and become gradually less steep at the base of the platform core. These similarities suggest that the non-depositional escarpment, as seen in the outcrops of the Montagna della Maiella, might continue in the subsurface of the Adriatic Sea. Another similarity of both sections is, that the relief between platform and basin across the escarpment becomes buried and subsequently forms a gentle platform-to-basin transition.

However, the seismically resembling geologic units of the two settings did not evolve simultaneously and the ages of the comparable reflections are different. The Maiella was incorporated in the Apennine thrustbelt in the Pliocene while the more eastern Adriatic area became the foredeep of the orogenic belt and is characterized by the deposition of a very thick Plio-Pleistocene section. The highest-amplitude basinal reflection on the Adriatic line (right-half of Figure 56, between 1.95 - 2.3 s) is likely to origin from the evaporitic layer deposited during the Messinian salinity crisis, which is overlain by a thick Plio-Pleistocene section. Most of the onlapping package of high-amplitude reflections below that prominent reflection would represent thus a much younger package than the equivalent seismic facies in the Maiella, where the wedge-like succession of high-amplitude reflections originates from the Cretaceous megabreccias intercalated with turbidites and Scaglia. In contrast to the Maiella, Cretaceous slope

sediments might not be imaged on the Adriatic section. The platform top reflection (right-hand limit of Figure 56, 1.7 s) could well be of Upper Cretaceous age, but might also be younger and the platform might have drowned at a later stage, possibly in the Eocene.

Unlike on the synthetic Maiella section (Figure 55 a) or on the Bahamas line (Figure 55 b), the offshore seismic section from the Adriatic Sea displays no signs of major progradational units. This difference in geologic evolution could be a result of different subsidence history and a connected change in sedimentary environment in the foredeep. It also could be related to a laterally variable growth potential and sedimentation rate of the carbonate platform. Such a variable growth potential can be explained by a change in orientation of the platform margin in respect to the main wind direction, which determines the direction of the off-bank shedding (Hine and Neumann, 1977). In fact, Figure 57 shows that the platform edge in the Maiella had a different orientation than the margin imaged on the Adriatic section. This could well be the reason for the observed different progradation-aggradation patterns.

Even if the time-frame of the platform-basin evolution is different in the subsurface of the Adriatic Sea than in the Maiella, the resembling seismic image suggests that both areas underwent a similar evolution with a steep bypass escarpment being gradually covered by slope sediments. This comparison shows how synthetic sections can be used to interpret seismic reflection patterns of real seismic lines.

PART D:

SYNTHESIS AND CONCLUSIONS

D.1. IMAGING OF CARBONATE SEDIMENTS ON SEISMIC SECTIONS

Variations of seismic reflection patterns of carbonate sediments result from the combined effect of several parameters. These parameters can be grouped into three categories that have a direct influence on the seismic image.

(1) *Physical properties of the rocks.* In particular *sonic velocity* and *bulk density,* which together define acoustic impedance.
(2) *Scale and geometrical arrangement of the rock units.*
(3) *Technical parameters and quality of the seismic survey.*

The controls and influences of (1) to (3) are summarized in the following three sections.

Physical Properties

Contrasts in acoustic impedance are necessary for the reflection of an acoustic signal and are thus a pre-requisite for the recognition of a geologic layer on a seismic section. Therefore, it is essential to know the range and to understand the parameters that control the velocities and densities of the different lithologies.

Laboratory measurements of velocities from 295 carbonate rock samples gave a remarkably wide range of over 4500 m/s for Vp and over 2500 m/s for Vs. The maximum velocities (Vp=6500 m/s, Vs=3400 m/s) are approximately four times higher than the minimum values (Vp=1700 m/s, Vs=800 m/s). Together with the density variations, these velocity contrasts cause large impedance differences that explain the excellent seismic reflectivity of pure carbonate rocks observed in seismic sections.

The performed laboratory analyses document that the variability of velocity in carbonates is a complex product of several factors that have different relevances and effects:

- Changes in carbonate mineralogy are not responsible for the large variability in velocities, since most measured samples contain only carbonate minerals that have similar physical properties. Fully dolomitized rocks can be extremely fast or extremely slow, demonstrating the low significance of mineralogical composition.

- Carbonate sediments deposited in shallow water generally have higher average velocities than carbonates from the deeper shelf, slope, or basin. This relation can be explained by the relatively high diagenetic potential of shallow water carbonates due to their high content in metastable aragonite and coarser grain size and by their exposure to fresh-water diagenesis. The narrow range of velocities and the resulting low reflectivity in platform carbonates explain the seismic transparency of platform sections seen on recorded seismic lines. This transparency is also reproduced on the synthetic seismic sections. The high variability of the velocities of slope and deeper water carbonates result in high seismic reflectivity.

- Comparison of velocity with burial depth and age shows that neither factor on its own exerts a significant control on velocity evolution. In fact, velocity inversions with increasing depth or age are common. For instance, a velocity increase caused by pure mechanical compaction, as measured in compacted carbonate mud, is lower than the observed velocity increase with decreasing porosities in natural rocks. This difference in the manner of velocity increase shows clearly that velocity is influenced primarily by post-depositional, diagenetic processes other than pure compaction during increasing burial depth and time.

- Porosity is the most important physical factor that influences velocity. Vp and Vs increase with decreasing porosity, but large departures from this general trend are possible.

- Different velocities in rocks with equal porosities are the result of different pore types. Rocks with frame-forming pore types, such as moldic or intraparticle porosity, can have very high velocities even with high-porosity fabrics, whereas

rocks with interparticle, intercrystalline, or high micro-porosity have much lower velocities at the same porosities.

- Increasing effective pressure can lead to fracturing of the rock and thus to a dramatic decrease in velocity. The critical pressure at which fractures form varies substantially, and can be as low as 5 MPa.

- The high values of elastic properties of self-supporting fabrics within a framework enable rocks to maintain extensive porosity even at relatively high overburden pressures. In particular, cementation and dissolution processes, which occur during early stages of burial, create very stable rock fabrics with high velocities. As a consequence, commonly used velocity-density or velocity-porosity functions, such as the general Gardner equation or the time-average equation, have to be modified towards higher velocities to produce reliable velocity data in carbonate rocks.

Most physical properties are a combined result of (1) the initial sediment-type and (2) the diagenetic alterations. The depositional lithology determines the diagenetic potential and thereby controls, together with the succession of diagenetic processes, the post-depositional history of the carbonate sediment. The timing of the diagenetic events determines the porosity-velocity evolution and therefore the velocity development.

In summary, it is impossible to make velocity predictions on carbonate rocks based solely on depth or age data. High susceptibility towards diagenetic alteration distinguishes carbonate sediments from other sedimentary rocks. Diagenetic processes, such as dissolution, cementation, or recrystallization, may occur so rapidly and at such a shallow depth of burial that the rock fabric is completely altered before compaction reduces porosity. The sediment is lithified mainly by early diagenesis, and to a lesser degree by increased overburden, which explains the poor correlation between velocity and age or depth.

Geometries of Lithological Units

Because vertical seismic resolution is limited to approximately one quarter of the signal's wavelength, seismic sections only display part of the geologic information that defines the geometrical distribution of acoustic impedance. Seismic modeling of outcrops provides insights into how the geometry of the rock units affect the seismic pattern and also which types of unconformities can be imaged on a seismic section.

The analyses of physical properties on discrete rock plugs showed that the pattern of acoustic impedance distribution follows mainly the sedimentary layering of the rock section. Most of the processes that alter velocity are tied to stratigraphic horizons, because the sediment type controls together with the suite of diagenetic events the velocity evolution. Because lithology and velocity are relatively homogeneous within any layer, the variability in velocity or impedance is much higher in a direction vertical to bedding than in a direction parallel to bedding. This observed impedance distribution implies a reflection pattern that follows the stratigraphic bedding of a sedimentary section. Seismic reflections thus generally image the bedding geometries of a sedimentary package. However, this relationship only describes the orientation and not the absolute travel-time of a reflection. Because vertical impedance variation is often much finer than seismic resolution, the resulting succession of seismic reflections is a product of interference from countless small impedance layers rather than being the image of one layer with a distinct impedance.

The geometrical relations between the lithologic layers are imaged on a seismic section if (1) the impedance contrast is high enough and (2) the layers are thick enough to produce reflections at the dominant seismic frequency. Only relatively thick layers with major impedance contrasts fulfill both requirements. If only requirement (1) is fulfilled, the seismic image might display reflections, but these would not be related to a single layer.

The recorded seismic lines and modeled synthetic sections showed that the geometries of the different depositional environments are imaged differently, depending on the scale and the contrasts in impedances:

- In the pure carbonate environments studied here, only the reefal buildups, platform top, and megabreccias yield individual reflections; their geometries are imaged clearly on seismic sections.

- Fine-grained redeposited sediments on the slope (turbidites) and pelagic carbonates have a vertical geometric distribution that is often too fine to form individual reflections. However, as a result of interference of reflections from thin layers, they may yield a succession of seismic reflections parallel to bedding, because the impedance variations are sufficiently high.

- Platform carbonates have usually neither the spatial distribution nor the impedance contrast to result in a strong reflection pattern that would document their internal geometry.

The unconformities seen on a seismic section represent the geometrical stratal pattern, even if the position of one particular reflection is not necessarily tied to a geologically significant layer. Some unconformities, such as the upper and lower unconformities of slope Supersequence 4 in the Maiella model, are not imaged at low frequencies (Figure 48 b-c). The limited thickness of this sequence precludes reflections that terminate against the overlying and underlying reflections, even though impedance variations are sufficient. Only the increasing seismic resolution offered by signals with frequencies higher than 50 Hz makes this sequence, together with its unconformities, detectable.

Many of the seismic unconformities are pseudo-unconformities caused by the thinning of layers below seismic resolution. These pseudo-unconformities may originate from concordant layers arranged in a wedge, as seen by the pseudo-onlap surface at the base of slope sequence 2 in the Maiella (Figures 48 b-e). They may also be real unconformities that display an incorrect character of reflection terminations. For instance, the seismic image from the top of slope sequence 1 demonstrates how reflections that form an onlap in reality, can be imaged seismically by terminations that show a toplap geometry (Figures 48 b-d). As a result, unconformities on seismic sections can represent true unconformities with the recognized characteristics, true unconformities with other geometric characteristics, or conformities. However, the increased seismic resolution offered by higher frequency signals can resolve the true pattern of most pseudo-unconformities.

Seismic Parameters

The distribution of acoustic impedances and layer geometries together define the physical characteristics of a rock section, which are converted into a seismic image during a reflection seismic survey. The quality and technical parameters of the acquisition and processing of the seismic data are crucial. Seismic modeling is able to simulate the effects of the various parameters on the seismic images as follows.

- Seismic frequency is the most important parameter, because it determines the wavelength of the acoustic signal and thus, the limits of seismic resolution. Increasing frequency improves the resolution, so that more geologic details can be recognized. In addition, some unconformities that are not recognized at all or were recognized with incorrect characteristics (pseudo-unconformities) at low frequencies may be resolved correctly with increasing frequency. The threshold frequency at which the unconformities are imaged is variable and depends on the

geometrical characteristics of the unconformity. In the discussed models, several pseudo-unconformities observed with 20 Hz dominant signals showed their true patterns when the signal frequencies were increased to 40 and 60 Hz. The number of seismic sequences separated by unconformities increased from five with 20 Hz signals to seven with 60 Hz signals. This change demonstrates the importance of frequency in seismic stratigraphic studies.

- Different seismic images can be produced by applying different methods of amplitude scaling to seismic data. An automatic gain control emphasizes low-amplitude events and consequently, most amplitude information concerning the hierarchy of reflection events is lost. In contrast, time-ramp scaling preserves amplitude information, and the differences between the individual reflections can be recognized by the characteristics of the reflection events.

- Background noise can mask low-amplitude reflections and make them invisible on a seismic section. Therefore, the signal-to-noise ratio of the seismic data is crucial for the recognition of geologic features, in particular for low-coherent reflections. Platform carbonates with a narrow range in impedance, such as the Lower Cretaceous platform section in the Montagna della Maiella, are not resolved by reflections in the synthetic sections if noise is added, even though they form layers that have lateral and vertical extents far above the limits of seismic resolution.

- A change of polarity of a seismic display produces an inversion of the black-white reflection pattern, but may also influence the recognition and interpretation of unconformities. A change to a negative polarity plot emphasizes the former white trough. In certain cases, this polarity change produces different lap-out positions and therefore different tracings of unconformities. In addition, the top of a unit with a downward negative impedance contrast, such as the low-velocity Calcari Cristallini of the Orfento Formation in the Maiella model, is imaged at positive polarity with a white trough and two flanking black peaks, due to the zero-phase wavelet that was used. The connected unconformity is either picked too high or too low on the section, whereas it is seen at its correct position on the negative polarity plot. A change in polarity thus not only alters some patterns and characteristics of unconformities, but also their relative positions.

In summary, the relation between a rock section and its seismic image not only depends on the rock physics, but also on the technical parameters of the seismic survey.

D.2. FEASIBILITY OF SEISMIC SEQUENCE STRATIGRAPHY IN CARBONATES

The comparison of the observed depositional sequences that were identified in the field with the equivalent synthetic seismic sequences allows the method of seismic stratigraphy to be tested in a pure carbonate environment. Two main assumptions have to be made to use seismic sequences for stratigraphic purposes: (1) the chronostratigraphic significance of the reflections has to be guaranteed, and (2) the depositional sequences should have seismic equivalents that can be identified by unconformities on a seismic section.

In all modeled synthetic sections of the Maiella, there are no major reflections that cut time lines. This fact does not imply that in other case studies of pure carbonate settings, the requirement of chronostratigraphic significance of the reflections is automatically fulfilled. The Maiella impedance model lacks critical lateral facies changes that would result in a misleading reflection pattern by having a thin-bedded, time transgressive stratal pattern. Most layers are laterally continuous and terminate at rather abrupt unconformities, such as on the platform escarpment.

More critical is the second requirement, that the seismic reflection pattern should image all major unconformities so that all sequences can be mapped on a seismic section. It is evident that some second-order depositional sequences, in particular platform sequences, have thicknesses that are below seismic resolution and can thus not be imaged as individual units by seismic data. Another problem for platform sequences is their geometry of conformable and parallel layers, which would not be imaged as unconformities even with greater thicknesses and sufficient impedance contrasts. Such platform sequence boundaries may only be recognized in rare cases, when they are associated with erosion and karstic features at the appropriate scale for seismic resolution.

The synthetic sections document well that the number of recognizable seismic slope sequences separated by unconformities increases with increasing signal frequency. In the Maiella example, all seven modeled supersequences can be recognized with the highest frequency signal of 60 Hz, whereas two sequences are missed using the lowest frequency signal of 20 Hz. The observed seismic unconformities, which separate the individual sequences, are often pseudo-unconformities, which have no equivalents in

nature or which show an incorrect geometrical relation to the overlying or underlying beds. These pseudo-unconformities may result in a misleading interpretation of depositional environments or rock type, but not necessarily in erroneous stratigraphic correlations obtained by seismic sequence analyses. The use of seismic sequences for stratigraphic purposes is more suspect because not all supersequences are recognized at low frequencies. This means that information concerning long time periods are missed or wrongly correlated when the section is compared with other sections or with a global signal, such as postulated by the global sea-level chart (Haq et al., 1988). In addition, the fact that the modeled supersequences (second-order) are only recognized incompletely on seismic data at low frequencies, demonstrates that in the studied case of a pure carbonate platform margin, the even smaller scale third-order depositional sequences cannot be used to perform seismic stratigraphic correlations. Only in part of the section, notably in the Cretaceous slope sediments with the onlapping megabreccias, sedimentation rate and geometrical characteristics are sufficient to result in third-order sequences that can be seen on seismic sections.

The performed case studies, which provided insight into the relations between the carbonate rock record and its seismic response, demonstrated that seismic interpretation (e.g., sequence analysis) has its limitations, which are caused by several factors. The most critical factor for a misleading seismic image are (1) insufficient impedance contrasts, (2) thin-bedded impedance patterns below seismic resolution that can result in pseudo-unconformities, (3) low seismic frequencies causing low seismic resolution, and (4) low signal-to-noise ratios. The understanding of the seismic imaging process and the knowledge of the limits are essential for any seismic interpreter to avoid misinterpretations of seismic data. The geological boundary conditions, such as expected sedimentation rate, which influences sequence thicknesses, or expected lithologies, which determine impedance variations, should also be incorporated in any seismic interpretation.

Despite all these limitations, this study shows that carbonate rocks have, due to their high impedance range and related diagenetic reactivity, a high potential to be imaged correctly by seismic survey methods.

REFERENCES

Accarie, H. (1988), Dynamique sédimentaire et structurale au passage plateforme/bassin. Les faciès carbonatés Crétacés et Tertiares: Massif de la Maiella (Abruzzes Italie): Ecole de Mines Paris, Mémoires Sciences de la Terre *5*, 162 p.

Anselmetti, F.S., Eberli, G.P., Sellami, S. and Bernoulli , D. (1991), From outcrops to seismic profiles: an attempt to model the carbonate platform margin of the Maiella, Italy: Abstracts Geological Society of America Annual Meeting, San Diego, California, U.S.A., 89-90.

Anselmetti, F.S. and Eberli G.P. (1993), Controls on sonic velocity in carbonates: Pure and Applied Geophysics *141/2-4*, 287-323.

Anselmetti, F.S. and Eberli, G.P. (1994), Sonic velocity in carbonates - a combined product of depositional lithology and diagenetic alterations, *submitted to:* Society of Economic Paleontologists and Mineralogists Concept Series.

Batzle, M. and Wang, Z. (1992), Seismic properties of pore fluids: Geophysics *57/11*, 1396-1408.

Bernoulli, D. and Jenkyns, H.C. (1974), Alpine, Mediterranean and central Atlantic Mesozoic facies in relation to the early evolution of the Tethys, *in:* Dott, R.H.Jr. and Shaver, R.H. (eds.), Modern and ancient geosynclinal sedimentation: Society of Economic Paleontologists and Mineralogists Special Publication *19*, 129-160.

Bernoulli, D., Eberli, G.P., Pignatti, J.S., Sanders, D. and Vecsei, A. (1992), Sequence stratigraphy of Montagna della Maiella: Quinto simposio di ecologia e paleoecologia delle comunita' bentoniche, Paleobenthos V, libro-guida delle escursioni, Dip. di Scienze della Terra, Univ. "La Sapienza", Roma, Italy, 85-109.

Biddle, K.V., Schlager, W., Rudolph, K.W. and Bush, T.L. (1992), Seismic model of a progradational carbonate platform, Picco di Vallandro, the Dolomites, Northern Italy: American Association of Petroleum Geologists Bulletin *76*, 14-30.

Biot, M.A. (1956), Theory of propagation of elastic waves in a fluid-saturated porous solid, I. Low frequency range, II. Higher frequency range: Journal of the Acoustical Society of America *28*, 168-191.

Birch, F. (1960), The velocity of compressional waves in rocks to 10 kilobars, Part 1: Journal of Geophysical Research *65*, 1083-1102.

Bourbié, T., Coussy, O. and Zinszner, B. (1987), Acoustics of porous media: EditionsTéchnip, Paris, 334 p.

Burns, S.J. and Swart, P.K. (1992), Diagenetic processes in Holocene carbonate sediments: Florida Bay mudbanks and islands: Sedimentology *39*, 285-304.

Campbell, A.E. and J. Stafleu (1992), Seismic modeling of an Early Jurassic drowned platform: The Djebel Bou Dahar, High Atlas, Morocco: American Association of Petroleum Geologists Bulletin *76*, 1760-1777.

Carmichael, R.S. (ed.) (1989), Practical Handbook of physical properties of rocks and minerals: CRC Press, Inc., Boca Raton, U.S.A, 741 p.

Christensen, N.I. and Szymanski, D.L. (1991), Seismic properties and the origin of reflectivity from a classic Paleozoic sedimentary sequence, Valley and Ridge province, southern Appalachians: Geological Society of America Bulletin *103*, 277-289.

Coyner, K.B. (1984), Effects of stress, pore pressure, and pore fluids on bulk strain, velocity and permability in rocks: Ph.D. Thesis, Massachusetts Institute of Technology, 361 p.

Crescenti, U., Crostella, A., Donzelli, G., Raffi, G. (1969), Stratigrafia della serie calcarea dal Lias al Miocene nella regione Marchigiano-Abruzzese, Parte II - Litostratigrafia, Biostratigrafia, Paleogeografia: Mem. Soc. Geol. Ital. *8*, 343-420.

Dawans, J.M. and Swart, P.K. (1988), Textural and geochemical alterations in late Cenozoic Bahamian dolomites: Sedimentology *35*, 385-403.

De Alteriis, G. and Aiello, G. (1993), Stratigraphy and tectonics offshore of Puglia (Italy, southern Adriatic Sea): Marine Geology *113*, 233-253.

Eberli, G.P. (1988), Physical properties of carbonate turbidite sequences surrounding the Bahamas: Implications for slope stability and fluid movements, *in:* Austin, J.A. Jr. and Schlager, W. (eds.): Proceedings of the Ocean Drilling Program, Scientific Results 101, 305-314.

Eberli, G.P., (1991), Growth and demise of isolated carbonate platforms: Bahamian controversies, *in:* Müller, D.W., McKenzie, J.A. and Weissert, H. (eds.), Controversies in Modern Geology: Academic Press Limited., 231-248.

Eberli, G.P. and Ginsburg, R.N. (1987), Segmentation and coalescence of Cenocoic carbonate platforms, northwestern Great Bahama Bank: Geology *15*, 75-79.

Eberli, G.P. and Ginsburg. R.N. (1989), Cenozoic progradation of Northwestern Great Bahama Bank, a record of lateral platform growth and sea-level fluctuations, *in:* Crevello, J.L., Wilson, J.L., Sarg, J.F. and Read, J.F. (eds.), Controls on carbonate platform and basin development: Society of Economic Paleontologists and Mineralogists Special Publication *44*, 339-351.

Eberli, G.P., Bernoulli, D., Sanders, D.,Vecsei, A. (1993), From aggradation to progradation: the Maiella platform (Abruzzi, Italy), *in:* Simo, J.T., Scott, R.W. and

Masse, J.-P. (eds.), Cretaceous Carbonate Platforms: American Association of Petroleum Geologists Memoir *56*, 213-232.

Eberli, G.P., Kenter, J.A.M., McNeill, D.F., Ginsburg, R.N., Swart, P.K. and Melim, L.A. (1994), Facies, diagenesis and timing of prograding seismic sequences on Western Great Bahama Bank, *submitted to:* Society of Economic Paleontologists and Mineralogists Concept Series.

Enos, P. and Perkins, R.D. (1979), Evolution of Florida Bay from island stratigraphy: Geological Society of America Bulletin *90*, 59-83.

Enos, P. and Sawatsky, L.H. (1981), Pore networks in Holocene carbonate sediments: Journal of Sedimentary Petrology *51*, 961-985.

Fagin, S.W. (1991), Seismic modeling of geologic structures: Geophysical Development Series *2*, Society of Exploration Geophysicists, Tulsa, Oklahoma, 269 p.

Fulthorpe, C.S. (1991), Geological control on seismic sequence resolution: Geology *19*, 61-65.

Galloway, W.E., Marshall, S.Y. and Whipple, A.P. (1977), Seismic stratigraphic model of depositional platform margin, Eastern Anadarko Basin, Oklahoma, *in:* Payton, C.E. (ed.), Seismic stratigraphy - applications to hydrocarbon exploration: American Association of Petroleum Geologists Memoir *26*, 439-449.

Gardner, G.H.F., Gardner, L.W. and Gregory, A.R. (1974), Formation velocity and density: the diagnostic basics for stratigraphic traps: Geophysics *39*, 770-780.

Gassmann, F. (1951), Elastic waves through a packing of spheres: Geophysics *16*, 673-685.

Ginsburg, R.N. (1994), The Bahamas Drilling Project: Summaries of background and acquisition of cores and logs, *submitted to:* Society of Economic Paleontologists and Mineralogists Concept Series.

Goetz, J.F., Dupal, L. and Bowler, J. (1979), An investigation into discrepancies between sonic log and seismic check shot velocities: APEA, 1-11.

Guadagno, F.M. and Nunziata, C. (1993), Seismic velocities of fractured carbonate rocks (southern Apennines, Italy): Geophysical Journal International *113*, 739-746.

Gregory, A.R. (1977), Aspects of rock physics from laboratory and logdata that are important to seismic interpretation, *in:* Payton, C.E. (ed.), Seismic stratigraphy - applications to hydrocarbon exploration: American Association of Petroleum Geologists Memoir *26*, 15-46.

Hamilton, E.L. (1971), Elastic properties of marine sediments: Journal of Geophysical Research *76/2*, 579-604.

Hamilton, E.L. (1980), Geoacoustic modeling of the sea-floor: Journal of the Acoustical Society of America *68*, 1313-1340.

Han, D., Nur, A. and Morgan, D. (1986), Effects of porosity and clay content on wave velocities in sandstones: Geophysics *51/11*, 2093-2107.

Haq, B.U., Hardenbol, J. and Vail, P. (1988), Mesozoic and Cenozoic chronostratigraphy and cycles of sea-level change, *in:* Wilgus, C.K., Hastings, B.S., Kendall, C.G.St.C., Posamentier, H.W., Ross, C.A. and Van Wagoner, J.C. (eds.), Sea-level changes: An integrated approach: Society of Economic Paleontologists and Mineralogists Special Publication *42*, 71-108.

Hine, A.C., and Neumann, C. (1977), Shallow carbonate-bank-margin growth and structure, Little Bahama Bank, Bahamas: American Association of Petroleum Geologists Bulletin *61*, 376-406.

Japsen, P. (1993), Influence of lithology and Neogene uplift on seismic velocities in Denmark: Implications for depth conversion of maps: American Association of Petroleum Geologists Bulletin *77*, 194-211.

Johnston, J.E. and Christensen, N.I. (1992), Shear wave reflectivity, anisotropies, Poisson's ratios and densities of a southern Appalachian Paleozoic sedimentary sequence: Tectonophysics *210*, 1-20.

Johnston, J.E. and Christensen, N.I. (1993), Compressional to shear velocity ratios in sedimentary rocks: Int. J. Rock. Mech. Min. Sci. and Geomech. Abstr. *30/7*, 751-754.

Jones, T. and Nur, A. (1982), Seismic velocities and anisotropy in mylonites and the reflectivity of deep crustal fault zones: Geology *10*, 260-263.

Kendall, C.G.St.C, and Schlager, W. (1981), Carbonates and relative changes in sea-level: Marine Geology *44*, 181-212.

Kenter, J.A.M. and Ivanov, M. (1994), Parameters controlling acoustic properties of carbonate and volcaniclastic sediments at sites 866 and 869: ODP Scientific results, 143.

Kenter, J.A.M. and Ginsburg, R.N. (1994), Lithologic and sedimentologic observations on two core borings through the western, prograding, Neogene-Quaternary margin of Great Bahama Bank, *submitted to:* Society of Economic Paleontologists and Mineralogists Concept Series.

Kenter, J.A.M., Eberli, G.P., Ginsburg, R.N., McNeill, D.F., Swart, P.K., Lidz, B.H., Bralower, T.J., Troelstra, S.R. and Beets, K.J. (1994), Depositional successions correlated between cores through platform and slope of the prograding Neogene-Quaternary Western margin of Great Bahama Bank, *submitted to:* Society of Economic Paleontologists and Mineralogists Concept Series.

Kievman, C.M. and Ginsburg, R.N. (1994), Pliocene to Pleistocene depositional history of the upper platform margin, Northwest Great Bahama Bank, *submitted to:* Society of Economic Paleontologists and Mineralogists Concept Series.

King, M.S. (1966), Wave velocities in rocks as a function of changes in overburden pressure and pore fluid saturants: Geophysics *31*, 50-73.

Laughton, A.S. (1957), Sound propagation in compacted ocean sediments: Geophysics *22*, 233-260.

Marion, D., Nur, A., Yin, H. and Han, D. (1992), Compressional velocity and porosity in sand-clay mixtures: Geophysics *57*, 554-563.

Meckel, L.D. Jr. and Nath, A.K. (1977), Geologic considerations for stratigraphic modeling and interpretation, *in:* Payton, C.E. (ed.), Seismic stratigraphy - applications to hydrocarbon exploration: American Association of Petroleum Geologists Memoir *26*, 417-438.

Melim, L.A. and Anselmetti, F.S. (1994), Permeability of Neogene carbonates from the Bahamas Drilling Project: variability and controls, *submitted to:* Society of Economic Paleontologists and Mineralogists Concept Series.

Melim, L.A., Swart, P.K. and Maliva, R.G. (1994), Diagenesis of carbonates from the Bahamas Drilling Project, Western margin Great Bahama Bank: Meteoric versus marine burial diagenesis, *submitted to:* Society of Economic Paleontologists and Mineralogists Concept Series.

Middleton, M.F. (1987), Seismic stratigraphy of Devonian reef complexes, Northern Canning Basin, Western Australia: American Association of Petroleum Geologists Bulletin *71/12*, 1488-1498.

Milholland, P., Manghani, M.H., Schlanger, S.O. and Sutton, G.H. (1980), Geoacoustic modeling of deep-sea carbonate sediments: Journal of the Acoustical Society of America *68/5*, 1351-1360.

Mitchum, R.M., Vail P.R., and Thompson, S. (1977), The depositional sequence as a basic unit for stratigraphic analyses, *in:* Payton, C.E. (ed.), Seismic stratigraphy - applications to hydrocarbon exploration: American Association of Petroleum Geologists Memoir *26*, 53-62.

Mitchum, R.M.Jr. and Vail, P.R. (1977), Seismic stratigraphic interpretation procedure, *in:* Payton, C.E. (ed.), Seismic stratigraphy - applications to hydrocarbon exploration: American Association of Petroleum Geologists Memoir *26*, 117-133.

Mutti, M. (1995), Porosity development and diagenesis in the Orfento supersequence and its bounding unconformities (Upper Cretaceous, Montagna della Maiella, Italy) *in:* D.Budd, A. Saller and M. Harris (eds.), Unconformities in carbonate strata: their recognition and the significance of associated porosity: American Association of Petroleum Geologists Memoir *(in press)*.

Mutti, M., Bernoulli, D. and Eberli, G.P. (1994), Progradation of the Late Cretaceous sequences of Montagna della Maiella: the importance of changes in sea-floor topography and sediment reworking in sequence organization: Abstracts 15th International Association of Sedimentologists Regional Meeting, Ischia, Italy, 300-301.

Nafe, J.E. and Drake, C.L. (1963), Physical properties of marine sediments: The Sea *3*, Interscience. 794-815.

Neidell, N.S. and Poggiagliolmi, E. (1977), Stratigraphic modeling and interpretation - geophysical principles and techniques, *in:* Payton, C.E. (ed.), Seismic stratigraphy - applications to hydrocarbon exploration: American Association of Petroleum Geologists Memoir *26*, 389-416.

Nur, A. and Simmons, G. (1969), The effect of saturation on velocity in low porosity rocks: Earth and Planetary Science Letters *7*, 183-193.

Nur, A., Marion. D. and Yin, H. (1991), Wave velocities in sediments, *in:* Hovem, J.M., Richardson, M.D. and Stoll, R.D. (eds.), Shear waves in marine sediments: Kluwer Academic Publishers, 131-140.

Rafavich, F., Kendall, C.H.St.C. and Todd, T.P. (1984), The relationship between acoustic properties and the petrographic character of carbonate rocks: Geophysics *49*, 1622-1636.

Rudolph, K.W., Schlager, W. and Biddle, K.T. (1989), Seismic models of a carbonate foreslope-to-basin transition, Picco di Vallandro, Dolomite Alps, northern Italy: Geology *17*, 453-456.

Rudolph, K.W. and Greenlee, S.M. (1991), Seismic modeling of a pinnacle reef: An example from the Williston Basin, *in:* Fagin (ed.), Seismic modeling of geologic structures: Geophysical Development Series *2*, Society of Economic Paleontologists and Mineralogists, Tulsa, Oklahoma, 197-208.

Sanders, D.G.K. (1994), Carbonate platform growth and erosion: The Cretaceous-Tertiary of Montagna della Maiella, central Italy: Dissertation ETH Nr. 10800, Zürich, Switzerland *(in press)*.

Sarg, J.F. (1988), Carbonate Sequence Stratigraphy, *in:* Wilgus, C.K., Hastings, B.S., Kendall, C.G.St.C., Posamentier, H.W., Ross, C.A. and Van Wagoner, J.C. (eds.), Sea-level changes: An integrated approach: Society of Economic Paleontologists and Mineralogists Special Publication *42*, 155-188.

Schlager, W. (1992), Sedimentology and sequence stratigraphy of reefs and carbonate platforms: American Association of Petroleum Geologists Continuing Education Course Note Series, *34*, 71 p.

Schlager, W., Biddle, K.T. and Stafleu J. (1991), Picco di Vallandro (Dürrenstein) - a platform-basin transition in outcrop and seismic model: Dolomieu Conference on carbonate plaforms and dolomitization, Guidebook Excursion D, Ortisei, 22 p.

Schlanger, S.O. and Douglas, R.G. (1974), The pelagic ooze-chalk-limestone transition and its implications for marine stratigraphy, *in:* Hsu, K.J and Jenkyns, H.C. (eds.), Pelagic sediments on land and under the sea: Special Publication International Association of Sedimentologists *1*, 117-148.

Schönberger, M. (1974), Resolution comparison of minimum-phase and zero-phase signals: Geophysics *39*, 826-833.

Sellami, S., Barblan, F., Mayerat, A.-M., Pfiffner, O.A., Risnes, K. and Wagner, J.-J. (1990), Compressional wave velocities of samples from the NFP-20 East seismic reflection profile: Mémoires Société Géologique Suisse *1*, 77-84.

Sheriff, R.E. (1977), Limitations on resolution of seismic reflections and geologic detail derivable from them, *in:* Payton, C.E. (ed.), Seismic stratigraphy - applications to hydrocarbon exploration: American Association of Petroleum Geologists Memoir *26*, 3-14.

Sheriff, R.E. (1985), Aspects of seismic resolution, *in:* Berg, O.R. and Woolverton, D.G. (eds.), Seismic stratigraphy II - An integrated approach: American Association of Petroleum Geologists Memoir *39*, 1-34.

Simmons, G. and Wang, H. (1971), Single crystal elastic constants and calculated aggregate properties: Handbook, the M.I.T. Press, Cambridge, 370 p.

Stafleu, J. and Schlager, W. (1993), Pseudo-toplap in seismic models of the Schlern-Raibl contact (Sella platform, northern Italy): Basin Research *5*, 55-65.

Stafleu, J. and Sonnenfeld, M.D. (1994), Seismic models of a shelf-margin depositional sequence: Upper San Andres Formation, Last Chance Canyon, New Mexico, *submitted to:* Journal of Sedimentary Petrology.

Stafleu, J., Everts, A.J.W. and Kenter, J.A.M. (1994), Seismic models of a prograding carbonate platform: Vercors, SE France: Marine and Petroleum Geology *11*, *(in press).*

Stäuble, M. and Pfiffner, O.A. (1991), Processing, interpretation and modeling of seismic reflection data in the Molasse Basin of eastern Switzerland: Eclogae Geol. Helv. *84/1*, 151-175.

Tatham, R.H. (1982), Vp/Vs and lithology: Geophysics *47/3*, 336-344.

Tipper, J.C. (1993), Do seismic reflections necessarily have chronostratigraphic significance?: Geological Magazine *130/1*, 47-55.

Toksöz, M.N., Cheng, C.H. and Timur, A. (1976), Velocities of seismic waves in porous rocks: Geophysics *41/4*, 621-645.

Urmos, J. and Wilkens, R.H. (1993), In situ velocities in pelagic carbonates: new insights from Ocean Drilling Program Leg 130, Ontong Java Plateau: Journal of Geophysical Research *98/B5*, 7903-7920.

Vail, P.R., Mitchum, R.M.Jr. and Thomson, S. (1977a), Relative changes of sea-level from coastal onlap, *in:* Payton, C.E. (ed.), Seismic stratigraphy - applications to hydrocarbon exploration: American Association of Petroleum Geologists Memoir *26*, 63-81.

Vail, P.R., Todd, A.G. and Sangree, J.B. (1977b), Chronostratigraphic significance of seismic reflections, *in:* Payton, C.E. (ed.), Seismic stratigraphy - applications to hydrocarbon exploration: American Association of Petroleum Geologists Memoir *26*, 99-116.

Van Wagoner, J.C., Posamentier, H.W., Mitchum, R.W., Vail, P.R., Sarg, J.F., Loutit, T.S. and Hardenbol, J. (1988), An overview of the fundamentals of sequence stratigraphy and key definitions, *in:* Wilgus, C.K., Hastings, B.S., Kendall, C.G.St.C., Posamentier, H.W., Ross, C.A. and Van Wagoner, J.C. (eds.), Sea-level changes - An integrated approach: Society of Economic Paleontologists and Mineralogists Special Publications *42*, 39-45.

Vecsei, A. (1991), Aggradation und Progradation eines Karbonatplattform-Randes: Kreide bis Mittleres Tertiär der Montagna della Maiella, Abruzzen: Mitteilungen aus dem Geologischen Institut der Eidgenössischen Technischen Hochschule und der Universität Zürich, Neue Folge *294*, 170 p.

Vernik, L. and Nur, A. (1992), Petrophysical classification of siliciclastics for lithology and porosity prediction from seismic velocities: American Association of Petroleum Geologists Bulletin *76*, 1295-1309.

Vidlock, S. (1983), The stratigraphy and sedimentation of Cluett Key, Florida Bay: M.S. thesis, University of Connecticut.

Wang, Z. and Nur, A. (1990), Dispersion analysis of acoustic velocities in rocks: Journal of Acoustical Society of America *87/6*, 2384-2395.

Wang, Z., Batzle, M.L. and Nur, A. (1990), Effect of different pore fluids on seismic velocities in rocks: Canadian Journal of Exploration Geophysics *26*, 104-112.

Wang, Z., Hirsche, W.K. and Sedgwick, G. (1991), Seismic velocities in carbonate rocks: The Journal of Canadian Petroleum Technology *30*, 112-122.

Warzeski, E.R. and Ginsburg, R.N. (1994), Lithologic calibration of geophysical logs in Neogene and Quaternary Bahamian carbonates: Boreholes Clino and Unda, *submitted to:* Society of Economic Paleontologists and Mineralogists Concept Series.

Wilkens, R., Simmons, G. and Caruso, L. (1984), The ratio Vp/Vs as a discriminant of composition for siliceous limestones: Geophysics *49*, 1850-1860.

Wilkens, R.H., Fryer, G.F. and Karsten, J. (1991), Evolution of porosity and seismic structure of upper oceanic crust: importance of aspect ratios: Journal of Geophysical Research *96/B11*, 17981-17995.

Wilson, J.L. (1975), Carbonate facies in geologic history: Springer, New York, 471 p.

Wood, A.B. (1941), A textbook of sound: Macmillan, New York, 578 p.

Wyllie, M.R., Gregory, A.R. and Gardner, G.H.F. (1956), Elastic wave velocities in heterogeneous and porous media: Geophysics *21/1*, 41-70.

Yilmaz, Ö. (1987), Seismic Data Processing: Society of Exploration Geophysicists, Tulsa, Oklahoma, 526 p.

Yin, H., Nur, A. and Mavko, G. (1993), Critical porosity - A physical boundary in poroelasticity: Int. J. Rock. Mech. Min. Sci. and Geomech. Abstr. *30/7*, 805-808.

ACKNOWLEDGMENTS

This thesis could not have been completed without the support of my two main advisors. I am very thankful to Prof. Daniel Bernoulli and Prof. Gregor Eberli, who initiated my fascinating thesis topic and who made this study possible.

While finishing my diploma in the Bernoullianum at the University of Basel, it was maybe not a coincidence that Dan Bernoulli, the 'true' Basler in Zürich, offered me the opportunity to join his team at the ETH. His open personality, which I already have experienced when I started my studies in Basel, made me feel quickly comfortable in Zürich. The discussions with Dan, either with a very pleasant and social field geologist, or even with a stressed professor at the institute, were helpful and could solve many questions. Gregor Eberli pointed my interest towards the rock-physical aspects of geology, something that was completely new to me, but he did 'lüpf mi uffs Velo', to use one of his favorite terms. I profited immensely from his experience in that special field somewhere between geology and geophysics. Thanks to Gregor, I became a guest student at the University of Miami, after having been only one year in Zürich. In Miami, he offered me to join the Bahamas Drilling Project, to install a new petrophysics lab, and to live in a (Latin-) American city; all these experiences made my stay in Miami exciting.

Prof. Alan Green gave me lots of advice from the geophysical side. He evaluated which steps were feasible and where the limits of the seismic modeling method were reached. His reviews of the manuscript helped to improve this thesis a lot. I also thank him for allowing me to use the hard- and software of the computer facilities on Hönggerberg. The whole reflection seismology group at the Geophysical Institute ETH-Hönggerberg helped and explained me the dangers and tricks of the seismic modeling software. A big 'thank you' to Eva Lanz, Martin Stäuble, and especially to Heinrich Horstmeyer, who spent many hours looking for the bugs I planted in the system - without his help, the modeling study would not have been possible.

'Grazie mille' to Maria Mutti, Diethard Sanders and to Adam Vecsei; their strenuous fieldwork in the sheep-country of the Maiella provided the basis to perform the seismic modeling study. The days I could spend with the whole group in the field, either on dry limestone-mountains or afterwards, in the Albergo Mamma Rosa, were always a great pleasure. Maria Mutti is also acknowledged for converting the abstract into a Riassunto.

During my stay in Miami, Jaap Focke and Volker Vahrenkamp from the K.S.E.P.L. Shell Research Laboratory in Rijswijk, Holland, financed my research time at the Rosenstiel School. I am very grateful for their support. My participation in the Bahamas Drilling Project was also made possible by the Swiss National Science Foundation, who made a big contribution to this drilling project, together with several industrial sponsors and the American National Science Foundation. It was a great pleasure to be part of the Bahamas Drilling Project team. Especially working on the drill site was an unforgettable experience; I am thankful to Bob Ginsburg, Peter Swart, Jeroen Kenter, Donald McNeill, Leslie Melim, Carry Kievman and Thierry Guyomard. Also thanks to the outboard-engine specialist Phil Kramer, who organized collection of mudsamples in Florida Bay.

The first petrophysical measurements were performed at the University of Geneva. A special thanks to Souad Sellami and Catia Moschella, who measured some samples and helped and explained me how to handle the equipment.

I am grateful to Karl Coyner, the genius from Verde GeoScience, who invented, built, installed, and repaired the ultrasonic velocity-meter in the petrophysics laboratory in Miami. His 'macchina verde' became famous, not only for the strange noise of the hand pump.

I am thankful to Dr. Martinelli from ELF Italiana in Pescara, who was so kind to provide a copy of the seismic section from the Adriatic subsurface.

Thanks to Lisa dell'Angelo and Trey Meckel who had to suffer during correcting my written English. I am also grateful to Eva Sauter who was 'die gute Seele' of our group, to Gabriella Carlini and Frowin Pirovino for preparing thin sections and to Urs Gerber, who prepared the photographs.

A huge 'danggscheen' to all my friends at the ETH in Zürich and at RSMAS in Miami for being always a great company. Luckily, you all were friendly, funny, and crazy enough, that we could spend lots of wonderful and memorable times.

But most of all, I thank my parents for all their love and support, and I dedicate this thesis to them.

CURRICULUM VITAE

Flavio Stefano Anselmetti

Date of birth: September 3, 1965
Place of birth: Basel, Switzerland
Citizenship: Berzona / Ti, Switzerland

Education:

1972 - 1976:	Primary School Wasserstelzen, Riehen/BS
1976 - 1984	Gymnasium Bäumlihof Basel, Matura (Type C)
1984 - 1990:	Studies of Geology at University of Basel
January 1990	Diploma in Geology; Diploma thesis: "Geologie und Tektonik der frontalen Wildhorndecke in der Morgenberghorn-Dreispitzgruppe (Suldtal-Kiental / Berner Oberland)" Supervisor: Prof. H.P. Laubscher
April 1990:	Begin as Ph.D. student at the Geological Institute of the Swiss Federal Institute of Technology, Zürich, Switzerland Supervisors: Prof. D. Bernoulli, ETH Zürich and Prof. G. Eberli, RSMAS-MGG, Univ. of Miami, U.S.A.; Topic: "Physical Properties and Seismic Response of Carbonate Sediments and Rocks"
1991 - 1993:	Visiting student at the Rosenstiel School of Marine and Atmospheric Science, Division of Marine Geology and Geophysics, University of Miami, U.S.A.; Participant of the Bahamas Drilling Project
1993 - 1994:	Continuation of Ph.D. thesis at the ETH in Zürich
1 Sept. 1994	Ph.D. defense, Zürich

Leer - Vide - Empty

APPENDIX

Table 5 : Petrophysical data of Maiella samples.

Tables 6 a, b: Compressional wave velocities of Maiella samples at different confining pressures (only samples with pressures higher than 300 MPa).

Table 7 a: Petrophysical data of samples from hole Clino on Great Bahama Bank.

Table 7 b: Petrophysical data of samples from hole Unda on Great Bahama Bank.

Table 8 a: Compressional wave velocities of Bahamas samples (# 1-54) at different effective pressures.

Table 8 b: Compressional wave velocities of Bahamas samples (# 57-93) at different effective pressures.

Table 9: Petrophysical data of Florida Bay samples.

sample #	location	forma-tion	dominant pore type (only when thinsection)	wet bulk density (g/cm^3)	grain density (g/cm^3)	porosity (%)	Vp	Vs1	Vs2 (m/s)	Vs mean	Vp/Vs	acoustic impe-dance
							at 8 (20) MPa effect. pressure					
FA154	Roccamorice	LIL	dense c.	2.58	2.72	8.4	5452	2986	2967	2976	1.83	14043
88092	Roccamorice	LIL		2.22	2.72	30	3680					8159
FA155	Roccamorice	LIL	micro-p.	2.43	2.72	17	4021	2264	2282	2273	1.77	9774
89150	Fonte Macchialunga	LIL		2.49	2.72	13	4969					12388
88092	Roccamorice	LIL		2.17	2.72	32	3336					7236
88092	Roccamorice	LIL		2.20	2.72	31	3656					8041
FA182	St. Bartolomeo	HEM		2.58	2.68	6.2	4505	2514	2533	2524	1.79	11614
FA184	St. Bartolomeo	HEM	micro-p.	2.48	2.72	14	4584	2610	2600	2605	1.76	11374
FA183	St. Bartolomeo	HEM	micro-p.	2.57	2.68	6.9	4355	2567	2556	2561	1.70	11176
FA181	St. Bartolomeo	HEM	micro-p.	2.48	2.72	14	4572	2579	2579	2579	1.77	11332
FA 30	Decontra	HEM	micro-p.	2.58	2.72	8.2	4883					12594
FA 29	Decontra	HEM	micro-p.	2.48	2.72	14	4687					11630
89148	Fonte Macchialunga	BRL		2.66	2.72	3.1	5876					15630
89148	Fonte Macchialunga	BRL		2.66	2.72	3.5	5864					15587
89148	Fonte Macchialunga	BRL		2.65	2.72	3.7	5775					15304
FA179	St. Bartolomeo	BRL	dense c.	2.67	2.72	2.6	6115	3231	3236	3234	1.89	16346
FA180	St. Bartolomeo	BRL	dense c.	2.58	2.72	7.9	5536	3048	3031	3040	1.82	14309
FA186	St. Bartolomeo	BRL	dense c.	2.64	2.72	4.5	5739	3145	3125	3135	1.83	15161
FA185	St. Bartolomeo	BRL	dense c.	2.63	2.72	5.3	5815	3136	3150	3143	1.85	15283
FA13v	Decontra	BRL	dense c.	2.57	2.72	8.5	5529	2946	2952	2949	1.87	14232
FA13h	Decontra	BRL	dense c.	2.59	2.72	7.4	5580	2988	2998	2993	1.86	14465
FA12	Decontra	BRL	dense c.	2.65	2.72	3.9	5938	3076	3062	3069	1.93	15745
89012	Pesco Falcone	PFR		2.60	2.72	7.2	5641					14645
90086	Tre Portoni	PFR	dense c.	2.68	2.72	2.3	6061					16240
90082	Tre Portoni	PFR	intra-p.	2.44	2.72	17	5157					12571
89076	Mt. Rapina	PFR		2.64	2.72	4.6	5957					15722
90086	TrePortoni	PFR	dense c.	2.70	2.72	1.3	5791					15616
89012	Pesco Falcone	PFR		2.57	2.72	8.5	5474					14090
89012	Pesco Falcone	PFR		2.58	2.72	8.0	5538					14302
90073	Tre Portoni	PFR	dense c.	2.57	2.72	8.7	5990					15398
FA135	Pesco Falcone	PFR	dense c.	2.43	2.72	17	5052	2795	2783	2789	1.81	12293
FA138	Pesco Falcone	PFR	dense c.	2.48	2.72	14	5116	2792	2749	2771	1.85	12678
FA136	Pesco Falcone	PFR	dense c.	2.62	2.72	6.0	6108	3203	3236	3220	1.90	15977
FA130	Tre Portoni	PFR	dense c.	2.54	2.72	11	5567	2967	3029	2998	1.86	14121
FA131	Pesco Falcone	PFR	dense c.	2.55	2.72	9.8	5742	3008	3041	3024	1.90	14656
FA132	Pesco Falcone	PFR	co. mold.	2.47	2.72	15	5322	2799	2800	2799	1.90	13119
FA129	Tre Portoni	PFR	dense c.	2.62	2.72	6.0	5746	3057	3061	3059	1.88	15030
FA126	Colle Daniele	PFS	inter-p.	2.47	2.72	15	4791	2706	2694	2700	1.77	11830
FA133	Pesco Falcone	PFS	micro-p.	2.44	2.72	16	4351	2428	2474	2451	1.78	10620
FA191	Mt. Focalone	PFS	micro-p.	2.40	2.72	19	4124	2395	2376	2386	1.73	9898
FA134	Pesco Falcone	PFS	micro-p.	2.47	2.72	15	4761	2648	2671	2660	1.79	11740
FA137	Pesco Falcone	PFS	micro-p.	2.45	2.72	16	4519	2553	2580	2567	1.76	11076
FA18vh1	Decontra	SSB	dense c.	2.64	2.72	4.7	5923	3128	3126	3127	1.89	15627
FA187	Mt. Focalone	SSB	dense c.	2.64	2.72	4.9	6021	3216	3220	3218	1.87	15870
FA18vh2	Decontra	SSB	dense c.	2.64	2.72	4.7	5982	2899	2927	2913	2.05	15781
FA17v2	Decontra	SSB		2.67	2.72	3.1	5957	3102	3070	3086	1.93	15877
BK 102	Decontra	SSB		2.62	2.72	5.9	5848	3109	3088	3099	1.89	15309
FA188	Mt. Focalone	SSB	dense c.	2.67	2.72	2.7	6136	3219	3235	3227	1.90	16392
FA189	Mt. Focalone	SSB	dense c.	2.52	2.72	12	5930	3135	3135	3135	1.89	14917
88163	Decontra	SSB	micro-p.	2.60	2.72	7.1	5683	2980	2918	2949	1.93	14761
FA190	Mt. Focalone	SSB	dense c.	2.62	2.72	5.6	6272	3262	3284	3273	1.92	16452
FA125	Colle Daniele	SSB	dense c.	2.63	2.72	5.0	5945	3142	3159	3151	1.89	15652
FA124	Colle Daniele	SSB	intra-p.	2.51	2.72	12	5630	2972	2981	2976	1.89	14142
88161	Decontra	SSB	dense c.	2.58	2.72	8.4	5541	2960	2963	2962	1.87	14272
89093	Monte Amaro	SSR		2.68	2.72	2.3	6434					17241
89093	Monte Amaro	SSR		2.69	2.72	1.7	6429					17284
89093	Monte Amaro	SSR		2.69	2.72	1.4	6395					17233
90067	Fondo di Maiella	SSR	micro-p.	2.41	2.72	18	4483					10799
90067	Fondo di Maiella	SSR	micro-p.	2.43	2.72	17	4690					11380
FA15h	Decontra	SSR	micro-p.	2.51	2.72	12	4324	2454	2442	2448	1.77	10842
90069	Fondo di Maiella	SSR	dense c.	2.70	2.72	0.84	6258					16920
88186	Monte Amaro	SSR	dense c.	2.61	2.72	6.2	5577					14577
88186	Monte Amaro	SSR	dense c.	2.58	2.72	8.1	5930					15305
90120	Ravone della Vespa	SSR	dense c.	2.64	2.72	4.7	6031					15910
88185	Monte Amaro	SSR	dense c.	2.62	2.72	6.1	5719					14957
88185	Monte Amaro	SSR	dense c.	2.61	2.72	6.3	5830					15223
88184	Monte Amaro	SSR		2.71	2.72	0.38	6460					17517
BI 196	Decontra	SSR		2.56	2.72	9.3	5449	2926	2936	2931	1.86	13953
BI 151	Decontra	SSR		2.67	2.72	2.9	5916	3117	3143	3130	1.89	15791
FA 15	Decontra	SSR	micro-p.	2.52	2.72	12	4128					10409
FA 17v1	Decontra	SSR		2.66	2.72	3.6	6070	3128	3125	3126	1.94	16128
88164	Decontra	SSR	dense c.	2.58	2.72	8.3	5461	2941	2954	2948	1.85	14073
88168	Decontra	SSR	micro-p.	2.67	2.72	2.8	5721	2942	2927	2935	1.95	15280
88140	Pesco Falcone	SSR		2.45	2.72	16	5021					12316

88159	Decontra	SSR	micro-p.	2.57	2.72	8.5	5373	2862	2858	2860	1.88	13827
88158	Decontra	SSR	dense c.	2.62	2.72	5.7	6264	3251	3235	3243	1.93	16419
88184	Monte Amaro	SSR		2.71	2.72	0.76	6398					17307
88080 .	Colle della Civita	SSR		2.49	2.72	13	4803					11971
88080	Colle della Civita	SSR		2.48	2.72	14	4720					11729
88160	Decontra	SSR	dense c.	2.62	2.72	5.9	5770	3105	3098	3101	1.86	15103
89018	Decontra	SSS		2.57	2.72	8.5	5320					13693
88162	Decontra	SSS	micro-p.	2.66	2.72	3.5	5600	3079	3061	3070	1.82	14884
89018	Decontra	SSS		2.58	2.72	8.4	5451					14038
89018	Decontra	SSS		2.58	2.72	8.1	5547					14320
88170	Decontra	SSS	micro-p.	2.66	2.72	3.6	5616	3027	3030	3029	1.85	14921
BI 206	Decontra	SSS		2.61	2.72	6.2	5796	3066	3057	3061	1.89	15147
89249	Mt. Rapina	SSS		2.47	2.72	15	4376					10791
BI 126	Decontra	SSS		2.64	2.72	4.4	5696	2838	2864	2851	2.00	15061
BI 150	Decontra	SSS		2.61	2.72	6.3	5401	2950	2947	2949	1.83	14104
88079	Colle della Civita	SSS		2.38	2.72	20	4215					10050
BK 66	Decontra	SSS		2.52	2.72	11	5001	2698	2726	2712	1.84	12625
BI 55	Decontra	SSS		2.64	2.72	4.9	5546	2917	2919	2918	1.90	14616
FA 16	Decontra	SSS		2.53	2.72	11	5107					12907
88079	Colle della Civita	SSS		2.37	2.72	21	4085					9683.3
BI 83	Decontra	SSS		2.60	2.72	6.7	5374	2847	2864	2856	1.88	13994
FA14h	Decontra	SSS	micro-p.	2.55	2.72	10	5168	2792	2797	2795	1.85	13170
88079	Colle della Civita	SSS		2.39	2.72	20	4080					9737.2
FA16v2	Decontra	SSS		2.53	2.72	11	4998	2724	2724	2724	1.83	12635
FA14v	Decontra	SSS	micro-p.	2.53	2.72	11	5047	2774	2770	2772	1.82	12749
FA 3	Valle Tre Grotte	??	dense c.	2.60	2.72	6.7	5472					14254
90028	Ravone della Vespa	CCS	micro-p.	2.56	2.72	9.5	4718					12061
90046	Fondo di Maiella	CCS	inter-p.	2.48	2.72	14	4487					11145
90028	Ravone della Vespa	CCS	micro-p.	2.55	2.72	9.7	5286					13503
FA102	Mt. Focalone	CCS	inter-p.	2.42	2.72	17	4657	2579	2544	2561	1.82	11292
90037	Fondo di Maiella	CCS	micro-p.	2.59	2.72	7.6	5024					13007
FA199	Mt. Focalone	CCS	inter-p.	2.23	2.72	29	4135	2339	2665	2502	1.65	9224
90005	Mt. Focalone	CCS	inter-p.	2.36	2.72	21	3668					8667
88147	Rava del Ferro	CCS		2.58	2.72	7.9	5542					14324
88132	Rava del Ferro	CCS		2.50	2.72	13	4838					12087
FA19	Decontra	CCS	inter-p.	2.44	2.72	16	4367	2373	2361	2367	1.85	10674
FA196	Mt. Rotondo	CCS	inter-p.	2.27	2.72	26	3734	2097	2077	2087	1.79	8487
FA193	Mt. Rotondo	CCS	micro-p.	2.42	2.72	18	4268	2448	2460	2454	1.74	10332
FA119	Mt. Focalone	CCS	inter-p.	2.47	2.72	15	4853	2667	2686	2677	1.81	11984
89031	Valle Santo Spirito	CCS		2.27	2.72	26	3663					8317
FA192	Mt. Rotondo	CCS	inter-p.	2.32	2.72	24	4200	2319	2218	2269	1.85	9733
88149	Rava del Ferro	CCS		2.65	2.72	3.8	5907					15679
FA122	Colle Daniele	CCS	inter-p.	2.31	2.72	24	4012	2260	2245	2253	1.78	9271
FA128	Colle Daniele	CCS	inter-p.	2.43	2.72	17	4827	2575	2626	2601	1.86	11744
FA123	Colle Daniele	CCS	inter-p.	2.14	2.72	34	3222	1645	1649	1647	1.96	6887
90092	Rava Sfonda	CCS	micro-p.	2.31	2.72	24	4204					9708
89031	Valle Santo Spirito	CCS		2.25	2.72	28	3859					8671
FA103	Mt. Focalone	CCS	inter-p.	2.27	2.72	26	3308	2029	1973	2001	1.65	7507
FA198	Mt. Focalone	CCS	micro-p.	2.29	2.72	25	3426	1857	1835	1846	1.86	7850
FA175	Valle Tre Grotte	CCS	inter-p.	2.27	2.72	27	3574	1966	1970	1968	1.82	8102
FA178	Valle Tre Grotte	CCS	inter-p.	2.23	2.72	29	3491	1866	1828	1847	1.89	7787
FA177	Valle Tre Grotte	CCS	micro-p.	2.41	2.72	18	4133	2247	2239	2243	1.84	9955
FA176	Valle Tre Grotte	CCS	micro-p.	2.39	2.72	19	4248	2342	2345	2343	1.81	10156
FA120	Mt. Focalone	CCB	dense c.	2.62	2.72	6.1	5650	2963	3024	2994	1.89	14777
90006	Mt. Focalone	CCB		2.57	2.72	8.6	5701					14660
FA174	Valle Tre Grotte	CCB	micro-p.	2.40	2.72	19	4301	2424	2428	2426	1.77	10315
FA168	Valle Tre Grotte	TGB	dense c.	2.55	2.72	10	5289	2755	2798	2776	1.90	13471
FA166	Valle Tre Grotte	TGB	dense c.	2.54	2.72	10	5394	2920	2944	2932	1.84	13727
FA167	Valle Tre Grotte	TGB	dense c.	2.53	2.72	11	5407	2959	2944	2951	1.83	13668
FA165	Valle Tre Grotte	TGB	dense c.	2.65	2.72	3.7	6214	3272	3242	3257	1.91	16496
FA164	Valle Tre Grotte	TGB	dense c.	2.68	2.72	2.4	6260	3281	3319	3300	1.90	16762
89027	Valle Tre Grotte	TGTS		2.48	2.72	14	4825					11966
FA162	Valle Tre Grotte	TGTS	micro-p.	2.47	2.72	14	4813	2674	2673	2674	1.80	11901
FA157	Valle Tre Grotte	TGTS	micro-p.	2.56	2.72	9.1	5440	2971	2960	2966	1.83	13946
FA169	Valle Tre Grotte	TGTS	micro-p.	2.37	2.72	21	4241	2373	2381	2377	1.78	10049
FA170	Valle Tre Grotte	TGTS		2.42	2.72	18	4321	2466	2467	2467	1.75	10441
FA160	Valle Tre Grotte	TGTS	micro-p.	2.46	2.72	16	4762	2666	2664	2665	1.79	11693
FA159	Valle Tre Grotte	TGTS	dense c.	2.65	2.72	3.9	6113	3221	3230	3226	1.90	16209
FA156	Valle Tre Grotte	TGTS	micro-p.	2.58	2.72	8.3	5453	2985	3001	2993	1.82	14056
FA158	Valle Tre Grotte	TGTS		2.54	2.72	10	5217	2864	2848	2856	1.83	13272
FA171	Valle Tre Grotte	VIU	dense c.	2.69	2.72	1.5	6277	3281	3295	3288	1.91	16903
FA172	Valle Tre Grotte	VIU	dense c.	2.57	2.72	8.7	5483	2986	2986	2986	1.84	14094
FA173	Valle Tre Grotte	VIU	dense c.	2.55	2.72	9.8	5041	2669	2709	2689	1.87	12861
FA117	Mt. Focalone	MUP	dense c.	2.66	2.72	3.4	5837	3061	3049	3055	1.91	15525
90091	Rava Sfonda	MUP	dense c.	2.65	2.72	4.3	5747					15201
FA 27	Rava del Ferro	MUP	dense c.	2.72	2.72	0.0	6411					17438
FA127	Colle Daniele	MUP	dense c.	2.60	2.72	7.1	6084	3201	3204	3202	1.90	15808
90013	Ravone della Vespa	MUP	inter-p.	2.50	2.72	13	4971					12422

FA139	Rava del Ferro	MUP	dense c.	2.64	2.72	4.5	5939	3137	3163	3150	1.89	15687
FA140	Rava del Ferro	MUP		2.61	2.72	6.2	6027	3118	3148	3133	1.92	15747
90019	Ravone della Vespa	MUP	dense c.	2.66	2.72	3.6	6227					16549
90013 .	Ravone della Vespa	MUP	inter-p.	2.56	2.72	9.6	5245					13405
FA 27	Rava del Ferro	MUP	dense c.	2.71	2.72	0.63	6418					17376
FA194	Mt. Rotondo	MUP	dense c.	2.65	2.72	3.8	6226	3264	3251	3258	1.91	16523
88060	Fondo di Maiella	MUP	dense c.	2.58	2.72	8.0	6178					15952
FA195	Mt. Rotondo	MUP	dense c.	2.68	2.72	2.0	6346	3335	3325	3330	1.91	17034
FA143	Rava del Ferro	MUP	dense c.	2.69	2.72	1.4	6280	3298	3286	3292	1.91	16919
520	Ravone della Vespa	MUP		2.55	2.72	9.7	5391					13766
88060	Fondo di Maiella	MUP	dense c.	2.63	2.72	5.0	6360					16750
88060	Fondo di Maiella	MUP	dense c.	2.62	2.72	5.7	6114					16029
506	RavaDelFerro	MUP		2.71	2.72	0.66	6228					16858
FA142	Rava del Ferro	MUP	dense c.	2.70	2.72	1.1	6440	3358	3371	3364	1.91	17385
FA141	Rava del Ferro	MUP	dense c.	2.69	2.72	1.5	6484	3352	3329	3341	1.94	17456
FA197	Mt. Rotondo	MUP	dense c.	2.62	2.72	6.0	5977	3070	3060	3065	1.95	15640
FA101	Mt. Focalone	MUB	co. mold.	2.39	2.72	20	5304					12653
FA100	Mt. Focalone	MUB	co. mold.	2.39	2.72	20	5039	3012	2994	3003	1.68	12027
FA118	Mt. Focalone	MUB	dense c.	2.65	2.72	3.8	6114	2964	3088	3026	2.02	16225
FA121	Mt. Focalone	MUB	co. mold.	2.58	2.72	8.0	5955	3163	3172	3168	1.88	15379
FA161	Valle Tre Grotte	MUB	co. mold.	2.38	2.72	20	5416	2858	2902	2880	1.88	12869
88053	Rava del Ferro	MCL		2.69	2.72	1.9	6377					17128
88065	Rava del Ferro	MCL		2.67	2.72	3.0	6272					16729
88065	Rava del Ferro	MCL		2.69	2.72	1.5	6129					16504
FA152	Rava del Ferro	MCL		2.75	2.85	5.7	6043	3191	3202	3196	1.89	16594
FA148	Rava del Ferro	MCL		2.70	2.72	1.0	6073	3263	3279	3271	1.86	16401
FA150	Rava del Ferro	MCL		2.72	2.89	9.0	6066	3150	3212	3181	1.91	16493
FA151	Rava del Ferro	MCB		2.74	3.00	13	4608	2502	2531	2516	1.83	12645
FA149	Rava del Ferro	MCB		2.89	3.18	13	4962	2894	2903	2899	1.71	14359
FA147	Rava del Ferro	MCB		2.79	3.01	11	4692	2559	2564	2561	1.83	13085
FA144	Rava del Ferro	LCP	dense c.	2.69	2.72	1.5	6280	3285	3287	3286	1.91	16908
FA145	Rava del Ferro	LCP	dense c.	2.68	2.72	2.1	6258	3282	3263	3273	1.91	16792
FA146	Rava del Ferro	LCP		2.70	2.72	1.0	6449	3168	3216	3192	2.02	17415
SD 19	Fondo di Maiella	LCP		2.69	2.72	1.6	6271					16877

Table 5: Petrophysical data of measured samples from Maiella. Formation codes: LIL=Lithothamnium Limestone (Bolognano Form.); HEM=hemipelagic marls (Bolognano Form.); BRL=bryozoan limestone (Bolognano Form.); PFR=Pesco Falcone coral reefs; PFS=Pesco Falcone sands/silts; SSB=Valle Santo Spirito Form. breccias; SST=Valle Santo Spirito Form. turbidites; SSS=Valle Santo Spirito Form. Scaglia; CCS=Calcari Cristallini (Orfento Form.) sands/silts; CCB=Calcari Cristallini breccias (Orfento Form.); TGB=Tre Grotte Form. breccias; TGTS=Tre Grotte Form. turbidites/Scaglia; VIU=Valle del Inferno unit; MUP=Cima delle Murelle Form. platform carbonates; MUB=Cima delle Murelle Form. rudist bisostromes; MCL=mid-Creataceous unconformity limestone breccias; MCB=mid-Cretaceous unconformity bauxites; LCP=Lower Cretaceous platform. Abbreviations for pore types: inter-p.= interparticle porosity; micro-p.=microporosity; intra p.=intraparticle porosity; co. mold.=coarse moldic porosity; dense c.=densely cemented.

conf. press. (MPa)	8860 -1	8860 -2	8860 -3	8865 -2	8879 -1	8879 -2	8879 -3	8892 -1	8892 -2	88132 -1	88140	88147	88185 -1	88185 -3	88186 -1	88186 -2	8912 -1	8912 -2	8912 -3	8976
0	5881	6058	6156	5937		4031	4013	3237	3522	3660	4665	5164	5603	5697	5089	5737	5266	5418	5566	5725
20	6114	6178	6360	6129	2788	4085	4080	3336	3708	4838	5021	5542	5719	5843	5640	5945	5474	5538	5641	5957
40	6176	6196	6376	6129	4215	4092	4080	3347	3751	5088	5103	5604	5732	5870	5691	6076	5486	5551	5654	6044
60	6191	6213	6393	6206	4233	4140	4115	3394	3751	5077	5124	5667	5746	5857	5691	6076	5498	5551	5667	6118
80	6191	6231	6393	6206	4252	4147	4150	3405	3626	5119	5124	5693	5759	5870	5771	6062	5498	5563	5680	6163
100	6223	6231	6409	6221	4252	4169	4150	3441	3708	5141	5145	5706	5759	5870	5784	6122	5511	5563	5693	6193
120	6238	6340	6426	6221	4270	4176	4186	3528	3765	5152	5156	5732	5759	5885	5784	6107	5511	5563	5706	6209
140	6238	6340	6426	6221	4270	4190	4150	3553	3809	5152	5177	5732	5759	5885	5784	6122	5511	5563	5706	6224
160	6238	6340	6426	6237	4289	4190	4186	3566	3839	5184	5188	5745	5759	5885	5784	6122	5522	5563	5706	6240
180	6238	6340	6426	6253	4270	4183	4186	3592	3869	5216	5231	5758	5759	5885	5797	6122	5522	5563	5706	6240
200	6238	6340	6426	6301	4288	4183	4186	3645	3962	5227	5242	5758	5772	5885	5811	6152	5522	5563	5706	6255
220	6238	6340	6442	6253	4288	4204	4186	3700	4011	5239	5242	5772	5772	5912	5852	6152	5522	5576	5706	6255
240	6238	6340	6442	6269	4308	4204	4186	3714	4028	5272	5253	5772	5772	5912	5852		5522	5576	5706	6255
260	6238	6340	6442	6317	4308	4233	4186	3728	4095	5250	5264	5772	5786	5912	5838	6137	5522	5588	5706	6255
280	6238	6340	6442	6317	4327	4255	4222	3757	4112		5286	5785	5786	5912	5838		5522	5588	5706	6271
300	6238	6340	6442	6317	4346	4293	4222	3786	4147	5272	5286	5785		5912	5851	6152	5522	5588	5706	6271
320				6301	4365	4331	4259	3800			5286	5785	5799	5912	5865		5522	5588		
340				6301	4404	4362	4297	3800				5785		5912	5893	6168	5535	5588		
360				6301	4444	4409	4335	3860				5785		5912	5893		5535			
380				6317	4547	4433	4374	3891				5785		5912	5907	6168	5535			
400				6317	4569	4473		3906				5785		5926	5907	6168	5535			

Table 6 a: Compressional wave velocities (Vp, m/s) at different confining pressures of samples from Montagna della Maiella. Only samples are displayed that were measured at confining pressures above 300 MPa (all measurements without pore fluid). For plotted curves see Figure 12 b.

conf. press. (MPa)	8993 -1	8993 -2	8993 -3	89148 -1	89150 -2	8924 9	905-B	906	9013 -A	9028 -B	9067 -A	9067 -B	9069	9091 -A	9092 -B	90120 -B	FA27 -A	FA27 -B	506
0	6401	6314	6347	5777	4881	4172	3062	5519	4788	4806	4068	4165	6061	5253	3803	5780	6242	6251	5851
20	6434	6395	6429	5876	4969	4376	3808	5741	5245	5286	4590	4690	6258	5747	4422	6031	6418	6411	6228
40	6434	6412	6446	5890	4989	4391	3928	5810	5465	5472	4676	4790	6289	5910	4486	6120	6418	6444	6243
60	6434	6412	6446	5904	4999	4406	4023	5895	5551	5545	4729	4826	6321	5995	4454	6150	6435	6461	6243
80	6434	6395	6480	5919	5009	4430	4088	5924	5627	5659	4747	4855	6321	6039	4398	6165	6435	6477	6274
100	6450	6395	6480	5947	5019	4445	4139	5998	5652	5711	4738	4874	6321	6068	4494	6165	6435	6477	6306
120	6450	6412	6480	5933	5029	4453	4191	5998	5666	5737	4765	4893	6321	6112	4375	6165	6451	6477	6322
140	6434	6428	6480	5947	5040	4461	4227	5998	5679	5737	4802	4893	6337	6112	4375	6180	6451	6477	6322
160	6450	6428	6480	5961	5050	4477	4244	5924	5718	5777	4821	4903	6337	6142	4390	6196	6451	6494	6337
180	6484	6428	6480	5976	5060	4485	4281	6027	5718	5804	4830	4903	6353	6157	4422	6196	6451	6494	6354
200	6484	6428	6480	5990	5060	4493	4318	6027	5744	5818	4839	4903	6353	6173	4454	6196	6451	6494	6354
220	6484	6428	6497	5976	5060	4501	4355	5953	5744	5831	4868	4903	6369	6173	4486	6211	6451	6494	6354
240	6467	6428	6497		5060	4509	4374	5953	5758	5845	4887	4903	6369	6188	4535	6211	6468	6511	6354
260	6467	6445	6497	5976	5060	4578	4394	5953	5758	5845	4896	4826	6369	6188	4569	6211	6468	6511	6354
280	6467	6445	6497		5060	4518	4413	5939	5771	5859	4915	4817	6369	6188	4646	6227	6468	6528	6370
300	6467	6445	6497	5990	5060	4526	4433	5968	5771	5872	4925	4817	6369	6188	4672	6227	6468	6528	6370
320	6467	6445				4534									4681				
340	6484	6445				4534									4690				
360	6484	6445				4542													
380	6484	6445				4542													
400	6484	6445				4550													

Table 6 b: Compressional wave velocities (Vp, m/s) at different confining pressures of samples from Montagna della Maiella. Only samples are displayed that were measured at confining pressures above 300 MPa (all measurements without pore fluid). For plotted curves see Figure 12 b.

sample #	depth (ft)	(bmp) (in)	original type of sediment	observed dominant pore type	wet bulk-density (g/cm^3)	grain density (g/cm^3)	perme-ability (md)	porosity (%)	cal-cite	dolo-mite (%)	arago-nite	Vp	Vs1 (m/s) at effect.	Vs2 8 MPa pressure	Vs mean	Vp/Vs	acoust. impedance $10^3 kg/m^2 s$
46	86	5	coral	intra-p.	2.26	2.77		29	75	0	25	4722	2414	2414	2414	1.96	10694
57	110	9	peloidal to skeletal grainstone	co. mold.	2.10	2.71		36	100	0	0	3801	1977	2062	2020	1.88	7970
58	182	4	coral	intra-p.	2.19	2.71		31	100	0	0	4917	2391	2370	2380	2.07	10747
16	185	7	coarse skeletal grainstone	co. mold.	1.87	2.71		50	100	0	0	3209	1428	1435	1432	2.24	6013
59	210	9	peloidal to skeletal grainstone	co. mold.	2.16	2.71		32	100	0	0	4876	2565	2582	2574	1.89	10556
17	281	6	halimeda-peloidal packstone	co. mold.	2.06	2.73	14	39	85	15	0	5043	1925	1936	1930	2.61	10386
18	294	5	packstone	fi. mold.	2.02	2.71		41	100	0	0	4392	1899	1938	1919	2.29	8854
19	341	2	halimeda packstone	dense c.	2.47	2.71		14	100	0	0	5818	3000	2860	2930	1.99	14393
47	365	10	coral	intra-p.	2.52	2.71	63	11	100	0	0	5855	3060	3046	3053	1.92	14783
20	442	6	skeletal(?) grainstone	co. mold.	1.81	2.71	81	53	100	0	0	3865	2090	2050	2070	1.87	6995
48	476	0	skeletal packstone	co. mold.	1.86	2.71		50	100	0	0	3864	1889	1777	1833	2.11	7189
60	488	7	skeletal to peloidal grainstone	co. mold.	2.05	2.71		39	100	0	0	3520	1946	1874	1910	1.84	7201
21	525	7	skeletal packstone	co. mold.	2.18	2.73	2.0	33	84	16	0	4110	2221	2105	2163	1.90	8943
61	526	6	halimeda packstone	co. mold.	2.00	2.75		43	84	0	16	2960	1455	1460	1458	2.03	5917
22	586	5	skeletal packstone	co. mold.	2.05	2.75	146	41	76	16	9	2986	1368	1384	1376	2.17	6107
23	611	5	skeletal packstone	fi. mold.	1.96	2.74	49	45	81	19	0	2675	1383	1399	1391	1.92	5245
24	693	8	wackestone	dense c.	2.55	2.71	<0.01	9	100	0	0	5454	2888	2885	2887	1.89	13934
62	720	10	skeletal wacke- to packstone	dense c.	2.60	2.71		7	100	0	0	5394	2912	2923	2918	1.85	14009
49	741	0	peloidal(?) grainstone	fi. mold.	2.33	2.75	0.08	24	78	22	0	4641	2528	2510	2519	1.84	10793
25	774	10	globigerina packstone	micro-p.	1.91	2.77		49	70	15	15	2503	1101	1090	1095	2.29	4783
26	840	3	skeletal packstone, redalgaes	dense c.	2.54	2.71	0.01	10	100	0	0	5350	2833	2840	2836	1.89	13588
27	955	7	wackestone with few globigerinas	micro-p.	1.97	2.79	0.9	47	57	21	22	2219	1078	1075	1076	2.06	4365
50	1042	10	mudstone	micro-p.	1.85	2.78		53	70	0	30	2365	1046	1051	1048	2.26	4364
28	1084	6	globigerina wackestone	micro-p.	2.08	2.79		40	58	17	24	2368	980	987	983	2.41	4923
63	1151	10	skeletal grainstone	dense c.	2.68	2.85		9	11	89	0	5661	3163	3154	3158	1.79	15198
29	1165	0	skeletal to peloidal grainstone	dense c.	2.68	2.74	<0.01	4	81	19	0	6045	3157	3144	3150	1.92	16171
30	1206	8	no original grains preserved	dense c.	2.62	2.79	<0.01	10	48	52	0	5478	3026	3024	3025	1.81	14336
64	1343	10	fine skeletal packstone	fi. mold.	2.09	2.73		37	84	16	0	3093	1505	1530	1518	2.04	6479
31	1503	2	fine skeletal packstone	fi. mold.	2.01	2.74	<0.01	43	83	17	0	2927	1431	1445	1438	2.03	5871
52	1597	7	fine skeletal packstone	fi. mold.	2.07	2.76	41	39	71	29	0	2646	1277	1305	1291	2.05	5485
65	1617	10	peri-platform ooze	fi. mold.	2.04	2.73		40	86	14	0	2913	1519	1545	1532	1.90	5955
32	1674	10	globigerina-echinoderm packst.	micro-p.	2.15	2.74	31	35	82	18	0	2983	1417	1423	1420	2.10	6403
66	1681	0	globigerina-echinoderms packst.	fi. mold.	2.09	2.71		37	100	0	0	3103	1538	1528	1533	2.02	6499
69	1732	11	globigerina packstone	micro-p.	1.98	2.71		43	100	0	0	2618	1105	1102	1104	2.37	5179
68	1756	4	globigerina (blackened) packst.	micro-p.	2.02	2.71		41	100	0	0	2791	1308	1303	1306	2.14	5638
33	1758	2	globigerina-echinoderm packst.	micro-p.	1.99	2.74	153	44	79	21	0	2409	1056	1054	1055	2.28	4804
53	1798	0	laminated globigerina-packstone	micro-p.	1.84	2.76		53	66	34	0	2156	920	929	924	2.33	3974
67	1812	2	globigerina wackestone	inter-p.	2.03	2.77		42	64	36	0	2700	1236	1233	1234	2.19	5477
34	1985	9	globigerina wackestone	micro-p.	1.94	2.75	131	47	75	25	0	2402	1079	1079	1079	2.23	4663
35	2046	0	wackestone with globigerinas	micro-p.	2.05	2.75	39	41	75	25	0	2602	1205	1205	1205	2.16	5334
70	2049	11	coarse globigerina packstone	micro-p.	2.05	2.74		40	81	19	0	2541	1177	1182	1180	2.15	5208
54	2056	1	peri-platform ooze	fi. mold.	2.05	2.75	85	40	76	24	0	2947	1525	1485	1505	1.96	6043
71	2155	0	laminated wacke to packstone	micro-p.	2.37	2.73		22	84	16	0	4373	2501	2504	2502	1.75	10342
72	2156	7	burrowed peri-platform ooze	fi. mold.	2.23	2.71		29	100	0	0	3162	1551	1558	1554	2.03	7046
74	2183	10	laminated globigerina packstone	micro-p.	2.04	2.71		40	100	0	0	2424	1088	1073	1080	2.24	4938
36	2197	0	peri-platform ooze	fi. mold.	2.09	2.73	16	38	85	15	0	3151	1611	1536	1574	2.00	6578
73	2216	10	globigerina packstone	micro-p.	1.97	2.71		44	100	0	0	2478	1353	1360	1356	1.83	4890

Table 7 a: Petrophysical and lithological data of measured samples from hole Clino on Great Bahama Bank. Abbreviations for pore types: inter p.=interparticle porosity; micro-p.=microporosity; fi. mold=fine (<300μm) moldic porosity; co. mold.=coarse (>300μm) moldic porosity; intra p.=intraparticle porosity; dense c.=densely cemented.

sample #	depth (bmp) (ft)	(in)	original sediment type	observed dominant pore type	wet bulk-density (g/cm^3)	grain density (g/cm^3)	perme-ability (md)	porosity (%)	cal cite	dolo-mite (%)	arago-nite	Vp	Vs1 (m/s) at effect.	Vs2 8 MPa pressure	Vs	Vp/Vs	acoust. impedance $10^3 kg/m^2 s$
75	87	6	peloidal-skeletal grainstone	co. mold.	2.30	2.71		24	100	0	0	5379	2763	2783	2773	1.94	12389
1	135	2	skeletal(?) packstone	co. mold.	2.01	2.71		41	100	0	0	4476	2230	2240	2235	2.00	9001
76	185	0	peloidal(?) grainstone	co. mold.	1.91	2.71		47	100	0	0	3776	1787	1807	1797	2.10	7224
77	212	9	peloidal (?) to skeletal grainstone	co. mold.	2.08	2.71		37	100	0	0	4105	1690	1591	1640	2.50	8554
2	272	0	skeletal packstone	co. mold.	2.33	2.71		23	100	0	0	4998	2601	2601	2601	1.92	11636
79	356	4	packstone(?)	fi. mold.	2.12	2.85		40	12	88	0	3549	1950	1930	1940	1.83	7510
3	357	6	skeletal packstone	fi. mold	1.88	2.80		52	44	56	0	2238	1089	1079	1084	2.06	4206
80	368	9	skeletal grainstone(?)	inter-p.	2.03	2.83		44	23	77	0	3168	1639	1624	1632	1.94	6421
78	388	11	peloidal pack to grainstone	inter-p.	1.79	2.76		56	67	33	0	2433	1467	1467	1467	1.66	4361
37	401	0	peloidal to skeletal grainstone	co. mold.	2.09	2.76	169	39	65	35	0	3025	1565	1544	1554	1.95	6311
38	443	0	skeletal to peloidal grainstone	inter-p.	1.90	2.75		49	73	27	0	2568	1095	1105	1100	2.33	4887
81	451	10	peloidal to skeletal packstone(?)	micro-p.	2.02	2.71		41	100	0	0	3046	1545	1548	1546	1.97	6159
83	464	2	peloidal to skeletal packstone(?)	micro-p.	2.22	2.73		30	86	14	0	3905	2116	2088	2102	1.86	8686
39	517	6	skeletal packstone	fi. mold.	1.84	2.77		53	62	38	0	2638	1099	1105	1102	2.39	4865
4	595	0	skeletal to peloidal packstone	fi. mold.	1.95	2.77	106	47	63	37	0	2649	1026	1022	1024	2.59	5154
82	656	3	skeletal to peloidal packstone	micro-p.	1.89	2.75		50	72	28	0	2544	1252	1280	1266	2.01	4816
40	673	0	skeletal packstone	fi. mold.	1.86	2.75	102	52	74	26	0	2477	1288	1316	1302	1.90	4600
85	860	6	peloidal to skeletal packstone	inter-p.	1.99	2.77		45	63	37	0	2629	1215	1230	1222	2.15	5224
41	884	0	only few echinoderms preserved	inter-p.	1.99	2.84	678	47	18	82	0	2501	1310	1345	1328	1.88	4981
86	889	0	only few echinoderms preserved	inter-p.	2.08	2.84		42	14	86	0	3481	1812	1794	1803	1.93	7256
5	917	0	skeletal packstone	inter-p.	1.96	2.78		46	55	45	0	2403	1114	1111	1113	2.16	4721
6	938	0	nothing preserved	inter-p.	1.96	2.87		49	0	100	0	2697	1053	1051	1052	2.56	5274
84	945	7	miliolids and echinoderms	inter-p.	2.00	2.81		46	34	66	0	1907	1139	1136	1138	1.68	3808
7	961	0	skeletal grainstone	dense c.	2.61	2.87	0.8	14	0	100	0	5953	3167	3206	3187	1.87	15535
87	992	2	coral	intra-p.	2.08	2.87		43	0	100	0	4015	2070	2061	2066	1.94	8343
8	994	0	coral, encrusting red algae	intra-p.	2.23	2.87		35	0	100	0	4858	2580	2580	2580	1.88	10831
89	1008	4	only few redalgaes preserved	inter-p.	2.12	2.87		41	0	100	0	3176	1740	1736	1738	1.83	6733
42	1016	6	no original grains preserved	inter-p.	2.09	2.84	571	41	14	86	0	3192	1351	1377	1364	2.34	6678
43	1037	0	only few redalgaes preserved	inter-p.	2.35	2.84		27	20	80	0	4567	2526	2496	2511	1.82	10743
9	1056	0	only few redalgaes preserved	inter-p.	2.02	2.85		46	12	88	0	2405	995	987	991	2.43	4850
88	1092	3	few skeletal grains preserved	inter-p.	2.06	2.87		44	0	100	0	3001	1538	1533	1536	1.95	6189
44	1105	8	only few redalgaes preseved	inter-p.	2.25	2.84		32	15	85	0	4928	2662	2602	2632	1.87	11100
10	1131	7	skeletal grainstone	dense c.	2.73	2.84	<0.01	6	17	83	0	6350	3487	3492	3490	1.82	17355
92	1154	0	skeletal grainstone	dense c.	2.46	2.87		22	0	100	0	5314	2950	2987	2968	1.79	13052
90	1161	9	skeletal pack- to wackestone	micro-p.	2.02	2.87		46	0	100	0	2415	1245	1254	1250	1.93	4887
12	1173	0	skeletal grainstone	dense c.	2.68	2.73	<0.01	3	87	13	0	6031	3137	3100	3118	1.93	16148
91	1174	4	muddy wackestone	micro-p.	1.95	2.76		47	71	17	13	2299	1181	1182	1182	1.95	4493
13	1238	6	skeletal packstone	inter-p.	1.97	2.77	137	45	64	36	0	2267	1073	1071	1072	2.12	4478
14	1285	3	skeletal packstone	co. mold.	2.27	2.71	3.0	26	100	0	0	4156	2281	2179	2230	1.86	9425
45	1339	5	skeletal packstone	co. mold.	1.90	2.76	256	50	70	30	0	2304	1398	1410	1404	1.64	4374
15	1452	6	skeletal packstone	fi. mold.	1.89	2.74	265	49	79	21	0	2353	1070	1064	1067	2.21	4456
93	1482	7	skeletal pack- to grainstone	co. mold.	1.93	2.71		46	100	0	0	2579	1388	1393	1390	1.85	4988

Table 7 b: Petrophysical and lithological data of measured samples from hole Unda on Great Bahama Bank. Abbreviations for pore types: inter p.=interparticle porosity; micro-p.=microporosity; fi. mold=fine (<300µm) moldic porosity; co. mold.=coarse (>300µm) moldic porosity; intra p.=intraparticle porosity; dense c.=densely cemented.

Unda Clino	sample #	depth (ft.)	Vp 3 MPa	Vp 7 MPa	Vp 10MPa	Vp 14 MPa	Vp 17 MPa	Vp 28 MPa	Vp 52 MPa	Vp 69 MPa	Vp 103MPa
U	1	135	4447	4475	4460	4475	4529				
U	2	272	4969	4997	4997	5007	5007	5026			
U	3	357	2099	2237	2401	2462	2598				
U	4	595	2640	2649	2637	2637	2720				
U	5	917	2363	2403	2580	2712	2766				
U	6	938	2696	2696	2696	2638	2723				
U	7	961	5952	5952	5952		5959	5966	5966	5973	
U	8	994	4813	4858	4858	4912	4940				
U	9	1056	2366	2404	2441	2476	2606				
U	10	1131		6349			6365	6373	6388	6388	
U	12	1173		6030			6037	6051	6058	6085	
U	13	1238	2257	2267	2365	2513	2595	2744			
U	14	1285	4143	4155	4169	4169	4175				
U	15	1452	2184	2353	2532	2686	2851	3137			
C	16	185	3008	3208	3267	3421	3487	3755	4073	4213	
C	17	281	4901	5043	5064	5064	5064	5022	4739	4721	
C	18	294	4376	4391	4391	4391	4376	4422	3513		
C	19	341	5793	5818	5830	5830	5856	5856			
C	20	442		3865			3870	3929	3842		
C	21	525	4109	4109	4122	4128	4134	4141	3934		
C	22	586	2985	2985	2958	2894	2907	3112			
C	23	611	2610	2675	2681	2738	2844	3069			
C	24	693		5454			5454	5454	5465	5471	
C	25	774	2406	2503	2631	2653	2662				
C	26	840		5350			5350	5366	5366	5372	5372
C	27	955	2116	2219	2280	2487	2620	2558			
C	28	1084	2174	2368	2486	2612	2680				
C	29	1165		6045			6045	6052	6052	6066	
C	30	1206		5478			5489	5500	5517	5529	
C	31	1503	2884	2926	2933	2920	2876				
C	32	1674	2953	2983	3023	3094	3112	3178			
C	33	1758	2397	2408	2495	2658	2692				
C	34	1985	2339	2402	2470	2570	2648				
C	35	2046	2528	2602	2633	2643	2622				
C	36	2197	3151	3151	3188	3208	3219	3117			
U	37	401	3010	3024	3024	3006	2934				
U	38	443	2386	2567	2781	2894	2999				
U	39	517	2520	2638	2795	2873	2951				
U	40	673	2465	2477	2605	2748	2825	3126			
U	41	884	2523	2500	2537	2656	2783	3141			
U	42	1016	3175	3191	3276	3330	3330				
U	43	1037	4530	4566	4566	4575	4585				
U	44	1105	4946	4927	4927	4946	4956				
U	45	1339	2308	2303	2439	2534	2665				
C	46	860	4721	4721	4704	4713	4713				
C	47	365	5829	5855	5855	5880	5906				
C	48	476	3810	3863	3874	3918	3941				
C	49	741	4649	4640	4658	4658	4658				
C	50	1042	2188	2365	2489	2647	2720				
C	52	1597	2590	2646	2674	2692	2698				
C	53	1798	1888	2156	2341	2464	2620	2948			
C	54	2056	2914	2947	2960	2967	2967				

Table 8 a: Compressional wave velocities (Vp, m/s) of Bahamas samples # 1-54 at different effective pressures.

Unda Clino	sample #	depth (ft.)	Vp 1 MPa	Vp 3 MPa	Vp 8 MPa	Vp 13 MPa	Vp 18 MPa	Vp 23 MPa	Vp 28 MPa	Vp 38 MPa	Vp 48 MPa	Vp 58 MPa	Vp 68 MPa	Vp 78 MPa	Vp 88 MPa	Vp 98 MPa
C	57	110	3801	3794	3801	3782	3813									
C	58	182	4830	4879	4917	4936	4942		4968	4974	4620					
C	59	210	4816	4870	4876	4894	4888	4900	4919	4912	4950					
C	60	488	3470	3501	3520	3501	3526	3609	3629	3649						
C	61	526		2956	2960	2983										
C	62	720		5386	5394		5401		5424	5424						
C	63	1151	5650	5655	5661	5666	5678		5683	5694	5700	5700		5711		
C	64	1343		3013	3093	3116	3081									
C	65	1617	2516	2678		2913	2893	2905								
C	66	1681	2939	3109	3103	3076										
C	67	1812		2574	2700	2715	2691	2584	2671	2831						
C	68	1756			2791	2725	2686									
C	69	1732	2363	2510	2618											
C	70	2049	2224	2349	2541	2599	2497									
C	71	2155	4340	4348	4373		4400		4413	4430	4443	4436	4439	4439		
C	72	2156	2999	3053	3162		3315		3381	3426	3450	3466	3466	3480		
C	73	2216		2421	2478	2418										
C	74	2183	2279	2339	2424	2447	2508		2701	2840						
U	75	870	5364	5334	5379		5410		5425	5410		5394		5410		
U	76	185	3782	3788	3776	3770	3788		3807							
U	77	212		4105	4112	4125										
U	78	388	2124	2243	2433											
U	79	356	3549	3559	3549	3539	3544		3573	3578						
U	80	368	3168	3181	3168	3083	3048									
U	81	451		2986	3046	2687										
U	82	656	2227	2465	2544	2718	2901									
U	83	464	3839	3886	3905	3925	3935		3935	3935	3915	3857	3867	3896		
U	84	945	1940	2045	1999											
U	85	860	2121	2289	2629	2830	3028									
U	86	889	3476	3492	3481	3476	3465		3349	3390						
U	87	992			4015	4011										
U	88	1092	2979	3001	3001											
U	89	1008	3117	3156	3176	3214	3231	3238	3183	2919	2948	3053	3183	3293	3411	3487
U	90	1161	2394	2424	2415	2406	2575		2877	3097	3233					
U	91	1174	2333	2329	2299											
U	92	1154	5272	5286	5300	5314	5328		5314	5321	5335	5335	5328			
U	93	1482	2475	2579	2053											

Table 8 b: Compressional wave velocities (Vp, m/s) of Bahamas samples # 57-93 at different effective pressures.

sample #	depth in core (cm below surface)	approx. compaction of sample length (%)	wet bulk-density before compaction	wet bulk-density after compaction	grain density (g/cm^3)	porosity before compaction (%)	porosity after compaction (%)	Vp (m/s)	Vs1 (m/s)	Vs2 (m/s)	Vs mean (m/s)	Vp/Vs	acoust. impedance ($10^3 kg/m^2 s$)
FAM 2	35	42	1.79	2.22	2.85	58	35	2144	944	953	948	2.26	4760
FAM 3	35	45	1.78	2.25	2.85	59	33	2257	970	982	976	2.31	5081
FAM 4	30	23	1.76	1.93	2.85	60	50	1894	672	694	683	2.77	3658
FAM 6	65	37	1.84	2.19	2.85	55	36	1952	892	883	887	2.20	4284
FAM 7	60	0	1.77	1.78	2.85	59	59	1701	no	shearwave	detectable		3026
FAM 8	55	0	1.83	1.79	2.85	56	58	1769	no	shearwave	detectable		3160
FAM 9	50	22	1.83	1.99	2.85	56	47	1831	744	735	739	2.48	3647
FAM 10	40	32	1.68	1.99	2.85	64	47	1841	814	824	819.0	2.25	3664
FAM 11	35	32	1.81	2.17	2.85	57	37	2026	997	974	985	2.06	4405
FAM 12	30	5	1.79	1.87	2.85	58	54	1725	no	shearwave	detectable		3223
FAM 13	25	31	1.82	2.16	2.85	57	38	1919	1046	1057	1052	1.83	4143
FAM 14	20	36	1.70	2.06	2.85	63	43	1855	949	1000	974	1.90	3828
FAM 15	65	36	1.76	2.18	2.85	60	37	1995	1185	1183	1184	1.68	4351
FAM 16	60	41	1.86	2.22	2.85	54	35	2100	915	911	913	2.30	4654
FAM 17	58	39	1.77	2.25	2.85	59	33	2044	912	917	914	2.24	4596
FAM 18	55	36	1.88	2.31	2.85	53	30	1953	792	801	796	2.45	4516
FAM 19	50	43	1.70	2.20	2.85	63	36	2138	1051	1039	1045	2.05	4710
FAM 20	40	38	1.67	2.03	2.85	65	45	1925	1100	1089	1094	1.76	3903
FAM 21	35	40	1.69	2.19	2.85	64	36	1992	1131	1092	1111	1.79	4359
FAM 22	25	49	1.67	2.27	2.85	65	32	2144	1026	998	1012	2.12	4859

Table 9: Petrophysical data of measured samples from Florida Bay.